Materials Science in Additive Manufacturing

eISSN: 2810-9635
Volume 4 Issue 1, 2025

ACCSCIENCE PUBLISHING

ACCSCIENCE PUBLISHING

Materials Science in Additive Manufacturing

Online ISSN: 2810-9635

Materials Science in Additive Manufacturing aims to bridge the cutting-edge research between additive manufacturing and the entire spectrum of materials science. The journal covers all applied and fundamentals of processing, synthesis, structure, composition, properties and performance of materials designed or manipulated for additive manufacturing. The journal covers a wide scope of innovative techniques, processes, methods, and applications.

About the Publisher

AccScience Publishing is a publishing company based in Singapore. We publish a range of high-quality, open-access, peer-reviewed journals and books from a broad spectrum of disciplines.

Contact Us

Managing Editor
msam.office@accscience.sg

AccScience Publishing
8 Burn Road, #15-03 Trivex, Singapore 369977.

Volume 4 • Issue 1 • March 2025
ISSN 2810-9635 (online)

MATERIALS SCIENCE IN ADDITIVE MANUFACTURING

Editor-in-Chief

Chee Kai Chua

Singapore University of Technology and Design, Singapore

ACCSCIENCE PUBLISHING

MATERIALS SCIENCE IN ADDITIVE MANUFACTURING

ISSN: 2810-9635 (online)

Editorial and Production Credits

Publisher: AccScience Publishing
Managing Editor: Wendy Yang
Editorial Assistant: Flora Kang
Production Editor: Puva Ramakrishnan
Article Layout and Typeset: Sinjore Technologies (India)

For all advertising queries, contact msam.office@accscience.sg.

Supplementary file

Supplementary files of articles can be obtained at https://accscience.com/journal/MSAM/4/1.

Disclaimer

AccScience Publishing is not liable to the statements, perspectives, and opinions contained in the publications. The appearance of advertisements in the journal shall not be construed as a warranty, endorsement, or approval of the products or services advertised and/or the safety thereof. AccScience Publishing disclaims responsibility for any injury to persons or property resulting from any ideas or products referred to in the publications or advertisements. AccScience Publishing remains neutral with regard to jurisdictional claims in published maps and institutional affiliations.

Material Science in Additive Manufacturing

Editorial Board

ACCSCIENCE PUBLISHING

Volume 4 | Issue 1 | March 2025 |

Materials Science in Additive Manufacturing

https://accscience.com/journal/msam

CONTENTS

ACCSCIENCE PUBLISHING

Materials Science in Additive Manufacturing

REVIEW ARTICLE

A review on development of eco-friendly natural fiber-reinforced composite filaments for 3D printing: Fabrication and characteristics

Raviduth Ramful*

Department of Mechanical and Production Engineering, University of Mauritius, Réduit, Mauritius

Abstract

Additive manufacturing (AM), commonly referred to as 3D printing, has revolutionized the modern manufacturing world by providing comprehensive benefits in terms of mass customization, automation, design optimization, quick prototyping, and reduced lead times among other factors. Given the increased popularity, rapid development, and implementation of AM technologies in numerous engineering applications, new methods to enhance the AM process for improved efficiency and to attain sustainability goals are being considered. One approach to achieve sustainability in AM is by considering greener input materials such as natural fiber-reinforced composite filaments (NFRCFs) with lower embodied energy. This review focuses on the latest advancements made in the research and development of advanced NFRCFs for the AM process. In the first section, the rationale of using natural fibers in modern NFRCFs is outlined, followed by a description of the key stages of their fabrication process involving the pre-processing of fibers and the addition of plasticizer to enhance their performance. In the second part of this review, a detailed overview of the typical fibers and matrices used in the development of NFRCFs is provided, and some of the typical challenges encountered when utilizing natural fibers, such as their lack of homogeneity, are highlighted. The fiber-matrix interaction and corresponding properties are further discussed, and means to achieve homogeneous NFRC filament are outlined. Finally, the degradability characteristics and recycling methods for NFRCF are discussed, and further means to optimize their performance for increased usage in AM and related applications are presented. To address and overcome the foregoing limitations posed by present-day NFRCF, further research for breakthrough solutions is still required. Further research and development in this area is a prerequisite to attain sustainability in AM, which will also promote the usage and integration of sustainable AM parts into a wider range of engineering applications in our modern society.

Keywords: Natural fiber-reinforced composite filament; 3D printing; Natural fibers; PLA matrix; Mechanical performance; Biodegradable

***Corresponding author:**
Raviduth Ramful
(r.ramful@uom.ac.mu)

Citation: Ramful R. A review on development of eco-friendly natural fiber-reinforced composite filaments for 3D printing: Fabrication and characteristics. *Mater Sci Add Manuf.* 2025;4(1):8533. doi: 10.36922/msam.8533

Received: January 14, 2025

Revised: February 1, 2025

Accepted: February 7, 2025

Published Online: February 27, 2025

1. Introduction

The general method of conventional manufacturing is at its turning point in time with the advent of new manufacturing technologies in line with Industry 4.0, whereby

intensive manual operations are being replaced by automated processes and advanced technologies as displayed in Figure 1. Additive manufacturing (AM), commonly referred to as 3D printing, is a layer-by-layer technique that has comprehensive benefits in terms of material usage for design optimization in comparison to conventional construction techniques. This non-conventional type of manufacturing has shown significant benefits in numerous fields with convincing results in pioneering applications ranging from medical implants to advanced composite developments.[1-4] Prospects involving 3D-printed constructions are substantial in key areas of development whereby conventional means would be inefficient, such as the establishment of temporary housing in remote areas.[5] Regardless of the significant advancement in AM, the realization of reliable 3D-printed structures of acceptable engineering standards through design optimization still demands notable attention for further research.[5]

AM enables the conceptualization of complex geometries with the added benefit of design optimization for improved performance in terms of strength-to-weight ratio. The bio-inspired solution in AM has been considered to enhance printing patterns[7] but, most importantly, to generate final components with comparable strength and hardness as observed in nature, such as the honeycomb[8] and seashell structures.[9-11] From the literature, the intricate structure of natural materials such as bamboo was successfully reproduced by AM for various applications ranging from crash-absorbing components[12] to optimized lightweight bionic beams.[13] Likewise, the fabrication of complex lattice structures such as the body-centered cubic lattice,[14] which is seemingly intensive through conventional means, is simply rendered possible by AM.[15] Additional lattice structures which can be machined by AM, namely the hierarchical honeycomb,[16] cube vertex centroid, and hex prism diamond, are displayed in Figure 2.

AM technologies have drastically expanded in the last decade, and the utilization of commonly used materials such as plastics,[4,8,11] cement,[17-21] and metals,[22,23] have all yielded up-to-standard results. To cater for the surge in demand for 3D-printed products in numerous fields of applications, AM technology has been developed and transformed into a multitude of distinctive systems.[24]

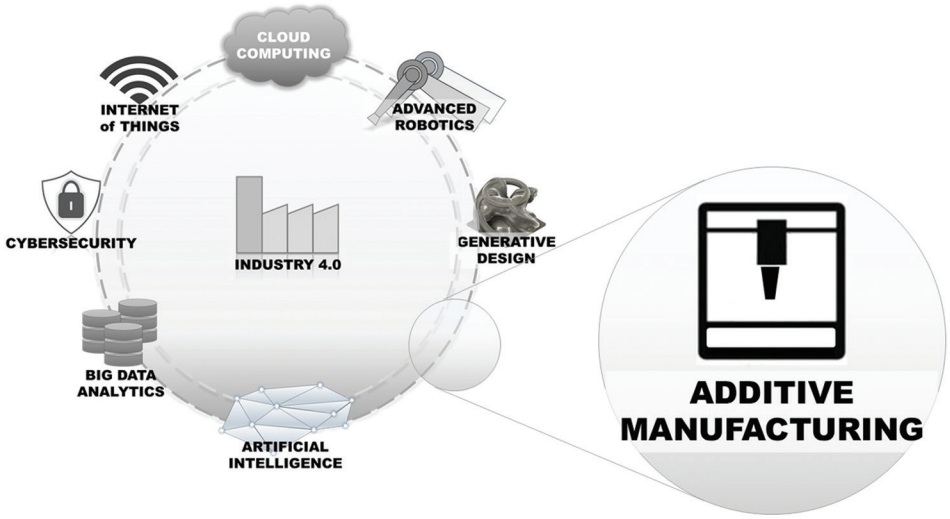

Figure 1. Advent of new manufacturing technologies in line with Industry 4.0, including additive manufacturing technology[6]

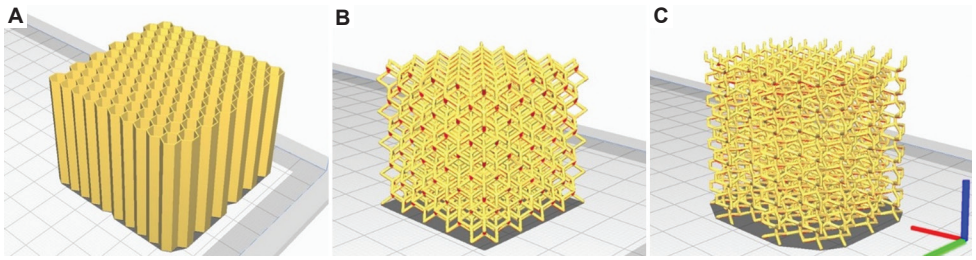

Figure 2. Lattice structures which can be machined by additive manufacturing, namely the (A) hierarchical honeycomb,[16] (B) Tet-vertex-centroid, and (C) hex-prism-diamond structures

Some of these developed systems include material extrusion (Figure 3A), vat photopolymerization (Figure 3B), binder jetting process, material jetting, powder bed fusion (Figure 3C), sheet lamination, and directed energy deposition[24] techniques. The fused deposition modeling (FDM) process is one noteworthy technique under the material extrusion category of AM, which has gained significant interest from industries and mass consumers in recent years. Besides their ease of implementation, reliability, and affordability, this material extrusion-based process uses ready-made and off-the-shelf filament reels as input material, as shown in Figure 4.

The basis of AM, which is conceived from the layer-by-layer material deposition technique, predominantly depends on its material characteristics. Some of these notable physical and mechanical material characteristics, which are prerequisites for AM, include viscosity, density, coefficient of thermal expansion, melting point, durability, stiffness, ultimate strength, and ultimate strain, among other factors.[25-27] For instance, 3D-printed filament materials with high viscosity will increase the load on the extruder as more extrusion force will be required. On the other hand, filament materials with increasingly low viscosity can lead to a lack of precision in the deposited layers as they will be difficult to control due to excessive flowability. Hence, achieving the optimum characteristics in filament material is key to securing the best results in AM.

A classification chart for commonly used filament materials in the FDM process is outlined in Figure 5. As evidenced by this figure, most developed filament materials for the FDM process are of a non-biodegradable nature. The specifications, characteristics, and application of commonly used non-biodegradable filament polymer materials developed in recent years for the FDM process are given in Table 1. Table 2**,** on the other hand, displays the specification, characteristics, and application of the few biodegradable filament materials that have been investigated in the literature.

Even though the material characteristics account for the main factor for optimum performance in 3D-printed parts, other factors pertaining to the printing settings

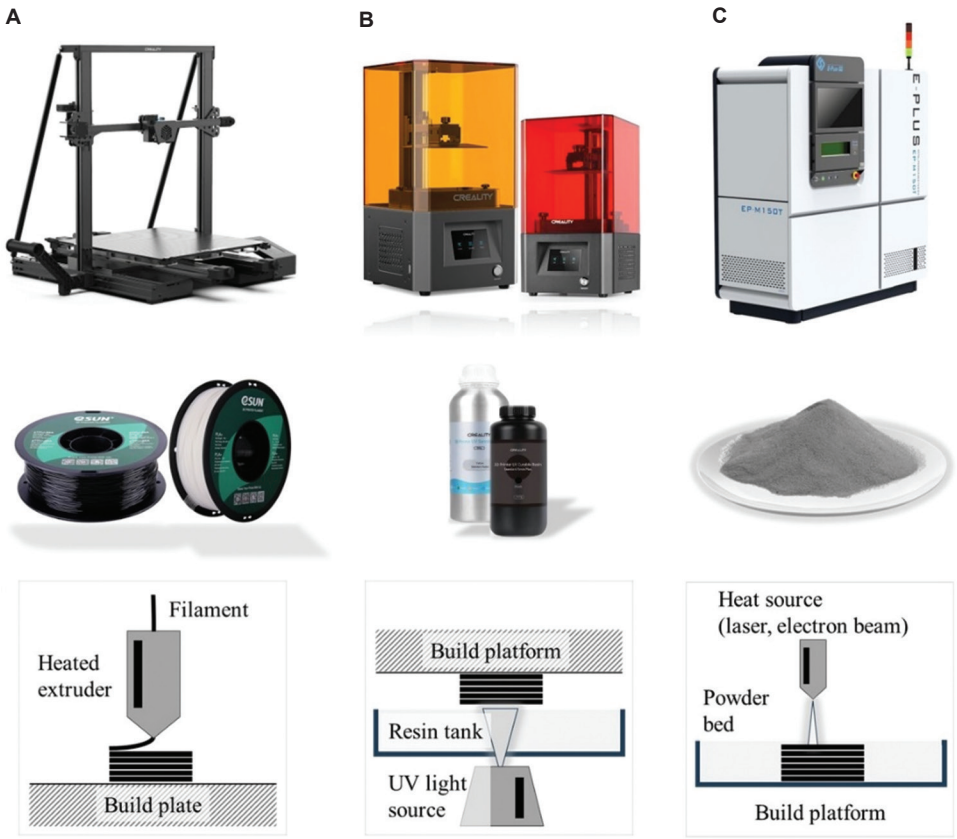

Figure 3. Developed additive manufacturing technologies and corresponding input material to suit the needs of specific engineering fields, namely the (A) material extrusion also known as fused deposition modeling, (B) vat photopolymerization, and (C) powder bed fusion techniques[6]

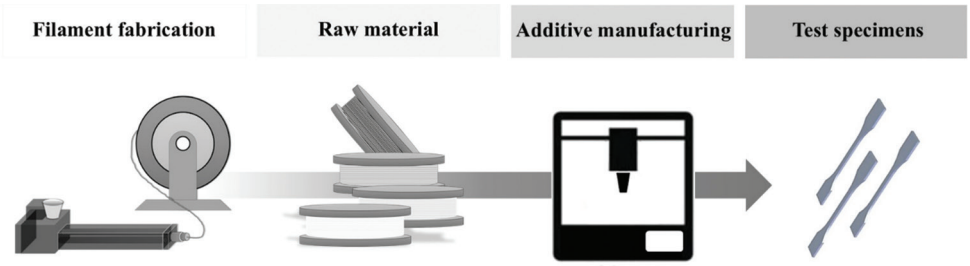

Figure 4. Overview of the fused deposition modeling process in additive manufacturing from the fabrication to specimen generation stage

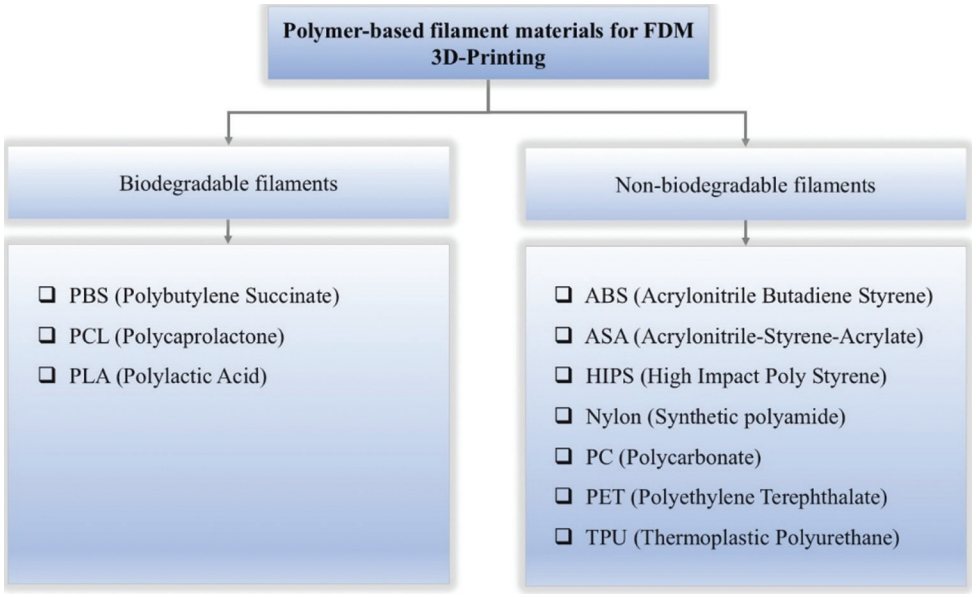

Figure 5. Classification chart for commonly used filament materials in the fused deposition modeling process

can also influence the quality of 3D prints and their corresponding structural features in the FDM process.[40] For instance, the infill pattern and cross-sectional features are generally associated with the shell outline of 3D-printed parts for optimum structural stability. Commonly applied infill geometrical patterns in AM involve grid, cross, cubic, hexagonal, and concentric patterns. In addition to the foregoing features, other printing parameters such as layer thickness and print path among others, also affect the print resolution, bonding strength, and deformation-resisting ability.[18,19,41] Therefore, printing parameters, as a consequence, influence the structural performance of 3D-printed constructions.[5]

In recent years, alternative materials have been considered for the development of composite filaments with enhanced cost, performance, and durability traits. One such example is fibers derived from natural or synthetic sources that are processed and integrated with the various types of polymer-based matrix, as highlighted in Tables 1 and 2. In contrast to synthetic fibers which are non-biodegradable, natural fibers have gained notable interest in composite development in general, given their distinctive, sustainable characteristics and biodegradable nature.[42]

Natural fibers derive their strength from their unique structural arrangement composed of primary and secondary cell walls.[42,43] Microfibrils which are composed of key plant derivatives, namely cellulose, hemicelluloses, and lignin,[44] have a determinant role in the corresponding mechanical performance of natural fibers. The mechanical characteristics were found to largely depend on the alignment of microfibrils in plant cell walls.[45,46] Even though animal fibers have been considered in the past, most natural fibers are derived from plant fibers, and their sources include bast, leaf, fruit, seed, and grass fibers.[42,47,48]

2. Rationale to use NFRCFs in AM

In recent years, alternative materials with sustainable attributes such as natural fibers have been considered for the development of advanced composites through the AM

Table 1. Specification, characteristics, and application of commonly used non-biodegradable filament polymer materials in the FDM process

S. No.	Specification of non-biodegradable filament polymer	Characteristics	Applications	References
1	ABS	High rigidity, medium impact strength, heat-resistant, and ease of fabrication	Widely used in FDM given its cost-effectiveness, used in moving parts, automotive parts, and functional parts	28
2	Nylon (synthetic polyamide)	Chemical-, wear- and UV-resistant; strong and durable; flexible with low friction coefficient	Used in FDM to produce semi-flexible and mechanical parts (industrial components)	29
3	PET	Good chemical resistance and mechanical properties, good dimensional stability, and heat resistance	Suitable for producing water-resistant products in FDM, it can be used to create custom tools and fixtures	30
4	ASA	Exhibit better UV resistance than ABS; good impact strength and resistant to harsh weather conditions	Suitable for general-purpose 3D printing applications, including prototyping and tooling	31
5	TPU	Has good shock-absorbing characteristics; flexible and durable	Widely used in applications whereby flexibility and rubber-like parts are required, namely hoses, sleeves, and flexible joints	32
6	PC	PC samples tend to display strong anisotropy as a function of raster orientation – suitable for higher temperatures and strong impacts	Can be used for prototyping and in functional components	33

Abbreviations: ABS: Acrylonitrile butadiene styrene; ASA: Acrylonitrile-styrene-acrylate; FDM: Fused deposition modeling; PC: Polycarbonate; PET: Polyethylene terephthalate; TPU: Thermoplastic polyurethane; UV: Ultraviolet.

Table 2. Specification, characteristics, and application of commonly used biofilament polymer materials in the FDM process

S. No.	Specification of biofilament polymer	Characteristics	Applications	References
1	PLA	Biodegradable, high dimensional stability, and odorless	Multipurpose material used for a wide variety of applications, including in the medical field	34,35
2	Impact PLA Grey	Biodegradable PLA with high strength and rigidity	Can be used to produce spare parts, tools, and prototypes	36
3	PLA and PLA-PHA	Biodegradable PLA	Used for marine structures	37
4	PBS and PBSA	Good thermal stability, biodegradable, high viability for FFF process	Can be used in 4D printing to create complex 3D architectures	38
5	PCL	Biodegradable, semi-crystalline polyester having a low glass transition temperature and melting point	Used in AM techniques to produce PCL scaffolds for various tissue engineering applications, including bone, muscle, cartilage, and skin	39

Abbreviations: AM: Additive manufacturing; FDM: Fused deposition modeling; FFF: Fused filament fabrication; PBS: Polybutylene succinate; PBSA: Polybutylene succinate ran adipate; PCL: Polycaprolactone; PHA: Polyhydroxyalkanoate; PLA: Polylactic acid.

process. The general consensus to consider natural fibers in the specialized field of AM, besides its numerous and well-known advantages ranging from the fabrication of complex parts to quick prototyping, is to foster the production of sustainable parts.[49] From an economic perspective, the abundance of natural fibers in the environment makes them an attractive and affordable alternative to synthetic composites.[50,51] Natural fibers, along with synthetic fibers, have been widely considered in the recent past for the development of advanced composite materials,[50] and their applications can range from medical science[52] to aerospace engineering.[53] The specific stiffness, impact energy absorption, and enhanced durability attributes of some of the developed composites have transformed them into excellent alternatives to conventional concrete, steel, and timber materials.[50]

In terms of physical characteristics, natural fibers bear a relatively low density and are lightweight in nature. This feature further strengthens their consideration and selection for high-strength-to-weight ratio components

in advanced engineering applications. The harvesting and processing of natural fibers is notably less intensive than other conventional materials such as concrete and metals. The energy requirement to process the material is subsequently lower, which translates into a relatively lower processing cost for natural fibers.[54] As a result, the use of natural fibers in the development of biodegradable composites in the production phase was advanced to lead to reduced embedded energy in the developed products.[54]

Besides their mechanical and physical attributes, some of the outstanding features of natural fibers that render them attractive for AM are their sustainability attributes. Given the potential of AM in numerous engineering applications, it is imperative to optimize the process for improved efficiency and attainment of sustainability attributes. One approach is to consider alternative input materials from greener or recycled sources at the expense of conventional ones. Besides, the use of greener or recycled input materials will address the growing ecological concerns as the promotion of renewable resources has a minimized environmental impact. In addition, such resources will possess a notably lower carbon footprint given their reduced embodied energy, hence addressing the issue of climate change.[50]

Product developers and manufacturers are looking at the entire lifecycle of products, including their disposal and recyclability, to address the growing issue of waste disposal around the world. The disposability of modern developed materials, which can have a reduced impact on the environment, is therefore regarded as a key requirement to attain sustainability. The conventional composite filaments used in the present-day AM process, which are mainly composed of non-biodegradable components, add to the challenge of recycling. The consideration of natural fibers for NFRCF development can address some of the foregoing issues encountered in the use of conventional filaments in the AM process.

The shift toward greener materials such as NFRCFs also aims to address the significant surge in the usage of non-biodegradable composites such as synthetic plastics. Their extensive usage has resulted in the accumulation of non-degradable material in delicate environments such as in the ocean, thereby greatly affecting the Earth's ecosystem.[55-59] Further research involving natural fiber-based composites aims to look at alternative measures that can enhance the degradability of conventional composites, thereby minimizing the impact of waste disposal on the environment. The use of natural fibers in NFRCF, which, however, poses numerous challenges from fabrication to the end of the lifecycle stage, is further examined in this review.

3. NFRCF fabrication

Unlike other materials, natural fibers that are derived from organic sources tend to exhibit significant variability as a result of maturity, environment, and harvest period, among other factors. Thus, specific considerations are needed when processing and when transforming natural fibers into alternative forms to ensure consistency during production. In their raw and unmodified state, natural fibers have a tendency to absorb moisture content while displaying overall lower mechanical and durability attributes.[50,60,61] Besides their limited physical and mechanical characteristics, natural fibers have a relatively low thermal stability which is below 200°C.[54] Therefore, specific treatment modifications are normally required in the pre-processing stage to prepare natural fibers, while care must be taken to ensure that the effects of thermal treatment do not lead to permanent alteration to their structure. Moreover, the lack of relevant standards regarding the fabrication and validation of 3D-printed materials and structures, respectively, adds to the list of challenges observed in the emerging field of AM.[62]

The fabrication of filament materials from natural fibers for use in the FDM technique has been successfully realized as reported in previous studies.[63,64] In one study, NFRC components were successfully produced via the FDM technique by considering two types of natural fibers involving hemp and New Zealand flax, which were impregnated in a polymeric matrix composed of lignin.[63] Before the filament fabrication stage, the natural fibers were subjected to an alkali treatment consisting of NaOH solution followed by a digestion cycle of around 30 min at 160°C.[63] Finally, the fibers were thoroughly washed with tap water, subjected to drying in an oven for 48 h above 100°C, and mixed in an intensive mixer consisting of two rotating shafts and a heated chamber set at 185°C.[63] A polylactic acid (PLA) binder in the form of power was used in the mixing stage. The mixed composite material was then subjected to a granulation stage followed by an extrusion process, which would produce continuous filament wire.[63]

One of the key parameters to control filament production is the cross-section of the filament wire.[63] To achieve a filament cross-section of acceptable tolerance, the electric spooling machine could be utilized to precisely control the extrusion and rotational speed of the filament spooling machine. The detailed outline of the filament fabrication process is given in Figure 6. The filament extrusion stage, which precedes the spooling stage, as displayed in Figure 6, is another decisive stage in the process of achieving a filament end-product with consistent mechanical properties and diameter. Even though both twin-screw extruders and single-screw extruder are widely considered for the filament extrusion process, the former was found

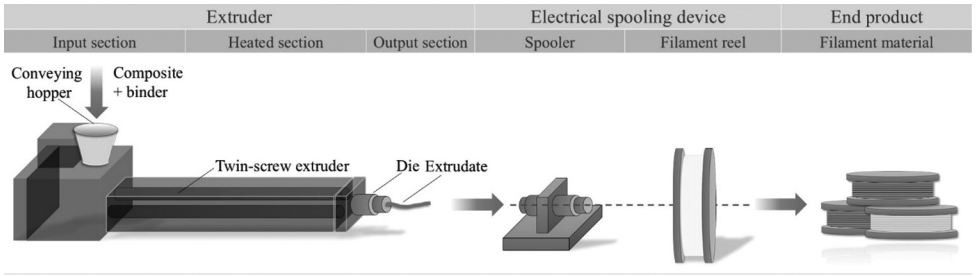

Figure 6. Detailed outline of the filament fabrication process through the twin-screw extruder device

to offer better features in terms of mixing capabilities, temperature control, and throughput efficiency.[65] Some of the commonly used extruders for filament fabrication include the Wellzoom desktop single-screw extruder[66] and the HAAKE Mini CTW Micro-Conical Twin Screw Compounder.[67]

As reported in several studies, a filament diameter of 1.75 mm was considered when extruding the biofilament material, which also corresponds to the standard filament diameter used in FDM printers.[68,69] Moreover, the 1.75 mm filament was mainly considered for further investigation as reported in previous studies, as they tend to provide finer details and better print quality overall.[70] Besides, the 1.75 mm-sized filament, which offers better compatibility with small-sized nozzles, was found to be less susceptible to breakage given their enhanced flexibility in contrast to large-diameter filaments. In the fabrication process of wood flour-PLA filament, a two-stage extrusion process was considered whereby a twin-screw extruder was used in the first place for pelleting followed by a single-screw extruder which was used for extrusion molding to generate the 1.75 mm in diameter filament material.[71] In another study, a two-stage extrusion process, consisting of a single screw and corotating meshing twin-screw extruders, was also considered in the filament formation involving PLA and biodegradable plasticizer.[64] The extrusion temperature of FDM filaments, which can vary over a wide range of temperatures ranging between 160°C and 230°C, is dependent on the properties of the source material from which the filament is derived.[72]

3.1. Pre-processing of fibers and addition of plasticizer for filament fabrication

In the AM process, the final strength of printed components largely depends on the characteristics of the filament material. Similar to the fabrication of conventional natural fiber composites, the utilization of natural fibers in the fabrication of filament material poses common challenges, namely incompatibility with the polymer matrix, susceptibility to moisture absorption, and inhomogeneous distribution of fibers among others.[61,73,74] To address the foregoing challenges and for consideration in filament-based material in AM, most natural fibers would, therefore require further treatment modification so as to improve their surface adhesion with the polymer matrix.[75] Natural fibers are thus subjected to a pre-processing stage consisting of chemical or thermal treatment modifications, which is an indispensable stage in the fabrication of filament material from natural fiber-reinforced polymer composites.[49] Typical pre-processing stages, which could have a direct impact on the characteristics and usability of the final filament material, include sieving of fibers, drying, and mixing methods. For instance, drying methods and surface treatment have been reported to promote good adhesion between natural fibers and polymer matrix in the NFRC mix, thereby enhancing their mechanical properties.[73]

To further enhance the properties of natural fiber-reinforced composite filaments (NFRCFs), additives are generally considered.[73] Typically used additives for this purpose can be classified in terms of compatibilizer, plasticizer, and toughening agent.[73] The addition of plasticizer in the composite mix for filament formation, for instance, was found to result in a notable improvement in their interfacial bonding.[76] The inclusion of plasticizer was thus found to improve printing parameters such as layer adhesion and surface finish.[73] In another study, the addition of plasticizer to polymeric filament was found to be beneficial to 3D-printed products as it had a positive impact on their thermal properties and shape stability, hence reducing the warping effect.[64] In one investigation, the use of glycerol as a plasticizer in wood flour-PLA filament was found to be most suited for extrusion processing of composite filaments as they exhibited a higher melt index.[71]

Besides their noteworthy contribution to the improvement of printing parameters, the inclusion of plasticizers in NFRCFs was found to significantly enhance their mechanical characteristics. On the other hand, another plasticizer, namely tributyl citrate (TBC), was found to enhance the mechanical properties, water absorption, and thermal stability of the wood flour-PLA filament despite resulting in an inferior melt index.[71] In

another study, the crystallization behavior was further investigated to probe into the effect of the addition of plasticizer, namely polyethylene glycol (PEG), on the mechanical and physical properties of filament materials produced through the fused filament fabrication (FFF) technique.[77] The addition of PEG plasticizer was found to result in 3D-printed parts with crystallinity values of up to 18% greater as compared to neat PLA, which also translated into improved mechanical and physical characteristics.[77] The inferior mechanical properties observed in neat poly(3-hydroxybutyrate) and PLA (PHB/PLA) blends were found to be significantly improved upon the addition of plasticized blends based on esters of citric acid.[64] Moreover, the inclusion of such plasticizers in the filament material blend led to a notable increase in the softening effect in the filament structure, thereby resulting in a significant increase in their elongation at break.[64]

4. Fibers and matrix selection for biodegradable NFRCFs

In previous studies, diverse types of natural fibers have been considered in the production of natural fiber-reinforced composite filaments.[73] Examples of such natural fibers consisted of rice straw, bamboo, hemp, sugarcane, and flax fibers.[63,73,78-80] The fiber content by weight in the NFRCFs was found to range between 15% and 30%.[63,73,78-80] Table 3 summarizes the specification, composition, characteristics, and applications of commonly used composite-based non-biodegradable filament materials for 3D printing. Even though the filament material developed in these studies displayed satisfactory mechanical performance, they were not fully biodegradable as a result of their polymeric matrix, which lacked the degradability trait. ABS is one such example that has poor degradable characteristics but nonetheless displays high tensile strength while being resistant to physical impacts.[49,81]

Besides the use of natural fibers, many studies have considered fibers in powdered form as an alternative reinforcement component for filament fabrication. One example is bamboo-plastic composite wires, which were developed through the FDM technique by considering printed wires made of bamboo flour, PLA matrix, and plasticizers.[76] Another powder-based material, namely wood flour, was considered to produce wood flour-PLA filament at a composition ratio of 1:2.3.[71] Before the filament fabrication, sieved wood flour from 140-mesh to 160-mesh size was mixed with PLA and distilled water, while experimental reagents, namely glycerol and TBC, were considered and added as plasticizer.[71] In another study, 3D printing composite filaments from agro-industrial and polymeric wastes were developed by considering cocoa bean shells and recycled polypropylene, respectively. The combination of these two materials in the filament production was found to result in a reduced shrinkage and warping behavior, thereby further enhancing the dimensional stability of the sample during the 3D printing process.[68]

Moreover, the development of biodegradable composites through 3D printing technology from the derivatives of natural fibers, namely cellulose, hemicellulose, and lignin, has also been realized in the recent past.[84] For instance, the optimum amounts of other naturally derived components, namely hemicellulose and lignin, which could be added in the preparation of composite filament for 3D printing, were found to be 25% and 5%, respectively.[69,85] In other studies, cellulose-based composite filament wire was successfully prepared by combining cellulose nanofiber (CNF) and PLA.[67] In contrast to pure PLA filament wires, the inclusion of cellulose reinforcement in the PLA-composite filament wires was found to yield an increase in its tensile strength.[84] Besides improvement in their mechanical properties, CNF-based biocomposite filament was also found to have enhanced thermal stability.[67]

4.1. Challenges of using natural fibers in NFRCFs for fused deposition modeling

The challenges associated with the consideration of natural fibers in the fabrication of biodegradable composite filaments and their utilization are further discussed in this section. One of the main concerns observed when dealing with natural fiber-based filament material during the AM process is the lack of homogeneity in the deposited layers.[73,86] The lack of homogeneity was found to arise due to the combined effects of several factors originating from the printer hardware, printing parameters, and material composition as outlined in Figure 7. For instance, it is to be noted that the homogeneity of 3D-printed structures is normally affected by the print direction, which has a significant impact on their load-bearing capacity, thereby resulting in an orthotropic behavior.[21,87,88]

In terms of material composition, the inhomogeneous mix of natural fiber composite for filament material can lead to a lack of homogeneity in the final product. As reported in previous studies, it is unfeasible to achieve a near-perfect homogeneous mixture of natural fiber composite for filament material in line with existing technologies. It is thus common to have an agglomeration of the reinforcement components or particles in the composite mix, thereby further contributing to the inhomogeneous and anisotropic nature of the 3D-printed parts.[73] Other issues that could potentially arise during the

Table 3. Specification, composition, characteristics, and application of commonly used composite-based non-biodegradable filament materials in the FDM process

S. No.	Specification of composite-based non-biodegradable filaments	Composition	Characteristics	Applications	References
1	ABS+jute	5 wt.% of jute fiber	Improved the amount of plastic deformation – increasing the strength at fracture by 28%	Lightweight reinforced filament	82
2	ABS+rice straw composite feedstock filament	5 – 15 wt.% of rice straw fibers	Flexural properties increased at 15 wt.% of fiber content; water absorption of the composite increased with increasing fiber content	Cost-effective filament to produce low-cost prototypes	78
3	ABS+OPF	5% mass fraction of OPF	Filament displayed enhanced tensile strength	Provide a solution for cost-effective fabrication method	81
4	PC+continuous CF bundles	12k bundles of CF were used	PC with CF displayed a modulus of elasticity which was 85% higher than neat PC specimens	Applications for improved and stronger parts	83

Abbreviations: ABS: Acrylonitrile butadiene styrene; CF: Carbon fiber; OPF: Oil palm fiber; PC: Polycarbonate.

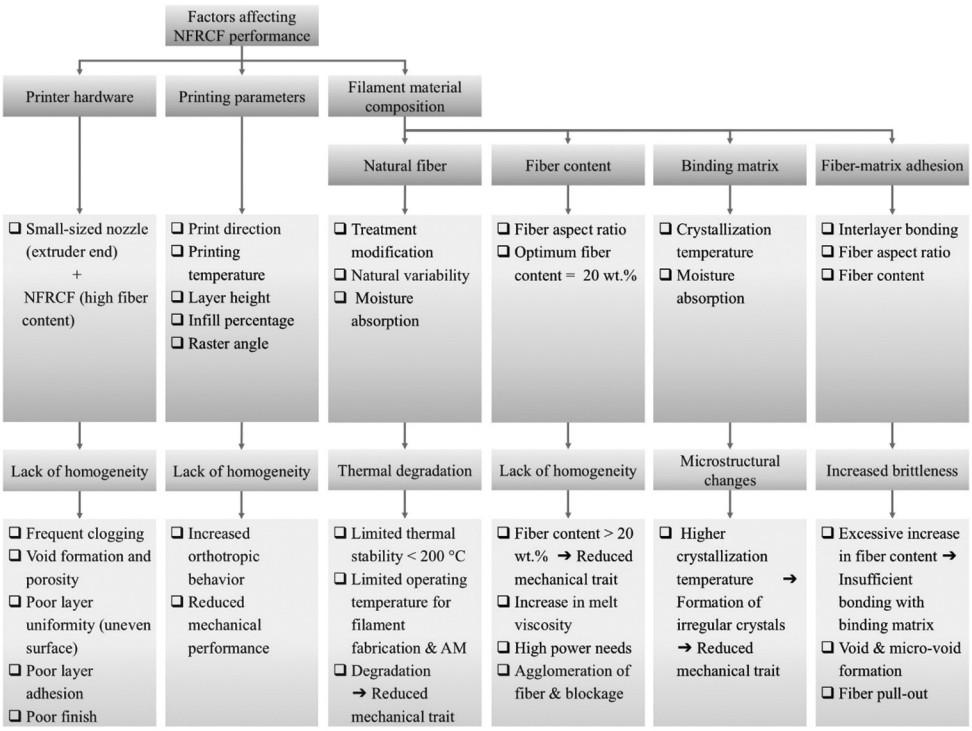

Figure 7. Detailed outline of factors originating from the printer hardware, printing parameters, and filament material composition, which affect the natural fiber-reinforced composite filaments performance due to a lack of homogeneity, thermal degradation, microstructural changes, and increased brittleness

deposition of an inhomogeneous mix of filament material are poor layer adhesion and uneven surface layers.[63] The former, also referred to as interlayer bonding, which can be affected by void formation and porosity, was found to affect the overall structural homogeneity and strength of 3D-printed components,[20,89] Moreover, the formation of voids and microvoids within the composite structure can notably affect their mechanical properties.[90,91]

From previous reports, the lack of homogeneity was found to be exacerbated by the small-sized nozzle located at the end of the extruder, which is typically in the range of 0.05 mm – 0.4 mm, resulting in frequent clogging.[73]

Clogging was commonly observed during the FDM process due to the presence of large-sized particles in the natural fiber composite mix.[86] Blockage in the extrusion process was reported to occur in filament material consisting of a weight percentage of fibers from 20% and above.[63] In line with the above, the presence of a higher amount of fibers in the filament material due to a non-homogeneous mixture was reported to lead to other printing issues besides blockage at the nozzle section.[92] For instance, an increase in the fiber content in the composite mix of the filaments would lead to an increase in their melt viscosity, thereby raising their power requirement for extrusion.[92] Moreover, another barrier associated with the excessive increase in the fiber content and a corresponding reduction in the binding matrix material was reported to accentuate the brittleness nature of the produced filaments.[93] Figure 8 displays the schematic outline of the filament extrusion process based on varying fiber content and varying fiber specifications.[94]

The full potential of natural fibers in filament material, namely their renowned tensile strength along their length, has not been fully exploited due to manufacturing restrictions. In one study involving composite-based biofilaments, a trial was made by integrating continuous flax fibers into a PLA matrix.[95] The prefabricated continuous flax yarns, which had a linear density of 68 Tex, yielded enhanced mechanical performance in terms of increased tensile modulus and strength values. On the downside, however, the transverse strength of the developed filament material was found to be inferior in comparison to similar flax-PLA thermocompressed composites.[95] Part of the weaknesses observed in the mechanical behavior of such filament material was attributed to poor dispersion and imperfect impregnation of flax yarns within the PLA matrix as a result of the fiber bundle organization.[95]

Besides fiber-related factors such as fiber treatment, composite preparation, and inclusion of compatibilizer agents, which can exert diverse influence on the FDM-based 3D printing process, the quality of the final 3D print largely depends on the printing parameters.[73] Some of the main printing parameters which are associated with the quality of natural fiber-reinforced polymer composites in FDM-based 3D printing are the printing temperature, layer height, and infill percentage, among others.[73] Besides the quality aspect, the mechanical properties of 3D-printed products in general have been reported to be affected by the layering technique, which also tends to result in a highly anisotropic material behavior,[96,97] as shown in Figure 9. In addition, layer-by-layer printing often leads to void formation that also affects the structural soundness.[73]

4.2. Matrix for biodegradable NFRCFs

As reported in the foregoing literature review, the binding matrix material plays an important role in NFRCFs fabrication as well as in the AM process. First, it is an indispensable component used to consolidate filament strength by solidifying the latter into a homogenous mix, which incorporates key filament elements such as reinforcement components and plasticizers. Second, to ensure high-quality prints, the binding matrix material provides numerous benefits that could affect the essential printing parameters in the FDM process, namely layer adhesion, surface finish, shape stability, and smooth extrusion, among other factors.[49]

PLA, which is widely recognized for its biodegradability, is the most commonly used polymeric matrix material in the production of NFRCFs.[49,86] PLA was also found to be the principal choice for binding matrix material, as was the case observed in hybrid composites composed of purely natural fibers.[73,98] Besides being biodegradable, PLA was found to display notable tensile strength despite exhibiting poor heat resistance. It is to be noted that the mechanical and heat resistance performances of PLA materials have been reported to depend on the crystallization temperature. At higher crystallization temperatures, imperfections in the form of irregular crystal formation were found to contribute to a deterioration in the mechanical performance of the PLA material.

In recent years, more attempts have been made to realize fully biodegradable composite-based biofilaments. Both the natural fiber reinforcement and biodegradable matrix components are combined to produce sturdy filament wires for 3D printing.[92] Table 4 summarizes some of the notable progress made in the development of fully biodegradable composite-based biofilaments for the FDM process. The table includes the specification, composition, characteristics, and applications of the various researched biofilaments composed of natural fibers integrated into a biodegradable matrix.

4.3. Fiber-matrix interaction and their corresponding properties

The reported physical and mechanical properties of FDM filaments are diverse, and these variations have been linked to the material source involving the fiber and matrix components. One notable factor that normally contributes to the inferior performance of natural fibers when integrated with NFRCFs is their poor fiber-matrix adhesion.[90] As reported in past literature studies, mechanical test evaluations were conducted to shed light on the mechanical performance of NFRCFs. Given the extensive use of PLA in NFRCFs, most of the reported

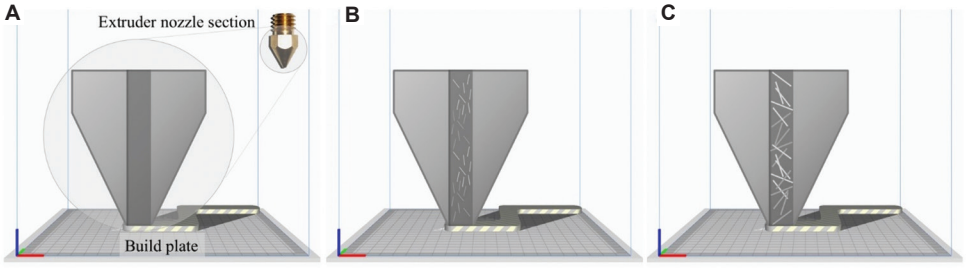

Figure 8. Schematic outline of the filament extrusion process based on varying fiber content and varying fiber specification,[94] namely (A) pure PLA filament, (B) PLA filament mix including thin and short fibers, and (C) PLA filament mix including thick and long fibers

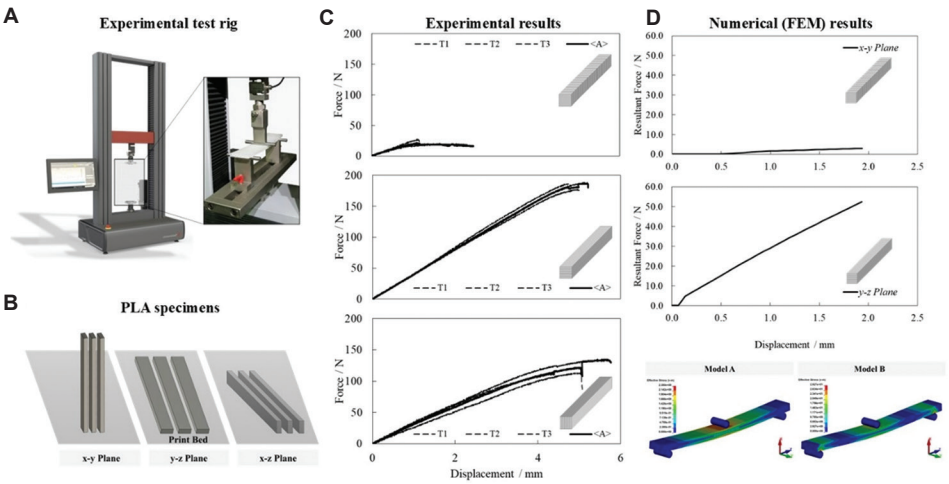

Figure 9. Orthotropic behavior in PLA specimens manufactured via the FDM process: (A) Mechanical test through the 3-point bending test rig,[97] (B) print orientations for PLA specimens, (C) 3-point bending test results, and (D) numerical simulation results including fringe plots of von-Mises stress distribution – Copyright disclosure –.
Abbreviations: FDM: Fused deposition modeling; PLA: Polylactic acid

mechanical properties in this area involved PLA as polymer matrix material. One mode of failure, which is commonly observed in NFRC, namely fiber pull-out, was also found to take place in NFRCF hence indicating poor adhesion prevailing between the fiber and matrix interface.[63] In some cases, it was also observed that the mechanical properties of biodegradable composites tend to be inferior to pure matrix material as a result of several factors pertaining to the nature of natural fibers.[72] The characteristics of various types of NFRCFs manufactured from diverse types of natural fibers are presented in Table 4.

For instance, the tensile strength and tensile modulus in fiber-reinforced PLA composites comprising Kraft pine lignin as fiber reinforcement were found to be around 48 MPa and 2.36 GPa, respectively, while those comprising flax fibers were found to be around 33 MPa and 3.4 GPa, respectively.[49] The mechanical properties in terms of their tensile modulus and tensile strength of natural fiber-reinforced composite components produced from 3 mm PLA filament reinforced with flax fibers were found to be approximately 42% and 5% greater, respectively, than the properties observed in neat PLA components.[63] In another study, the mechanical properties in terms of the ultimate tensile strength and Young's modulus of neat PLA filament were found to be around 57.5 MPa and 3200 MPa, respectively.[72] Similar properties involving filament with a combination of PLA, PHA, and 10 – 20% fiber content, on the other hand, were found to be around 25 MPa and 3750 MPa, respectively.[72]

Similar to NFRC fabrication, the volume composition of natural fibers by weight percentage had direct implications on the mechanical properties of NFRCFs. A general decreasing trend in the mechanical properties of the fiber-reinforced composite filament was observed to occur with increasing fiber content.[63] Identical observations were found during the mechanical characterization of palm fiber-reinforced polyhydroxyalkanoate (PF-PHA) composites for 3D-printing filaments. In that study, the notable increase in the tensile strength was attributed to the strong interaction observed between the fiber reinforcement and

Table 4. Specification, composition, characteristics, and applications of commonly used composite-based biofilament materials in the FDM process

S. No.	Specification of composite-based biofilaments	Composition	Characteristics	Applications	References
1	PLA+PHB+plasticizer blends	60 wt.% of PHB 15 wt.% of plasticizer blends	Displayed satisfactory degradation	Designed for use in eco-friendly application	64
2	CNF+PLA+PEG	2.5 wt.% of CNF	Fulfilled requirements for FDM 3D printing	Can be considered for the high-value utilization of CNF in 3D printing for consumer product applications	66
3	PLLA+flax fiber	10 wt.% of flax fibers	Reinforced filament material with biodegradable attributes	Potential to successfully develop fully compostable filaments	99
4	PLA+lignin	5 wt.% of lignin	Optimum wt.% of lignin to develop 3D-printed filament	Potential to convert lignin into new high-value products	69
5	PLA+inorganic nanotubes	0.5 wt.% of inorganic nanotubes	Printing flexibility observed in the FFF process	Can be used in custom-made biodegradable scaffolds of soft implants	100
6	PLA+cork	5 wt.% of cork	Specific modulus and specific tensile strength properties improved as the cork content increased	Cork–PLA composites have potential for use in light and impact-resistant 3D structures	101
7	PLA+wood	10 – 20 wt.% of fiber content	Mechanical properties are strongly dependent on printing orientation due to fiber anisotropy	Can be considered to produce biocomposites with a faster moisture-induced bending response	102
8	PLA+continuous flax fibers	Continuous flax yarns with a linear density of 68 Tex	Increased tensile modulus and strength values	High-measured performance observed opens up 3D-printed biocomposites to further structural applications	95

Abbreviations: CNF: Cellulose nanofibrils; FDM: Fused deposition modeling; FFF: Fused filament fabrication; PEG: Polyethylene glycol; PHB: Polyhydroxy butyrate; PLA: Polylactic acid; PLLA: Poly-l-lactic acid.

the PHA matrix.[103] The optimum mechanical performance of the mentioned biocomposite filament, which exceeded both the tensile strength at break and Young's modulus of neat PHA, was found to occur at a weight percentage of fiber content of 20%.[103] In another investigation involving the use of hemp and New Zealand flax for the fabrication of NFRCF, the optimum mechanical properties in terms of their Young's modulus were also observed to occur at a fiber content of 20%.[63] Moreover, the discrepancy in terms of mechanical performance observed between the two composites was attributed to the finer fiber having a better aspect ratio that yielded better results.[63]

4.4. How to achieve homogeneous NFRC filament?

The quality of 3D prints largely depends on the nature and characteristics of the filament material in the FDM process. One such key characteristic is the degree of homogeneity in the filament material.[73] The more homogenous the filament material, the better the quality of the 3D prints in terms of their layers' uniformity, layer adhesion, and surface finish.[63] The overall FDM process is also impacted as the frequent obstruction of the nozzle is minimized by the utilization of homogenous filament material.[71,86] The degree of homogeneity in NFRCFs, specifically between the filler and polymer matrix, depends on a few notable factors ranging from the manufacturing process to the composition of the filament mix.

In terms of the manufacturing process, extrusion was found to be the most adopted process to produce filament materials with the best results.[64,71] As displayed in Figure 10, the extrusion process was successfully considered in a previous study to generate biofilament materials.[66] However, the extrusion process, in turn, was dependent on the filament melt index. For the best extrusion and generation of high-quality NFRCFs, an optimum melt index is identified. The selected melt index is not excessively high so as to prevent the degradation of natural fibers, as well as not exceedingly low as this could lead to clogging issues.[92,104]

Besides the manufacturing process, a homogeneous mix of the NFRCFs could be further achieved by enhancing

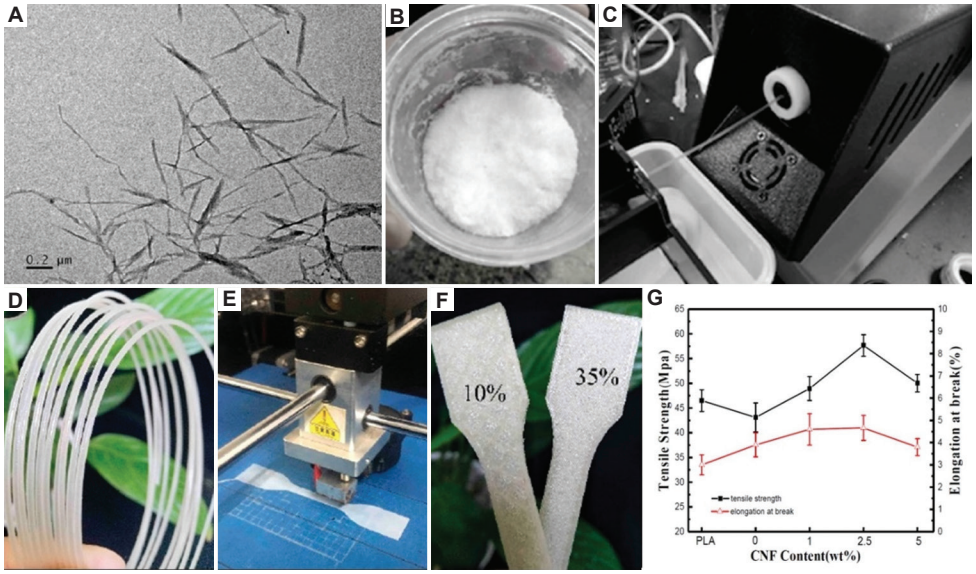

Figure 10. The generation of biofilament material from CNF and PLA using the extrusion process. Key stages of the investigation include: (A) enzymatic hydrolysis of cellulose with high-pressure homogenization, (B) CNF powder, (C) extrusion process via the Wellzoom desktop extruder, (D) extrusion of composite filament material with a diameter of 1.75 mm, (E) specimen generation via the M3036 FDM desktop 3D printer, (F) tensile testing of specimens with 10% and 35% infill, and (G) testing of tensile strength of composite filament material with varying CNF composition. Illustration reproduced from ref.[66] – an open-access article distributed under the CC BY License of MDPI (Basel, Switzerland)
Abbreviations: CNF: Cellulose nanofibrils; PLA: Polylactic acid

its material composition. The strength and homogeneity in filament material could also be enhanced by including a pre-mixing stage to produce a homogeneous mix, which will also minimize the frequent clogging of the nozzle in the FDM process.[73,86] For instance, the addition of additives, such as compatibilizer and coupling agents through customized treatments, was found to improve the interfacial bonding between the polymer matrices and filler components, thus affecting the homogeneity of the filament material.[73] In another study, the consideration of continuous natural fiber with PLA for biofilament fabrication evidenced a homogeneous distribution within the cross-section.[95]

In previous studies, several techniques have been considered to examine the homogeneity of composite filament materials. One such technique, namely the Thermogravimetric Analysis, was utilized to verify the composition of composite-based filament material, such as polymer-ceramic and PLA–potato thermoplastic starch filament materials.[105,106] Other microscopy techniques, such as scanning electron microscopy (SEM), have been considered to study the fractured surface of the composite filament, whereby the distribution of the reinforcement components could also be clearly examined.[107,108] To closely study the internal morphological characteristics of 3D-printed composite filament, the X-ray microscopy technique was even considered it could afford additional information as compared to the SEM technique, which provides limited information pertaining to the surface of the observed specimen only.[109]

5. Natural degradation and recycling of NFRCFs

The integration of natural fibers as reinforcement in filament material has not only enhanced their mechanical attributes but has also improved their biodegradability trait.[49] The transition toward using biodegradable products in the field of AM is also being propelled by the incorporation of PLA-based filament materials into usage. Besides, in terms of benefits, biodegradable filaments made of PLA and polyvinyl alcohol (PVA) have been reported to be non-toxic.[72] On the downside, biodegradable filaments, namely PLA and PHA, have been reported to have a brittle nature, while PVA and polyethylene terephthalate were found to be susceptible to moisture absorption.[72] Moreover, similar to neat polymeric-based biodegradable filaments, fabricated NFRCF should also be stored in a controlled environment to avoid degradation to external factors such as ultraviolet, temperature, and moisture content.[67]

To determine the biodegradable characteristics of biodegradable material, the soil burial test, also known as the soil degradability test, has been previously considered.[110-112] In such experiments, the rate of degradation of biocomposite filaments can be monitored by assessing their weight loss.[103] In this method involving

the open soil environment, living microorganisms such as aerobic bacteria were found to decompose organic matter via microbial activity.[110] The degradation rate of such biocomposite 3D-printed parts in marine environments was found to depend on the surface roughness of the printed parts, the extent of crystallinity in their structure, and the ratio of wet to dry cycles during the cyclic submersion test.[37] The cause of the embrittlement effect, which was predominantly observed in the PLA-PHA-printed biocomposite parts following the cyclic submersion test, was linked to environmental stress cracking resulting from the penetration of salt crystals and other impurities in the failure regions.[37] In another study, the degradation rate of PF-PHA biocomposite filament was monitored by assessing their weight loss in the soil burial test.[103]

For 3D-printed materials with reduced biodegradability, other alternative options of reuse and recycling are being considered.[72] With projected growth in AM and the corresponding upward surge in the use of filament materials in the coming years and decades, other aspects in the large-scale utilization of such materials, namely their recycling, have to be considered to ensure a sustainable approach. The recycling and reuse of end-of-service-life products is imperative in today's society as there is a growing need for better waste management and disposal for a reduced impact on the environment. The various means to recycle filament materials include shredding, melting, and re-extruding, among other means. The recycling of filament materials not only reduces the amount of energy and carbon emissions required to produce new materials but also conserves resources and reduces wastes.[113,114]

Besides enabling effective waste utilization, the potential of repurposing polymeric materials from recycled NFRCFs as new consumer products is providing an alternative means for material valorization.[115] In one study, the mechanical recycling of printed products made from commercial-grade PLA was conducted via shredding prior to re-extrusion into new filament material for reuse. As revealed from the results of a life cycle assessment, this approach, termed as closed-loop recycling, was found to be a better alternative than landfill disposal.[116] Moreover, the process of reprocessing the filament material led to a reduction in their viscosity, which indicates a deterioration in their performance for the FDM process. One proposed solution to enhance their viscosity was to blend virgin PLA with recycled ones to enable their re-utilization in filament materials.[116]

6. Future works to optimize NFRCF performance

The inferior mechanical performance observed in NFRCFs as a result of poor bonding strength and adhesion prevailing between the fiber-matrix interfaces is signaling a need for further research.[49] One way to improve interfacial adhesion is by overcoming the hydrophilic characteristic of natural fibers, which will also positively contribute to the enhancement of their overall dimensional stability.[49] Another target is to achieve a homogeneous NFRCF, which will be decisive in the future development of biodegradable products in the AM field. Further research needs to be conducted on NFRCFs to fill in the gap of information arising due to a lack of data about their mechanical behavior.[117]

The significant growth observed in the AM field and the increasing demand for AM-manufactured products are calling for further optimization of the NFRCF filament. The current targets set by material scientists and engineers in the field of AM are high-quality 3D prints, reduced printing time, and low cost of production.[73] To achieve the set targets, optimization of the process parameters through design of experiment was found to be essential.[73] Other techniques which could be considered to analyze and optimize the process efficiency in AM are the Taguchi method and the response surface methodology.[73]

The hybridization of natural fibers is a proven technique that has yielded conclusive results when applied to improve the strength of NFRCs.[118,119] The hybridization of natural fibers is a technique to combine two or more types of fibers with the aim of achieving maximum mechanical performance in terms of toughness and strength. In past literature, satisfactory results were obtained when the hybridization technique was applied to a variety of natural fibers, namely pineapple leaf fiber, kenaf, jute, hemp, sugar palm, and coir.[119] Moreover, to reduce the delamination and fiber pull-outs during machinability, the hybrid natural fiber composite could be further enhanced by the addition of specific filler materials.[120] The aforementioned observations about the hybridization of natural fibers for NFRCs have not been well explored and considered for the development of advanced NFRCFs and will thus require further attention.

7. Conclusion

With the increasing use of AM technologies for product development in recent years, there is a growing need to look into alternative and more sustainable materials bearing a lower carbon footprint. This review addresses this gap by probing into the latest progress made in the development of biodegradable NFRCFs for 3D printing. The rationale for using NFRCFs in modern AM processes is covered in this review. Factors contributing to the performance attributes of NFRCFs, namely their fabrication procedure, fibers and matrix selection, the fiber-matrix interaction,

their corresponding properties, and their degradation assessment, are also covered in this paper. The limitations posed by present-day NFRCFs and the typical challenges faced when integrating natural fibers into the NFRCF fabrication procedure are highlighted. The success of the developed NFRCFs is found to mainly rest on the fiber-matrix adhesion. Besides their lack of homogeneity, additional factors that affect the performance of NFRCF include limited thermal stability, susceptibility to moisture absorption, and increase in melt viscosity with increasing fiber content. The degradability of recently developed NFRCFs is reviewed, and means to recycle those with poor degradable characteristics are also discussed. Finally, the means to further optimize NFRCFs for enhanced performance for the AM process is outlined. This review highlights the necessity for additional research in various areas to enhance both the physical and mechanical characteristics of NFRCFs in order to improve their dimensional stability and strength, respectively. The creation of high-grade NFRCFs would further increase their integration into the AM industry while promoting a sustainable alternative option.

Acknowledgments

The author would like to express his gratitude to The World Academy of Sciences (TWAS) for providing support to the new African Principal Investigator for conducting this research study and to The University of Mauritius for providing the necessary facilities and resources required to accomplish this research work.

Funding

This research study was funded by TWAS under the Seed Grant for New African Principal Investigators (SG-NAPI) scheme (Agreement No. 4500474979).

Conflict of interest

The author declares no competing interests.

Author contributions

This is a single-authored article.

Ethics approval and consent to participate

Not applicable.

Consent for publication

Not applicable.

Availability of data

Not applicable.

References

1. Sangkert S, Kamolmatyakul S, Gelinsky M, Meesane J. 3D printed scaffolds of alginate/polyvinylalcohol with silk fibroin based on mimicked extracellular matrix for bone tissue engineering in maxillofacial surgery. *Mater Today Commun*. 2021;26:102140.

   doi: 10.1016/j.mtcomm.2021.102140

2. Aati S, Akram Z, Ngo H, Fawzy AS. Development of 3D printed resin reinforced with modified ZrO2 nanoparticles for long-term provisional dental restorations. *Dent Mater*. 2021;37(6):e360-e374.

   doi: 10.1016/j.dental.2021.02.010

3. Alshaer AW, Harland DJ. An investigation of the strength and stiffness of weight-saving sandwich beams with CFRP face sheets and seven 3D printed cores. *Compos Struct*. 2021;257:113391.

   doi: 10.1016/j.compstruct.2020.113391

4. Berde NN, Sanap SB, Thorat SG. Study of impact and fatigue on 3D printed composites. *Mater Today Proc*. 2021;47:2376-2378.

   doi: 10.1016/j.matpr.2021.04.330

5. Schuldt SJ, Jagoda JA, Hoisington AJ, Delorit JD. A systematic review and analysis of the viability of 3D-printed construction in remote environments. *Autom Constr*. 2021;125:103642.

   doi: 10.1016/j.autcon.2021.103642

6. Ramful R. A Paradigm shift towards sustainable production with additive manufacturing in the industry 4.0 era. In: Fowdur TP, Milovanovic DA, Bojkovic ZS, editors. *Intelligent and Sustainable Engineering Systems for Industry 4.0 and Beyond*. United States: CRC Press; 2025. p. 92-116.

7. Sun Y, Tian W, Zhang T, Chen P, Li M. Strength and toughness enhancement in 3d printing via bioinspired tool path. *Mater Des*. 2020;185:108239.

   doi: 10.1016/j.matdes.2019.108239

8. Compton BG, Lewis JA. 3D-printing of lightweight cellular composites. *Adv Mater*. 2014;26(34):5930-5935.

   doi: 10.1002/adma.201401804

9. Gu GX, Takaffoli M, Hsieh AJ, Buehler MJ. Biomimetic additive manufactured polymer composites for improved impact resistance. *Extreme Mech Lett*. 2016;9:317-323.

   doi: 10.1016/j.eml.2016.09.006

10. Gu GX, Takaffoli M, Buehler MJ. Hierarchically enhanced impact resistance of bioinspired composites. *Adv Mater*. 2017;29(28):1700060.

    doi: 10.1002/adma.201700060

11. Podroužek J, Marcon M, Ninčević K, Wan-Wendner R. Bio-inspired 3d infill patterns for additive manufacturing and structural applications. *Materials* (*Basel*). 2019;12(3):499.

doi: 10.3390/ma12030499

12. Chen BC, Zou M, Liu GM, Song JF, Wang HX. Experimental study on energy absorption of bionic tubes inspired by bamboo structures under axial crushing. *Int J Impact Eng*. 2018;115:48-57.

doi: 10.1016/j.ijimpeng.2018.01.005

13. Zhang T, Wang A, Wang Q, Guan F. Bending characteristics analysis and lightweight design of a bionic beam inspired by bamboo structures. *Thin Walled Struct*. 2019;142:476-498.

doi: 10.1016/j.tws.2019.04.043

14. Jiang H, Ziegler H, Zhang Z, Meng H, Chronopoulos D, Chen Y. Mechanical properties of 3D printed architected polymer foams under large deformation. *Mater Des*. 2020;194:108946.

doi: 10.1016/j.matdes.2020.108946

15. Xu Y, Zhang H, Šavija B, Chaves Figueiredo S, Schlangen E. Deformation and fracture of 3D printed disordered lattice materials: Experiments and modeling. *Mater Des*. 2019;162:143-153.

doi: 10.1016/j.matdes.2018.11.047

16. Chen Y, Li T, Jia Z, Scarpa F, Yao CW, Wang L. 3D printed hierarchical honeycombs with shape integrity under large compressive deformations. *Mater Des*. 2018;137:226-234.

doi: 10.1016/j.matdes.2017.10.028

17. Martens P, Mathot M, Bos F, Coenders J. Optimising 3D printed concrete structures using topology optimisation. In: *High Tech Concrete: Where Technology and Engineering Meet*. Berlin, Germany: Springer International Publishing; 2018. p. 301-309.

doi: 10.1007/978-3-319-59471-2_37

18. Chen Y, Veer F, Çopuroğlu O. A critical review of 3D concrete printing as a low Co_2 concrete approach. *Heron*. 2017;62:167-194.

19. Wolfs RJM, Bos FP, Salet TAM. Hardened properties of 3D printed concrete: The influence of process parameters on interlayer adhesion. *Cem Concr Res*. 2019;119:132-140.

doi: 10.1016/j.cemconres.2019.02.017

20. Nerella VN, Hempel S, Mechtcherine V. Effects of layer-interface properties on mechanical performance of concrete elements produced by extrusion-based 3D-printing. *Constr Build Mater*. 2019;205:586-601.

doi: 10.1016/j.conbuildmat.2019.01.235

21. Heras Murcia D, Genedy M, Reda Taha MM. Examining the significance of infill printing pattern on the anisotropy of 3D printed concrete. *Constr Build Mater*. 2020;262:120559.

doi: 10.1016/j.conbuildmat.2020.120559

22. Nurhudan AI, Supriadi S, Whulanza Y, Saragih AS. Additive manufacturing of metallic based on extrusion process: A review. *J Manuf Process*. 2021;66:228-237.

doi: 10.1016/j.jmapro.2021.04.018

23. Lvov VA, Senatov FS, Stepashkin AA, Veveris AA, Pavlov MD, Komissarov AA. Low-cycle fatigue behavior of 3D-printed metallic auxetic structure. *Mater Today Proc*. 2020;33:1979-1983.

doi: 10.1016/j.matpr.2020.06.130

24. Shahrubudin N, Lee TC, Ramlan R. An overview on 3D printing technology: Technological, materials, and applications. *Procedia Manuf*. 2019;35:1286-1296.

doi: 10.1016/j.promfg.2019.06.089

25. Caminero M, Chacón J, García-Plaza E, Núñez P, Reverte J, Becar J. Additive manufacturing of PLA-based composites using fused filament fabrication: Effect of graphene nanoplatelet reinforcement on mechanical properties, dimensional accuracy and texture. *Polymers* (*Basel*). 2019;11(5):799.

doi: 10.3390/polym11050799

26. Cicala G, Giordano D, Tosto C, Filippone G, Recca A, Blanco I. Polylactide (PLA) filaments a biobased solution for additive manufacturing: Correlating rheology and thermomechanical properties with printing quality. *Materials* (*Basel*). 2018;11(7):1191.

doi: 10.3390/ma11071191

27. Camargo JC, Machado ÁR, Almeida EC, Silva EFMS. Mechanical properties of PLA-graphene filament for FDM 3D printing. *Int J Adv Manuf Technol*. 2019;103(5-8):2423-2443.

doi: 10.1007/s00170-019-03532-5

28. Novaković D, Kašiković N, Vladić G, Pál M. Screen printing. In: *Printing on Polymers*. Amsterdam, Netherlands: Elsevier; 2016. p. 247-261.

doi: 10.1016/B978-0-323-37468-2.00015-4

29. Srivatsan TS, Sudarshan TS, editors. *Additive Manufacturing: Innovations, Advances, and Applications*. United States: CRC Press; 2015.

doi: 10.1201/b19360

30. Wojtyła S, Klama P, Baran T. Is 3D printing safe? Analysis of the thermal treatment of thermoplastics: ABS, PLA, PET, and nylon. *J Occup Environ Hyg*. 2017;14(6):D80-D85.

doi: 10.1080/15459624.2017.1285489

31. El Magri A, Ouassil S, Vaudreuil S. Effects of printing parameters on the tensile behavior of 3D-printed Acrylonitrile Styrene Acrylate (ASA) material in Z direction. *Polym Eng Sci*. 2022;62(3):848-860.

doi: 10.1002/pen.25891

32. Harris CG, Jursik NJS, Rochefort WE, Walker TW. Additive manufacturing with soft TPU - adhesion strength in multimaterial flexible joints. *Front Mech Eng*. 2019;5:37.

doi: 10.3389/fmech.2019.00037

33. Rohde S, Cantrell J, Jerez A, *et al*. Experimental characterization of the shear properties of 3D-printed abs and polycarbonate parts. *Exp Mech*. 2018;58(6):871-884.

    doi: 10.1007/s11340-017-0343-6

34. Ekinci A, Johnson AA, Gleadall A, Engstrøm DS, Han X. Layer-dependent properties of material extruded biodegradable polylactic acid. *J Mech Behav Biomed Mater*. 2020;104:103654.

    doi: 10.1016/j.jmbbm.2020.103654

35. Lee CY, Liu CY. The influence of forced-air cooling on a 3D printed PLA part manufactured by fused filament fabrication. *Addit Manuf*. 2019;25:196-203.

    doi: 10.1016/j.addma.2018.11.012

36. Mazurchevici SN, Pricop B, Istrate B, *et al*. Technological parameters effects on mechanical properties of biodegradable materials using FDM. *Mater Plast*. 2019;57(2):215-227.

    doi: 10.37358/MP.20.2.5368

37. Montalvão GR, Moshrefi-Torbati M, Hamilton A, Machado R, João A. Behaviour of 3D printed PLA and PLA-PHA in marine environments. *IOP Conf Ser Earth Environ Sci*. 2020;424(1):012013.

    doi: 10.1088/1755-1315/424/1/012013

38. Candal MV, Calafel I, Aranburu N, *et al*. Thermo-rheological effects on successful 3D printing of biodegradable polyesters. *Addit Manuf*. 2020;36:101408.

    doi: 10.1016/j.addma.2020.101408

39. Backes EH, Harb SV, Beatrice CAG, *et al*. Polycaprolactone usage in additive manufacturing strategies for tissue engineering applications: A review. *J Biomed Mater Res B Appl Biomater*. 2022;110(6):1479-1503.

    doi: 10.1002/jbm.b.34997

40. Suiker ASJ. Mechanical performance of wall structures in 3D printing processes: Theory, design tools and experiments. *Int J Mech Sci*. 2018;137:145-170.

    doi: 10.1016/j.ijmecsci.2018.01.010

41. Paul SC, Tay YWD, Panda B, Tan MJ. Fresh and hardened properties of 3D printable cementitious materials for building and construction. *Arch Civil Mech Engineering*. 2018;18(1):311-319.

    doi: 10.1016/j.acme.2017.02.008

42. Ramful R. Mechanical performance and durability attributes of biodegradable natural fibre-reinforced composites-a review. *J Mater Sci Mater Eng*. 2024;19(1):50.

    doi: 10.1186/s40712-024-00198-0

43. Kabir MM, Wang H, Lau KT, Cardona F. Chemical treatments on plant-based natural fibre reinforced polymer composites: An overview. *Compos B Eng*. 2012;43(7):2883-2892.

    doi: 10.1016/j.compositesb.2012.04.053

44. Ho MP, Wang H, Lee JH, *et al*. Critical factors on manufacturing processes of natural fibre composites. *Compos B Eng*. 2012;43(8):3549-3562.

    doi: 10.1016/j.compositesb.2011.10.001

45. Shao Z, Wang F. Mechanical characteristics of bamboo structure and its components. In: *The Fracture Mechanics of Plant Materials*. Singapore: Springer; 2018. p. 125-146.

    doi: 10.1007/978-981-10-9017-2_7

46. Shao Z, Wang F. Transverse fracture of wood. In: *The Fracture Mechanics of Plant Materials*. Singapore: Springer; 2018. p. 63-86.

    doi: 10.1007/978-981-10-9017-2_4

47. Siakeng R, Jawaid M, Ariffin H, Sapuan SM, Asim M, Saba N. Natural fiber reinforced polylactic acid composites: A review. *Polym Compos*. 2019;40(2):446-463.

    doi: 10.1002/pc.24747

48. Al Faruque MA, Salauddin M, Raihan MM, Chowdhury IZ, Ahmed F, Shimo SS. Bast fiber reinforced green polymer composites: A review on their classification, properties, and applications. *J Nat Fiber*. 2022;19(14):8006-8021.

    doi: 10.1080/15440478.2021.1958431

49. Aida HJ, Nadlene R, Mastura MT, Yusriah L, Sivakumar D, Ilyas RA. Natural fibre filament for Fused Deposition Modelling (FDM): A review. *Int J Sustain Eng*. 2021; 14(6):1988-2008.

    doi: 10.1080/19397038.2021.1962426

50. Dittenber DB, GangaRao HVS. Critical review of recent publications on use of natural composites in infrastructure. *Compos A Appl Sci Manuf*. 2012;43(8):1419-1429.

    doi: 10.1016/j.compositesa.2011.11.019

51. Awais H, Nawab Y, Amjad A, Anjang A, Md Akil H, Zainol Abidin MS. Environmental benign natural fibre reinforced thermoplastic composites: A review. *Compos C Open Access*. 2021;4:100082.

    doi: 10.1016/j.jcomc.2020.100082

52. Reddy MSB, Ponnamma D, Choudhary R, Sadasivuni KK. A comparative review of natural and synthetic biopolymer composite scaffolds. *Polymers* (*Basel*). 2021;13(7):1105.

    doi: 10.3390/polym13071105

53. Ghori SW, Siakeng R, Rasheed M, Saba N, Jawaid M. The role of advanced polymer materials in aerospace. In: *Sustainable Composites for Aerospace Applications*. Amsterdam, Netherlands: Elsevier; 2018. p. 19-34.

    doi: 10.1016/B978-0-08-102131-6.00002-5

54. Dorigato A. Recycling of thermosetting composites for wind blade application. *Adv Ind Eng Polym Res*. 2021;4(2):116-132.

    doi: 10.1016/j.aiepr.2021.02.002

55. Hubbe MA, Lavoine N, Lucia LA, Dou C. Formulating bioplastic composites for biodegradability, recycling, and performance: A review. *Bioresources*. 2020;16(1):2021-2083.

doi: 10.15376/biores.16.1.Hubbe

56. Mtibe A, Motloung MP, Bandyopadhyay J, Ray SS. Synthetic biopolymers and their composites: Advantages and limitations-an overview. *Macromol Rapid Commun*. 2021;42(15):e2100130.

doi: 10.1002/marc.202100130

57. Moore CJ. Synthetic polymers in the marine environment: A rapidly increasing, long-term threat. *Environ Res*. 2008;108(2):131-139.

doi: 10.1016/j.envres.2008.07.025

58. Krauklis AE, Karl CW, Gagani AI, Jørgensen JK. Composite material recycling technology-state-of-the-art and sustainable development for the 2020s. *J Compos Sci*. 2021;5(1):28.

doi: 10.3390/jcs5010028

59. Gu JD, Wang YS. Coastal and marine pollution and ecotoxicology. *Ecotoxicology*. 2015;24(7-8):1407-1410.

doi: 10.1007/s10646-015-1528-3

60. Muneer Ahmed M, Dhakal HN, Zhang ZY, Barouni A, Zahari R. Enhancement of impact toughness and damage behaviour of natural fibre reinforced composites and their hybrids through novel improvement techniques: A critical review. *Compos Struct*. 2021;259:113496.

doi: 10.1016/j.compstruct.2020.113496

61. Dharani Kumar S, Aravindh M, Manoj VK, Madhumithra C, Kaviya P, Yaswanth S. Fracture toughness of bio-fiber reinforced polymer composites- a review. *Mater Today Proc*. 2023;1-8.

doi: 10.1016/j.matpr.2023.01.334

62. El-Sayegh S, Romdhane L, Manjikian S. A critical review of 3D printing in construction: Benefits, challenges, and risks. *Arch Civil Mech Eng*. 2020;20(2):34.

doi: 10.1007/s43452-020-00038-w

63. Stoof D, Pickering K, Zhang Y. Fused deposition modelling of natural fibre/polylactic acid composites. *J Compos Sci*. 2017;1(1):8.

doi: 10.3390/jcs1010008

64. Menčík P, Přikryl R, Stehnová I, *et al*. Effect of selected commercial plasticizers on mechanical, thermal, and morphological properties of poly (3-hydroxybutyrate)/poly (Lactic Acid)/plasticizer biodegradable blends for three-dimensional (3D) print. *Materials* (*Basel*). 2018;11(10):1893.

doi: 10.3390/ma11101893

65. Singh R, Ranjan N. Experimental investigations for preparation of biocompatible feedstock filament of Fused Deposition Modeling (FDM) using twin screw extrusion process. *J Thermoplast Compos Mater*. 2018;31(11):1455-1469.

doi: 10.1177/0892705717738297

66. Wang Q, Ji C, Sun L, Sun J, Liu J. Cellulose nanofibrils filled poly (Lactic Acid) biocomposite filament for FDM 3D printing. *Molecules*. 2020;25(10):2319.

doi: 10.3390/molecules25102319

67. Manoj A, Panda RC. Biodegradable filament for 3D printing process: A review. *Eng Sci*. 2022;18:11-19.

doi: 10.30919/es8d616

68. Morales MA, Maranon A, Hernandez C, Porras A. Development and characterization of a 3D printed cocoa bean shell filled recycled polypropylene for sustainable composites. *Polymers* (*Basel*). 2021;13(18):3162.

doi: 10.3390/polym13183162

69. Gkartzou E, Koumoulos EP, Charitidis CA. Production and 3D printing processing of bio-based thermoplastic filament. *Manuf Rev*. 2017;4:1.

doi: 10.1051/mfreview/2016020

70. Chacón JM, Caminero MÁ, Núñez PJ, García-Plaza E, Bécar JP. Effect of nozzle diameter on mechanical and geometric performance of 3D printed carbon fibre-reinforced composites manufactured by fused filament fabrication. *Rapid Prototyp J*. 2021;27(4):769-784.

doi: 10.1108/RPJ-10-2020-0250

71. Xie G, Zhang Y, Lin W. Plasticizer combinations and performance of wood flour-poly (Lactic Acid) 3D printing filaments. *Bioresources*. 2017;12(3):6736-6748.

doi: 10.15376/biores.12.3.6736-6748

72. Pakkanen J, Manfredi D, Minetola P, Iuliano L. About the Use of Recycled or Biodegradable Filaments for Sustainability of 3D Printing. In: *Sustainable Design and Manufacturing: Proceedings of the 8th International Conference on Sustainable Design and Manufacturing* (*KES-SDM 2021*). Cham: Springer; 2017. p. 776-785.

doi: 10.1007/978-3-319-57078-5_73

73. Rajendran Royan NR, Leong JS, Chan WN, Tan JR, Shamsuddin ZSB. Current state and challenges of natural fibre-reinforced polymer composites as feeder in FDM-based 3D printing. *Polymers* (*Basel*). 2021;13(14):2289.

doi: 10.3390/polym13142289

74. Tserki V, Panayiotou C, Zafeiropoulos NE. A study of the effect of acetylation and propionylation on the interface of natural fibre biodegradable composites. *Adv Compos Lett*. 2005;14(2):65-71.

doi: 10.1177/096369350501400202

75. Ganguly A, Shankar S, Das A, Shukla M, Swaroop C, Bhardwaj T. Natural fibre reinforced composites: A review

based on additive manufacturing routes and biodegradability perspective. *Mater Today Proc*. 2022;62:131-135.

doi: 10.1016/j.matpr.2022.02.607

76. Zhao DX, Cai X, Shou GZ, Gu YQ, Wang PX. Study on the preparation of bamboo plastic composite intend for additive manufacturing. *Key Eng Mater*. 2015;667:250-258.

doi: 10.4028/www.scientific.net/KEM.667.250

77. Gao X, Qi S, Yang B, Su Y, Li J, Wang D. Synergistic effect of plasticizer and nucleating agent on crystallization behavior of polylactide during fused filament fabrication. *Polymer*. 2021;215:123426.

doi: 10.1016/j.polymer.2021.123426

78. Osman MA, Atia MRA. Investigation of ABS-rice straw composite feedstock filament for FDM. *Rapid Prototyp J*. 2018;24(6):1067-1075.

doi: 10.1108/RPJ-11-2017-0242

79. Depuydt D, Balthazar M, Hendrickx K, *et al*. Production and characterization of bamboo and flax fiber reinforced polylactic acid filaments for fused deposition modeling (FDM). *Polym Compos*. 2019;40(5):1951-1963.

doi: 10.1002/pc.24971

80. Liu H, He H, Peng X, Huang B, Li J. Three-dimensional printing of poly(lactic acid) bio-based composites with sugarcane bagasse fiber: Effect of printing orientation on tensile performance. *Polym Adv Technol*. 2019;30(4):910-922.

doi: 10.1002/pat.4524

81. Ahmad MN, Wahid MK, Maidin NA, Ab Rahman MH, Osman MH, Alis@Elias IF. Mechanical characteristics of oil palm fiber reinforced thermoplastics as filament for Fused Deposition Modeling (FDM). *Adv Manuf*. 2020;8(1):72-81.

doi: 10.1007/s40436-019-00287-w

82. Torrado Perez AR, Roberson DA, Wicker RB. Fracture surface analysis of 3D-Printed tensile specimens of novel ABS-based materials. *J Fail Anal Preven*. 2014;14(3):343-353.

doi: 10.1007/s11668-014-9803-9

83. Jahangir MN, Billah KMM, Lin Y, Roberson DA, Wicker RB, Espalin D. Reinforcement of material extrusion 3D printed polycarbonate using continuous carbon fiber. *Addit Manuf*. 2019;28:354-364.

doi: 10.1016/j.addma.2019.05.019

84. Bi X, Huang R. 3D printing of natural fiber and composites: A state-of-the-art review. *Mater Des*. 2022;222:111065.

doi: 10.1016/j.matdes.2022.111065

85. Xu W, Pranovich A, Uppstu P, *et al*. Novel biorenewable composite of wood polysaccharide and polylactic acid for three dimensional printing. *Carbohydr Polym*. 2018;187:51-58.

doi: 10.1016/j.carbpol.2018.01.069

86. Petchwattana N, Channuan W, Naknaen P, Narupai B. 3D printing filaments prepared from modified poly (Lactic Acid)/teak wood flour composites: An investigation on the particle size effects and silane coupling agent compatibilisation. *J Phys Sci*. 2019;30(2):169-188.

doi: 10.21315/jps2019.30.2.10

87. Panda B, Paul SC, Hui LJ, Tay YWD, Tan MJ. Additive manufacturing of geopolymer for sustainable built environment. *J Clean Prod*. 2017;167:281-288.

doi: 10.1016/j.jclepro.2017.08.165

88. Xiao J, Liu H, Ding T. Finite element analysis on the anisotropic behavior of 3D printed concrete under compression and flexure. *Addit Manuf*. 2021;39:101712.

doi: 10.1016/j.addma.2020.101712

89. Zareiyan B, Khoshnevis B. Interlayer adhesion and strength of structures in contour crafting - effects of aggregate size, extrusion rate, and layer thickness. *Autom Constr*. 2017;81:112-121.

doi: 10.1016/j.autcon.2017.06.013

90. Sundar D, Narasimalu S, Yaowen Y, Sharma S. Opportunities for Natural Fiber Reinforced Composites towards Tropical wind Turbine Material Needs. In: *2017 Asian Conference on Energy, Power and Transportation Electrification* (*ACEPT*). IEEE; 2017. p. 1-7.

doi: 10.1109/ACEPT.2017.8168549

91. Venkateshwaran N, Elayaperumal A, Sathiya GK. Prediction of tensile properties of hybrid-natural fiber composites. *Compos B Eng*. 2012;43(2):793-796.

doi: 10.1016/j.compositesb.2011.08.023

92. Filgueira D, Holmen S, Melbø JK, Moldes D, Echtermeyer AT, Chinga-Carrasco G. Enzymatic-assisted modification of thermomechanical pulp fibers to improve the interfacial adhesion with poly(lactic acid) for 3D printing. *ACS Sustain Chem Eng*. 2017;5(10):9338-9346.

doi: 10.1021/acssuschemeng.7b02351

93. Nguyen NA, Bowland CC, Naskar AK. A general method to improve 3D-printability and inter-layer adhesion in lignin-based composites. *Appl Mater Today*. 2018;12:138-152.

doi: 10.1016/j.apmt.2018.03.009

94. Wang X, Jiang M, Zhou Z, Gou J, Hui D. 3D printing of polymer matrix composites: A review and prospective. *Compos B Eng*. 2017;110:442-458.

doi: 10.1016/j.compositesb.2016.11.034

95. Le Duigou A, Barbé A, Guillou E, Castro M. 3D printing of continuous flax fibre reinforced biocomposites for structural applications. *Mater Des*. 2019;180:107884.

doi: 10.1016/j.matdes.2019.107884

96. Mazzanti V, Malagutti L, Mollica F. FDM 3D printing

of polymers containing natural fillers: A review of their mechanical properties. *Polymers* (*Basel*). 2019;11(7):1094.

doi: 10.3390/polym11071094

97. Ramful R, Shoaib Casseem M. Improving the Flexural Behaviour of Small Clear 3D-Printed PLA Specimens through Generative Design. In: *2023 International Conference on Sustainable Technology and Engineering* (*i-COSTE*). IEEE; 2023. p. 1-5.

doi: 10.1109/i-COSTE60462.2023.10500778

98. Mukherjee T, Kao N. PLA based biopolymer reinforced with natural fibre: A review. *J Polym Environ*. 2011;19(3):714-725.

doi: 10.1007/s10924-011-0320-6

99. Badouard C, Traon F, Denoual C, Mayer-Laigle C, Paës G, Bourmaud A. Exploring mechanical properties of fully compostable flax reinforced composite filaments for 3D printing applications. *Ind Crops Prod*. 2019;135:246-250.

doi: 10.1016/j.indcrop.2019.04.049

100. Shalom H, Kapishnikov S, Brumfeld V, Naveh N, Tenne R, Lachman N. Strong, tough and bio-degradable polymer-based 3D-ink for Fused Filament Fabrication (FFF) using WS2 nanotubes. *Sci Rep*. 2020;10(1):8892.

doi: 10.1038/s41598-020-65861-w

101. Daver F, Lee KPM, Brandt M, Shanks R. Cork -PLA composite filaments for fused deposition modelling. *Compos Sci Technol*. 2018;168:230-237.

doi: 10.1016/j.compscitech.2018.10.008

102. Le Duigou A, Castro M, Bevan R, Martin N. 3D printing of wood fibre biocomposites: From mechanical to actuation functionality. *Mater Des*. 2016;96:106-114.

doi: 10.1016/j.matdes.2016.02.018

103. Wu CS, Liao HT, Cai YX. Characterisation, biodegradability and application of palm fibre-reinforced polyhydroxyalkanoate composites. *Polym Degrad Stab*. 2017;140:55-63.

doi: 10.1016/j.polymdegradstab.2017.04.016

104. Kim DJ, Yu MH, Lim J, Nam B, Kim HS. Prediction of the mechanical behavior of fiber-reinforced composite structure considering its shear angle distribution generated during thermo-compression molding process. *Compos Struct*. 2019;220:441-450.

doi: 10.1016/j.compstruct.2019.04.043

105. Lee J, Ruckdashel R, Patil N, Pugatch M, Joshi K, Park JH. Highly filled coextruded dual-layer polymer/ceramic filament for material extrusion additive manufacturing. *ACS Appl Polym Mater*. 2023;5(4):2867-2876.

doi: 10.1021/acsapm.3c00089

106. Haryńska A, Janik H, Sienkiewicz M, Mikolaszek B, Kucińska-Lipka J. PLA -potato thermoplastic starch filament as a sustainable alternative to the conventional PLA filament: Processing, characterization, and FFF 3D printing. *ACS Sustain Chem Eng*. 2021;9(20):6923-6938.

doi: 10.1021/acssuschemeng.0c09413

107. Çanti E, Aydın M, Yıldırım F. Production and characterization of composite filaments for 3D printing. *J Polytech*. 2018;21:397-402.

doi: 10.2339/politeknik.389591

108. Deb D, Jafferson JM. Natural fibers reinforced FDM 3D printing filaments. *Mater Today Proc*. 2021;46:1308-1318.

doi: 10.1016/j.matpr.2021.02.397

109. Yu S, Hwang YH, Hwang JY, Hong SH. Analytical study on the 3D-printed structure and mechanical properties of basalt fiber-reinforced PLA composites using X-ray microscopy. *Compos Sci Technol*. 2019;175:18-27.

doi: 10.1016/j.compscitech.2019.03.005

110. Satyanarayana KG, Arizaga GGC, Wypych F. Biodegradable composites based on lignocellulosic fibers-An overview. *Prog Polym Sci*. 2009;34(9):982-1021.

doi: 10.1016/j.progpolymsci.2008.12.002

111. Nandi P, Das D. Mechanical, thermo-mechanical and biodegradation behaviors of green-composites prepared from woven structural nettle (*Girardinia diversifolia*) reinforcement and poly (Lactic acid) fibers. *Ind Crops Prod*. 2022;175:114247.

doi: 10.1016/j.indcrop.2021.114247

112. Ji M, Li F, Li J, *et al*. Enhanced mechanical properties, water resistance, thermal stability, and biodegradation of the starch-sisal fibre composites with various fillers. *Mater Des*. 2021;198:109373.

doi: 10.1016/j.matdes.2020.109373

113. Hasan MR, Davies IJ, Pramanik A, John M, Biswas WK. Potential of recycled PLA in 3D printing: A review. *Sustain Manuf Serv Econ*. 2024;3:100020.

doi: 10.1016/j.smse.2024.100020

114. Oladapo BI, Bowoto OK, Adebiyi VA, Ikumapayi OM. Net zero on 3D printing filament recycling: A sustainable analysis. *Sci Total Environ*. 2023;894:165046.

doi: 10.1016/j.scitotenv.2023.165046

115. Mikula K, Skrzypczak D, Izydorczyk G, *et al*. 3D printing filament as a second life of waste plastics-a review. *Environ Sci Pollut Res*. 2021;28(10):12321-12333.

doi: 10.1007/s11356-020-10657-8

116. Zhao P, Rao C, Gu F, Sharmin N, Fu J. Close-looped recycling of polylactic acid used in 3D printing: An experimental investigation and life cycle assessment. *J Clean Prod*. 2018;197:1046-1055.

doi: 10.1016/j.jclepro.2018.06.275

117. Shah DU, Schubel PJ, Clifford MJ, Licence P. Fatigue Characterisation of Natural Fibre Composites for Small-Scale Wind Turbine Blade Applications. In: *ECCM15-15th European Conference*; 2012. p. 24-28.

118. Bhardwaj D, Gupta A, Chaudhary V, Gupta S. Hybridization of natural fibers to develop the polymeric composite materials: A review. In: *Advances in Engineering Materials. Lecture Notes in Mechanical Engineering*. Singapore: Springer; 2021. p. 355-363.

doi: 10.1007/978-981-33-6029-7_33

119. Nurazzi NM, Asyraf MRM, Fatimah Athiyah S, *et al*. A review on mechanical performance of hybrid natural fiber polymer composites for structural applications. *Polymers* (*Basel*). 2021;13(13):2170.

doi: 10.3390/polym13132170

120. Jani SP, Kumar AS, Khan MA, Kumar MU. Machinablity of hybrid natural fiber composite with and without filler as reinforcement. *Mater Manuf Processes*. 2016;31(10):1393-1399.

doi: 10.1080/10426914.2015.1117633

ACCSCIENCE PUBLISHING

Materials Science in Additive Manufacturing

ORIGINAL RESEARCH ARTICLE

Multicavity structures with triply periodic minimal surface for broadband and perfect sound absorption manufactured by laser powder bed fusion

Mingkang Zhang[1], Mingjian Deng[1], Guanhao Wang[1], Sihua Yin[1], Wenbin Liu[1], Chang Liu[1], and Jie Chen[2]*

[1]Additive Manufacturing Laboratory, School of Mechanical and Energy Engineering, Guangdong Ocean University, Yangjiang, Guangdong, China

[2]Guangdong Key Laboratory of Modern Control Technology, Institute of Intelligent Manufacturing, Guangdong Academy of Sciences, Guangzhou, Guangdong, China

Abstract

This research proposes a multicavity and a graded structure design method for triply periodic minimal surface (TPMS) structures with broadband and perfect sound absorption. TPMS structures were manufactured by laser powder bed fusion. The sound absorption coefficient curves and acoustic band structure of TPMS are analyzed using a two-microphone impedance tube. As the thickness of TPMS structures increases, the noise reduction coefficient of TPMS structures increases linearly, and the first resonance frequency shifts to the lower frequency. The acoustic band structures indicate that the acoustic bandgap of TPMS structures shifts to a lower frequency with increasing thickness. Diamond has the highest noise reduction coefficient among these four types of TPMS. The TPMS with a multicavity design has multiple resonance peaks. Notably, the five resonance peaks of the multicavity-I-Wrapped Package (IWP) are all above 0.94, achieving near-perfect sound absorption over a wide frequency range. The semi-absorption bandwidth of the multicavity-TPMS structure has been widened, except for multicavity-diamond structures. Both uniform and multicavity TPMS present a subwavelength absorption peak. The graded design method can broaden the semi-absorption bandwidth of TPMS, and the combination of graded and multicavity designs can further enhance broadband and achieve perfect sound absorption.

Keywords: Triply periodic minimal surface; Laser powder bed fusion; Acoustic metamaterials; Sound absorption; Broadband

***Corresponding author:**
Jie Chen
(j.chen@giim.ac.cn)

Citation: Zhang M, Deng M, Wang G, *et al*. Multicavity structures with triply periodic minimal surface for broadband and perfect sound absorption manufactured by laser powder bed fusion. *Mater Sci Add Manuf*. 2024;4(1):5737. doi: 10.36922/msam.5737

Received: October 31, 2024

Revised: December 2, 2024

Accepted: December 13, 2024

Published Online: January 10, 2025

1. Introduction

A 3D phononic crystal was designed based on a local resonance mechanism, which has subwavelength elastic wave/acoustic wave modulation characteristics.[1] The wavelength corresponding to the bandgap of the phononic crystal is much larger than the lattice size, surpassing the limitations of the Bragg scattering mechanism and classifying it as an acoustic metamaterial. Acoustic metamaterial is an artificial structural material

with unusual acoustic properties, which cannot be found in natural materials, such as the reflection, absorption, filtering, guided waves, focusing, superlensing, and acoustic stealth of sound waves.[2] Acoustic metamaterials are usually at the subwavelength scale, whose characteristic length is smaller than the wavelength of acoustic waves, which necessitates accounting for viscous and thermal losses.[3]

Sound absorption metamaterials, a subset of acoustic metamaterials, have broad application prospects in sound absorption and noise reduction in ships, submarines, airplanes, automobiles, and construction fields. Sound absorption metamaterials include thin-film acoustic metamaterials,[4] 2D plate-like acoustic metamaterials,[5] Helmholtz-like acoustic metamaterials,[6] and porous structural acoustic metamaterials.[7] Thin-film sound-absorbing structures require large cavities and have poor mechanical properties. The perforated plate sound absorption structure can be approximated as an array of Helmholtz resonators arranged in a regular manner; however, its narrow sound absorption peak limits its application. Porous sound absorption structures convert sound energy into thermal energy due to viscous loss generated by the propagation of sound waves inside the pores, thereby achieving sound absorption effects. However, the resonant absorption peak of porous structures is related to the thickness of the pores, due to the quarter wavelength resonance of the hard-backed porous material.[8] Due to the thickness limitation of porous structures, their broadband and low-frequency sound absorption performance is not ideal.

Design methods for expanding the sound absorption bandwidth of metamaterials have garnered significant attention from researchers.[9,10] Based on the performance of the absorber array, which features varying sizes and spatial arrangements of the component absorbers, it is proposed to arrange three subcavities of different depths in parallel on a microperforated plate.[11] This design effectively expands the sound absorption bandwidth of the microperforated panel absorber by utilizing the local resonance effect of subcavities of different depths and frequencies. A series-parallel-coupled composite micro-perforated panel (MPP) sound-absorbing device was proposed, and a theoretical model was established based on the acoustic-electric analogy method, experimental verification was conducted, and the results indicated that the series-parallel-coupled sound-absorbing device could broaden the absorption bandwidth.[12] According to the characteristic that the resonant frequency of MPP shifts with changes in cavity depth, MPPs with different cavity depths have been designed and optimized.[13] Different depths of honeycomb cores can achieve broadband sound absorption. It is demonstrated that the multiple internal reflections could be harnessed to achieve highly absorptive acoustic metamaterials.[14] In general, lengthened paths or multiple resonant cavities lead to enhanced dissipation in the structure-coiled absorbers.[15]

Triply periodic minimal surface (TPMS) is a potential sound absorption metamaterial due to its pore size and porosity that can be adjusted within the typical range of other open-pore porous materials. In addition, TPMS also has lightweight and high-strength characteristics. TPMS structures, including primitive, gyroid, and diamond, have been manufactured by stereolithography and tested using the two-microphone impedance method.[16] The results indicate that diamond exhibits excellent sound absorption performance among these three types of structures across a wide bandwidth. The sound insulation performances of primitive and gyroid sandwich panels have been investigated; the gyroid sandwich panel is significantly superior to the primitive sandwich panel,[17] and the gyroid structure can achieve sound insulation of more than 20 dB across a broad frequency range. This demonstrates the advantage of TPMS structures in sound absorption and insulation; however, their bandwidth and low-frequency absorption remain limited. Porosity affects sound absorption, and the reduced porosity of TPMS structures can improve the sound absorption coefficient.[18] A composite structure with TPMS and a MPP structure has been proposed, displaying good sound absorption performance. The maximum sound absorption coefficients exceed 0.8, with the resonance frequency shifting to lower frequencies.[19] A modular multicavity geometry with TPMS and aerogel-3D has been designed, offering application-specific low-frequency and broadband absorption performance.[20] The ultrabroad half-absorption band from 0.96 to 6.00 kHz is obtained by the multicavity and multilayered design.[21]

In addition to the multicavity composite design, the graded structure design can broaden the absorption frequencies of porous structures. The average sound absorption coefficient of four-layer gradient compressed porous metals with different permutations is 60.33% at 100 – 6000 Hz, with a total thickness of 11 mm.[22] The gradient interface between the porous media inside the sound absorption structure is beneficial for improving the sound absorption performance, as sound waves are absorbed by secondary reflection due to impedance mismatch when encountering the interface inside the porous structure.[23] A 2D continuously graded phononic crystal (CGPC) has been proposed, capable of enhancing acoustic scattering and lengthening propagation paths, leading to increased energy dissipation and improved sound absorption performance.[24] Compared to the uniform porous structure, the first resonance frequency of CGPC shifts to a lower frequency, and the increase in sound absorption is associated with the increased absorbed energy.[25] The

numerical results demonstrate a shift of the perfect absorption peak to lower frequencies or a widening of the perfect absorption frequency range for graded materials.[26] The Johnson-Champoux-Allard-Lafarge model was applied to calculate the sound absorption of a graded primitive (GP) absorber, indicating that the graded direction can affect the sound absorption curves.[27] These studies have demonstrated that the graded design can broaden the bandwidth of TPMS and lower the resonance peak frequency.

In this study, the sound absorption characteristics of four TPMS structures, including gyroid, primitive, I-Wrapped Package (IWP), and diamond, were studied using an impedance tube, and laser powder bed fusion (LPBF) technology was applied to manufacture the TPMS structures. The sound absorption curves and Bloch wave vector k of TPMS structures are applied to analyze the impact of thickness and graded direction on the acoustic bandgap and bandwidth. A design method of multicavity TPMS is proposed to achieve broadband and perfect sound absorption. In addition, a composite design of multicavity and graded TPMS structures is further proposed to enhance the sound absorption characteristics of acoustic metamaterials.

2. Methods

2.1. Design method

2.1.1. Design of uniform TPMS structures

TPMS cellular structures, including gyroid, primitive, IWP, and diamond, were generated using MATLAB codes and functions (Equations I-IV). Design parameters are listed in Table 1. The unit cell size was set by parameter *s* in the function, and the unit cell size of the uniform structure was set as 3 × 3 × 3 mm. The diameter of the design space was 29 mm, and the structures' thickness was changed from 6 to 30 mm. The offset thickness of the surfaces of gyroid, primitive, IWP, and diamond was designed at 0.265, 0.3, 0.22, and 0.208 mm, respectively, and the porosity of the four TPMS structures was fixed at 75%. Design models of the uniform TPMS structures are displayed in Figure 1.

$$F_{Gyroid} = \sin\left(\frac{2\pi x}{s}\right)\times\cos\left(\frac{2\pi y}{s}\right)+\sin\left(\frac{2\pi y}{s}\right)\times\cos\left(\frac{2\pi z}{s}\right)+\sin\left(\frac{2\pi z}{s}\right)\times\cos\left(\frac{2\pi x}{s}\right) \quad (I)$$

$$F_{Prmitive} = 10^{*}\left[\cos\left(\frac{2\pi x}{s}\right)+\cos\left(\frac{2\pi y}{s}\right)+\cos\left(\frac{2\pi z}{s}\right)\right] - 5^{*}\left[\begin{array}{l}\cos\left(\frac{2\pi x}{s}\right)\times\cos\left(\frac{2\pi y}{s}\right)+\cos\left(\frac{2\pi y}{s}\right)\\ \times\cos\left(\frac{2\pi z}{s}\right)+\cos\left(\frac{2\pi z}{s}\right)\times\cos\left(\frac{2\pi x}{s}\right)\end{array}\right] \quad (II)$$

$$F_{Iwp} = 10^{*}\left[\begin{array}{l}\cos\left(\frac{2\pi x}{s}\right)\times\cos\left(\frac{2\pi y}{s}\right)+\cos\left(\frac{2\pi y}{s}\right)\\ \times\cos\left(\frac{2\pi z}{s}\right)+\cos\left(\frac{2\pi z}{s}\right)\times\cos\left(\frac{2\pi x}{s}\right)\end{array}\right] - 5^{*}\left[\cos\left(\frac{4\pi x}{s}\right)+\cos\left(\frac{4\pi y}{s}\right)+\cos\left(\frac{4\pi z}{s}\right)\right] \quad (III)$$

$$F_{Diamond} = 10^{*}\left[\begin{array}{l}\sin\left(\frac{2\pi x}{s}\right)\times\sin\left(\frac{2\pi y}{s}\right)\times\sin\left(\frac{2\pi z}{s}\right)\\ +\sin\left(\frac{2\pi x}{s}\right)\times\cos\left(\frac{2\pi y}{s}\right)\times\cos\left(\frac{2\pi z}{s}\right)\\ +\cos\left(\frac{2\pi x}{s}\right)\times\sin\left(\frac{2\pi y}{s}\right)\times\cos\left(\frac{2\pi z}{s}\right)\\ +\cos\left(\frac{2\pi x}{s}\right)\times\cos\left(\frac{2\pi y}{s}\right)\times\sin\left(\frac{2\pi z}{s}\right)\end{array}\right] - 0.5^{*}\left[\cos\left(\frac{8\pi x}{s}\right)+\cos\left(\frac{8\pi y}{s}\right)+\cos\left(\frac{8\pi z}{s}\right)\right] \quad (IV)$$

2.1.2. Design of multicavity TPMS structures

The multicavity structures with four cavity depths were designed according to the characteristic that the resonant frequency of the structure shifts and broadband sound absorption can be achieved when the cavity depth changes. The design parameters of the multicavity structure are listed in Table 2, and the design models are displayed in Figure 2. For example, the multicavity-gyroid structures were composed of four depth cavities, and each cavity was filled with a uniform gyroid structure with 75% porosity, including Gyroid-12 mm, Gyroid-18 mm, Gyroid-24 mm, and Gyroid-30 mm. The porosity of all multicavity TPMS structures is 75%.

2.1.3. Design of graded TPMS

To explore the influence of the graded structure on the sound absorption characteristics, GP structures were designed (Figure 3); the designed parameters are listed in Table 3. A linear function determined the graded structures of GP. In type I, the unit cell size on the incident face is 2 mm, and the unit cell size on the rigid face is 4 mm. On the contrary, in type II, the unit cell size on the incident face is 4 mm, and the unit cell size on the rigid face is 2 mm.

Multicavity GP type I (multicavity-GP-I) structures were designed with four GP thicknesses, including GP-12 mm-I, GP-18 mm-I, GP-24 mm-I, and GP-30 mm-I. Multicavity GP type II (multicavity-GP-II) structures were also designed with four GP thicknesses,

Table 1. Design parameters of uniform triply periodic minimal surface (TPMS) structures

Specimen	Size of unit cell (mm)	Thickness of porous structure (mm)	Offset thickness of surface (mm)	Porosity (%)
Gyroid-6 mm	3	6	0.265	75
Gyroid-12 mm	3	12	0.265	75
Gyroid-18 mm	3	18	0.265	75
Gyroid-24 mm	3	24	0.265	75
Gyroid-30 mm	3	30	0.265	75
Primitive-6 mm	3	6	0.3	75
Primitive-12 mm	3	12	0.3	75
Primitive-18 mm	3	18	0.3	75
Primitive-24 mm	3	24	0.3	75
Primitive-30 mm	3	30	0.3	75
IWP-6 mm	3	6	0.3	75
IWP-12 mm	3	12	0.3	75
IWP-18 mm	3	18	0.3	75
IWP-24 mm	3	24	0.3	75
IWP-30 mm	3	30	0.3	75
Diamond-6 mm	3	6	0.208	75
Diamond-12 mm	3	12	0.208	75
Diamond-18 mm	3	18	0.208	75
Diamond-24 mm	3	24	0.208	75
Diamond-30 mm	3	30	0.208	75

Abbreviation: IWP: I-Wrapped Package.

Table 2. Design parameters of multicavity triply periodic minimal surface (TPMS) structures

Specimen	Size of unit cell (mm)	Constituent part
Multicavity-gyroid	3	Gyroid-12 mm+Gyroid-18 mm +Gyroid-24 mm+Gyroid-30 mm
Multicavity-primitive	3	Primitive-12 mm+Primitive-18 mm+Primitive-24 mm +Primitive-30 mm
Multicavity-IWP	3	IWP-12 mm+IWP-18 mm +IWP-24 mm+IWP-30 mm
Multicavity-diamond	3	Diamond-12 mm+Diamond-18 mm+Diamond-24 mm +Diamond-30 mm

Abbreviation: IWP: I-Wrapped Package.

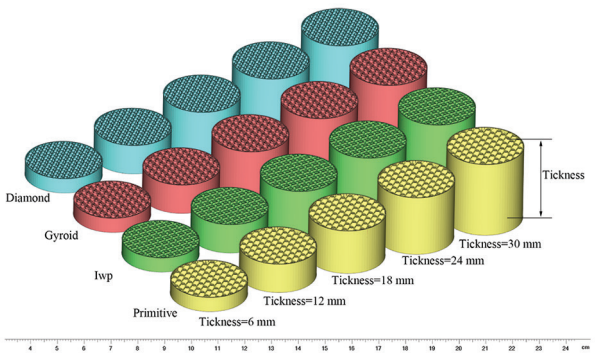

Figure 1. Design models of uniform triply periodic minimal surface (TPMS) structures
Abbreviation: IWP: I-Wrapped Package

including GP-12 mm-II, GP-18 mm-II, GP-24 mm-II, and GP-30 mm-II. The design parameters and design model of multicavity-GP-I and multicavity-GP-II structures are displayed in Table 3 and Figure 4. The porosity of GP and multicavity GP structures was fixed at 75%.

2.2. LPBF preparation procedure

The acoustic metamaterials were manufactured using LPBF equipment (Dimetal-280; Laseradd Co., Ltd., China), and the manufacturing parameters are listed in Table 4. AlSi7Mg powder was applied to LPBF, and its particle size distribution is: D10 = 19.2 μm; D50 = 34.6 μm; and D90 = 60.8 μm. The chemical composition of AlSi7Mg powder is listed in Table 5. TPMS specimens manufactured by LPBF are displayed in Figure 5.

2.3. Sound absorption coefficient test

According to the ASTM E1050-12 standard, the absorption coefficient of acoustic metamaterial was measured using

Table 3. Design parameters of graded primitive structures

Specimen	Size of a unit cell on the incident face (mm)	Size of a unit cell on rigid face (mm)	Thickness of porous structure (mm)	Linear function
GP-12 mm-I	2	4	12	$s=\frac{1}{6}*z+2$
GP-12 mm-II	4	2	12	
GP-18 mm-I	2	4	18	$s=\frac{1}{9}*z+2$
GP-18 mm-II	4	2	18	
GP-24 mm-I	2	4	24	$s=\frac{1}{12}*z+2$
GP-24 mm-II	4	2	24	
GP-30 mm-I	2	4	30	$s=\frac{1}{15}*z+2$
GP-30 mm-II	4	2	30	
Multicavity-GP-I	2	4	12+18+24+30	N/A
Multicavity-GP-II	4	4	12+18+24+30	N/A

Note: The thickness of multicavity-GP-I and multicavity-GP-II is based on the combined thickness of Design models for multicavity structures.
Abbreviation: GP: Graded primitive; N/A: Not available.

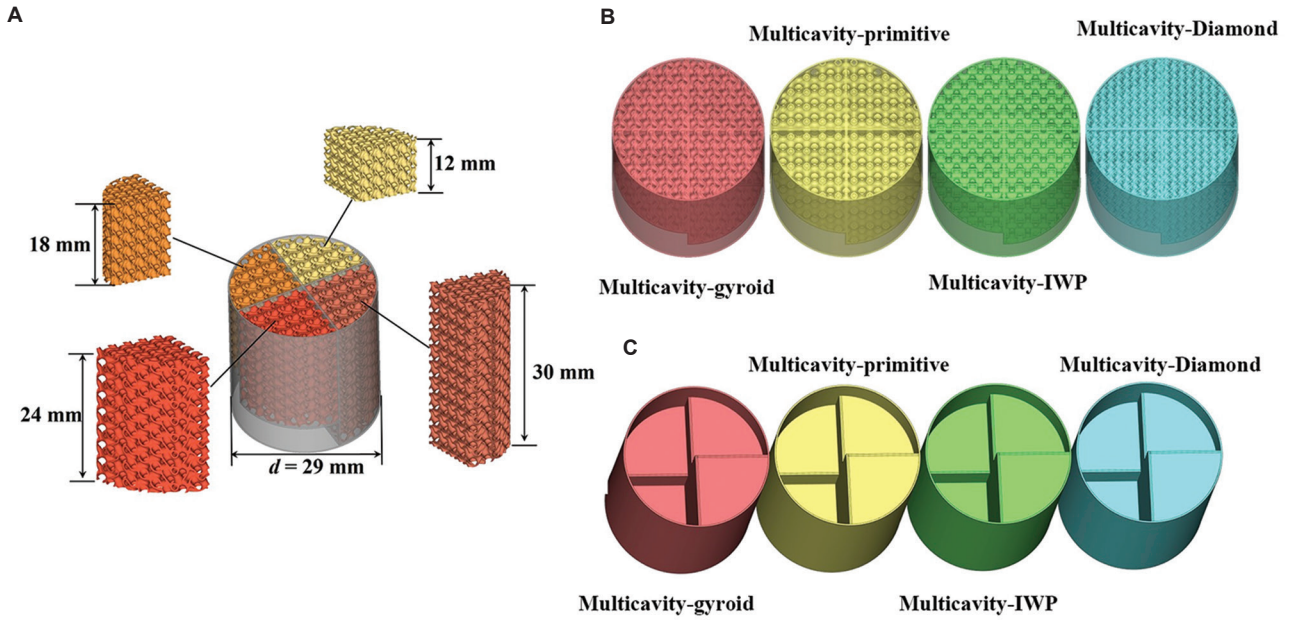

Figure 2. Design models for multicavity structures. (A) Design method for multicavity triply periodic minimal surface (TPMS) structures. (B) Design models of multicavity TPMS structures (top view). (C) Design models of multicavity TPMS structures (bottom view).

an impedance tube (SW4661; BSWA Technology Co. Ltd., China) with a 29 mm diameter at a relative humidity of 68.2%, a temperature of 27°C, and a wave propagation speed in the air of 347 m/s (Figure 6).

The reflection coefficient R with a rigid back was calculated using the following function (Equation V):

$$R=\frac{H-e^{-jks}}{e^{jks}-H}e^{j2k(l+s)} \quad \text{(V)}$$

where H is the ratio of pressure between two microphones, k is equivalent to 2pf/c (wavenumber [m^{-1}]), j is the imaginary part, $\sqrt{-1}$, l is the distance from the test sample to the center of the nearest microphone (m), and s is the center-to-center spacing between microphones (m).

The sound absorption coefficient α was calculated using the following function (Equation VI):

$$\alpha=1-|R|^2 \quad \text{(VI)}$$

The noise reduction coefficient (NRC) was applied to evaluate the sound absorption capability as a single index. We calculated NRC as the average of the absorption

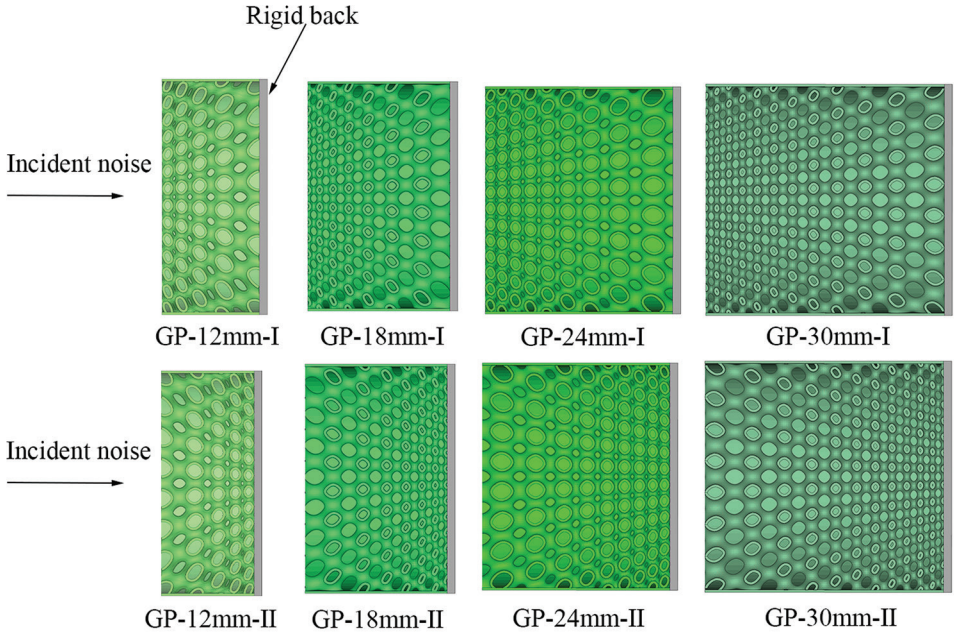

Figure 3. Design model of graded primitive structures with different thicknesses
Abbreviation: GP: Graded primitive

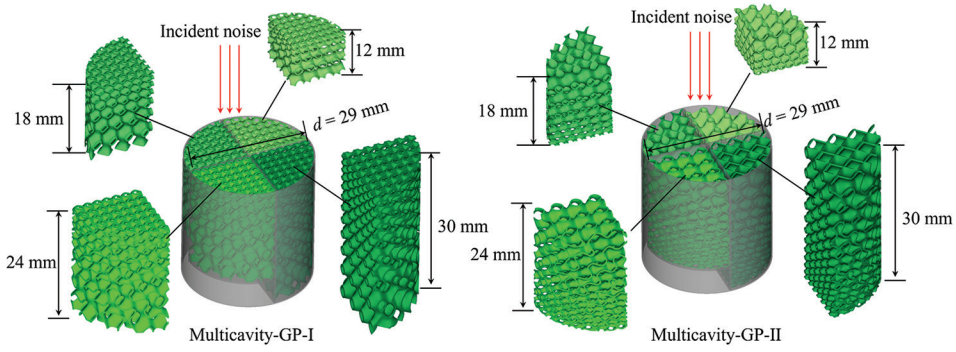

Figure 4. Design model of multicavity-GP-I and multicavity-GP-II
Abbreviation: GP: Graded primitive

coefficients at 500, 630, 800, 1000, 1250, 1600, 2000, 2500, 3150, 4000, 5000, and 6300 Hz.

2.4. Acoustic band structure

The Bloch wave vector k of TPMS is applied to analyze the band gap of the acoustic metamaterial and is considered a complex (Equation VII); k' is the real component, and k'' is the imaginary component of the Bloch wave vector k. The imaginary part represents the amplitude attenuation characteristics of a wave. When $k'' = 0$, it indicates that the wave is a free-traveling wave, and the phase changes along the wave propagation direction, whereas the amplitude remains unchanged. When $k'' \neq 0$, it indicates that the wave is attenuated. Therefore, by analyzing the changes in the curve of the imaginary part k'' of the Bloch wave vectwith frequency, the bandgap range of the acoustic metamaterial can be determined.

Table 4. The processing parameter for laser powder bed fusion

Laser power (W)	Scanning speed (mm/s)	Layer thickness (mm)	Scanning space (mm)
200	1200	0.03	0.09

Table 5. Chemical composition of AlSi7Mg powder

Element	Al	Si	Mg	Ti	Fe	Zn
Composition (wt. %)	Balance	7.01	0.56	0.15	0.073	0.015

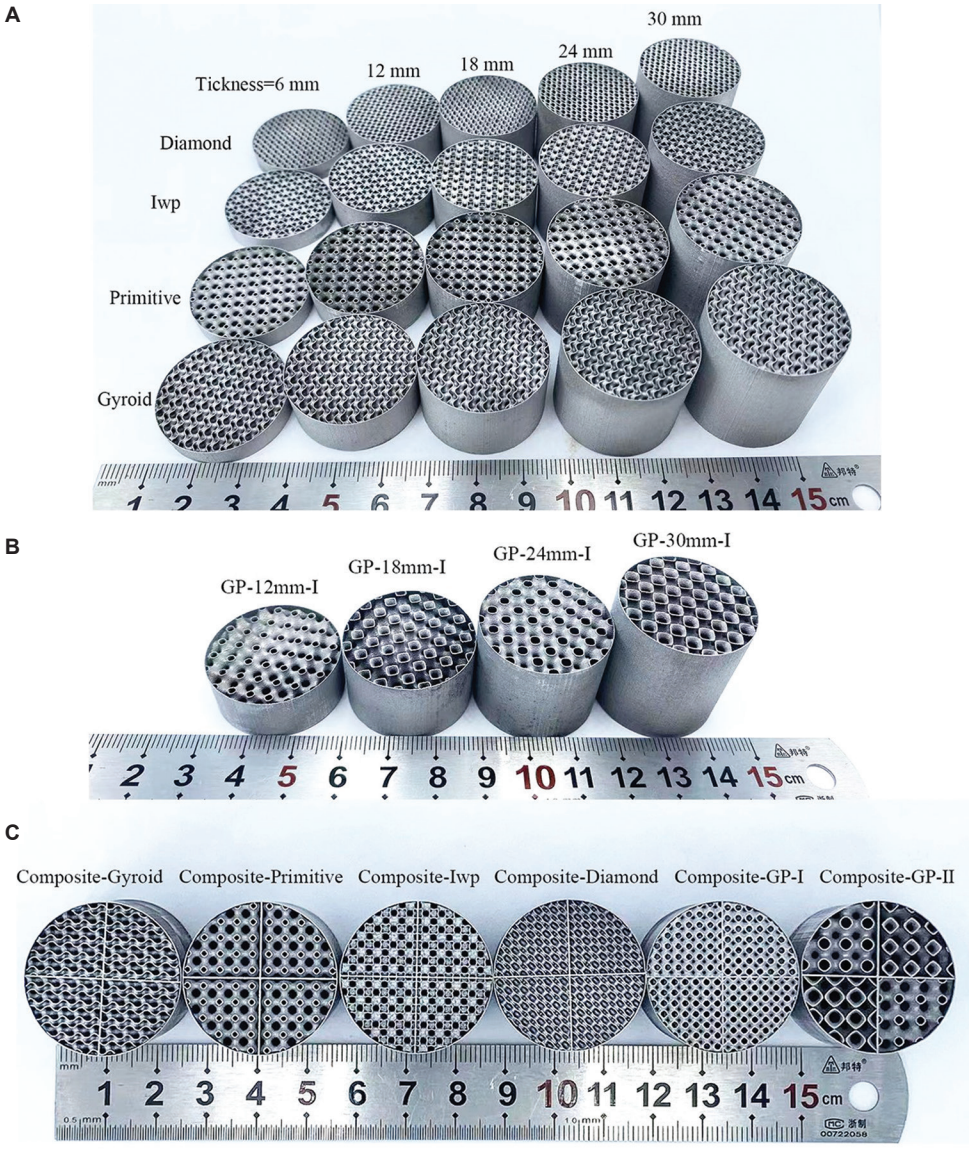

Figure 5. Triply periodic minimal surface (TPMS) structures manufactured by laser powder bed fusion (LPBF): (A) Uniform TPMS, (B) graded primitive, and (C) multicavity TPMS

$$k = k' - jk'' \quad \text{(VII)}$$

The test method for Bloch wave vector q is described as follows. The TPMS structure was placed in the impedance tube, ensuring that the end face was flush with the inner end face of the tube. Assuming a rigid scale of 30 mm, the cavity was extended from 10 to 40 mm for sound absorption testing, and the sound impedance file was saved. Next, the cavity was extended from 40 to 50 mm, creating a cavity length of 20 mm; sound absorption testing was performed again, and the acoustic impedance file was saved accordingly. Finally, the two distance acoustic impedance files were imported, and the Bloch wave vector k of the acoustic metamaterial was calculated. Due to the rigid baffle structure at the bottom of the multicavity structure, adjusting the distance between the tail cavity has little effect on the overall impedance value of the structure, making it difficult to determine the true wavenumber frequency graph of the multicavity structure. Therefore, this measurement is only effective for structures without rigid walls and is invalid for multicavity structures.

3. Results and discussion

3.1. Sound absorption characteristics of multicavity without TPMS

The sound absorption coefficient curves of the multicavity structure with four depths, including 12, 18, 24, and

30 mm (Figure 7). There are four main resonance absorption peaks above 1500 Hz, namely 2670, 3310, 4560, and 6200 Hz. The ratio of the first absorption peak wavelength to structure thickness (λ_{peak}/T) is 4.34. This represents a subwavelength absorption peak, as the λpeak/T is >4, which exhibits a quarter wavelength resonance frequency (QWRF) of 2891 Hz at 30 mm. The sound absorption coefficient of the first, second, third, and fourth absorption peaks are 0.944, 0.944, 0.499, and 0.240, respectively. These four peaks correspond to the acoustic resonance of four cavities with different depths. The resonance peak of the multicavity structure without porous structure filling is narrow, and the frequency band of the first peak with sound absorption coefficients exceeding 0.5 is only 210 Hz.

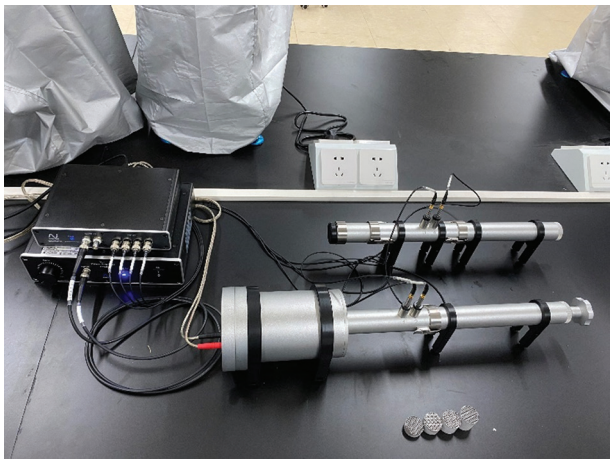

Figure 6. A two-microphone impedance tube

3.2. Sound absorption characteristics of gyroid and multicavity-gyroid structures

The sound absorption coefficient curves of gyroid structures with individual cavity and multicavity-gyroid structures are displayed in Figure 8. The first resonance peak of the gyroid structure was identified. The analysis of resonance peaks is listed in Table 6. As the thickness of the gyroid structure increases from 12 to 30 mm, the resonance peaks decrease from 5590 to 2000 Hz, indicating that the resonance absorption peak of the gyroid structure shifts toward lower frequencies as the thickness increases. A quarter-wavelength resonance has been found in periodic porous structures with hard-backing,[8] and the QWRF is equal to c/4T, where c is the wave propagation speed in air and T is the thickness of porous structures. The theoretical QWRF of periodic porous structures with 6, 12, 18, 24, and 30 mm is 14458, 7229, 4819, 3614, and 2891 Hz, respectively (i.e., f = c/4T; c = 347 m/s). The λ_{peak}/T of the gyroid structure is calculated and listed in Table 6. The uniform gyroid structures present a subwavelength absorption peak, as the λ_{peak}/T is >4. The experimental first absorption peak frequency of the Gyroid-24 mm structure is 2590 Hz, which is 1024 Hz lower than the QWRF, suggesting that the sheet-based gyroid structure has better absorption capability than the theoretical periodic porous structures.

Five peaks are visible on the spectrum of the multicavity-gyroid structure, the first four peaks (2160, 2670, 3600, and 4810 Hz) corresponding to the four individual absorption peaks for each cavity with Gyroid-12 mm, Gyroid-18 mm, Gyroid-24 mm, and Gyroid-30 mm, respectively. The fifth

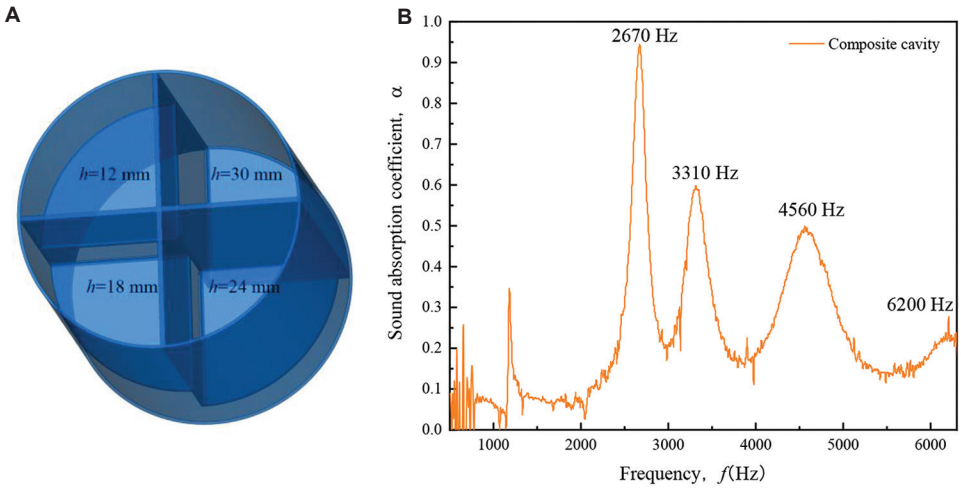

Figure 7. Sound absorption coefficient curves of multicavity structures. (A) Multicavity model without TPMS. (B) Sound absorption curve of multicavity model
Abbreviation: *h*: Height of cavity

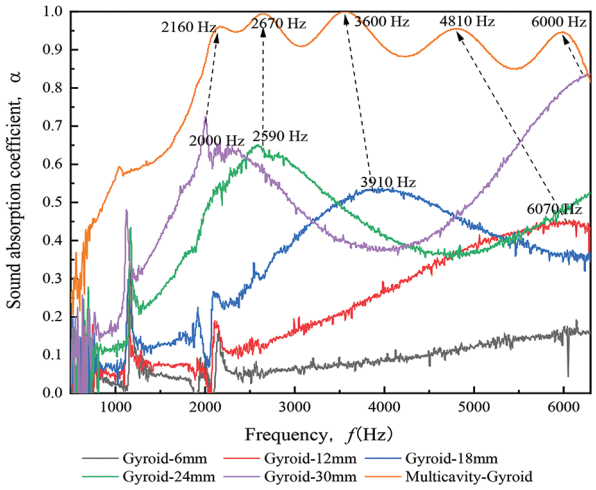

Figure 8. Sound absorption coefficient curves of gyroid and multicavity-gyroid structures

Table 6. Sound absorption characteristics of uniform gyroid and multicavity-gyroid structures

Specimen	Thickness, T (mm)	Frequency at first peak, f_1 (Hz)	Absorption at first peak, α_1	λ_{peak}/T
Gyroid-6 mm	6	-	-	-
Gyroid-12 mm	12	5590	0.449	5.18
Gyroid-18 mm	18	3900	0.535	4.95
Gyroid-24 mm	24	2590	0.651	5.59
Gyroid-30 mm	30	2000	0.725	5.34
Multicavity-gyroid	30	2160	0.962	5.79

peak, at 6000 Hz, corresponds to the second individual absorption peak of Gyroid-30 mm. The sound absorption coefficient at the resonance peak of a uniform gyroid structure also increases as the thickness increases. Moreover, the third, fourth, and fifth resonance peaks of the multicavity-gyroid structure shift to a lower frequency compared with the single gyroid cavity. The frequency shift can be attributed to the interaction of the inter-resonator, which corresponds to the multicavity filled with the gyroid structure. It can be observed that the five resonance peaks of the multicavity-gyroid structure are all above 0.95, and the third peak achieves 100% sound absorption. It is demonstrated that the multicavity design for the gyroid structure can obtain more absorption peaks and reach perfect sound absorption.

The acoustic bandgap of the gyroid structure was analyzed through the Bloch wave vector and frequency spectrum (Figure 9). The k" corresponding to the bandgap's starting frequency and cutoff frequency is 0. By examining the variation curve of k" with frequency, the bandgap range (i.e., the frequency range where $k" \neq 0$) can be determined, as marked with a black diagonal line. The gyroid structure with a thickness of 18 mm exhibits a wide flat band, which is an acoustic bandgap between 3460 and 4320 Hz (Figure 9C). This acoustic bandgap corresponds to the first resonance peak (f_1 = 3900 Hz; α_1 = 0.535) of Gyroid-18 mm, and the sound absorption coefficient between 3460 and 4320 Hz is higher than 0.5. The acoustic bandgap of Gyroid-24 mm is between 2080 and 3000 Hz, corresponding to the first resonance peak (f_1 = 2590 Hz; α_1 = 0.651) of Gyroid-24 mm. In contrast, two acoustic bandgaps were observed for Gyroid-30 mm. The first bandgap is between 2020 and 2770 Hz, corresponding to the first resonance peak (f_1 = 2000 Hz; α_1 = 0.725) of Gyroid-30 mm; the second bandgap is between 4540 and 4850 Hz, corresponding to the second resonance peak of Gyroid-30 mm. It is demonstrated that the characteristics of the sound absorption coefficient match the bandgap variation characteristics of the gyroid structures.

A sharp peak characteristic was also observed in Gyroid-12 mm, Gyroid-18 mm, Gyroid-24 mm, and Gyroid-30 mm, with a frequency corresponding to the attenuation sharp peak at 4340, 4860, 4370, and 4350 Hz, respectively. The attenuation peak is caused by the resonance effect of the local resonator, and the frequency at which this peak occurs corresponds to the natural frequency of the local resonator.

In general, the bandgap marked with a black diagonal line of the gyroid structure (Figure 9) refers to the Bragg bandgap, and the attenuation characteristics within the Bragg bandgap are relatively smooth with frequency variation. The frequency range in which this Bragg bandgap occurs is determined jointly by the constituent units of acoustic metamaterials. The bandgap with a sharp peak is referred to as the local resonance bandgap, and the significant peaks appear with frequency changes in the local resonance bandgap.

3.3. Sound absorption characteristics of primitive and multicavity-primitive structures

The sound absorption coefficient curves of primitive with individual cavity and multicavity-primitive structures are displayed in Figure 10. The sound absorption characteristics, including frequency, absorption, and λ_{peak}/T of the first peak are listed in Table 7. The resonance peaks of Primitive-12 mm, Primitive-18 mm, Primitive-24 mm, and Primitive-30 mm are 5440, 4150, 2840, and 2180 Hz, respectively. This result indicates that the resonance absorption peak of the primitive structure shifts toward lower frequencies as the thickness increases. Compared to the gyroid structure, the resonance

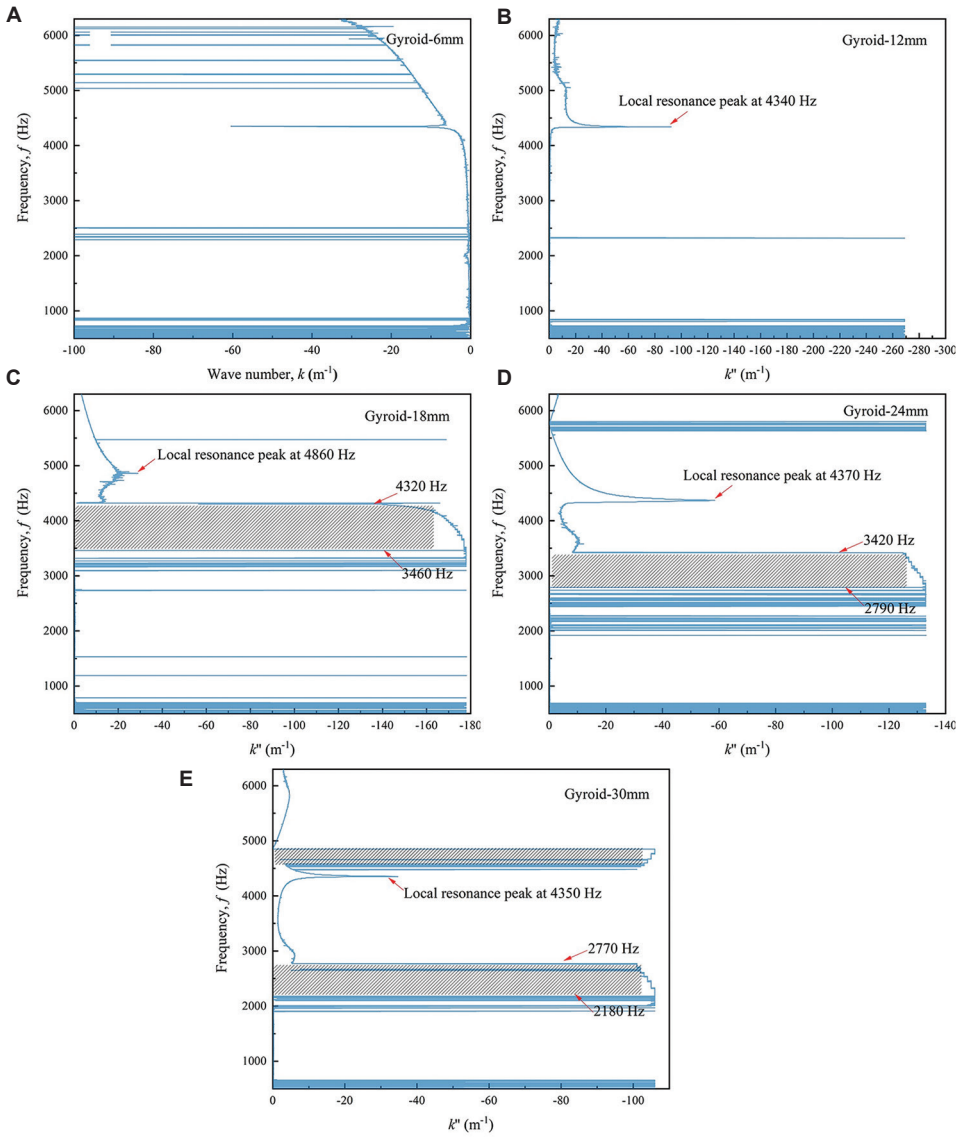

Figure 9. Acoustic band structure of: (A) Gyroid-6 mm, (B) Gyroid-12 mm, (C) Gyroid-18 mm, (D) Gyroid-24 mm, and (E) Gyroid-30 mm
Abbreviation: k": Bloch wave vector, imaginary part

Table 7. Sound absorption characteristics of primitive and multicavity-primitive

Specimen	Thickness, T (mm)	Frequency at first peak, f_1 (Hz)	Absorption at first peak, α_1	λ_{peak}/T
Primitive-6 mm	6	-	-	-
Primitive-12 mm	12	5440	0.465	5.32
Primitive-18 mm	18	4050	0.505	4.76
Primitive-24 mm	24	2850	0.524	5.08
Primitive-30 mm	30	2190	0.550	5.29
Multicavity-primitive	30	2090	0.913	5.54

frequency of the primitive structure with the same thickness is higher than that of the gyroid structure, except for the structure with a 12 mm thickness. The sound absorption coefficient of the resonance peak α_1 of Primitive-12 mm, Primitive-18 mm, Primitive-24 mm, and Primitive-30 mm are 0.465, 0.505, 0.524, and 0.55, respectively. The α_1 of Primitive-18 mm, Primitive-24 mm, and Primitive-30 mm is 5.6%, 19.5%, and 15.9% lower than that of Gyroid-18 mm, Gyroid-24 mm, and Gyroid-30 mm, respectively. The uniform primitive structures also present a subwavelength absorption peak, as the λ_{peak}/T is >4. The experimental first absorption peak frequency of the Primitive-24 mm structure is 2850 Hz, which is 764 Hz lower than the QWRF.

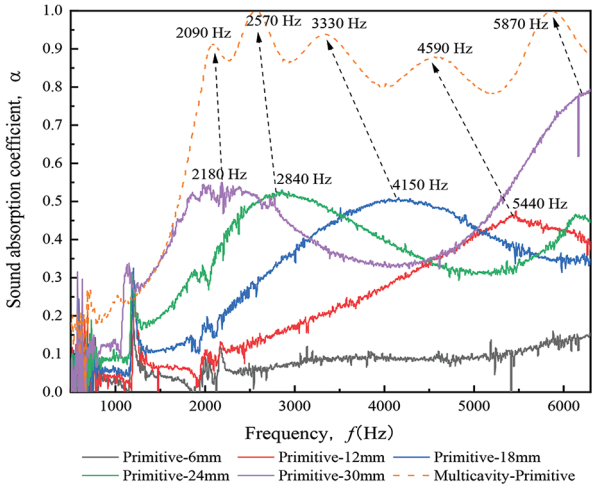

Figure 10. Sound absorption curves of primitive and multicavity-primitive structures

Five peaks are also visible on the spectrum of the multicavity-primitive structure. The first four peaks at frequencies of 2090, 2570, 3330, and 4590 Hz correspond to the four individual absorption peaks for each cavity with Primitive-12 mm, Primitive-18 mm, Primitive-24 mm, and-30 mm; the fifth peak (5870 Hz) corresponds to the second individual absorption peak of Primitive-30 mm. In addition, the primitive structure with a single cavity primarily exhibits semi-absorption at its first peak. The five resonance peaks of the multicavity-primitive structure are all above 0.75, and the second peak achieves 100% sound absorption. It is demonstrated that the multicavity design for the primitive structure can result in more absorption peaks and enhance sound absorption. However, the sound absorption coefficient at the third and fourth peaks of the multicavity-primitive structure is lower than that of the multicavity-gyroid structure.

The acoustic bandgap of the primitive structure was analyzed through the Bloch wave vector and frequency spectrum (Figure 11). The primitive structure with a thickness of 18 mm exhibits a wide flat band, which is a Bragg bandgap between 3330 and 4330 Hz (Figure 11C) and corresponds to the first resonance peak (f_1 = 4150 Hz; α_1 = 0.505) of Primitive-18 mm. The acoustic bandgap of Primitive-24 mm is between 2620 and 3240 Hz, corresponding to the first resonance peak (f_1 = 2840 Hz; α_1 = 0.524) of Primitive-24 mm. There is a sharp peak characteristic in Primitive-12 mm, Primitive-18 mm, Primitive-24 mm, and Primitive-30 mm, and the frequency corresponding to the attenuation sharp peak is 4340, 4860, 4370, and 4350 Hz, respectively; the frequency of these attenuation sharp peaks is consistent with the gyroid structures. It is illustrated that the sharp attenuation peak is not related to the type of TPMS structure, and the bandgap variation depends on the thickness of the TPMS structures.

Table 8. Sound absorption characteristics of uniform I-Wrapped Package (IWP) and multicavity-IWP structures

Specimen	Thickness, T (mm)	Frequency at first peak, f_1 (Hz)	Absorption at first peak, α_1	λ_{peak}/T
IWP-6 mm	6	-	-	-
IWP-12 mm	12	5480	0.574	5.28
IWP-18 mm	18	3860	0.619	5.00
IWP-24 mm	24	2670	0.750	5.42
IWP-30 mm	30	1890	0.821	6.13
Multicavity-IWP	30	2150	0.944	5.39

3.4. Sound absorption characteristics of IWP and multicavity-IWP structures

The sound absorption coefficient curves of IWP and multicavity-IWP are displayed in Figure 12, and the resonance peak analysis is listed in Table 8. The resonance peaks of IWP-12 mm, IWP-18 mm, IWP-24 mm, and IWP-30 mm are 5480, 3860, 2670, and 1890 Hz, respectively. The α_1 of IWP-12 mm, IWP-18 mm, IWP-24 mm, and IWP-30 mm are 0.574, 0.619, 0.750, and 0.821, respectively. These results indicate that the resonance peak frequency of the IWP structure shifts toward lower frequencies as the thickness increases; the sound absorption coefficient of the resonance peak of the IWP structure is enhanced as the thickness increases. The sound absorption coefficient of the IWP structure at the first resonance peak is higher than that of the gyroid and primitive structures with the same thickness. The QWRF of the IWP structures with different thicknesses are all higher than the theoretical QWRF.

Five peaks are visible on the spectrum of the multicavity-IWP structure; the first four peaks (2150, 2660, 3450, and 4850 Hz) correspond to the four individual absorption peaks for each cavity with IWP-12 mm, IWP-18 mm, IWP-24 mm, and IWP-30 mm; the fifth peak (5900 Hz) corresponds to the second individual absorption peak (6130 Hz) of IWP-30 mm. The resonance of multicavity-IWP structure frequencies shifts due to inter-resonator interactions, and the frequencies of peaks of the multicavity-IWP shift to the lower frequencies, except for the first peak. This indicates that the five resonance peaks of the multicavity-IWP are above 0.94, and the third peak achieves 100% sound absorption.

The acoustic bandgap of the IWP structure was analyzed through the Bloch wave vector and frequency

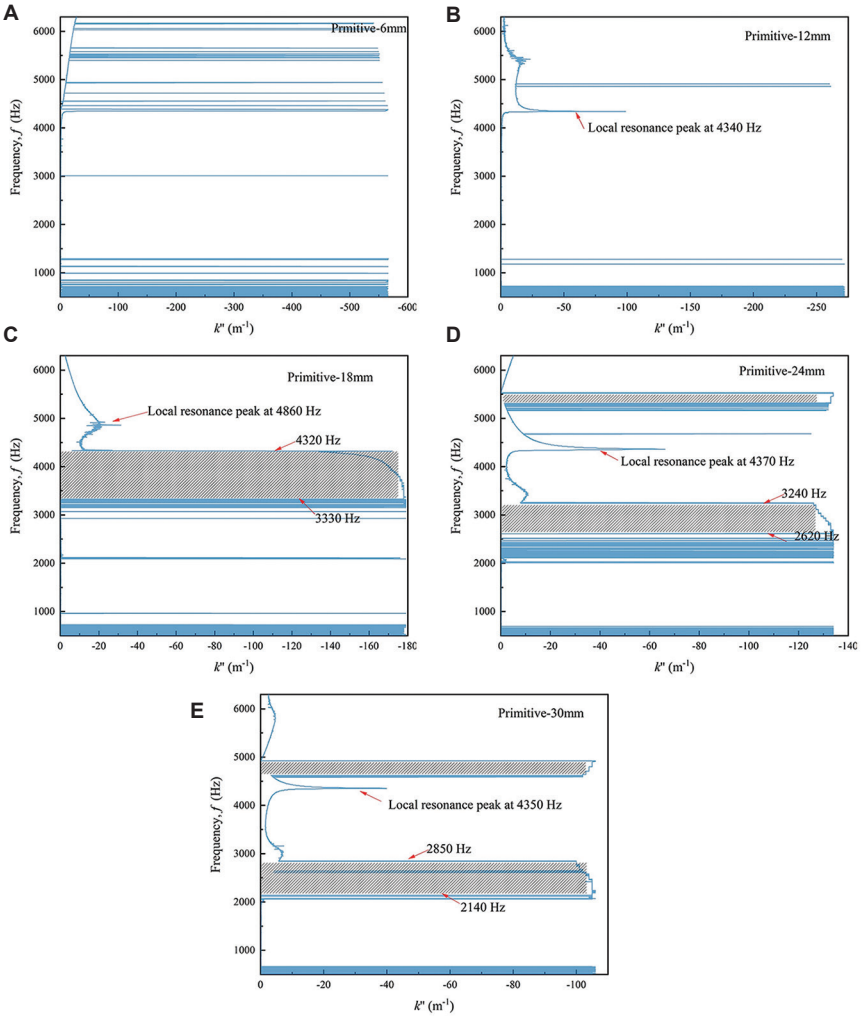

Figure 11. Acoustic band structure of: (A) Primitive-6 mm, (B) Primitive-12 mm, (C) Primitive-18 mm, (D) Primitive-24 mm, and (E) Primitive-30 mm Abbreviation: k": Bloch wave vector, imaginary part

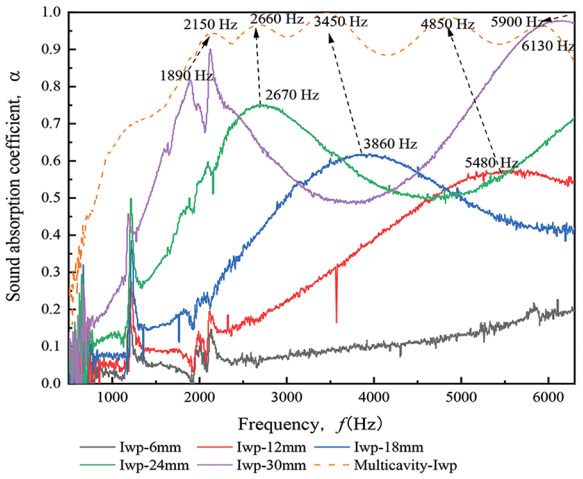

Figure 12. Sound absorption curves of: I-Wrapped Package (IWP) and multicavity-IWP structures

spectrum (Figure 13). The upper limit frequency of the bandgap of IWP-18 mm is 4140 Hz, and the lower limit frequency of the bandgap of IWP-18 mm is 3130 Hz. The resonance frequency (f_1 =3860 Hz) of the first peak of IWP-18 mm is within the above range. The width of the bandgap of IWP-18 mm, IWP-24 mm, and IWP-30 mm are 1010, 710, and 410 Hz, respectively, indicating that the bandgap of IWP decreases as the thickness increases; the bandgap of the IWP structure also shifts to a lower frequency. This pattern is similar to the variation pattern of the sound absorption coefficient curve: as the porosity thickness increases, the sound absorption peak gradually narrows and moves toward a lower frequency. A second narrow bandgap at IWP-24 mm and IWP-30 mm in the higher frequency region was observed, corresponding to the second resonance peak of the sound absorption coefficient curves of IWP-24 mm and IWP-30 mm.

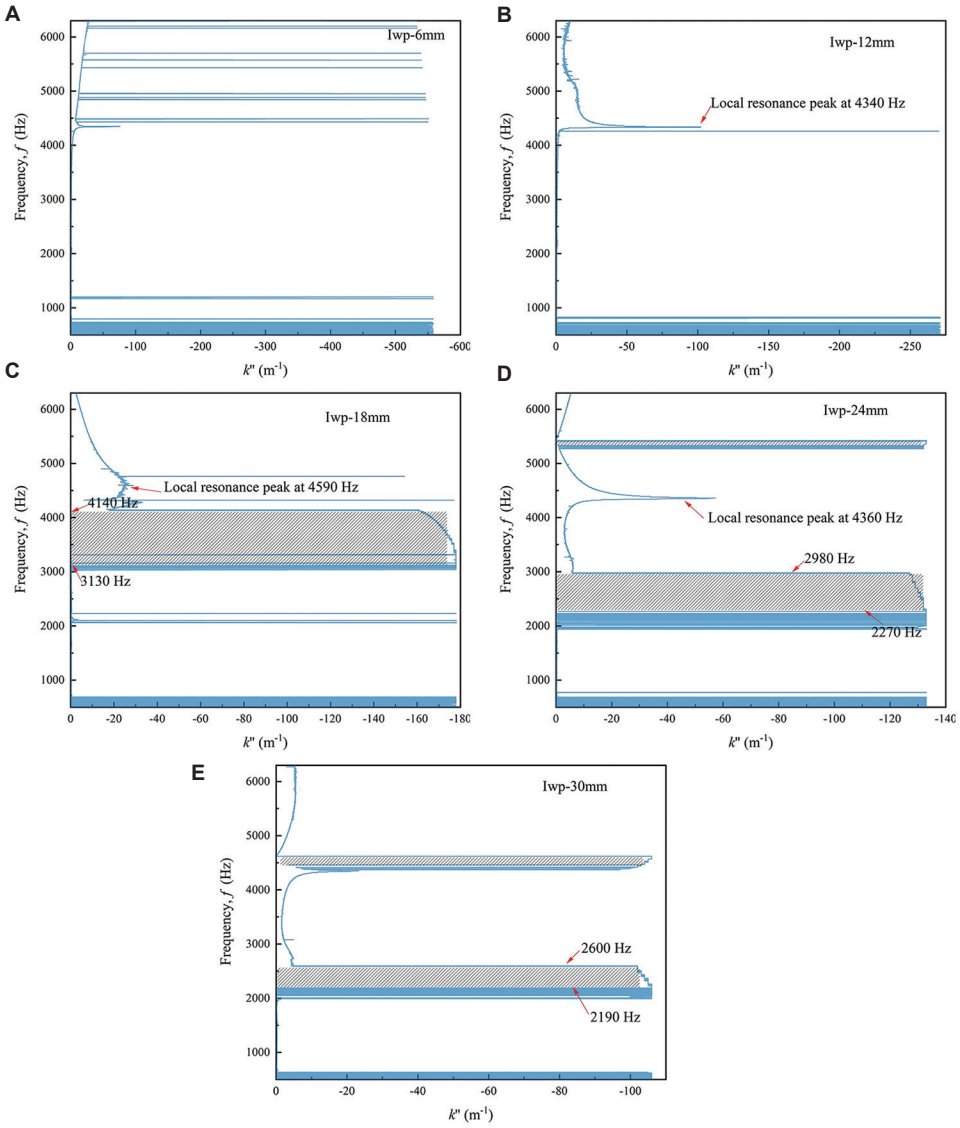

Figure 13. Acoustic band structure of: (A) IWP-6 mm, (B) IWP-12 mm, (C) IWP-18 mm, (D) IWP-24 mm, and (E) IWP-30 mm
Abbreviation: k": Bloch wave vector, imaginary part; IWP: I-Wrapped Package

3.5. Sound absorption characteristics of diamond and multicavity-diamond structures

The sound absorption coefficient curves of diamond and multicavity-diamond structures are displayed in Figure 14, and the characteristics of the first resonance peak are listed in Table 9. The resonance peaks of Diamond-12 mm, Diamond-18 mm, Diamond-24 mm, and Diamond-30 mm are 5870, 3790, 2620, and 1990 Hz, respectively. The α_1 of Diamond-12 mm, Diamond-18 mm, Diamond-24 mm, and Diamond-30 mm are 0.583, 0.679, 0.816, and 0.921, respectively, indicating that the resonance absorption peak of the diamond structure shifts toward lower frequencies with increasing thickness. As the thickness increases, the

Table 9. Sound absorption characteristics of the uniform diamond and multicavity-diamond structures

Specimen	Thickness, T (mm)	Frequency at first peak, f_1 (Hz)	Absorption at first peak, α_1	λ_{peak}/T
Diamond-6 mm	6	-	-	-
Diamond-12 mm	12	5870	0.583	4.93
Diamond-18 mm	18	3790	0.679	5.09
Diamond-24 mm	24	2620	0.816	5.52
Diamond-30 mm	30	1990	0.921	5.82
Multicavity-Diamond	30	2070	0.923	5.59

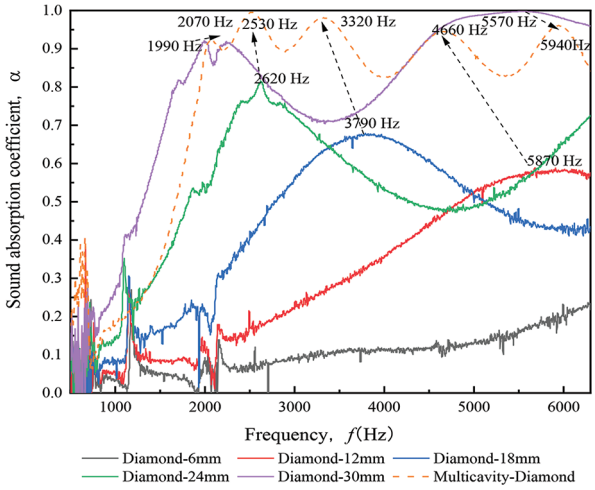

Figure 14. Sound absorption curves of diamond and multicavity-diamond structures

λ_{peak}/T of the diamond structure also increases from 4.93 to 5.82. The α_1 of the diamond structure with different thicknesses is the highest among the four kinds of uniform TPMS structures, including gyroid, primitive, IWP, and diamond. It is demonstrated that the diamond structure has the best sound absorption performance at high frequency among these four TPMS structures.

There are five peaks on the sound absorption curve of the multicavity-diamond structure at frequencies of 2070, 2530, 3320, 4660, and 5940 Hz. The first four peaks of the multicavity-diamond structure correspond to the resonance peaks of Diamond-12 mm, Diamond-18 mm, Diamond-24 mm, and Diamond-30 mm; the fifth peak of multicavity-diamond corresponds to the second resonance peak of Diamond-30 mm. The appearance of five peaks is related to the interaction between the sound absorption peaks of the porous structure of four cavities with different heights in the multicavity-diamond structure, with all five resonance peaks above 0.83. Additionally, the second peak achieves perfect sound absorption ($\alpha = 1$).

The acoustic band structures of the diamond structure with different thicknesses are displayed in Figure 17. The acoustic bandwidth of the diamond structure decreases as the thickness increases from 18 to 30 mm. The upper limit frequencies of the bandgap of Diamond-18 mm, Diamond-24 mm, and Diamond-30 mm are 3830, 2900, and 1860 Hz, respectively, and the lower limit frequency of bandgap of Diamond-18 mm, Diamond-24 mm, and Diamond-30 mm are 2890, 2070, and 1500 Hz, respectively. The resonance frequency of the first peaks of Diamond-18 mm and Diamond-24 mm are within the above range.

3.6. Sound absorption of graded TPMS structures

To enhance the sound absorption of the primitive structure, a graded design method was applied to the primitive acoustic metamaterials. The sound absorption coefficient curves of GP-I and GP-II are displayed in Figure 16, and the sound absorption characteristics are listed in Table 10. As the thickness of GP-I and GP-II increases, the frequency at the first peak f_1 shifts to a lower frequency. GP-30 mm-I has the lowest resonance frequency (1660 Hz) compared to the graded and uniform structures. Notably, the sound absorption coefficients at the first peak of GP-I are all higher than those of GP-II with the same thickness, and the frequency at the first peak f_1 of GP-I are all lower than that of GP-II with the same thickness. The λ_{peak}/T of GP-24 mm-II and GP-30 mm-II is lower than 4, indicating that the type II primitive structure has poorer absorption capability than the theoretical periodic porous structures. On the contrary, the λ_{peak}/T of GP-18 mm-I, GP-24 mm-I, and GP-30 mm-I are higher than 6, suggesting the presence of a subwavelength absorption peak.

There are two peaks in GP-18 mm-I, GP-24 mm-I, and GP-30 mm-I. After a combination of four cavities with 12, 18, 24, and 30 mm thickness, five peaks are found in the curves of multicavity-GP-I; the resonance peaks include 1980, 2420, 3060, 3970, and 5940 Hz. The sound absorption coefficient at the second peak of multicavity-GP-I is 0.998, reaching the perfect absorption. Six peaks are found in the curves of multicavity-GP-II; the resonance peaks include 1200, 2280, 2850, 3630, 5090, and 5940 Hz. Notably, the α_1 of the first resonance peak of multicavity-GP-II is 0.618, and this absorption value is lower than that of multicavity-GP-I, but the frequency of multicavity-GP-II is lower than that of multicavity-GP-I. The sound absorption coefficient at the third peak of multicavity-GP-II is 0.988, which is close to perfect sound absorption. The λ_{peak}/T of multicavity-GP-II is 9.65, which is the highest among all the TPMS structures assessed in this study.

The acoustic band structures of GP-I and GP-II with different thicknesses are displayed in Figure 15. The upper limit frequencies of the bandgap of GP-18 mm-I, GP-24 mm-I, and GP-30 mm-I are 4310, 3350, and 2890 Hz, respectively; the lower limit frequency of the bandgap of GP-18 mm-I, GP-24 mm-I, and GP-30 mm-I are 3580, 2800, and 2350 Hz, respectively. The first bandgap of GP-18 mm-I, GP-24 mm-I, and GP-30 mm-I are 730, 500, and 540 Hz, respectively. A second bandgap was identified in GP-24 mm-I and GP-30 mm-I at a higher frequency, suggesting that the lower limit frequency of GP-I shifts to the lower frequency as the thickness increases. The width of the bandgap of GP-18 mm-II is 21.9% wider than that of GP-18 mm-I; the width of the bandgap of GP-24 mm-II is 32%

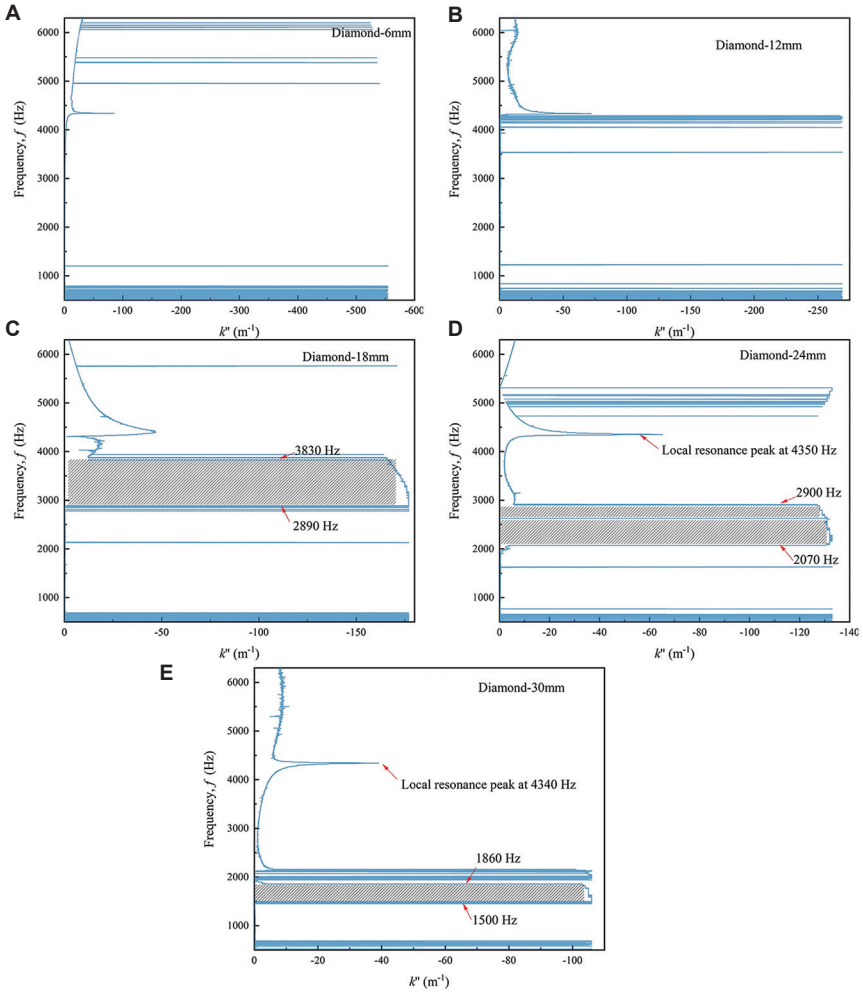

Figure 15. Acoustic band structure of: (A) Diamond-6 mm, (B) Diamond-12 mm, (C) Diamond-18 mm, (D) Diamond-24 mm, and (E) Diamond-30 mm
Abbreviation: k": Bloch wave vector, imaginary part

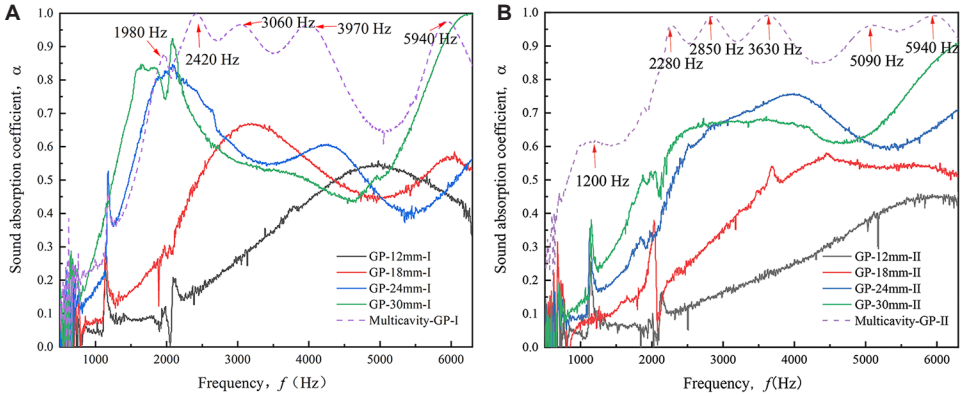

Figure 16. Sound absorption curves of graded primitive (GP) and multicavity GP structures: (A) Type I, and (B) Type II

wider than that of GP-24 mm-I. This result indicates that the sound waves incident from one side of a large unit cell size can increase the bandgap's width, which is related to the impedance-matching mechanism of acoustic metamaterials.

3.7. Comparison of sound absorption characteristics of TPMS structures

The NRC of all of the TPMS structures is displayed in Figure 18. The curves of thickness and NRC of uniform

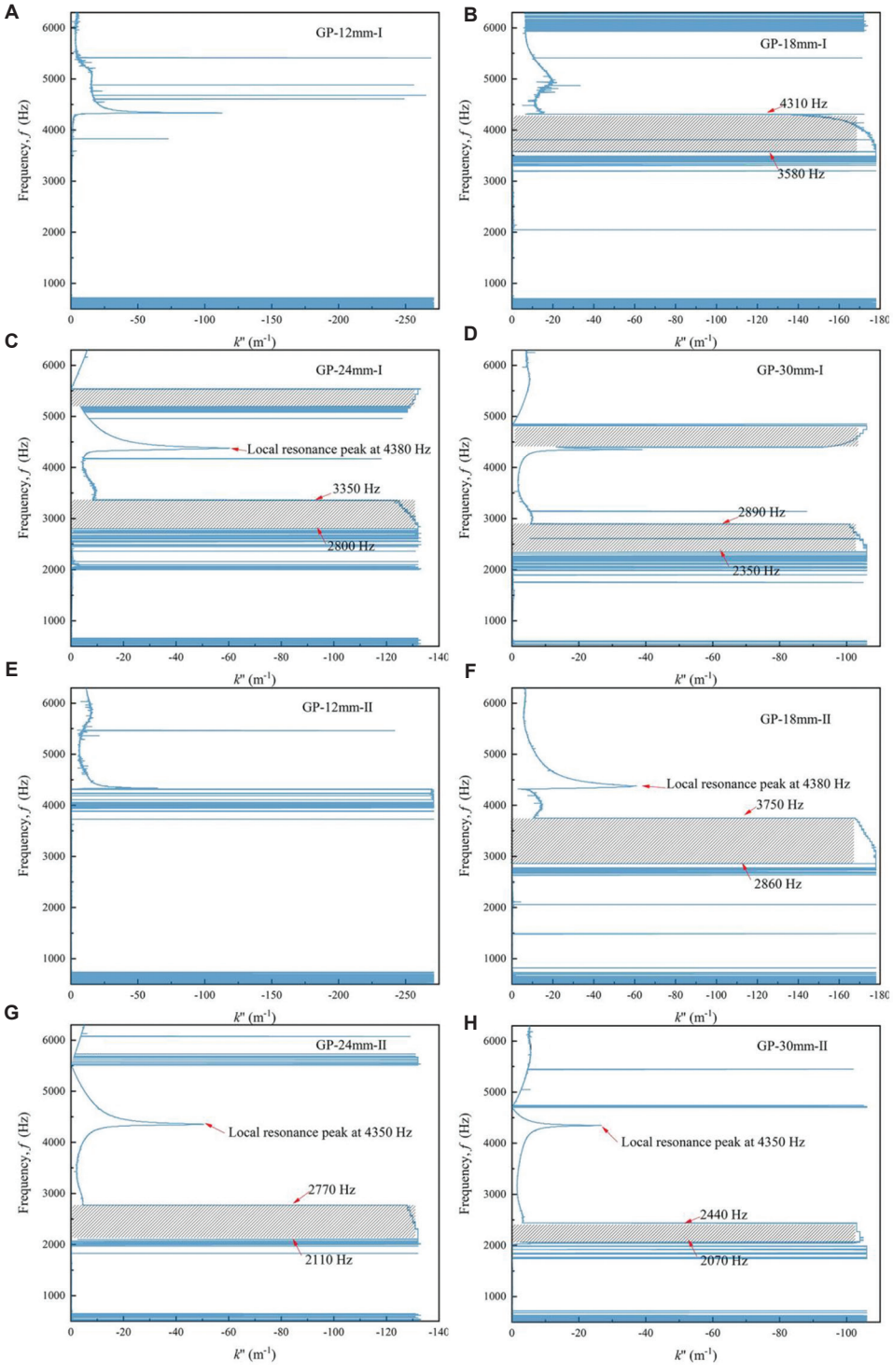

Figure 17. Acoustic band structure of (A) GP-12 mm-I, (B) GP-18 mm-I, (C) GP-24 mm-I, (D) GP-30 mm-I, (E) GP-12 mm-II, (F) GP-18 mm-II, (G) GP-24 mm-II, and (H) GP-30 mm-II
Abbreviation: k": Bloch wave vector, imaginary part; GP: Graded primitive

TPMS structures, including gyroid, primitive, IWP, and diamond, exhibit a linear relationship. As the thickness of TPMS structures increases, their NRC also increases linearly. Notably, the slope size order is as follows: diamond > IWP > gyroid > primitive. This result indicates that the average sound absorption coefficient at a range of

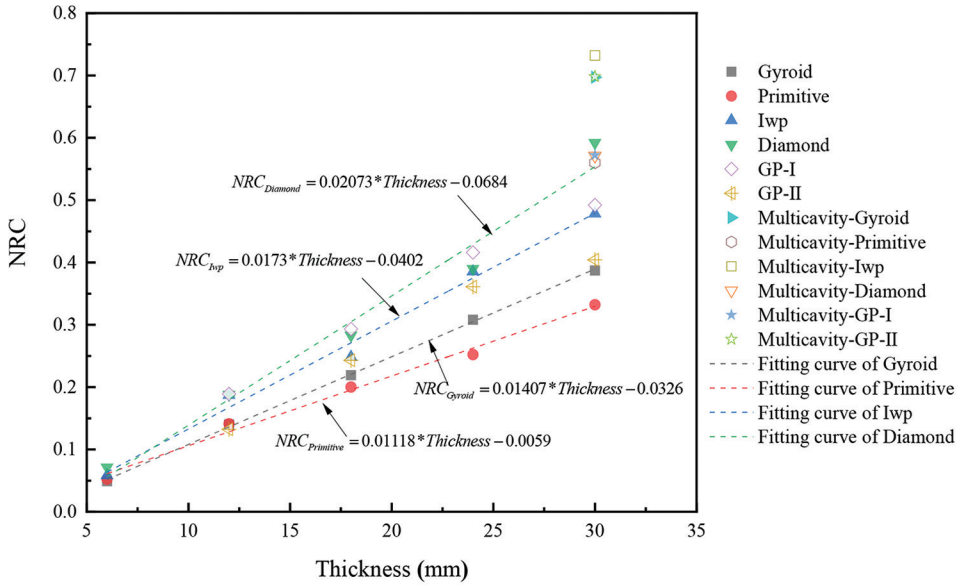

Figure 18. The NRC of TPMS structures
Abbreviations: NRC: Noise reduction coefficient; TPMS: Triply periodic minimal surface

Table 10. Sound absorption characteristics of graded triply periodic minimal surface (TPMS) structures

Specimen	Thickness, T (mm)	Frequency at first peak, f_1 (Hz)	Absorption at first peak, α_1	λ_{peak}/T
GP-12 mm-I	12	4980	0.557	5.81
GP-18 mm-I	18	3200	0.670	6.03
GP-24 mm-I	24	2080	0.846	6.96
GP-30 mm-I	30	1660	0.847	6.98
GP-12 mm-II	12	5970	0.452	4.85
GP-18 mm-II	18	4450	0.581	4.34
GP-24 mm-II	24	4000	0.758	3.62
GP-30 mm-II	30	3520	0.682	3.29
Multicavity-GP-I	30	1970	0.873	5.88
Multicavity-GP-II	30	1200	0.618	9.65

Abbreviation: GP: Graded primitive.

500 – 6300 Hz for diamond structures is the best among the four kinds of uniform TPMS structures, while primitive structures have the lowest average sound absorption coefficient among the uniform TPMS structures. For the GP design, the NRC of GP-12 mm-I, GP-18 mm-I, and GP-24 mm-I are 0.189, 0.293, and 0.416, respectively; these values are similar to the NRC of diamond structures with the same thickness. Diamond structures with 85% porosity manufactured by stereolithography also demonstrated the best sound absorption among diamond, gyroid, and primitive structures[16]. The comparison of results between uniform primitive and GP structures indicates that the graded design method can enhance the average sound absorption coefficient of the primitive structure. The enhanced mechanism of graded porous structures with larger pore sizes on the incident wave side is attributed to the impedance-matching effect. Large pores near the sound source facilitate the propagation of acoustic waves into the graded porous structures, resulting in reduced reflection and increased acoustic energy.[28] In contrast, the enhanced mechanism of graded porous structure with smaller pore sizes on the incident wave side is attributed to Helmholtz-like resonance,[18] resembling a Helmholtz resonator composed of a neck (an aperture in a large surface with low porosity) and a cavity with high porosity.

The ranking of the NRC of TPMS structures with multicavity is as follows: multicavity-IWP > multicavity-GP-II > multicavity-gyroid > multicavity-GP-I > multicavity-diamond > multicavity-primitive. Multicavity-IWP has the highest NRC (NRC = 0.732) among all the TPMS structures in this study. Despite the enhanced average sound absorption coefficient of multicavity-primitive structures, their NRC remains the lowest among the multicavity-TPMS structures mentioned above. To improve the sound absorption of primitive structures, the multicavity design was applied to the primitive structure, leading to NRC of 0.572 and 0.698 for multicavity-GP-I and multicavity-GP-II, respectively. Compared with Primitive-30 mm, the multicavity design of types I and II enhanced the noise reduction coefficient by 72.3% and 110.2%, respectively. Compared with

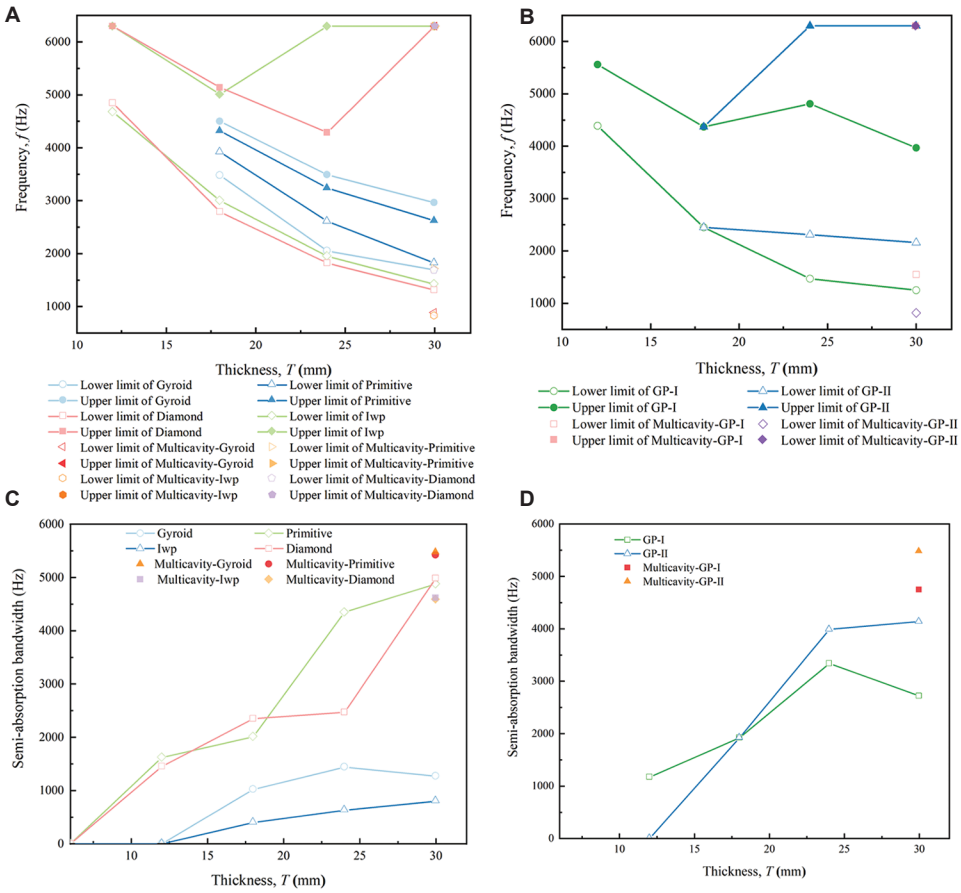

Figure 19. The upper and lower limits of sound absorption coefficient frequency band above 0.5: (A) uniform triply periodic minimal surface (TPMS) and multicavity-TPMS, and (B) graded TPMS and multicavity-graded TPMS. The semi-absorption bandwidth of: (C) Uniform TPMS and multicavity-TPMS, and (D) graded TPMS and multicavity-graded TPMS

multicavity-primitive structures, the multicavity design of types I and II enhanced the noise reduction coefficient by 2.1% and 24.6%, respectively.

The upper and lower limits of the frequency band of the sound absorption coefficient above 0.5 (semi-absorption) are displayed in Figure 19A. The diamond structure has the lowest frequency lower limit, while the primitive structure has the highest frequency lower limit. As the thickness of TPMS increases, the lower limit frequency shifts to a lower frequency. The lowest frequency lower limit of Diamond-30 mm is 1310 Hz, which is 510 Hz lower than Primitive-30 mm. The upper limit of the primitive and gyroid structures exhibits a decreasing trend with increasing thickness, but the upper limit of IWP and diamond structures decreases first and then increases with increasing thickness. For the multicavity design of TPMS structures, the multicavity-IWP structure has the lowest frequency (820 Hz), which is 490 Hz and 600 Hz lower than that of Diamond-30 mm and IWP-30 mm, respectively. This indicates that the multicavity design can further reduce the lower frequency limit. Additionally, the upper limit of multicavity-gyroid, multicavity-primitive, multicavity-IWP, and multicavity-diamond structures are all higher than 6300 Hz, which is the test limit of the impedance tube (500 – 6300 Hz) used in this study.

The upper and lower limits of the frequency band of the semi-absorption of graded TPMS structures are displayed in Figure 19B. As the thickness of GP increases, the lower limit frequency of GP-I and GP-II shifts to a lower frequency. The lower limit frequency of GP-30 mm-I is 1250 Hz, which is 570 Hz lower than that of Primitive-30 mm. However, the lower limit frequency of GP-30 mm-II is 2160 Hz, which is 340 Hz higher than that of Primitive-30 mm. This highlights that the graded design with a small unit cell size on the side of the incident sound wave can lower the limit of the semi-absorption frequency, but the graded design with a large unit cell size on the side of the incident sound wave increases the lower limit of the semi-absorption frequency. After the multicavity composite design of GP structures, the lower limit of the semi-absorption frequency

of multicavity-GP-I and multicavity-GP-II are 1550 and 816 Hz, respectively, demonstrating that the lower limit of the semi-absorption frequency of multicavity-GP-II is lower than that of multicavity-IWP.

The semi-absorption bandwidth (i.e., sound absorption coefficient > 0.5) of TPMS structures is featured in Figure 19C and D. The semi-absorption bandwidth of uniform gyroid, primitive, IWP, and diamond structures increased non-linearly with increasing thickness. The semi-absorption bandwidth of Diamond-30 mm is 4990 Hz, which is the widest bandwidth among these four kinds of uniform TPMS structures. The broadband sound absorption of TPMS structures in our research is better than the sound absorption of TPMS structures with 5.8 × 5.8 × 5.8 mm cell size.[29] Through multicavity composite design, the semi-absorption bandwidth of multicavity-gyroid, multicavity-primitive, multicavity-IWP, and multicavity-diamond was altered by 327%, 474%, 12%, and −7.4%, respectively. This finding suggests that the multicavity design can significantly expand the semi-absorption bandwidth of gyroid and primitive structures, but it has little impact on the semi-absorption bandwidth of IWP and diamond structures. The semi-absorption bandwidth of GP-30 mm-I and GP-30 mm-II are 2720 and 4140 Hz, respectively, which are 240% and 417% higher than the semi-absorption bandwidth of Primitive-30 mm. It is demonstrated that the graded design also can significantly expand the semi-absorption bandwidth of primitive structures. Based on the graded and multicavity designs, the semi-absorption bandwidth of multicavity-GP-I and multicavity-GP-II are 4750 and 5484 Hz, respectively. Multicavity-GP-II has the widest semi-absorption bandwidth among the TPMS structures in this study. Therefore, the graded and multicavity coupling designs can further enhance the semi-absorption bandwidth of TPMS structures.

4. Conclusion

This study proposes design methods for TPMS structures with broadband and perfect sound absorption manufactured by additive manufacturing, including multicavity design and graded design. The key findings obtained are as follows:

(i). As the thickness of TPMS structures increases, the noise reduction coefficient of TPMS structures increases linearly, and the first resonance frequency decreases. The acoustic bandgap of TPMS structures shifts to a lower frequency as the thickness increases. The order of noise reduction coefficient is: diamond > IWP > gyroid > primitive

(ii). The TPMS structures with multicavity design have multiple resonance peaks. The five resonance peaks of multicavity-IWP are above 0.94, and the third peak achieves perfect sound absorption. The semi-absorption bandwidth of multicavity-IWP increased to 5480 Hz, achieving broadband absorption

(iii). The graded design method can significantly broaden the semi-absorption bandwidth of TPMS structures, and the sound absorption coefficient of the first resonance peak can also be enhanced. The combination of graded and multicavity designs can further enhance broadband and perfect sound absorption, decreasing the frequency band's lower limit

Acknowledgments

None.

Funding

This research was funded by the Guangdong Basic and Applied Basic Research Foundation (No. 2023A1515012704), GDA's Project of Science and Technology Development (No. 2022GDASZH-2022010107), Yangjiang City Key Industry Talent Revitalization Plan Project for Alloy Materials and Hardware Scissors (Grant No. RCZX2023002), Undergraduate Innovation Team Project of Guangdong Ocean University (No. CXTD2023021), and National College Students' Innovation and Entrepreneurship Training Program Project of Guangdong Ocean University (No. 202310566036).

Conflict of interest

The authors declare that they have no known competing financial interests or personal relationships that could have appeared to influence the work reported in this paper.

Author contributions

Conceptualization: Mingkang Zhang
Formal analysis: Mingjian Deng, Chang Liu, Wenbin Liu
Funding acquisition: Mingkang Zhang, Jie Chen
Investigation: Jie Chen, Mingkang Zhang, Mingjian Deng
Methodology: Mingjian Deng, Wenbin Liu
Project administration: Mingkang Zhang, Jie Chen
Supervision: Guanhao Wang
Writing – original draft: Mingkang Zhang
Writing – review & editing: Mingkang Zhang, Mingjian Deng, Jie Chen
Visualization: Guanhao Wang, Sihua Yin

All authors have read and agreed to the published version of the manuscript.

Ethics approval and consent to participate

Not applicable.

Consent for publication

Not applicable.

Availability of data

The data that support the findings of this study are openly available in the Science Data Bank (https://doi.org/10.57760/sciencedb.08074).

References

1. Liu Z, Zhang X, Mao Y, *et al*. Locally resonant sonic materials. *Science*. 2000;289(5485):1734-1736.

   doi: 10.1126/science.289.5485.1734

2. Zhang S, Xia C, Fang N. Broadband acoustic cloak for ultrasound waves. *Phys Rev Lett*. 2011;106(2):024301.

   doi: 10.1103/PhysRevLett.106.024301

3. Yang M, Sheng P. Sound absorption structures: From porous media to acoustic metamaterials. *Annu Rev Mater Res*. 2017;47:83-114.

   doi: 10.1146/annurev-matsci-070616-124032

4. Liu CR, Wu JH, Lu K, Zhao ZT, Huang Z. Acoustical siphon effect for reducing the thickness in membrane-type metamaterials with low-frequency broadband absorption. *Appl Acoust*. 2019;148:1-8.

   doi: 10.1016/j.apacoust.2018.12.008

5. Zhao H, Wen J, Yang H, Lv L, Wen X. Backing effects on the underwater acoustic absorption of a viscoelastic slab with locally resonant scatterers. *Appl Acoust*. 2014;76:48-51.

   doi: 10.1016/j.apacoust.2013.07.022

6. Guo J, Fang Y, Jiang Z, Zhang X. An investigation on noise attenuation by acoustic liner constructed by Helmholtz resonators with extended necks. *J Acoust Soc Am*. 2021;149(1):70-81.

   doi: 10.1121/10.0002990

7. Zhang X, Wu J, Mao Q, Zhou W, Xiong Y. Design of a honeycomb-microperforated panel with an adjustable sound absorption frequency. *Appl Acoust*. 2020;164:107246.

   doi: 10.1016/j.apacoust.2020.107246

8. Leclaire P, Umnova O, Dupont T, Panneton R. Acoustical properties of air-saturated porous material with periodically distributed dead-end pores. *J Acoust Soc Am*. 2015;137(4):1772-1782.

   doi: 10.1121/1.4916712

9. Costa-Baptista J, Fotsing ER, Mardjono J, Therriault D, Ross A. Design and fused filament fabrication of multilayered microchannels for subwavelength and broadband sound absorption. *Addit Manuf*. 2022;55:102777.

   doi: 10.1016/j.addma.2022.102777

10. Pierre J, Iervolino F, Farahani RD, Piccirelli N, Lévesque M, Therriault D. Material extrusion additive manufacturing of multifunctional sandwich panels with load-bearing and acoustic capabilities for aerospace applications. *Addit Manuf*. 2023;61:103344.

    doi: 10.1016/j.addma.2022.103344

11. Wang C, Huang L. On the acoustic properties of parallel arrangement of multiple micro-perforated panel absorbers with different cavity depths. *J Acoust Soc Am*. 2011;130(1):208-218.

    doi: 10.1121/1.3596459

12. Qian YJ, Zhang J, Sun N, Kong DY, Zhang XX. Pilot study on wideband sound absorber obtained by adopting a serial-parallel coupling manner. *Appl Acoust*. 2017;124:48-51.

    doi: 10.1016/j.apacoust.2017.03.021

13. Yan S, Wu J, Chen J, Xiong Y, Mao Q, Zhang X. Optimization design and analysis of honeycomb micro-perforated plate broadband sound absorber. *Appl Acoust*. 2022;186:108487.

    doi: 10.1016/j.apacoust.2021.108487

14. Shen C, Cummer SA. Harnessing multiple internal reflections to design highly absorptive acoustic metasurfaces. *Phys Rev Appl*. 2018;9(5):054009.

    doi: 10.1103/PhysRevApplied.9.054009

15. Elayouch A, Addouche M, Khelif A. Extensive tailorability of sound absorption using acoustic metamaterials. *J Appl Phys*. 2018;124(15):155103.

    doi: 10.1063/1.5035129

16. Yang W, An J, Chua CK, Zhou K. Acoustic absorptions of multifunctional polymeric cellular structures based on triply periodic minimal surfaces fabricated by stereolithography. *Virtual Phys Prototyp.* 2020;15(2):242-249.

    doi: 10.1080/17452759.2020.1740747

17. Lin C, Wen G, Yin H, Wang ZP, Liu J, Xie YM. Revealing the sound insulation capacities of TPMS sandwich panels. *J Sound Vib*. 2022;540:117303.

    doi: 10.1016/j.jsv.2022.117303

18. Zhang M, Liu C, Deng M, Li Y, Li J, Wang D. Graded minimal surface structures with high specific strength for broadband sound absorption produced by laser powder bed fusion. *Coatings*. 2023;13(11):1950.

    doi: 10.3390/coatings13111950

19. Li Z, Zhou Y, Kong X, *et al*. Sound absorption performance of a micro-perforated plate sandwich structure based on selective laser melting. *Virtual Phys Prototyp.* 2024;19(1):e2321607.

    doi: 10.1080/17452759.2024.2321607

20. Xue Y, Paige Nobles L, Sharma B, Stuart Bolton J. Designing hybrid aerogel-3D printed absorbers for simultaneous low frequency and broadband noise control. *Mater Des*. 2024;242:113026.

    doi: 10.1016/j.matdes.2024.113026

21. Wang Z, Guo Z, Li Z, Zeng K. Design, manufacture,

and characterisation of hierarchical metamaterials for simultaneous ultra-broadband sound-absorbing and superior mechanical performance. *Virtual Phys Prototyp*. 2022;18(1):e2111585.

doi: 10.1080/17452759.2022.2111585

22. Yang X, Shen X, Bai P, *et al*. Preparation and characterization of gradient compressed porous metal for high-efficiency and thin-thickness acoustic absorber. *Materials* (*Basel*). 2019;12(9):1413.

doi: 10.3390/ma12091413

23. Meng H, Ren S, Xin F, Lu T. Sound absorption coefficient optimization of gradient sintered metal fiber felts. *Sci China Technol Sci*. 2016;59(5):699-708.

doi: 10.1007/s11431-016-6042-1

24. Zhang X, Qu Z, Xu Y. Enhanced sound absorption in two-dimensional continuously graded phononic crystals. *Jpn J Appl Phys*. 2019;58(9):090904.

doi: 10.7567/1347-4065/ab3686

25. Zhang XH, Qu ZG, Tian D, Fang Y. Acoustic characteristics of continuously graded phononic crystals. *Appl Acoust*. 2019;151:22-29.

doi: 10.1016/j.apacoust.2019.03.002

26. Boulvert J, Cavalieri T, Costa-Baptista J, *et al*. Optimally graded porous material for broadband perfect absorption of sound. *J Appl Phys*. 2019;126(17):175101.

doi: 10.1063/1.5119715

27. Guan X, Yang J, Deckers E, Hornikx M. Computational Characterization of Functionally Graded Porous Ansorbers Based On Triply Periodic Minimal Surfaces (TPMS). In: *Proceedings of the 10th Convention of the European Acoustics Association Forum Acusticum*; 2023

28. Zhang XH, Qu ZG, He XC, Lu DL. Experimental study on the sound absorption characteristics of continuously graded phononic crystals. *AIP Adv*. 2016;6(10):105205.

doi: 10.1063/1.4965923

29. Xiang-Nan K, Bin L, Zhong-Hua L, Peng-Fei Z, Chao S. Research on sound absorption properties of tri-periodic minimal surface sandwich structure of selective laser melting titanium alloy. *Mater Trans*. 2023;64(4):861-868.

doi: 10.2320/matertrans.MT-M2022164

ACCSCIENCE PUBLISHING

Materials Science in Additive Manufacturing

ORIGINAL RESEARCH ARTICLE

Understanding the antibacterial efficacy of additively manufactured copper-added 316L stainless steel

Michael B. Myers and Amit Bandyopadhyay*

W. M. Keck Biomedical Materials Research Lab, School of Mechanical and Materials Engineering, Washington State University, Pullman, Washington, United States of America

Abstract

In response to the growing demand for advanced materials with inherent infection resistance, this research investigates the properties of 316L stainless steel with copper, produced through laser-directed energy deposition additive manufacturing. The study focuses on three compositions: pure 316L, 316L with 3 wt.% Cu, and 316L with 5 wt.% Cu. Compressive strength measurements and Vickers hardness tests were conducted to assess mechanical properties, while microstructural characterization and X-ray diffraction analysis provided insights into the material's physical properties. This research extends beyond physical and mechanical properties by exploring the on-contact antibacterial efficacy against *Staphylococcus aureus* and *Pseudomonas aeruginosa* up to 72 h. The addition of Cu reduced the ability of bacterial colonization of both strains on the metal surface. The findings of this investigation have the potential to benefit the biomedical devices, contributing to both structural and biofunctional properties of materials.

Keywords: 316L stainless steel; Directed energy deposition; Additive manufacturing; Copper; Infection control

***Corresponding author:**
Amit Bandyopadhyay
(amitband@wsu.edu)

Citation: Myers MB, Bandyopadhyay A. Understanding the antibacterial efficacy of additively manufactured copper-added 316L stainless steel. *Mater Sci Add Manuf.* 2024;4(1):7357. doi: 10.36922/msam.7357

Received: December 12, 2025

Revised: January 14, 2025

Accepted: January 24, 2025

Published Online: February 26, 2025

1. Introduction

Approximately 2 million fracture fixation devices are inserted annually in the United States, amounting to a market value of US$3.6 billion.[1,2] These devices, such as screws, rods, and plates, are implanted within the body to facilitate healing and strengthen injured limbs. However, infections associated with implanted devices can lead to severe complications, with 25% of infected patients dying within five years.[3] Implants can potentially introduce foreign bacteria to the surgical site, leading to complications such as delayed healing and necessitating additional surgeries. Revision surgeries can be traumatic and costly for patients, as reimplanted devices have an infection rate that is several times higher than that of first-time implants.[1] Furthermore, the median cost for treatment of a surgical site infection is approximately US$108,000.[4] Therefore, reducing the risk of infection is crucial for improving patient outcomes.

Metallic materials are frequently favored over ceramics and polymers for implant production due to their superior strength and fatigue resistance.[5] Implant materials experience not just static loading but also dynamic loads associated with joints and

movement. In addition, implant materials must be biocompatible, resistant to corrosion, and not introduce toxicity to the body. While materials such as titanium or cobalt-chromium alloys are some of the many options available, 316L stainless steel (SS) is commonly used in implants and fracture management devices due to its high strength, excellent corrosion resistance, and good biocompatibility while remaining relatively low cost.[6] These properties are crucial for a material that will be subjected to fluctuating loads while exposed to the biological environment of the human body. However, 316L does not possess inherent antibacterial properties.[7] Patients are often required to take antibiotic medication to address concerns of post-surgery infection, but this provides only temporary protection. Moreover, bacterial strains can become antibiotic-resistant, rendering the patient vulnerable to infection. As a result, there is a need for an alloy with similar mechanical properties to 316L while incorporating antibacterial features.

Copper (Cu) has long been recognized for its antibacterial properties, as it can disrupt bacterial cell membranes and inhibit the growth of various pathogens.[7-12] Due to its antibacterial effect, Cu is used in critical surfaces found in drinking water distribution and hospital applications.[13] Yet, its antibacterial effect is joined with concerns of toxicity. Other antibacterial metals, like Ag, have also been studied for toxicity when used for implant applications. Increased Ag levels can be found in bodily fluids, though most effects are seen in local tissue surrounding the implant site.[14] Therefore, toxicity may depend on the alloy's dose and the implant site's sensitivity. Similarly, Cu toxicity may depend on several factors. A Cu ion concentration of 46 μg/mL is highly toxic to fibroblasts in mice, while 2 mg/L may reach harmful levels in humans.[15,16]

While the exact method of Cu contact killing is still not fully understood, this has not withheld the element from being used as an antibacterial material.[8] Even though toxicity may not be boiled down to a simple alloying percentage, previous work has suggested Cu loadings up to 3% to be non-toxic while still providing an antibacterial effect.[9] In contrast, separate studies suggested that a 316L-5Cu composition has a lower tensile strength than 316L, but a 316L-3.5Cu alloy has improved hardness over 316L after undergoing an aging treatment.[7,17] 316L-Cu alloys have the potential to significantly improve the function of biomedical implants by becoming intrinsically resistant to bacterial colonization. However, a challenge lies in achieving the right balance of Cu to enhance antibacterial effects without compromising the alloy's mechanical integrity or resulting in toxicity to the body.

Additive manufacturing (AM) is a manufacturing method with ever-expanding popularity due to its various advantages over traditional production methods. Among other benefits, AM enables the production of intricate designs, easily customizable parts, and small batch production.[18] These properties make AM an ideal method for producing biomedical devices. AM enables varying part sizes and geometry, allowing implants to be custom-fit to a patient. The process also makes producing custom and small numbers of parts financially accessible because it does not rely on fixed tooling. In addition, the AM process is well-suited for producing custom alloy compositions due to its particle form feedstock. Within the family of AM processes, laser-directed energy deposition (L-DED) is well-fitted for biomedical device manufacturing due to its higher material deposition rate over other methods and precise control over alloy composition in small volumes.[19,20] DED can also produce functionally graded materials for optimized performance, such as hard surfaces for wear resistance and tough cores for load-bearing capacity. Therefore, AM and DED are attractive processes for producing metallic biomedical devices. While previous work has explored the mechanical and antibacterial properties of 316L-Cu, there is limited insight into this alloy produced by AM.

This research aims to test the mechanical and antibacterial properties of 316L, 316L-3Cu (SS-3Cu), and 316L-5Cu (SS-5Cu) for implants and fracture management devices. It is hypothesized that adding Cu into a 316L matrix will provide inherent antibacterial properties and similar mechanical performance to 316L when produced through laser DED. Mechanical properties were evaluated by compressive loading and hardness measurements, along with microstructure characterization. Antibacterial performance was measured with 316L as the control against *Staphylococcus aureus* and *Pseudomonas aeruginosa* to measure the effect of Cu addition against two common implant-related bacterial strains.[1,3]

2. Materials and methods

2.1. Sample preparation

The raw materials used in this study consisted of 316L SS powder (Höganäs, Sweden) with particle sizes ranging from 20 to 55 μm and Cu powder (GKN Hoeganaes, Cinnaminson, NJ, USA) with particle sizes ranging from 15 to 53 μm. Although the L-DED system used in this study supports a larger powder size distribution, this particle size range was chosen to balance several properties. Finer particles were found to reduce powder

flowability due to agglomeration, while coarser particles lead to increased porosity and surface roughness on the final part. Two alloy compositions were prepared: SS-3Cu and SS-5Cu. These powders were tumble-mixed in batches of 250 g and mixed at 160 rpm for 2 h with no pause time to reach a uniform particle size distribution. The powder mixtures were contained in 500 mL jars with an air atmosphere. All samples were fabricated using a FormAlloy laser DED system (Spring Valley, CA, USA). The processing parameters consisted of 350 W laser power and 575 mm/min scan speed for contour and infill paths, with 0.3 mm layer thickness, 0.78 mm hatch spacing, and 20°C build plate temperature. Powder feed settings included 0.5 rpm powder feeder disc rate, 9 L/min carrier gas flow rate, and 13 L/min shield gas flow rate. It was observed that the Cu addition did not affect the processing parameters, as the same settings were used for all three compositions. To minimize oxidation, the printing environment was carefully maintained with an oxygen concentration below 20 ppm, and the chamber was filled with argon gas. The samples were designed as vertical cylinders with a diameter of 9 mm and a height of 18 mm and were printed onto a 316L substrate.

2.2. Microstructure and phase analysis

Samples for microstructural analysis were produced by sectioning the cylindrical specimens longitudinally, exposing a vertical cross-section. These sections were then mounted in phenolic resin and ground using silicon carbide (SiC) pads in sequential order of increasing grit size from 320 to 1200. The samples were subsequently polished with alumina suspensions of 1 μm, 0.3 μm, and 0.05 μm particle size, using deionized water as the medium. Etching was performed following ASTM E407 – 23.[21] The etching solution comprised 10 mL HNO_3, 35 mL HCl, and 30 mL H_20, with a 60-s immersion, followed by a rinse in water and air drying. Microstructure imaging was done using a digital microscope (VHX-970F, Keyence, Itasca, IL, USA). The grain size was calculated using the average grain intercept method, where the number of grain intercepts was divided by the line length. Phase analysis was performed using X-ray diffraction (XRD) with a Rigaku MiniFlex 600 diffractometer (Rigaku, Japan). The samples were scanned using Cu-K α radiation (1.54 Å at 40 kV and 20 mA) with a 2θ theta range of 25° – 100° and a scan rate of 5°/min. Energy dispersive spectroscopy (EDS) was conducted using a field emission scanning electron microscope (FE-SEM; Sirion, USA) for 5 min. For EDS analysis, samples were cut in the XY plane, which refers to the horizontal plane parallel to the build platform and perpendicular to the build direction (Z-axis), to map elemental distribution across the print plane.

2.3. Compression and hardness testing

Cylindrical compression test specimens were machined using a computer numerical control mill (770MX, Tormach, Madison, WI, USA) equipped with a lathe attachment. The diameter of the specimens was milled to 7.5 mm, and the length was faced to 15 mm, resulting in a length-to-diameter (L/D) ratio of 2. Compression testing was performed following ASTM E9 – 19.[22] The tests were conducted using a universal test machine (600DX, Instron, Norwood, MA, USA) at a constant crosshead displacement rate of 0.1 mm/min. These tests were terminated once the specimens reached 4% engineering strain, with $n = 3$ tests performed for each composition. Hardness testing was conducted according to ASTM E92 – 23,[23] using a Micro Vickers Hardness Tester (Phase II Plus, Upper Saddle River, NJ, USA). Hardness samples were prepared in the same manner as the microstructure samples. Vickers hardness measurements were taken at 0.5 mm intervals, starting from the base of the sample and extending up to a height of 5 mm. A load of 1.961 N (HV 0.2) was applied, with a dwell time of 15 s.

2.4. *In vitro* bacterial studies

The antibacterial efficacy of Cu addition into 316L was evaluated *in vitro* against *S. aureus* and *P. aeruginosa* bacterial strains (Carolina Biological, Burlington, NC, USA) at 24, 48, and 72 h. The AM-produced cylindrical specimens were sliced into 1 mm thick sections using a low-speed diamond saw, then mounted and ground with SiC pads up to 1200 grit. These samples were subsequently cleaned via ultrasonication and sterilized by autoclaving at 121°C for 1 h. *S. aureus* and *P. aeruginosa* were rehydrated with rehydration media and incubated at 37°C for 24 h to reactivate. Serial dilutions of the bacterial cultures were performed to achieve a concentration corresponding to the 0.5 McFarland standard, equivalent to 1.5×10^8 colony-forming units (CFU)/mL, as confirmed by optical absorbance measurements within a range of 0.08 – 0.1 at a wavelength of 625 nm. For antibacterial testing, the sterilized samples were placed into 24-well plates, with 10^6 CFU applied on the surface of each sample, followed by 1 mL of nutrient broth. The plates were then incubated at 37°C until the specified time points. At each time point, the nutrient broth was carefully removed and replaced with a fixative solution (2% paraformaldehyde/2% glutaraldehyde in 0.1 M phosphate-buffered saline [PBS]) overnight. After removal of the fixative solution, the samples underwent secondary fixation with 1% osmium tetroxide (OsO_4) overnight, followed by a rinse in deionized water. The samples were then subjected to a serial dehydration process using increasing concentrations of ethanol (30%,

50%, 70%, 90%, and 100%). After dehydration, the samples were treated with hexamethyldisilane (HMDS) overnight. A gold coating layer was applied to the samples to facilitate the imaging of organic material through SEM. A minimum of $n = 3$ images were collected per time point and composition for bacterial colony quantification. The antibacterial efficacy of each material composition was determined by counting the number of bacterial colonies (N) on the surface of the samples using an open-source object counting software (DotDotGoose, USA).[24] Antibacterial efficacy (R), based on the control and treatment CFU counts at each time point, was calculated as follows:

$$R = \frac{N_{control} - N_{treatment}}{N_{control}} \times 100 \quad \text{(I)}$$

3. Results

3.1. Microstructure, EDS, and phase analysis

The microstructure of 316L consisted of distinct regions exhibiting both cellular and columnar dendritic solidification modes. The regions appeared to have a uniform structure, with clear boundaries between the two formations. Figure 1A displays a low-magnification image of 316L, showing four printed layers, with a mix of cellular and columnar structures across the layers. The transition between these two formations is distinctly visible at higher magnification. The columnar dendrites are oriented along the heat flow direction, or normal to the top and bottom surface of each layer, and largely aligned in the vertical direction due to cooling provided by the substrate. Figure 1B and **C** also reveal a similar mix of cellular and columnar dendrite structures, with no significant differences between these compositions and the 316L base material. Equiaxed structures for 316L, SS-3Cu, and SS-5Cu were measured with diameters of 5 ± 1 µm, showing that Cu addition did not change grain size significantly. All three compositions resulted in fully dense samples, except for minor gas entrapment defects. These defects, caused by trapped gas particles during the solidification of the melt pool, appeared as spherical voids of 30 µm or less.

EDS was conducted to examine the Cu distribution within the 316L base composition. As seen in Figure 2, Cu was uniformly distributed within 316L, suggesting the formation of a solid solution. Chromium and nickel, the main alloying elements of 316L,[25] also appeared evenly distributed. Achieving a uniform Cu distribution is ideal for implant applications where a consistent antibacterial effect is desired across the surface of an implant. Since bacteria and other foreign materials typically contact the outer surface of an implant first upon entering the body, the surface properties play a critical role in determining the overall antibacterial efficacy.

XRD measurements were performed on all three compositions to identify the phases present, as shown in Figure 3 listed in Table 1. The XRD pattern of 316L exhibited a primary characteristic peak at a 2θ value of 43.64°, corresponding to face-centered cubic (FCC) austenite in the (111) plane. Notably, the SS-3Cu and SS-5Cu compositions showed an increased intensity of the (111) peak relative to 316L, which can be attributed to adding Cu. However, the intensities of the secondary peaks [(200), (220), and (311)] remained essentially unchanged. This selective enhancement of the (111) peak suggests that Cu addition induces a preferential orientation of the grains. In addition, SS-3Cu peaks exhibited a slight shift in the negative direction (~0.15°), which further increased in SS-5Cu (~0.22°). No martensitic phases were detected in the XRD patterns of 316L, and no new peaks were detected in SS-3Cu and SS-5Cu within the detection limit, suggesting that Cu addition did not lead to the formation of any new phases compared to the 316L scan pattern.

3.2. Compression and hardness testing

The compressive behavior of all three compositions was found to be similar, as illustrated by the representative stress-strain curves shown in Figure 4A. The yield stress values for 316L, SS-3Cu, and SS-5Cu were 334 ± 9 MPa, 329 ± 12 MPa, and 317 ± 1 MPa, respectively. Cu addition appeared to have minimal impact on the yield stress. This is advantageous for implant applications, where 316L is commonly used, as adding Cu would not result in a substantial change in strength. Figure 4B presents the Vickers hardness measurements taken along the build direction, starting from the bottom of the sample. The hardness values of 316L, SS-3Cu, and SS-5Cu were 209 ± 12, 183 ± 9, and 186 ± 10 HV 0.2, respectively. Although both Cu compositions exhibited lower hardness than 316L, no significant difference was observed between SS-3Cu and SS-5Cu. Moreover, hardness measurements for all three compositions showed no significant variation across

Table 1. XRD angle and peak intensity values of 316L, SS-3Cu, and SS-5Cu

Peak no.	*hkl*	316L (2θ, Intensity a.u.)	SS-3Cu (2θ, intensity a.u.)	SS-5Cu (2θ, intensity a.u.)
1	(111)	43.64°, 313	43.49°, 455	43.42°, 429
2	(200)	50.69°, 146	50.51°, 149	50.47°, 161
3	(220)	74.52°, 52	74.38°, 52	74.35°, 49
4	(311)	90.41°, 61	90.27°, 66	90.13°, 67

Abbreviation: *hkl*: Miller indices denoting crystallographic plane orientation.

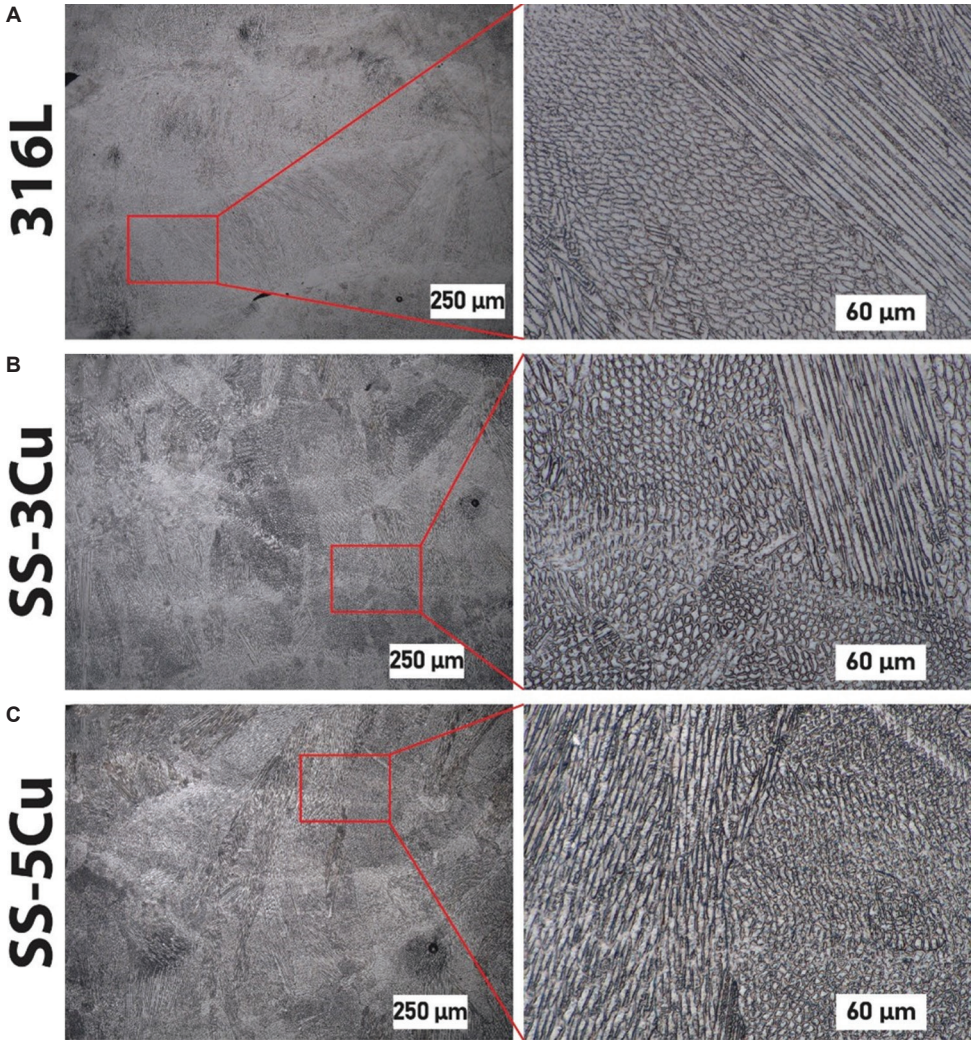

Figure 1. Microstructure of 316L and Cu-alloyed compositions. (A) 316L control composition displayed a mix of cellular and columnar structures visible in high magnification (B and C) SS-3Cu and SS-5Cu showed microstructures similar to those of the control composition (left column is ×200, right column is ×1000)

the height of the samples, suggesting a consistent hardness distribution along the build direction.

3.3. *In vitro S. aureus* bacterial study

Cu is known for its antibacterial properties and was expected to reduce bacterial surface colonization when incorporated into 316L.[7,10] Gram-positive *S. aureus* was tested on the metal surfaces at 24, 48, and 72 h, simulating the time points immediately following a surgical procedure. As shown in Figure 5A1-3, the 316L control surfaces were heavily colonized by *S. aureus*. In contrast, Cu addition reduced bacterial colonization on the treated surfaces. The SS-3Cu samples demonstrated lower CFU counts at all-time points (Figure 5B1-3), while the SS-5Cu samples exhibited even more significant reductions in bacterial growth (Figure 5C1-3). Quantification of visible CFU is summarized in Figure 5D, while the normalized bacterial viability is presented in Figure 5E. On SS-3Cu surfaces, *S. aureus* colonization decreased from 30% at 24 h to 25% at 48 h and 18% at 72 h. This corresponds to a 5% reduction between 24 h and 48 h and a 7% reduction between 48 h and 72 h. SS-5Cu surfaces displayed superior antibacterial performance, with remaining CFU values of 19% at 24 h, 14% at 48 h, and 12% at 72 h, reflecting 5% and 2% reductions between respective time points. The antibacterial efficacy followed a logarithmic trend, with the most significant reduction occurring within the first 24 h. While the rate of antibacterial performance slowed at later time points, incremental improvements in efficacy were observed. Notably, the inset image in Figure 5C1

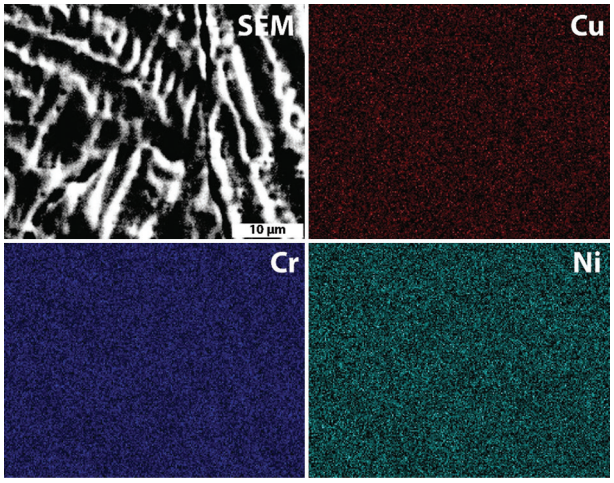

Figure 2. EDS mapping of the SS-5Cu surface revealed a homogenous copper, chromium, and nickel distribution
Abbreviation: EDS: Energy dispersive spectroscopy

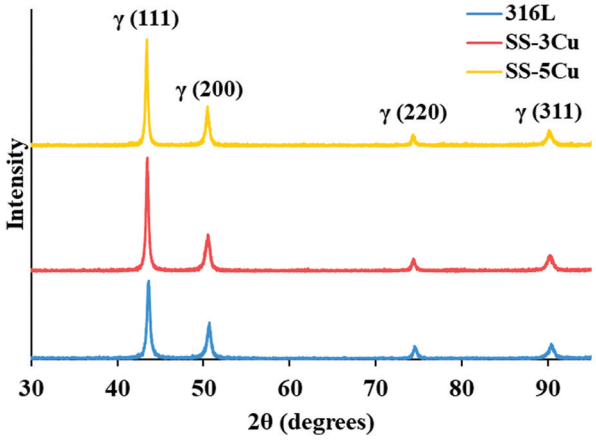

Figure 3. XRD patterns of 316L, SS-3Cu, and SS-5Cu. Cu addition in SS-3Cu and SS-5Cu resulted in an enlarged relative peak height at ~44°, corresponding to face-centered cubic austenite
Abbreviation: XRD: X-ray diffraction

highlights an *S. aureus* cell exhibiting cell wall rupture and exposed cytoplasm, providing visual evidence of the antibacterial effect of Cu addition and its potential use in infection-resistant materials.

3.4. *In vitro P. aeruginosa* bacterial study

Antibacterial performance was further evaluated at 24 h and 48 h against *P. aeruginosa*, Gram-negative bacteria. The 316L control surfaces displayed a pronounced increase in bacterial colony count over time, with CFU counts rising significantly from 422 ± 46 at 24 h to 1819 ± 226 at 48 h, as seen in Figures 6A1 and A2. This increase demonstrates an environment conducive to bacterial proliferation on the 316L surface. In contrast, the SS-3Cu surface showed substantially reduced bacterial viability, with CFU counts of 92 ± 25 and 114 ± 40 at 24 h and 48 h, respectively, corresponding to 22% and 6% of the control bacterial colonies, as shown in Figure 6B1 and B2. A similar trend was observed on SS-5Cu surfaces, which demonstrated even higher antibacterial efficacy, with CFU counts of 63 ± 12 and 57 ± 10 at the same time points, representing 15% and 3% bacterial viability, respectively, as shown in Figure 6C1 and C2. While the 316L samples demonstrated a significant increase in CFU between time points, the Cu-loaded samples effectively suppressed bacterial growth, with minimal changes in CFU counts from 24 h to 48 h. This inhibition of bacterial proliferation highlights the role of Cu as an antimicrobial agent.

4. Discussion

316L SS is widely used in the medical industry for its strength and corrosion resistance while maintaining good biocompatibility. These properties are critical for implant and fracture management applications, where the environment of the human body presents a dynamic situation ideally suited for corrosion and infection. When alloyed with 316L, Cu has been shown to inhibit bacterial proliferation and holds promising potential for use in biomedical settings. This study aimed to measure the mechanical and antibacterial properties of 316L-Cu alloys produced through DED.

4.1. Microstructure and mechanical properties

Microstructural analysis revealed two distinct formations within 316L. Cellular and columnar dendritic solidification was observed in all three compositions, as shown in Figure 1. Columnar formations result from the pronounced thermal gradient experienced during the DED process, with structures growing preferentially along the heat flow direction towards the chilled substrate. On the other hand, the growth of cellular structures can be attributed to the rapid solidification rate, moderate thermal gradients present within the melt pool, and lack of heat flow in the XY plane, all of which favor the development of cellular dendritic structures. In contrast, traditional manufacturing methods, such as cold-rolling, begin with equiaxed austenitic grains and transform into elongated martensitic structures due to the rolling process. Strain-induced martensite can be reversed into austenite through annealing, increasing its strength through grain size reduction and achieving finer grain sizes than the original austenite.[26]

The incorporation of Cu did not appear to significantly alter the microstructure of 316L, which is consistent with

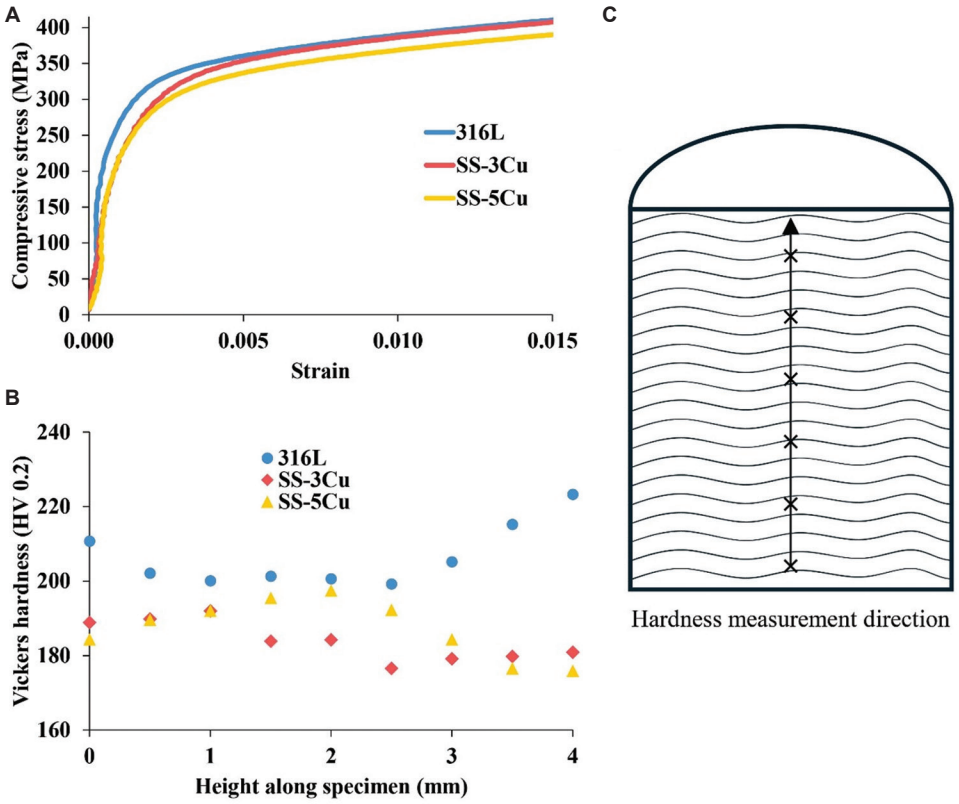

Figure 4. Compressive stress-strain and hardness behavior of 316L and Cu-alloyed compositions (A) Representative stress-strain curves for all three compositions show similar behavior under uniaxial compression loading. (B) Vickers hardness measurements showed a slight reduction with Cu presence, plotted as a three-point moving average. (C) Illustration of hardness measurement locations on a cylinder cross-section

previous findings in other studies of Cu-alloyed 316L produced through traditional manufacturing methods.[7] Cu addition into 316L has also been achieved through powder bed fusion (PBF), another popular AM process, and exhibited similar Cu dissolution in a 316L matrix.[27] Although this study found similarly sized equiaxed structures for all three compositions, it has been reported that higher Cu loadings may lead to increased temperature gradients due to the higher thermal conductivity of Cu over 316L (385 vs. ~20 W/m.K), causing grain refinement.[28]

EDS mapping was conducted to determine the elemental distribution across sample surfaces. As shown in Figure 2, the analysis confirmed the uniform distribution of Cu with no preferential concentrations in the grain structure. 316L, composed of approximately 18% Cr and 14% Ni,[25] appeared to form a solid solution with Cu addition, as shown in previous works.[27,28] A homogenous Cu distribution ensures consistent mechanical and antibacterial properties. Phase analysis was performed using XRD (Figure 3), which revealed an exclusive FCC austenite phase within the detection limit across all compositions, with diffraction peaks corresponding to the (111), (200), (220), and (311) planes. The slight shift in peak positions for SS-3Cu and SS-5Cu has also been reported in similar work involving 316L-Cu alloys.[27-30] A possible cause for this shift could be residual stresses caused by substituting Cu atoms into the Fe lattice, leading to a change in lattice parameters due to the difference in atomic radius of the two elements.

Compressive stress-strain behavior (Figure 4) showed that all compositions had similar compressive strength values. A slight reduction in yield strength was observed for SS-5Cu (317 ± 1 MPa) compared to 316L (334 ± 9 MPa) and SS-3Cu (329 ± 12 MPa). Similarly, a minor reduction in hardness was measured in the Cu compositions (183 ± 9 and 186 ± 10 HV 0.2 for SS-3Cu and SS-5Cu, respectively) compared to 316L (209 ± 12 HV 0.2). Previous studies have reported similar reductions in strength and hardness with Cu addition in samples produced by laser PBF (LPBF).[17] This trend has also been recorded in alloys produced through forging,[7] though the same study also demonstrated a notable increase in strength and hardness after applying a heat treatment cycle. Conversely, increases in strength and hardness have been reported directly after production through PBF.[27,29] This property variation could be credited to varying amounts of Cu and differing manufacturing methods, leading to differences in the microstructure.

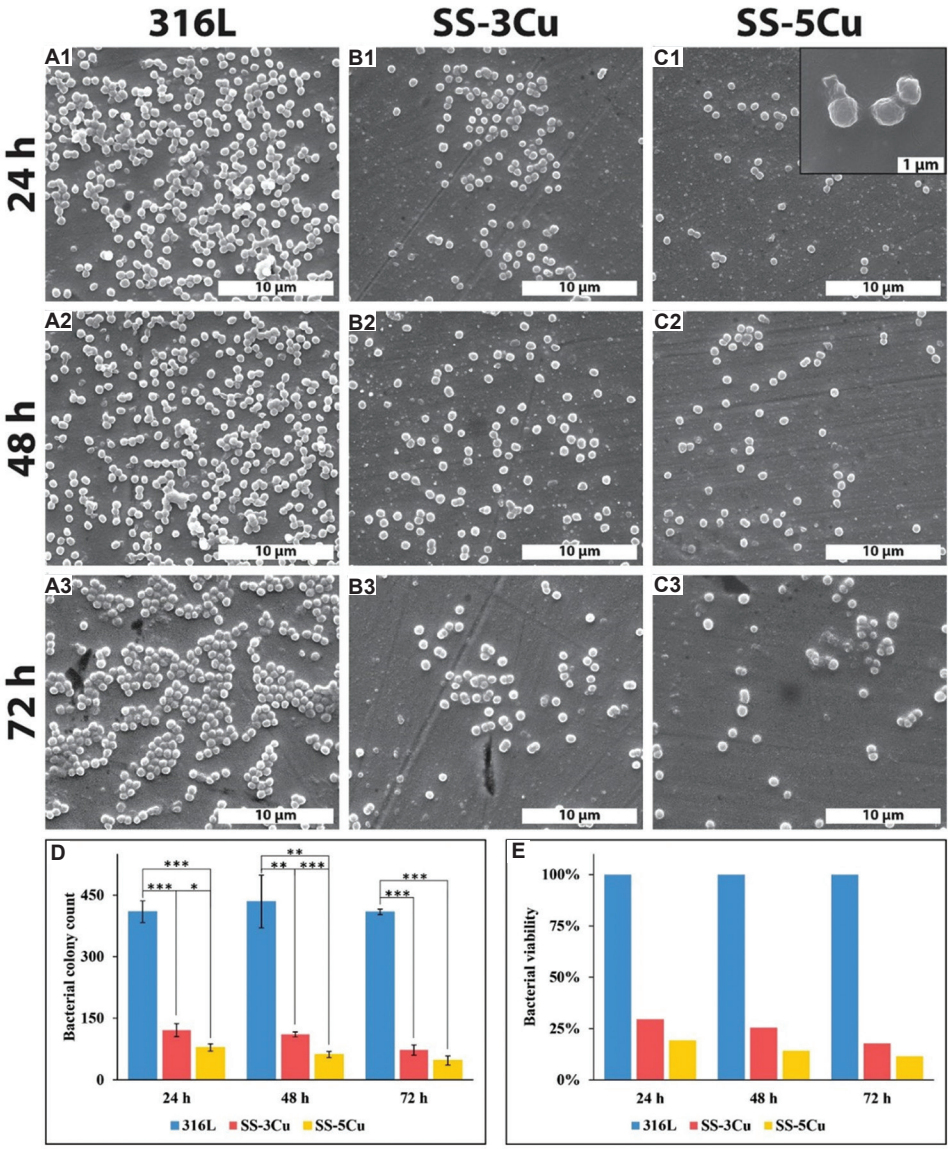

Figure 5. SEM imaging and quantification of visible *S. aureus* CFU. (A1, A2, A3) 316L control shows significantly higher CFU count than (B1, B2, B3) SS-3Cu and (C1, C2, C3) SS-5Cu across all time points. These images are taken at ×5000. The inset image within Figure 5C1 is taken at ×40000. (D) CFU quantification of SEM images with $n = 3$ per condition. Statistically significant values are marked as $^{*}P < 0.05$, $^{**}P < 0.01$, $^{***}P < 0.001$. (E) Normalized bacterial viability for each time point
Abbreviations: CFU: Colony-forming units; SEM: Scanning electron microscopy

While the magnitude of property variation from the base 316L is minor, this lack of consensus highlights the variability of material properties in AM-produced alloys and their dependence on processing parameters.

4.2. Antibacterial properties

While Cu is known to have antibacterial properties, its exact method of killing bacteria remains a topic of ongoing research, with no single definite consensus. One accepted theory of contact killing involves the ability of released Cu ions to degrade the cell membrane, leading to leakage of cellular contents and eventual cell death. An alternative hypothesis suggests that Cu ions penetrate the membrane and generate reactive oxygen species, which causes oxidative stress that damages cellular contents, including DNA.[8,31] Both theories converge on the same outcome: cell death resulting from membrane damage due to surface contact with Cu.

Although Cu alloying has great antibacterial potential, more established and trusted infection prevention methods are widely employed. Antibiotic medication may be administered post-surgery to address infection risks, but

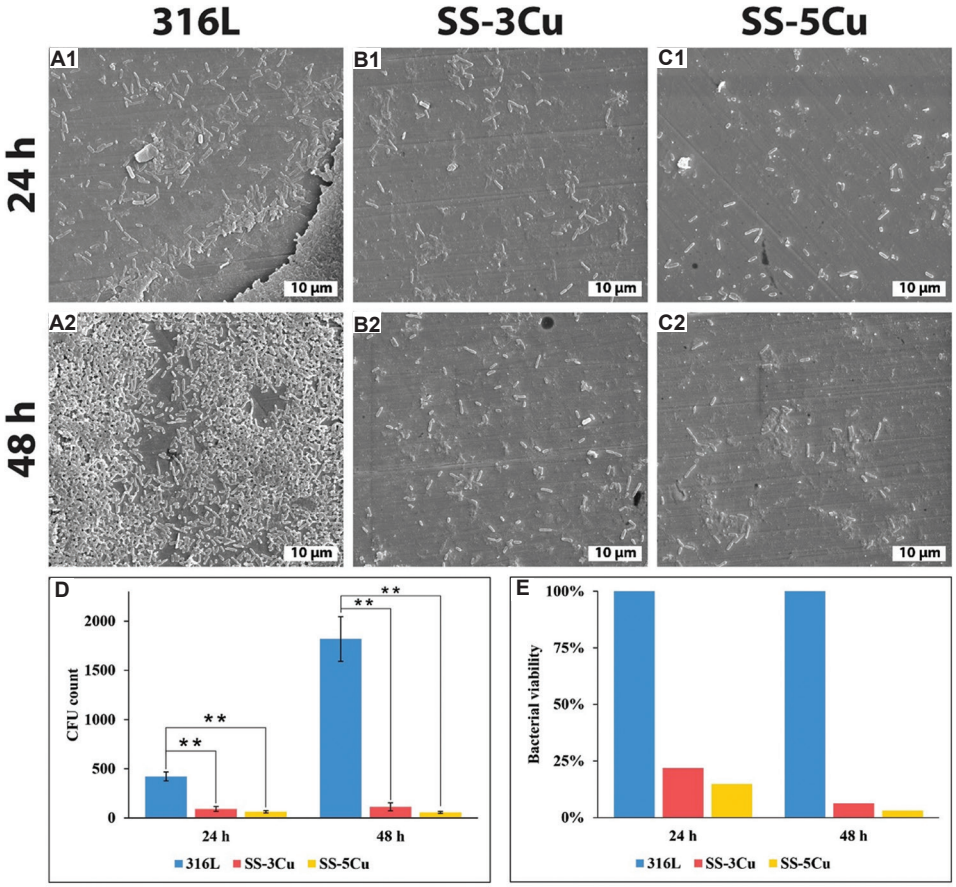

Figure 6. SEM imaging and agar plate quantification of *P. aeruginosa* activity. (A1 and A2) 316L control surface with increasing CFU count over time. (B1 and B2) SS-3Cu and (C1 and C2) SS-5Cu show a significant reduction in bacteria with respect to the control composition. (D) CFU quantification of SEM images with $n = 3$ per condition. Statistically significant values are marked as $^{*}P < 0.05$, $^{**}P < 0.01$, $^{***}P < 0.001$. (E) Normalized bacterial viability for each time point

Abbreviations: CFU: Colony-forming units; SEM: Scanning electron microscopy

this protection is temporary. Similarly, antibacterial coatings can be applied to implants, but their efficacy may diminish as the coatings degrade. In contrast, Cu addition provides an inherent antibacterial effect that may last for the entire lifespan of an implant, preventing bacterial colonization and biofilm formation for extended periods after implantation. However, antibacterial implants alone may not address infection risks on surfaces not in direct contact with the device, such as adjacent tissue near the surgical site. Therefore, 316L-Cu alloys could be used in conjunction with antibiotics or coatings to provide both short- and long-term antibacterial protection.

This study measured antibacterial performance against *S. aureus* (Figure 5) and *P. aeruginosa* (Figure 6). The results demonstrated that both Cu compositions exhibited significant antibacterial efficacy compared to 316L. SS-5Cu showed greater effectiveness than SS-3Cu due to its higher Cu content, consistent with prior studies that report increased antibacterial efficacy with progressive Cu addition.[7-9,12] The growth of both *S. aureus* and *P. aeruginosa* was significantly inhibited in SS-3Cu and SS-5Cu samples, emphasizing the potential of these alloys for biomedical applications. These findings align with previous studies on 316L-Cu alloys produced using AM and conventional methods.[7,10,29]

5. Conclusions

This study investigated the microstructural, mechanical, and antibacterial properties of 316L SS with 3 wt.% and 5 wt.% Cu produced through powder-based laser-directed energy deposition. The following conclusions can be drawn from this study:

(a) The incorporation of Cu resulted in no significant change in the microstructure and appeared to form a homogenous distribution of Cu within the matrix, as confirmed by SEM, EDS, and XRD.

(b) Compressive strength and hardness values remained comparable to 316L despite these elemental modifications. A slight reduction in yield strength was observed for SS-5Cu (317 ± 1 MPa) compared to 316L (334 ± 9 MPa)

and SS-3Cu (329 ± 12 MPa). Similarly, a minor reduction in hardness was measured in the Cu compositions (183 ± 9 and 186 ± 10 HV 0.2 for SS-3Cu and SS-5Cu, respectively) compared to 316L (209 ± 12 HV 0.2).

(c) Cu addition demonstrated significant antibacterial efficacy. SS-3Cu and SS-5Cu effectively inhibited the growth of *S. aureus* and *P. aeruginosa* across all time points, with efficacy increasing proportionally with the Cu content. After being tested against *S. aureus*, the two compositions exhibited 18% and 12% bacterial viability at 72 h, respectively. More effectively, results for *P. aeruginosa* at 48 h indicate 6% and 3% bacterial viability. This highlights the potential of these alloys for use in biomedical environments, particularly in infection-prone applications such as fracture management devices.

The findings suggest that 316L with Cu addition offers a promising balance between mechanical performance and antibacterial functionality, making it a viable material for advanced biomedical devices.

Acknowledgments

The authors would like to acknowledge financial support from the National Science Foundation under Grant Number CMMI1934230 and the National Institute of Arthritis and Musculoskeletal and Skin Diseases of the National Institutes of Health under Award Number R01 AR078241 (PI: Bandyopadhyay). The content is solely the authors' responsibility and does not necessarily represent the National Institutes of Health's official views. The authors would also like to acknowledge experimental help from Aruntapan Dash and Nathaniel Zuckschwerdt.

Conflicts of interest

Amit Bandyopadhyay is the Editorial Board Member of the journal but did not in any way involve in the editorial and peer-review process conducted for this paper, directly or indirectly. The authors declare that they have no competing interests.

Authors' contributions

Conceptualization: Amit Bandyopadhyay
Formal analysis: Michael B. Myers
Funding acquisition: Amit Bandyopadhyay
Investigation: Michael B. Myers
Project administration: Amit Bandyopadhyay
Supervision: Amit Bandyopadhyay
Writing – original draft: Michael B. Myers
Writing – review & editing: Amit Bandyopadhyay

Ethics approval and consent to participate

Not applicable.

Consent for publication

Not applicable.

Availability of data

Data are available from the corresponding author on reasonable request.

References

1. Darouiche RO. Device-associated infections: A macroproblem that starts with microadherence. *Clin Infect Dis*. 2001;33(9):1567-1572.

   doi: 10.1086/323130

2. iData Research. *Orthopedic Trauma Devices Market Size, Share and COVID-19 Impact Analysis. United States. 2019-2025*. iData Research; 2019. Available from: https://idataresearch.com/product/trauma-devices-market-united-states [Last accessed on 2024 Nov 25].

3. Ciliveri S and Bandyopadhyay A. Enhanced osteogenesis and bactericidal performance of additively manufactured MgO-and Cu-added CpTi for load-bearing implants. *Int J Bioprinting*. 2023;9(6):1167.

   doi: 10.36922/ijb.1167

4. Thakore RV, Greenberg SE, Shi H, *et al*. Surgical site infection in orthopedic trauma: A case-control study evaluating risk factors and cost. *J Clin Orthop Trauma*. 2015;6(4):220-226.

   doi: 10.1016/j.jcot.2015.04.004

5. Ciliveri S, Bandyopadhyay A. Additively manufactured SiO_2 and Cu-added Ti implants for synergistic enhancement of bone formation and antibacterial efficacy. *ACS Appl Mater Interfaces*. 2024;16(3):3106-3115.

   doi: 10.1021/acsami.3c14994

6. Devasconcellos P, Bose S, Beyenal H, Bandyopadhyay A, Zirkle LG. Antimicrobial particulate silver coatings on stainless steel implants for fracture management. *Mater Sci Eng C Mater Biol Appl*. 2012;32(5):1112-1120.

   doi: 10.1016/j.msec.2012.02.020

7. Xi T, Shahzad MB, Xu D, *et al*. Effect of copper addition on mechanical properties, corrosion resistance and antibacterial property of 316L stainless steel. *Mater Sci Eng C Mater Biol Appl*. 2017;71:1079-1085.

   doi: 10.1016/j.msec.2016.11.022

8. Vincent M, Duval RE, Hartemann P, Engels-Deutsch M. Contact killing and antimicrobial properties of copper. *J Appl Microbiol*. 2018;124(5):1032-1046.

   doi: 10.1111/jam.13681

9. Bandyopadhyay A, Mitra I, Ciliveri S, *et al*. Additively manufactured Ti-Ta-Cu alloys for the next-generation load-bearing implants. *Int J Extreme Manuf*. 2023;6(1):015503.

   doi: 10.1088/2631-7990/ad07e7

10. Zhuang Y, Zhang S, Yang K, Ren L, Dai K. Antibacterial activity of copper-bearing 316L stainless steel for the prevention of implant-related infection. *J Biomed Mater Res B Appl Biomater*. 2020;108(2):484-495.

doi: 10.1002/jbm.b.34405

11. Dash A, Bose S, Bandyopadhyay A. Additively manufactured 17-4 PH stainless steels for fracture management devices. *Virtual Phys Prototyp.* 2024;19(1):e2397698.

doi: 10.1080/17452759.2024.2397698

12. Chen KK, Chao CY, Chen JH, Wu JH, Chang YH, Du JK. Effect of low copper addition to as-forged 304 stainless steel for dental applications. *Metals*. 2021;11(1):43.

doi: 10.3390/met11010043

13. Vincent M, Hartemann P, Engels-Deutsch M. Antimicrobial applications of copper. *Int J Hyg Environ Health*. 2016;219(7 Part A):585-591.

doi: 10.1016/j.ijheh.2016.06.003

14. Hadrup N, Sharma AK, Jacobsen NR, Loeschner K. Distribution, metabolism, excretion, and toxicity of implanted silver: A review. *Drug Chem Toxicol*. 2022;45(5):2388-2397.

doi: 10.1080/01480545.2021.1950167

15. Cao B, Zheng Y, Xi T, *et al*. Concentration-dependent cytotoxicity of copper ions on mouse fibroblasts *in vitro*: Effects of copper ion release from TCu380A vs TCu220C intra-uterine devices. *Biomed Microdevices*. 2012;14(4):709-720.

doi: 10.1007/s10544-012-9651-x

16. Badhe RV, Akinfosile O, Bijukumar D, Barba M, Mathew MT. Systemic toxicity eliciting metal ion levels from metallic implants and orthopedic devices-A mini review. *Toxicol Lett*. 2021;350:213-224.

doi: 10.1016/j.toxlet.2021.07.004

17. Foadian F, Kremer R, Post M, Taghizadeh Tabrizi A, Aghajani H. Investigation of *in-situ* low copper alloying of 316L using the powder bed fusion process. *Solids*. 2023;4(3):156-165.

doi: 10.3390/solids4030010

18. Bandyopadhyay A, Bose S. *Additive Manufacturing*. 2nd ed. United States: CRC Press; 2019.

doi: 10.1201/9780429466236

19. ASTM F3413-19e1: *Guide for Additive Manufacturing-Design-Directed Energy Deposition*. United States: ASTM International; 2019.

doi: 10.1520/F3413-19E01

20. Bandyopadhyay A, Traxel KD, Lang M, Juhasz M, Eliaz N, Bose S. Alloy design via additive manufacturing: Advantages, challenges, applications and perspectives. *Mater Today*. 2022;52:207-224.

doi: 10.1016/j.mattod.2021.11.026

21. ASTM E407-23: *Standard Practice for Microetching Metals and Alloys*. United States:ASTM International; 2023.

doi: 10.1520/E0407-23

22. ASTM E9-19: *Standard Test Methods of Compression Testing of Metallic Materials at Room Temperature*. United States: ASTM International; 2019.

doi: 10.1520/E0009-19

23. ASTM E92-23: *Standard Test Methods for Vickers Hardness and Knoop Hardness of Metallic Materials*. United States: ASTM International; 2023.

doi: 10.1520/E0092-23

24. Ersts PJ. *DotDotGoose*. Available from: https://biodiversityinformatics.amnh.org/open_source/dotdotgoose [Last accessed on 2024 Nov 25].

25. STM E92-23: *Standard Specification for Wrought 18Chromium-14Nickel-2.5Molybdenum Stainless Steel Bar and Wire for Surgical Implants (UNS S31673)*. United States: ASTM International; 2019.

doi: 10.1520/F0138-19

26. Kheiri S, Mirzadeh H, Naghizadeh M. Tailoring the microstructure and mechanical properties of AISI 316L austenitic stainless steel via cold rolling and reversion annealing. *Mater Sci Eng A*. 2019;759:90-96.

doi: 10.1016/j.msea.2019.05.028

27. Behjat A, Shamanian M, Iuliano L, Saboori A. Laser powder bed fusion *in situ* alloying of AISI 316L-2.5%Cu alloy: Microstructure and mechanical properties evolution. *Prog Addit Manuf*. 2024;9:2031-2039.

doi: 10.1007/s40964-023-00557-x

28. Liu Y, Yang J, Yang H, *et al*. Cu-bearing 316L stainless steel coatings produced by laser melting deposition: Microstructure and corrosion behavior in simulated body fluids. *Surf Coat Technol*. 2021;428:127868.

doi: 10.1016/j.surfcoat.2021.127868

29. Behjat A, Shamanian M, Sadeghi F, Iuliano L, Saboori A. Additive manufacturing of a novel *in-situ* alloyed AISI316L-Cu stainless steel: Microstructure and antibacterial properties. *Mater Lett*. 2024;355:135363.

doi: 10.1016/j.matlet.2023.135363

30. Płatek P, Sienkiewicz J, Janiszewski J, Jiang F. Investigations on mechanical properties of lattice structures with different values of relative density made from 316L by Selective Laser Melting (SLM). *Materials* (*Basel*). 2020;13:2204.

doi: 10.3390/ma13092204

31. Grass G, Rensing C, Solioz M. Metallic copper as an antimicrobial surface. *Appl Environ Microbiol*. 2011;77(5):1541-1547.

doi: 10.1128/AEM.02766-10

ACCSCIENCE PUBLISHING

Materials Science in Additive Manufacturing

ORIGINAL RESEARCH ARTICLE

Effect of *in situ* electromagnetic field manipulation on the microstructure and hardness of titanium alloy during laser melting deposition

Chang Liu[1,2†], Yongjian Wu[1,2†], Jian Zhou[1,2], Yan Wen[1,2*], Liqiang Wang[3], and Lechun Xie[1,2*]

[1]Hubei Key Laboratory of Advanced Technology for Automotive Components, Wuhan University of Technology, Wuhan, Hubei, China

[2]Hubei Collaborative Innovation Center for Automotive Components Technology, Wuhan University of Technology, Wuhan, Hubei, China

[3]State Key Laboratory of Metal Matrix Composites, School of Materials Science and Engineering, Shanghai Jiao Tong University, Shanghai, China

Abstract

The electromagnetic field is a non-contact physical field that can influence the internal flow of the melt pool and regulate the microstructure properties of alloy through electromagnetic force during laser melting deposition (LMD). This study proposes a 3D numerical model of LMD Ti-6Al-4V coupled with an electromagnetic field and investigates the effect of the electromagnetic field on the fluid dynamics of the melt pool during LMD. The results indicated that a steady electromagnetic field can suppress the internal flow of the melt pool. In an electromagnetic field of 39.40 mT, the length of β-columnar grains significantly decreases from 490 to 354 μm, resulting in fragmentation and equiaxed tendencies, thereby enhancing the hardness of the deposition layer. This study provides a new method for *in situ* manipulation of the microstructure and mechanical properties of titanium alloys during LMD.

Keywords: *In situ* manipulation; Electromagnetic field; Laser melting deposition; Ti-6Al-4V; Molten pool

†These authors contributed equally to this work.

***Corresponding authors:**
Yan Wen
(gubi2008@whut.edu.cn)
Lechun Xie
(xielechun@whut.edu.cn)

Citation: Liu C, Wu Y, Zhou J, Wen Y, Wang L, Xie L. Effect of *in situ* electromagnetic field manipulation on the microstructure and hardness of titanium alloy during laser melting deposition. *Mater Sci Add Manuf*. 2025;4(1):8332.
doi: 10.36922/msam.8332

Received: December 31, 2024

Revised: January 23, 2025

Accepted: January 23, 2025

Published Online: March 18, 2025

1. Introduction

Field-assisted additive manufacturing has garnered significant attention in recent years.[1,2] Laser melting deposition (LMD) is an additive manufacturing process widely reported by many researchers due to its various advantages, such as large product size, high efficiency, a wide range of available materials, and excellent product properties.[3-7] As a typical titanium alloy, Ti-6Al-4V has been extensively studied by researchers in terms of its microstructure and properties when produced using LMD.[8-10] A high-energy laser beam serves as the energy source of LMD. With the movement of the focus position, the high-energy laser beam increases the temperature of the substrate and powder, resulting in powder melting, rapid cooling, and solidification; the cooling rate of the metal molten pool can reach up to 10^3 – 10^5 K/s.[11] The coarse structure formed during the rapid cooling process of the LMD alloy is prone to residual stress concentration, posing a challenge in the application of LMD technology.[12] Hence, new technical methods are in demand to

modify the microstructure and enhance the properties of LMD titanium alloys.

Electromagnetic field treatment has been reported to effectively enhance the microstructure and properties of titanium alloys.[13,14] Qin *et al.*[15] investigated axisymmetric sequential and loose electromagnetic-structural coupling simulation models of the electromagnetic riveting process for a Ti-6Al-4V titanium rivet. The results indicated that increasing the displacement of the punch from 3.38 to 3.81 mm led to an 80.55% increase in the maximum radial displacement of the rivet shaft. Li *et al.*[16] investigated the effect of an alternating electromagnetic field on the microstructure and properties of the Ti-Al coating on the titanium alloy surface; the results demonstrated that the coating diffused under the magnetic field with a current intensity of 20 A and displayed good overall quality, strong bonding with the substrate, a relatively flat interface, a dense and uniform fine structure, and no obvious cracks or holes. Song *et al.*[17] investigated the effect of cryogenic coupled magnetic field (CCMF) treatment on the microstructure and mechanical properties of Ti-6Al-4V titanium alloy and found that the CCMF-treated samples displayed a lower ultimate tensile strength but a higher elongation compared to samples that underwent either single cryogenic treatment or single magnetic treatment. Hence, studying the *in situ* manipulation of the microstructure and properties of LMD titanium alloy using an electromagnetic field is of great significance.

An electromagnetic field primarily influences the microstructure of materials by inducing electromagnetic forces within the molten pool. The transfer and convection of heat in the molten pool are regulated by the parameters and direction of the electromagnetic field, temperature gradient, and flow pattern during metal solidification. The effect of an electromagnetic field in LMD is dependent on its ability to suppress convection in the molten pool. Bachmann *et al.*[18] developed a 3D welding molten pool model with an applied electromagnetic field, where the direction of the steady electromagnetic field was perpendicular to the welding direction. The steady electromagnetic field could alter the molten pool flow pattern, affect the weld geometry, and consequently impact welding quality by suppressing convection within the molten pool. Velde *et al.*[19] conducted a numerical study on the development process of the aluminum molten pool under the influence of a steady electromagnetic field of different strengths during LMD. The researchers demonstrated that a steady electromagnetic field can suppress eddy currents, effectively mitigating the uneven temperature distribution resulting from unstable convection, thereby improving the material properties.

Researchers have proposed various theoretical studies and numerical models to clarify the effect of electromagnetic fields on molten pool dynamics. However, due to the coupling of multiple physical fields and the high computational requirements, the development of a more comprehensive and accurate 3D numerical model for electromagnetic field coupling in LMD is warranted.[20] Research on *in situ* manipulation of LMD of Ti-6Al-4V titanium alloy using an electromagnetic field has rarely been reported in recent years. Different materials respond differently to electromagnetic fields, which in turn affect deposition process parameters, molten pool flow behavior, and cooling rates, ultimately influencing the microstructure and properties of the deposition layer. Hence, conducting experimental and simulation research on the *in situ* manipulation of the LMD process for Ti-6Al-4V titanium alloy using electromagnetic fields is of great significance.

2. Methods

2.1. Numerical model for LMD

2.1.1. Geometric model

A 3D numerical model was utilized to study the size and morphology of the deposition layer, as well as the flow behavior of the molten pool. However, the approach resulted in a higher computational load. The symmetrical model with half of the computational domain in the x-direction was used. The schematic of the geometric model is illustrated in Figure 1.The dimension of the geometric model is 5 × 15 × 10 mm; the upper blue area represents the argon environment, whereas the lower gray area represents the Ti-6Al-4V substrate (Figure 1A). The geometric model was divided into six regions to optimize the calculation while maintaining the accuracy of the molten pool area. Local mesh refinement was applied in the molten pool area, as depicted by the light blue and gray areas (Figure 1A). A hexahedral structured mesh was used to divide the geometric model (Figure 1B), where the yellow surface represents the symmetry plane of the model. The five interfaces of the argon gas domain in the model are pressure outlets, and the mesh size of the locally refined molten pool area is 0.1 mm. The scanning direction of the LMD is in the positive y-axis direction.

2.1.2. Basic assumptions of the numerical simulation model

The following assumptions were made when establishing the multiphase model coupled with the electromagnetic field:

(i) The liquid metal in the molten pool during the LMD process is assumed to be an incompressible Newtonian fluid, and the flow regime is laminar[21]

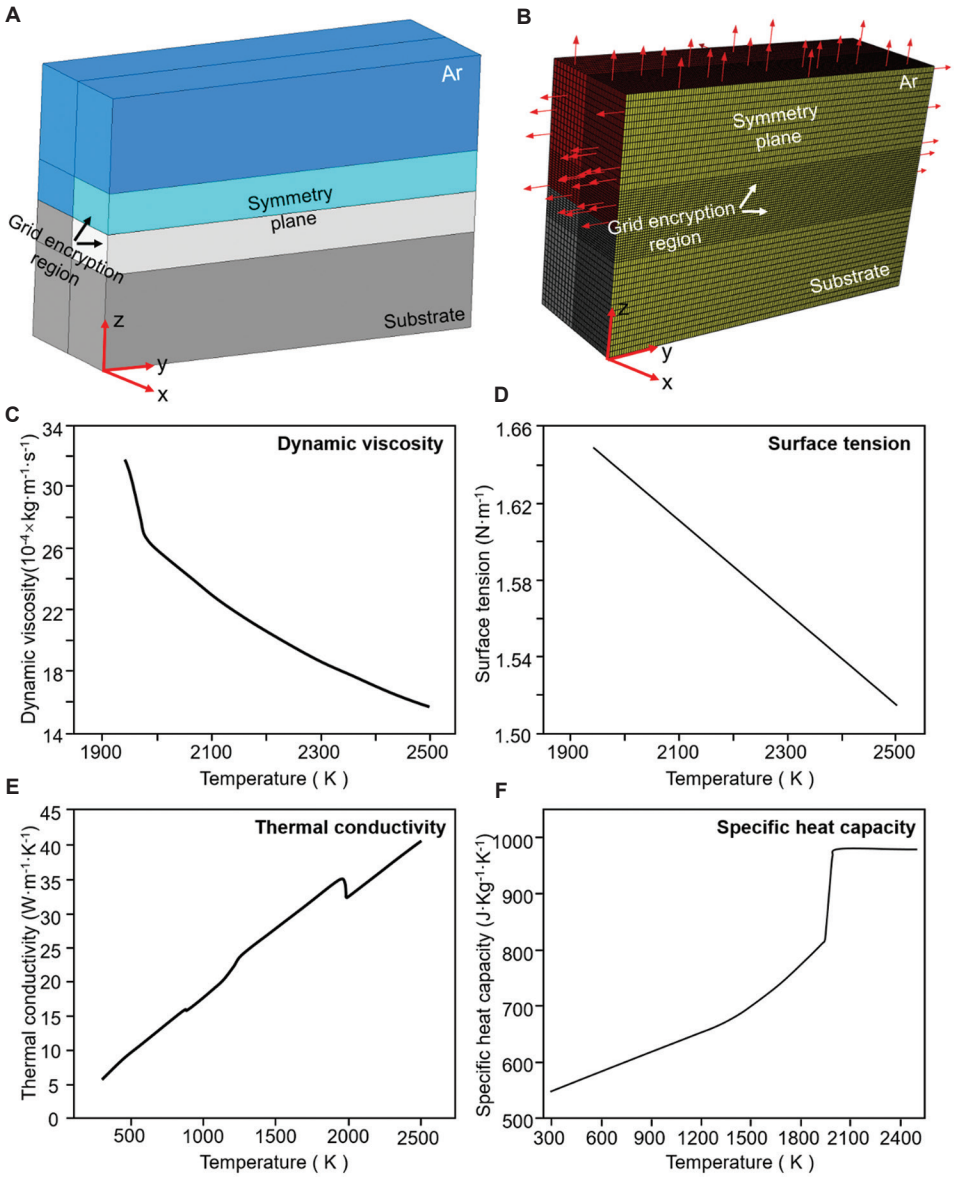

Figure 1. Experimental simulation conditions and parameter setting: (A) Schematic of the geometric model of laser melting deposition (LMD). (B) Mesh model of LMD. (C-F) Temperature-dependent thermophysical parameters calculated using JmatPro

(ii) Given the symmetry of the applied source terms and boundary conditions relative to the centerline of the deposition layer, it is sufficient to establish only half of the geometric model

(iii) The energy distribution of the laser beam and the concentration distribution of the coaxial powder are assumed to follow a Gaussian distribution

(iv) The flow of fluid is driven by buoyancy, gravity, and the surface tension gradient at the gas-liquid interface within the molten pool. The influence of the concentration of surface-active elements on surface tension is neglected in the analysis.

2.2. Free interface tracking

The volume of fluid (VOF) method is typically used in interface tracking of LMD. The VOF model simulates multiple immiscible fluids by solving momentum equations and tracking the volume fraction of different fluid phases throughout the computational domain. The basic principle is that a parameter representing the phase volume fraction is introduced into each computational cell within the entire computational domain when the model introduces new components. The sum of the volume fractions of different phases in each cell is 1, and the physical properties of the

cell depend on the volume fractions of each phase, which can be calculated using the volume-weighted average of each phase. In practical simulation studies, the VOF method for tracking the interface can often be inaccurate, leading to situations where local computational domains within the substrate are incorrectly identified as gas-liquid interfaces. In addition, it cannot accurately control the size of the free interface region.

An improved method for tracking the interface using volume fraction gradients based on the VOF method was proposed.[22] This approach solves for the gradient of the metal phase volume fraction in the computational domain at each iteration through a user-defined function. Since the internal region of the metal substrate contains only the metal phase, its volume fraction gradient is 0. Similarly, the gradient is also 0 for the argon gas phase in the argon region. The change in phase volume fractions in different directions causes a significant volume fraction gradient at the metal-argon interface. The gradient value is related to the mesh size; the position and size of the free interface can be accurately captured by selecting an appropriate volume fraction gradient value based on the model's mesh size. A more precise addition of mass, energy, and momentum source terms can be achieved, leading to more accurate simulation results.

2.3. Basic control equations

The model in the study calculates the pressure field, velocity field, and temperature field of each element by solving Equations I, II, and III, corresponding to the mass, momentum, and energy conservation, respectively:[11,23-25]

$$\frac{\partial \rho}{\partial t} + \nabla\left(\rho \boldsymbol{v}\right) = S_{mass} \tag{I}$$

$$\frac{\partial\left(\rho \boldsymbol{v}\right)}{\partial t} + \nabla\left(\rho \boldsymbol{v}\boldsymbol{v}\right) = \mu\nabla\left(\rho \boldsymbol{v}\right) - \nabla p + \rho g + S_{mom} \tag{II}$$

$$\frac{\partial \rho H}{\partial t} + H\nabla\left(\rho \boldsymbol{v}\right) = \nabla\left(k\nabla T\right) + h_s + S_{energy} \tag{III}$$

where ρ is the metal density, t is time, v is the fluid velocity, S_{mass} is the mass source term, μ is viscosity, g is gravitational acceleration, p is pressure, S_{mom} is the momentum source term, H is enthalpy, k is thermal conductivity, h_s is the enthalpy increment of external filling materials, and S_{energy} is the energy source term.

The enthalpy variation of the material in Equation IV is the sum of sensible enthalpy and latent heat, where the melting latent heat ΔH can be represented by Equation V:

$$H = h + \Delta H \tag{IV}$$

$$\Delta H = Lf_l \tag{V}$$

Where H is the enthalpy change of the material, h is sensible enthalpy, ΔH is latent heat, L is the melting, latent heat, and f_l is the liquid phase volume fraction.

The enthalpy-porosity method is used to simulate the melting and solidification processes of materials. The mushy zone (solid–liquid two-phase region) is treated as a porous medium, where the porosity in each cell equals the liquid phase fraction in that cell. The porosity is 0, and the velocity in the region is reduced to 0 when fully solidified; the porosity is 1 when completely melted. The mushy zone exists when the porosity is between 0 and 1. The function expression for the liquid phase volume fraction is obtained from Equation VI:[26]

$$f_l = f\left(x\right) = \begin{cases} 1, T > T_l \\ \dfrac{T - T_s}{T_l - T_s}, T_s \le T \le T_l \\ 0, T < T_s \end{cases} \tag{VI}$$

Where T_l and T_s represent the liquidus and solidus lines of the material, respectively.

2.3.1. Mass addition equation

The metal powder is ejected through a coaxial nozzle under the conveying of powder feed gas in the process of LMD, and the spatial concentration distribution of the powder approximates a Gaussian distribution. The synchronous powder addition is implemented in the form of a mass source term S_{mass}, and the expression of the mass source term is expressed in Equation VII:[27]

$$S_{mass} = \frac{\omega_1 \eta_p m_s}{\pi r_p^{\,2}} exp\left\{-\frac{\omega\left[\left(x - v_s t\right)^2 + y^2\right]}{r_b^{\,2}}\right\} \tag{VII}$$

Where ω_1 represents the Gaussian distribution coefficient of the powder, η_p denotes the powder utilization efficiency, and m_s is the powder mass flow rate, r_p is the radius of the powder Gaussian distribution region, and v_s represents the scanning speed of the laser head.

2.3.2. Moving Gaussian heat source and thermal boundary conditions

In the process of LMD, apart from the substrate's absorption of laser heat, the heat flux density due to thermal convection and thermal radiation losses on the substrate surface should also be included. The equation for S_{energy} is as follows:

$$S_{energy} = Q_{laser} - Q_{con} - Q_{rad} \tag{VIII}$$

Where Q_{laser} represents the laser heat source, Q_{con} is the energy loss due to convection, and Q_{rad} represents the energy loss due to thermal radiation.

The high-energy beam formed by semiconductor lasers is unevenly distributed, exhibiting a trend of high energy density in the center that gradually decreases toward the periphery. The Gaussian distribution laser heat source model is adopted and expressed as follows:[25]

$$Q_{laser} = \frac{\omega_2 P \eta_l}{\pi r_l} \exp\left\{ -\frac{\omega_2 \left[\left(x - v_s t \right)^2 + y^2 \right]}{r_b^2} \right\} \quad \text{(IX)}$$

Where P represents the laser power, ω_2 is the Gaussian distribution coefficient of the laser, η_l is the laser utilization efficiency, and r_b is the effective laser radius.

Convective heat transfer exists in the four lateral surfaces of the substrate, while both convective and radiative heat transfer occurs on the substrate surface. Heat dissipation through convection and radiation is represented by the following equation:[28]

$$Q_{losses} = Q_{con} + Q_{rad} = h \cdot \left(T - T_0 \right) + \varepsilon \cdot \sigma_b \cdot \left(T^4 - T_0^4 \right) \quad \text{(X)}$$

Where h represents the convective heat transfer coefficient, T is the real-time wall surface temperature, T_0 is the ambient temperature, ε is the surface emissivity of the material, and σ is the Stefan-Boltzmann constant.

2.3.3. Surface force equation

The numerical model includes two surface tensions: (i) the surface tension $f_{S,n}$ generated due to the curvature between argon gas and the liquid molten pool interface, which acts perpendicular to the surface, and (ii) the Marangoni shear stress $f_{S,t}$ arises from the uneven thermal distribution on the molten pool surface, resulting in larger temperature gradients tangent to the free surface. The specific equation for surface forces is presented as follows:[29]

$$F_S = f_{S,n} + f_{S,t} = \sigma.\kappa.n + \nabla_t \sigma \quad \text{(XI)}$$

Where σ represents surface tension, κ is surface curvature, and n is a vector perpendicular to the surface. The equations for surface tension and Marangoni shear stress are as follows:[30,31]

$$n = \frac{\nabla \gamma}{\left| \nabla \gamma \right|} \quad \text{(XII)}$$

$$\nabla_t \sigma = \frac{d\sigma}{dT} \nabla_t T = \frac{d\sigma}{dT} \left[\nabla T - n \cdot \left(n \cdot \nabla T \right) \right] \quad \text{(XIII)}$$

Where $\frac{d\sigma}{dT}$ represents the temperature coefficient of surface tension.

2.3.4. Buoyancy equation for heat

Thermal buoyancy is typically generated by density variations caused by temperature changes in liquid metals. The density gradient is related to the expansion of the liquid metal, commonly represented by Boussinesq. It is assumed that the density of the fluid is constant in the time derivative and convective terms, with only the buoyancy term affected by density fluctuations. The relevant equations are simplified, and the spatial variation of density is confined to the buoyancy term. The equation for buoyancy is as follows:[32]

$$F_{buoyancy} = \rho_l \, g\beta(T\text{-}T_l) \quad \text{(XIV)}$$

Where ρ_l represents the density of the metal at the liquidus temperature T_l, and β is the thermal expansion coefficient of the metal.

2.3.5. Electromagnetic force equation

The movement of conductive particles in an electromagnetic field produces current density during the scanning process of the laser head. The electromagnetic force is generated under the influence of an externally applied longitudinal electromagnetic field, and the electromagnetic force in the molten pool can be expressed by the following equation:

$$F = J \times B \quad \text{(XV)}$$

Where F represents the Lorentz force, J is the current density vector, and B is the magnetic flux density vector.

2.4. Material thermophysical parameters

The thermophysical parameters of the Ti-6Al-4V alloy used in the simulation are listed in Table 1. The parameters are determined by commercial material

Table 1. Physical parameters used in the simulation

Property	Value	Unit
Density (ρ)	4440	kg·m^{-3}
Dynamic viscosity (μ_0)	2.6×10^{-3} (1878 K)	kg·m^{-1}·s^{-1}
Solidus temperature (TS)	1878	K
Liquidus temperature (TL)	1928	K
Specific heat capacity (cp)	550 (297 K)	J·kg^{-1}·K^{-1}
Thermal conductivity (k)	5.74 (297 K)	W·m^{-1}·K^{-1}
Latent heat of fusion (L)	2.92×10^5	J·kg^{-1}
Thermal expansion coefficient (β)	1.6×10^{-4}	K^{-1}
Surface tension (σ)	1.65 (1928 K)	N·m^{-1}
Surface tension coefficient $\left(\frac{d\sigma}{dT}\right)$	−2.44×10^{-4}	N·m^{-1}·K^{-1}
Stefan-Boltzmann constant (σS)	5.67×10^{-8}	K
Radiation emissivity (ε)	0.8	-

property simulation software JMatPro and adjusted based on reference literature.[26,33-36] The material thermophysical parameters indicate significant variations in temperature during the numerical simulation of LMD, and the influence of temperature-dependent thermophysical parameters cannot be ignored. The crucial parameters (thermal conductivity, specific heat capacity, viscosity, and surface tension) utilized in the simulation are described as functions of temperature (Figure 1C-F).

2.5. Experimental process

The experiment was conducted using a self-developed *in situ* LMD manipulation system for the Ti-6Al-4V alloy. The *in situ* LMD manipulation system mainly consists of electromagnetic coils and a laser nozzle (Figure 2A). The chemical composition of the Ti-6Al-4V powder is presented in Table 2. The laser power of 1400 W, scan rate of 7.5 mm/s, and powder feed rate of 8.5 g/min were selected for the LMD experiments with and without electromagnetic field, and the morphology, microstructure, and hardness of LMD Ti-6Al-4V were studied. The electromagnetic field was controlled by the input voltage and current of the power supply. The LMD experiments were conducted with different output voltage and current settings, and the experiment parameters are listed in Table 3.

The sample was cut in the direction parallel to the laser beam, and the combination between the deposition layer and the substrate was observed. The measurement position is displayed in Figure 2B. The sample was ground using sandpapers via standard metallurgical process (with 240 #,

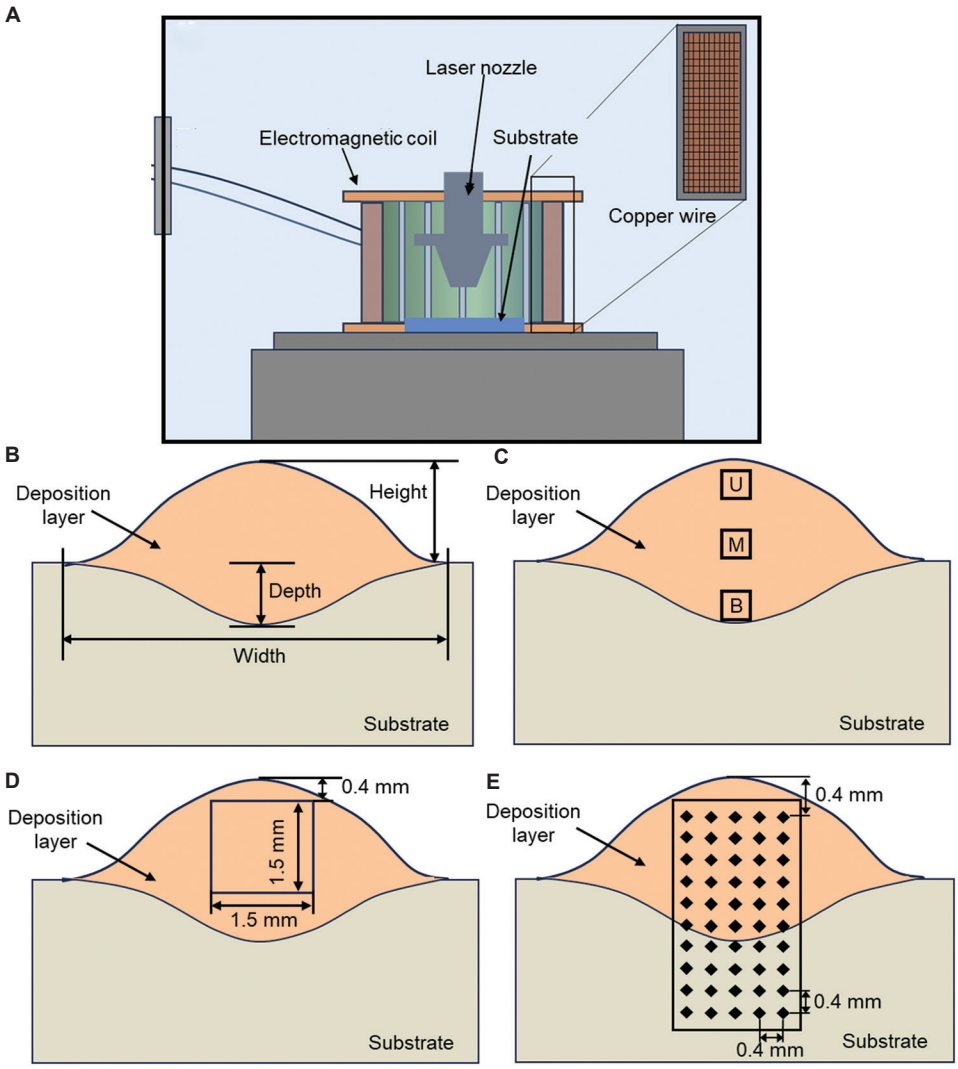

Figure 2. Schematic diagram of the experimental process: (A) Schematic of the *in situ* laser melting deposition manipulation system. (B) Schematic for geometric dimension measurement of the deposition layer. (C) Characterization areas for scanning electron microscopy. (D) Characterization areas for electron backscattering diffraction. (E) Schematic of the hardness test

600 #, 1200 #, and 4000 # sandpaper in turn) and polished using OPS (SiO_2 suspension) with 40% H_2O_2 as volume fraction. Before the microstructure characterization, the sample was immersed in an etchant solution (V_{HF}:HNO_3:H_2O=3:5:92) for 60 – 70 s. The microstructure characterization was conducted using a scanning electron microscope (JSM-IT800, HL; Japan). The upper (U), middle (M), and bottom (B) areas of the deposition layer were selected for microstructure characterization (Figure 2C). Texture analysis was conducted via electron backscattering diffraction (EBSD). The electrolytic polishing of samples was performed using 5% perchloric acid solution for 13 – 15 s after mechanical polishing but before the EBSD test, with a scan area of 1.5 × 1.5 mm (Figure 2D).

The hardness of the cross-section of the deposition layer was determined using a Vickers hardness tester (Hua Yin HV-1000A; China). The hardness test points were selected in the form of a 5 × 10 matrix, and 50 points were tested for each sample (Figure 2E). The distance between each test point was 0.4 mm, and the selected position of the highest point was 0.4 mm from the top of the deposition layer.

Table 2. Chemical composition of Ti-6Al-4V powder

Element	Ti	Al	V	Fe	C	N	O	H
Wt%	Balance	6.2	4.15	0.056	0.01	0.015	0.15	0.0016

Table 3. Sample number and electromagnetic parameters

Sample number	Voltage (V)	Current (A)	Magnetic intensity (mT)
EM-0	0	0	0
EM-1	8	20	39.40
EM-2	12	30	57.12
EM-3	16	40	72.93

3. Results and discussion

3.1. Morphological analysis of the molten pool

Figure 3 displays the molten pool morphology of the deposition layer with different electromagnetic parameters. The deposition layer comprises a molten pool and a heat-affected area. The solid yellow line delineates the boundary between the molten pool and the heat-affected area, while the dashed yellow line indicates the boundary between the heat-affected area and the substrate. As displayed in Figure 3A-D, the area (including height, width, and melt depth) of the deposition layer in samples EM-1 to EM-3 is reduced significantly. The coarse columnar grain can be observed in sample EM-0 (Figure 3A); reduced grain size and equiaxed grains can be observed in sample EM-1 (Figure 3B). The long columnar grain in sample EM-2 appears plate-like (Figure 3C), whereas coarse grains are observed in sample EM-3 (Figure 3D) with the increase in electromagnetic intensity.

As depicted in Table 4, the width, height, and melt depth of the deposition layers in sample EM-0 are 1.16, 4.11, and 0.77 mm, respectively. Under the electromagnetic field, the area of sample EM-1 is the smallest, with a length, width, and height of 0.92, 3.46, and 0.75 mm, respectively. This could be due to inhibition of the molten pool flow due to the electromagnetic field that results in a reduction in the flow of high-temperature melt toward the periphery from the center of the laser beam; subsequently, the size

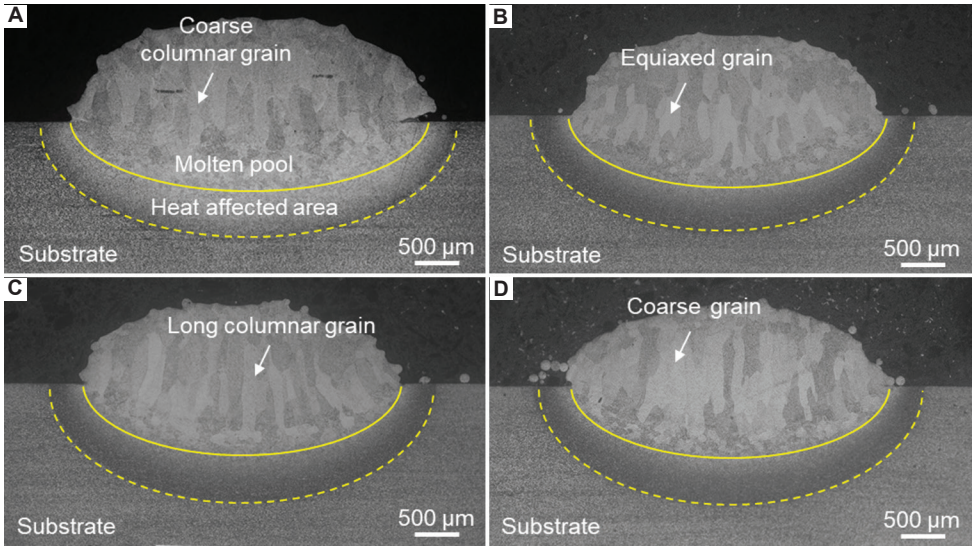

Figure 3. The optical microscopic image of deposition layers of different samples: (A) EM-0; (B) EM-1; (C) EM-2; and (D) EM-3. Scale bars: 500 μm

of the molten pool and the amount of powder falling into the molten pool are both reduced. Both the width and height of the deposition layers increased with slight increases in electromagnetic intensity. The aggregation effect on the powder appears as the electromagnetic intensity constantly increases, resulting in more powder falling into the molten pool. In addition, a further increase in the width and height of the deposition layer can be observed. The depth of the molten pool depends on the internal flow toward the bottom and associated heat transfer. The inhibitory effect on molten pool flow and heat transfer becomes stronger as the electromagnetic intensity increases.

Table 4. Geometric dimensions of the deposition layers of the samples

Sample number	Height (mm)	Width (mm)	Depth (mm)
EM-0	1.16	4.11	0.77
EM-1	0.92	3.46	0.75
EM-2	0.95	3.61	0.72
EM-3	0.99	3.67	0.70

3.2. Temperature and flow field analysis of the molten pool

The numerical simulation of the coupled *in situ* manipulated LMD layer is conducted under the electromagnetic intensity of sample EM-1. The simulation results were compared and analyzed against the numerical simulation results of the LMD layer without electromagnetic assistance. Figure 4 displays the temperature distribution of single-track deposition layers of samples EM-0 and EM-1 at different times. The highest temperature of the molten pool is increased from 2708 K for sample EM-0 to 2717 K for sample EM-1. The high temperature flows from the center of the laser beam toward the periphery, and the heat is transferred to the surroundings during the LMD process. The inhibitory effect on heat transfer by electromagnetic field promotes the highest temperature increase in the molten pool.

Figure 5 displays the velocity distribution vectors in the molten pool at different times for samples EM-0 and EM-1. The more regular and orderly velocity vector distributed on the top surface can be found for sample EM-0 (Figure 5A and D), with the melt flowing from the

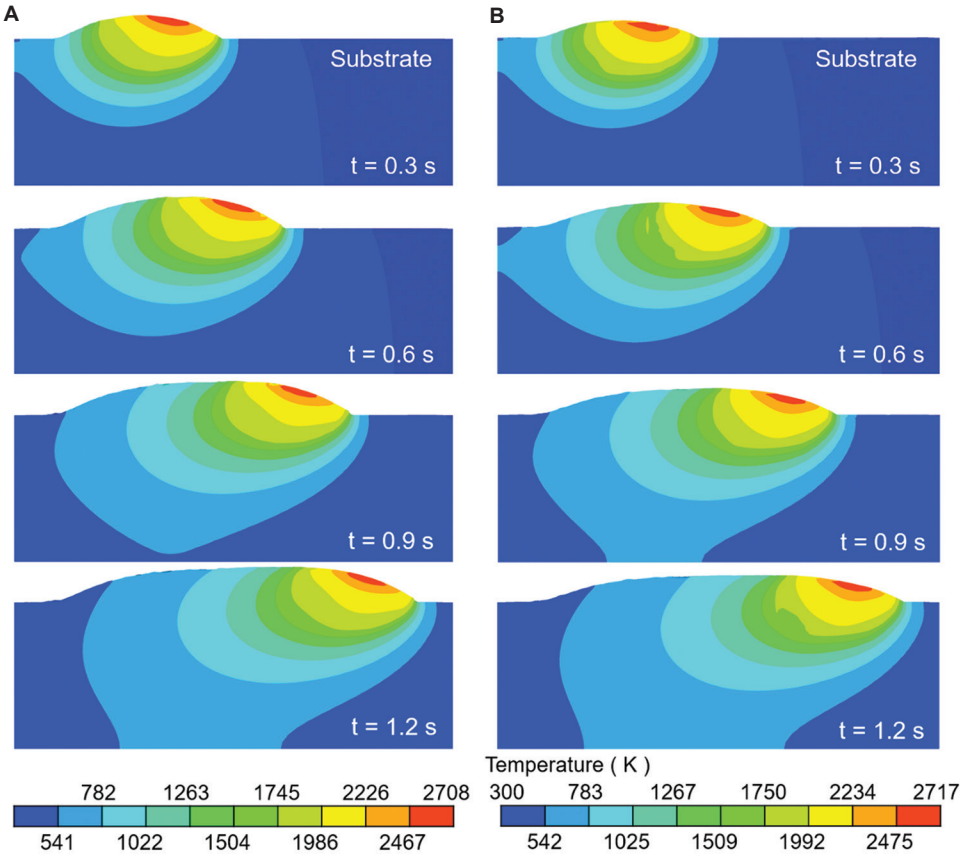

Figure 4. Numerical simulation of *in situ* manipulated laser melting deposition layers of samples at different times: (A) EM-0 and (B) EM-1

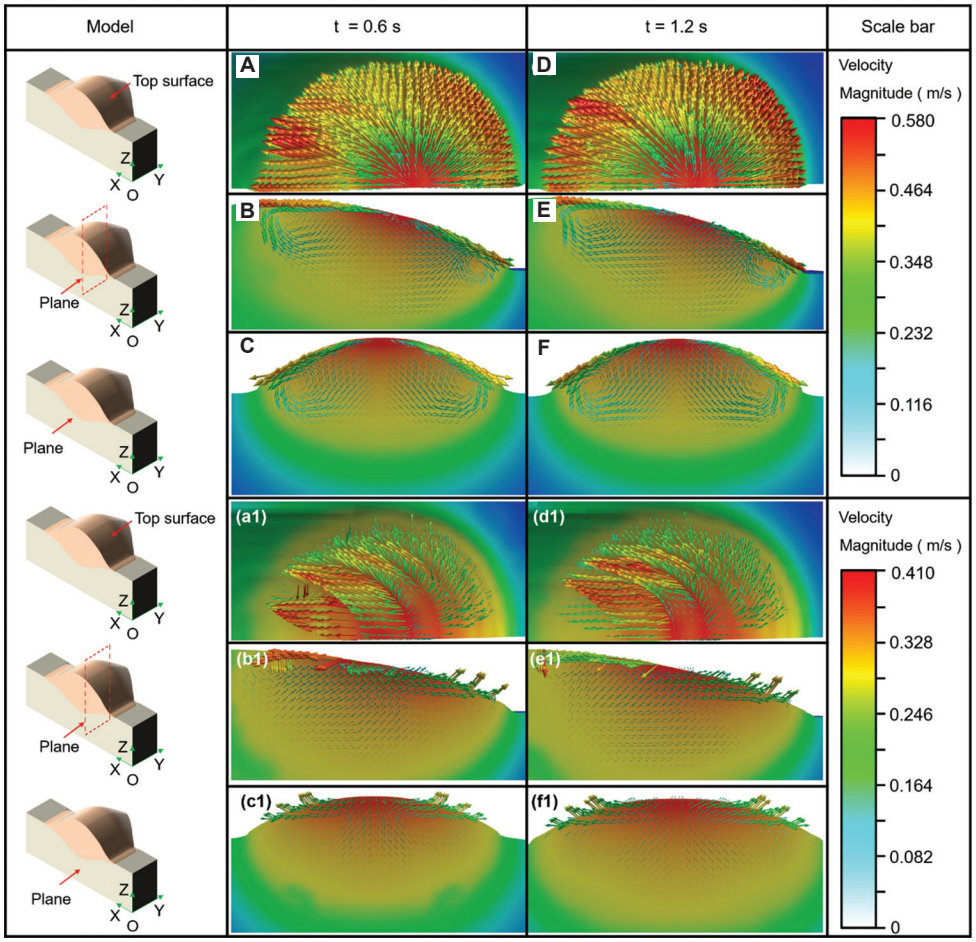

Figure 5. Different surface velocity vectors in the molten pool at different times. (A, D, a1, and d1) Half of the top surface on the molten pool for samples EM-0 (A and D) and EM-1 (a1 and d1). (B, E, b1, and e1) Half of the cross-section parallel to the YOZ plane along the scanning trajectory of the molten pool for samples EM-0 (B and E) and EM-1 (b1 and e1). (C, F, c1, and f1) Cross-section parallel to the XOZ plane and vertical to the scanning trajectory of the molten pool for samples EM-0 (C and F) and EM-1 (c1 and f1)

center of the laser beam toward the periphery. The velocity vector distribution on the top surface of sample EM-1 displays relative chaos and disorder (Figure 5a1 and d1). A similar pattern is observed at the cross-section parallel to the YOZ plane along the scanning trajectory (Figure 5B, E, b1, and e1), as well as the cross-section parallel to the XOZ plane and vertical to the scanning trajectory (Figure 5C, F, c1, and f1). The maximum flow velocity in the molten pool of samples EM-0 and EM-1 are 0.58 and 0.41 m/s, respectively. The maximum flow velocity in the molten pool with an application of 39.40 mT constant electromagnetic field decreases by 29% compared to that without an electromagnetic field, indicating that the constant electromagnetic field exhibits a significant inhibitory effect on the internal flow within the molten pool.

The inhibitory effect of a constant electromagnetic field on the internal flow within the molten pool can be attributed to variations in the Lorentz force within the molten pool (Figure 6). When the electromagnetic coil is energized, the induced electromagnetic field traverses the molten pool along the Z-axis (Figure 6A). It is assumed that the initial velocity of the internal flow, denoted as v, in the absence of an electromagnetic field, can be decomposed into horizontal (v_1) and vertical (v_2) components (Figure 6B). Driven by the Marangoni force, the molten pool flow circulates the center of the laser beam on the free surface. It then flows toward the bottom, encountering boundary resistance, and subsequently returns to the center of the laser beam along the bottom of the molten pool. Due to the negative pressure and thermal buoyancy of the liquid melt flowing off the surface, the molten pool flow rises upward and forms two circular flows in opposite directions (Figure 6B). A similar phenomenon can also be observed in Figure 5A-F. The direction of the induced current (marked by green crosses) can be determined by the right-hand rule under the action

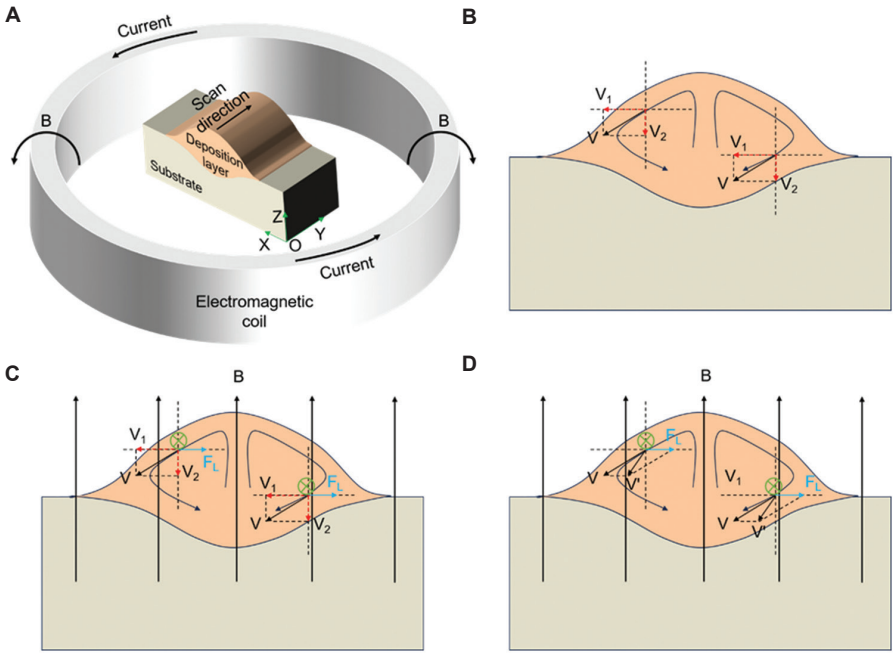

Figure 6. Schematic of the Lorentz force action mechanism on the molten pool flow with electromagnetic field. (A) The induced electromagnetic field passes through the deposition layer. (B) Vector decomposition of molten pool flow. (C) Lorentz force action mechanism. (D) Electromagnetic field changes the flow direction

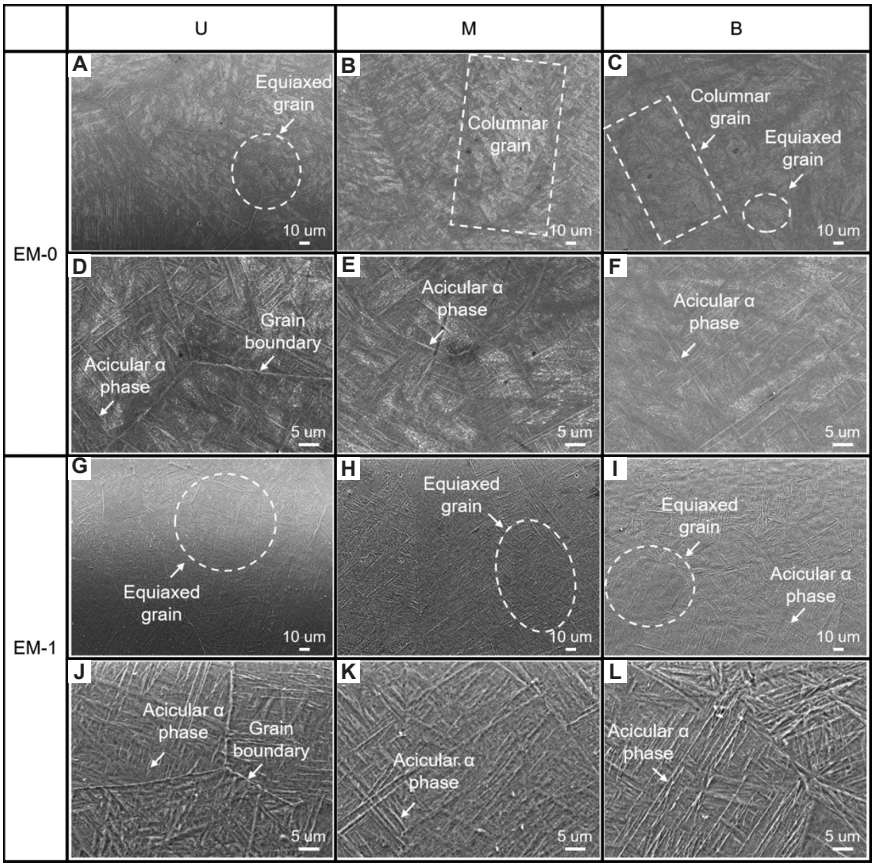

Figure 7. The scanning electron microscopy images of deposition layers for samples EM-0 and EM-1. (A-F) EM-0. (G-L) EM-1. Scale bars: 10 μm (A-C; G-I); 5 μm (D-F; J-L)

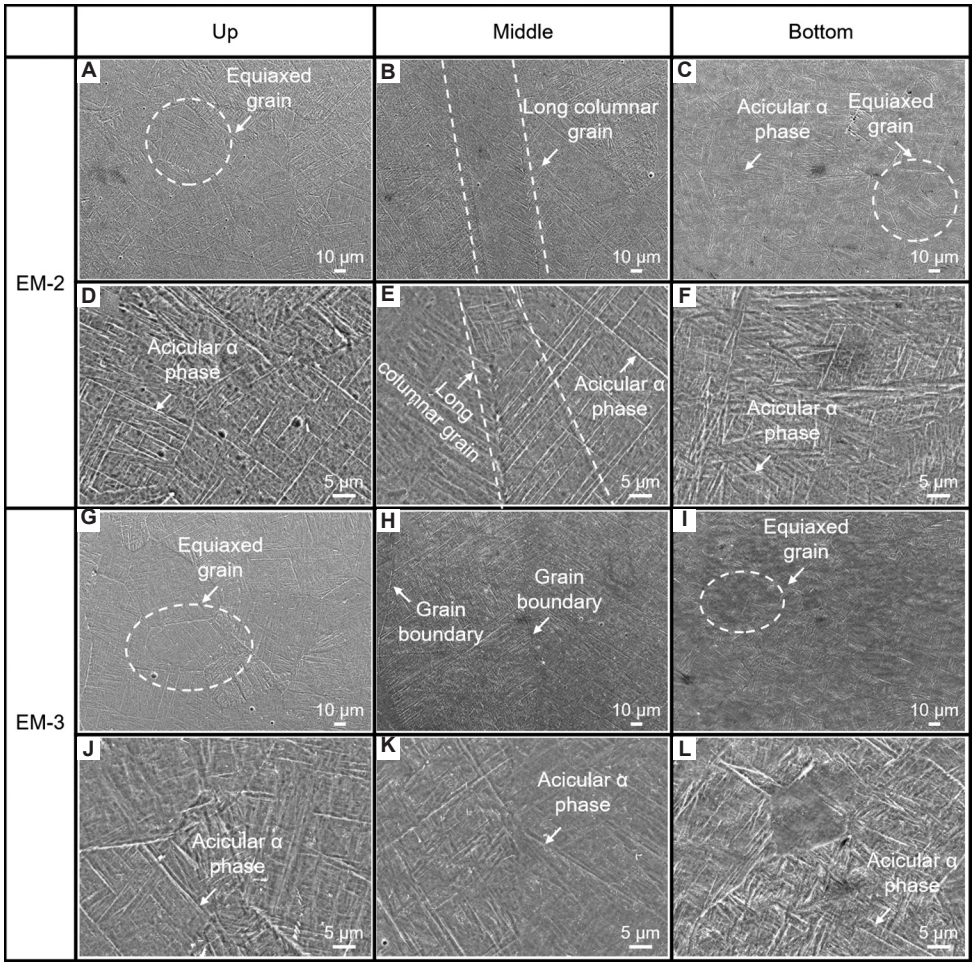

Figure 8. Scanning electron microscopy (SEM) images of the deposition layers for samples EM-2 and EM-3. (A-F) EM-2. (G-L) EM-3. Scale bars: 10 μm (A-C; G-I); 5 μm (D-F; J-L)

of the induced electromagnetic field (Figure 6C). The molten pool flow-induced current is subjected to Lorentz force under the action of the electromagnetic field. The direction of the Lorentz force (F_L) opposes the horizontal velocity component (v_l) of v, inhibiting the flow within the molten pool. In addition, the direction of the molten pool flow shifts, resulting in a new flow velocity (v') under the influence of F_L. This leads to a relatively chaotic and disordered velocity vector distribution within the molten pool (Figure 6D). Due to the inhibiting effect of the Lorentz force (F_L) opposing the horizontal velocity component (v_l) of v, the flow circulation circle driven by the Marangoni force in the molten pool and the corresponding width of the molten pool decreases, which is consistent with the scanning electron microscopy (SEM) results depicted in (Figure 3).

3.3. Microstructural analysis

The microstructure of the deposition layer for different samples is presented in Figures 7 and 8. The microstructure is composed of α- and β-phases in the LMD process. A large number of α-phases are precipitated and intertwined to form a network structure in the rapid cooling process.[37,38] The deposition layer of samples EM-0, EM-1, EM-2, and EM-3 is primarily composed of α- and β-phases. The structure in the upper area of the deposition layer for samples EM-0 (Figure 7A), EM-1 (Figure 7G), EM-2 (Figure 8A), and EM-3 (Figure 8G) is primarily equiaxed grains. The structure at the bottom of the deposition layer for samples EM-0 (Figure 7C), EM-1 (Figure 7I), EM-2 (Figure 8C), and EM-3 (Figure 8I) is composed of both columnar and equiaxed grains. The temperature gradient on the surface of the molten pool is large, and the air medium radiates heat to the surrounding environment, causing the molten pool to radiate heat in various directions, which is conducive to the formation of equiaxed grain. In addition, more α-phases can be observed in the upper area of EM-1 (Figure 7J), EM-2 (Figure 8D), and EM-3 (Figure 8J) compared to EM-0 (Figure 7D). The middle area of the deposition layers for

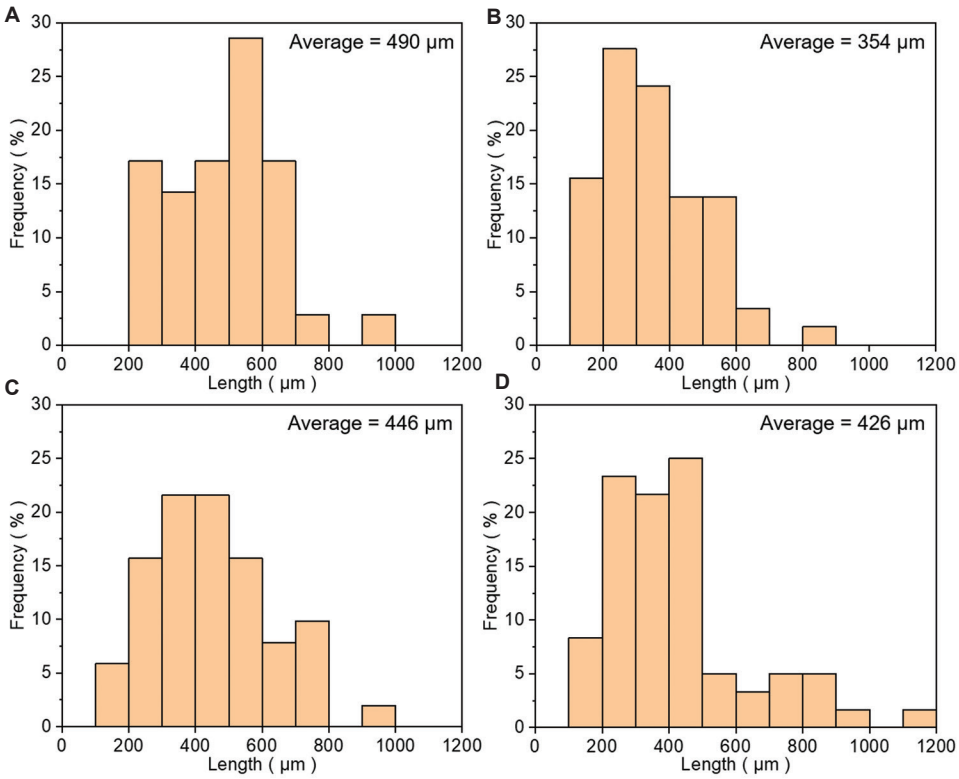

Figure 9. β-grain size distribution of different samples: (A) EM-0; (B) EM-1; (C) EM-2; and (D) EM-3

sample EM-1 (Figure 7B) mainly consists of large columnar grains. This is attributed to the slow heat dissipation rate in the middle area caused by the effect of multiple remelting, which promotes the formation of directionally grown columnar crystals. The coarse columnar crystals were not observed in sample EM-1 under an electromagnetic field of 39.40 mT (Figure 7H), but equiaxed grains were present. Long columnar grains (Figure 8B and E) were present in sample EM-2 as the electromagnetic field intensity increased to 57.12 mT. A similar observation was also noted in Figure 6C.

The flow velocity direction in the molten pool becomes disordered under the action of Lorentz force (Figure 6), thereby interfering with grain growth and refinement. Hence, complete grains cannot be observed; only grain boundaries can be found, evidenced by the coarse grains in sample EM-3 under an electromagnetic field of 72.93 mT (Figure 8H). A similar result is observed in Figure 6D, which can be attributed to the inhibitory effect of the Lorentz force on speed v_1 in the molten pool flow. This inhibition reduces the molten pool cooling rate and promotes grain growth.

From the high-magnification SEM images, samples EM-0 (Figure 7D-F), EM-1 (Figure 7J-L), EM-2 (Figure 8D-F), and EM-3 (Figure 8J-L) exhibit a similar

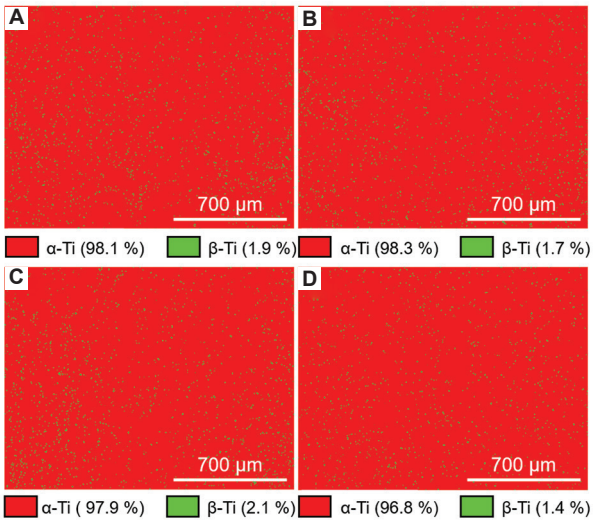

Figure 10. Phase map of different samples: (A) EM-0; (B) EM-1; (C) EM-2; and (D) EM-3. Scale bars: 700 μm

structure. The microstructure comprises a combination of equiaxed and columnar grains, with the small α-phase interwoven to form a network structure. This is attributed to the area at the bottom being in contact with the substrate, as well as the large temperature gradient, both of which facilitate the formation of equiaxed grains. Conversely, the

cooling rate is affected by the effect of multiple remelting, which leads to the formation of columnar grain.

3.4. Texture analysis

ImageJ was used for statistical analysis of the length distribution of β-columnar grain size (Figure 3), and the results are presented in Figure 9. The average length of β-grains in sample EM-0 is 490 μm (Figure 9A). The length of β-columnar grains significantly decreases from 490 μm to 354 μm in an electromagnetic field strength of 39.40 mT. The average length of β-grains in samples EM-1, EM-2, and EM-3 is 354, 446, and 426 μm, respectively, under the electromagnetic field (Figure 9B-D). From the histogram, the frequency of short β-columnar grains (<200 μm) increased to 15.5%, suggesting that the constant electromagnetic field positively influences the grain size of the Ti-6Al-4V alloy in LMD. The elongated large-sized β-columnar grains can be observed in samples EM-2 and EM-3 with increasing electromagnetic field strength. The constant electromagnetic field inhibits the molten pool flow and subsequently shifts its direction (Figure 6). When the flow velocity of the disordered molten pool dominates, the growth of grains is interrupted, and the grains are refined (Figure 9B). The flow velocity slows down, and the cooling rate decreases when the inhibition of molten pool flow is dominant, promoting the growth of grains (Figure 9C and D). The phase map (Figure 10) displays the contents of α-Ti in samples EM-1, EM-2, and EM-3, which changed from the initial 98.1% to 98.3%, 97.9%, and 96.8%, respectively. The phase content revealed no obvious variations, which suggests that the introduction of a magnetic field to the LMD process does not induce a drastic phase transition.

Figure 11 displays the pole figures of the α-phase in the Ti-6Al-4V alloy deposition layer under different

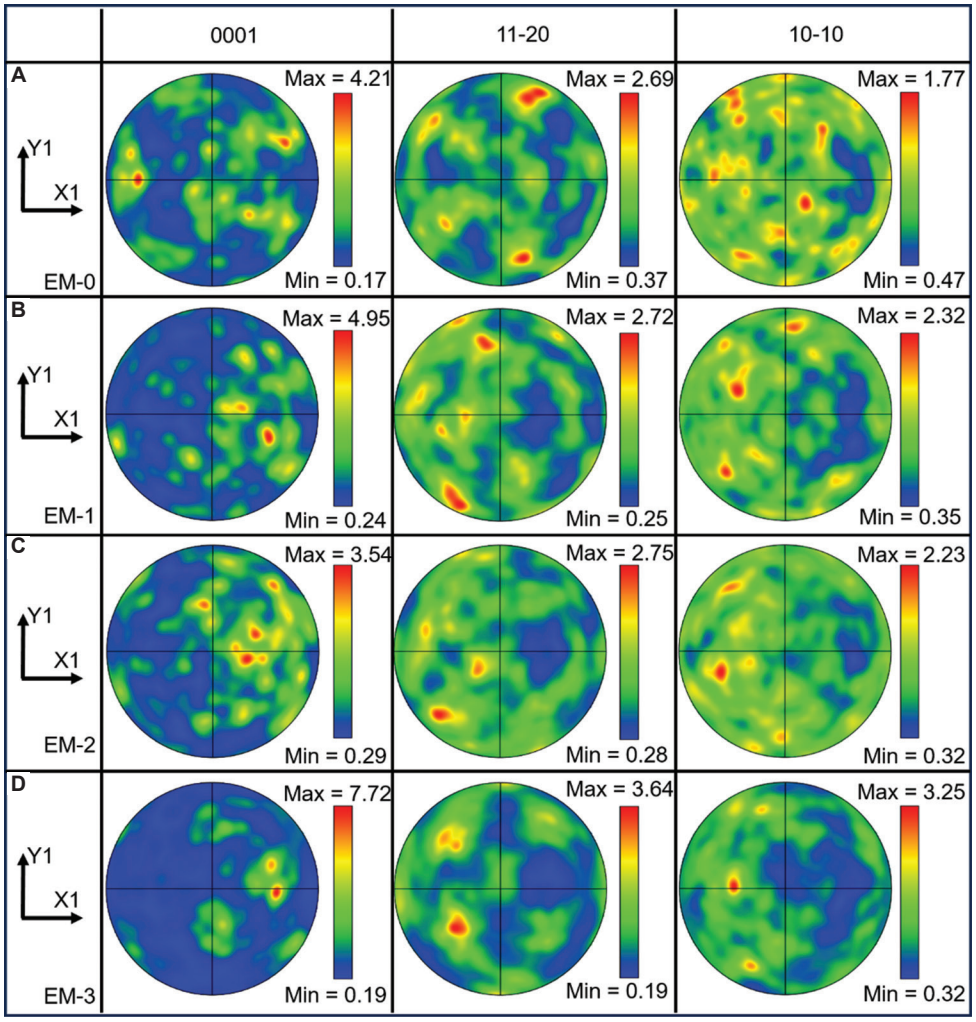

Figure 11. Pole figures of the α-phase in the plane (0001), (11 – 20), and (10 – 10) of Ti-6Al-4V alloy deposition layer: (A) EM-0; (B) EM-1; (C) EM-2; and (D) EM-3

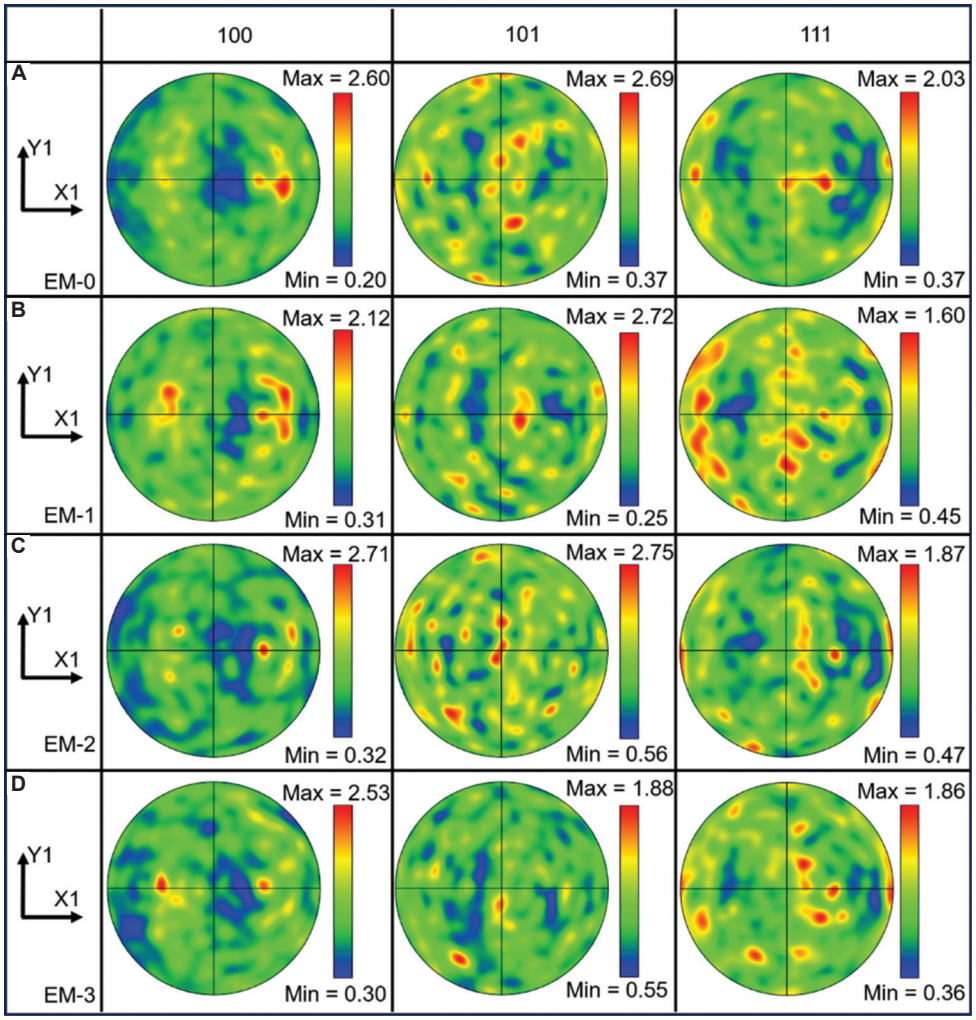

Figure 12. Pole figures of the β-phase in the plane (100), (101), and (111) of Ti-6Al-4V alloy deposition layer: (A) EM-0; (B) EM-1; (C) EM-2; and (D) EM-3

electromagnetic field intensities. The maximum texture intensity in the (0001) plane of samples EM-0, EM-1, EM-2, and EM-3 is 4.21, 4.95, 3.54, and 7.72, respectively. The shift in texture orientation in the (0001) plane toward the X1 direction can be observed as the electromagnetic field is applied to the samples (Figure 11B-D). The maximum texture strength appears in the (0001) plane, which is consistent with the growth of columnar grains along the deposition direction observed in Figure 3. The inhibitory effect of F_L (as depicted in Figure 6) on the flow introduced by the electromagnetic field leads to more α-phase precipitation, and the precipitated α-phase in the same grain presents a close texture orientation, increasing the texture intensity.[39]

Figure 12 depicts the pole figures of the β-phase in the Ti-6Al-4V alloy deposition layer under different electromagnetic field intensities. The maximum texture intensity of the β-phase in the (101) plane of samples EM-0, EM-1, and EM-2 is 2.69, 2.72, and 2.75, respectively. The maximum texture intensity of the β-phase in the (100) plane of sample EM-3 is 2.53. The strong texture can be observed in the X1 direction in the (100) plane for samples EM-0, EM-1, EM-2, and EM-3. The texture distribution is uniform in the (100) plane when the electromagnetic field intensity is 39.40 mT (Figure 12B). The directional growth of β-grains is affected by F_L in the shifting flow direction (as depicted in Figure 6), resulting in the formation of equiaxed grains and uniform texture distribution. Long columnar β-grains (Figure 3C) and coarse β-grains (Figure 3D) are formed with increasing electromagnetic field intensity. Segregation of the texture distribution in the (100) plane is observed in Figure 12C and D.

3.5. Hardness analysis

Figure 13 displays the hardness distribution of samples, analyzed using the hardness test depicted in Figure 2E.

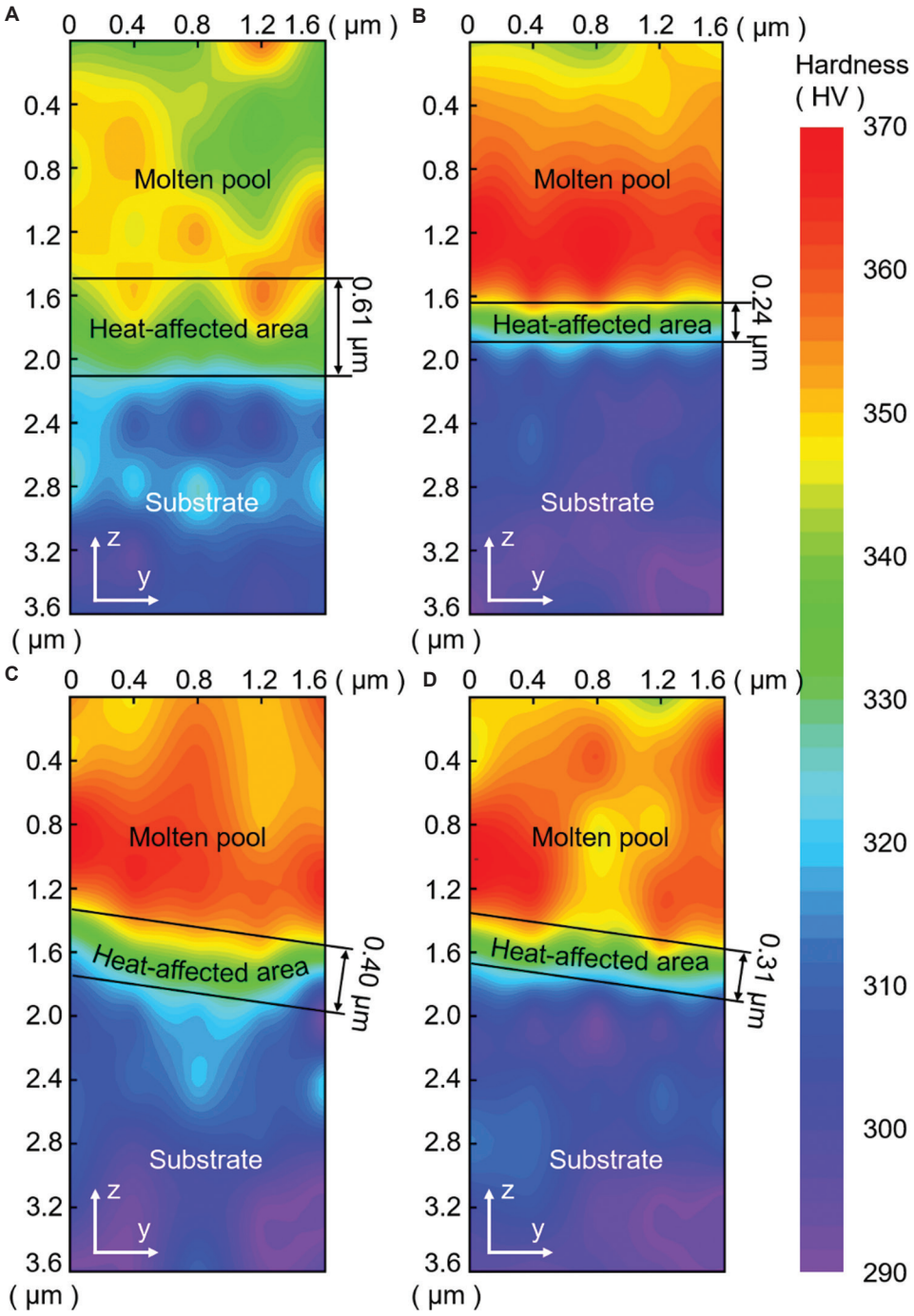

Figure 13. Hardness distribution of deposition layers for different samples: (A) EM-0; (B) EM-1; (C) EM-2; and (D) EM-3. z represents the deposition direction, and y represents the scanning direction

The results indicate that the distribution range of hardness in the molten pool, heat-affected area, and substrate area is 350 – 370, 320 – 350, and 290 – 320 HV, respectively. The observation corresponded to the large number of tiny α-phases that are precipitated during the cooling process of LMD, subsequently increasing the hardness of the sample via fine grain strengthening.[40] The hardness distribution in the heat-affected area near the deposition layer is affected by the thermal radiation of LMD, whereby the hardness distribution gradually decreases from the heat-affected areas to the substrate. The width of the heat-affected area of samples EM-0, EM-1, EM-2, and EM-3 is 0.61, 0.24, 0.40,

and 0.31 μm, respectively. This width is reduced when the electromagnetic field intensity is 39.40 mT. The uniformity of hardness distribution in the molten pool area is the most obvious, indicating enhanced uniformity of the surface structure. In addition, it can be observed that the hardness in the molten pool of samples EM-1 (Figure 13B), EM-2 (Figure 13C), and EM-3 (Figure 13D) increased with the effect of electromagnetic field compared to sample EM-0 (Figure 13A).

The F_L exhibits an inhibitory effect on the flow of the molten pool after the introduction of an electromagnetic field, which reduces heat dissipation and increases the maximum temperature. Further precipitation of the α-phase was observed in samples EM-1 (Figure 7J), EM-2 (Figure 8D), and EM-3 (Figure 8J) during cooling compared to EM-0 (Figure 7D), increasing the overall hardness. Due to the disordered molten pool flow caused by F_L in sample EM-1, thermal radiation spreads evenly, resulting in a consistent microstructure. The decreased cooling rate caused by F_L in samples EM-2 and EM-3 leads to the observed differences in microstructure, i.e., long columnar grain in EM-2 (Figure 3C) and coarse grain in EM-3 (Figure 3D).

4. Conclusion

This study investigated the effect of *in situ* manipulation of the electromagnetic field on the microstructure and hardness of titanium alloy during LMD. The microstructure, texture orientation, and hardness of the Ti-6Al-4V alloy were investigated via a combination of experiments and numerical simulation. The key findings are summarized as follows:

(i) The width, height, and melt depth of the deposition layer were significantly reduced under the electromagnetic field. The electromagnetic field inhibits the heat transfer and mass transport flow from the center of the laser beam to the surroundings, thereby reducing the size of the molten pool

(ii) The numerical simulation results indicated that the maximum flow velocity in the molten pool was 0.58 m/s without the electromagnetic field, whereas the maximum flow velocity in the molten pool region was 0.41 m/s under an electromagnetic field intensity of 39.40 mT; i.e., a 29% decrease. In addition, the velocity vector of the molten pool flow distribution became disordered

(iii) The average length of β-grains was 490 μm without the electromagnetic field, which was decreased to 354 μm under an electromagnetic field intensity of 39.40 mT. The elongated large β-columnar grains were also observed with increasing electromagnetic field intensity

(iv) The effect mechanisms of the Lorentz force induced by electromagnetic field include the directional flow velocity in the molten pool becoming disordered under the influence of the Lorentz force, interfering with grain growth and refinement; and the restraining effect of the Lorentz force on the molten pool flow that reduced the cooling rate, thereby promoting grain growth.

Based on the above results, it can be concluded that the *in situ* manipulation of the electromagnetic field via Lorentz force during LMD is significant, offering a novel and effective approach for controlling the microstructure and mechanical properties of titanium alloys.

Acknowledgments

None.

Funding

This work was financially supported by the Major Research Plan of the National Natural Science Foundation of China (Grant No. 92266102), National Natural Science Foundation of China (No. 52271135), Innovation Funding Project of National Engineering and Research Center for Commercial Aircraft Manufacturing (COMAC-SFGS-2022-1871), Overseas Expertise Introduction Project for Discipline Innovation (B17034), and Innovative Research Team Development Program of Ministry of Education of China (IRT_17R83).

Conflicts of interest

Both Lechun Xie and Liqiang Wang serve as the Editorial Board Members of the journal but were not involved in any way (directly or indirectly) in the editorial and peer-review process conducted for this paper. Other authors declare they have no competing interests.

Author contributions

Conceptualization: Lechun Xie, Yan Wen
Data curation: Chang Liu, Yongjian Wu
Investigation: Chang Liu, Yongjian Wu
Methodology: Lechun Xie
Supervision: Lechun Xie
Writing - original draft: Chang Liu, Yongjian Wu
Writing - review & editing: Jian Zhou, Yan Wen, Liqiang Wang, Lechun Xie

Ethics approval and consent to participate

Not applicable

Consent for publication

Not applicable.

Availability of data

The data that support the findings of this study are presented in the paper. They are also available from the corresponding authors upon reasonable request.

References

1. Tan C, Li R, Su J, *et al*. Review on field assisted metal additive manufacturing. *Int J Mach Tools Manuf*. 2023;189:104032.

   doi: 10.1016/j.ijmachtools.2023.104032

2. Zhang M, Wang B, Li X, Jiao G, Fang X, Huang H. Grain refinement of NiTi alloys during ultrasound-assisted wire-arc directed energy deposition. *Virtual Phys Prototyp*. 2024;19(1):e2289465.

   doi: 10.1080/17452759.2023.2289465

3. Santos EC, Shiomi M, Osakada K, Laoui T. Rapid manufacturing of metal components by laser forming. *Int J Mach Tools Manuf*. 2006;46(12):1459-1468.

   doi: 10.1016/j.ijmachtools.2005.09.005

4. Thompson SM, Bian L, Shamsaei N, Yadollahi A. An overview of direct laser deposition for additive manufacturing; Part I: Transport phenomena, modeling and diagnostics. *Addit Manuf*. 2015;8:36-62.

   doi: 10.1016/j.addma.2015.07.001

5. Wang G, Zhao H, Liang H, Deng C, Ma W. Multi-objective optimisation of process parameters for laser-based directed energy deposition of a mixture of H13 and M2 steel powders on 4Cr5Mo2SiV1 steel. *Virtual Phys Prototyp*. 2024;19(1):e2290184.

   doi: 10.1080/17452759.2023.2290184

6. Su J, Li Q, Teng J, *et al*. Programmable mechanical properties of additively manufactured novel steel. *Int J Extrem Manuf*. 2024;7(1):015001.

   doi: 10.1088/2631-7990/ad88bc

7. Haley J, Karandikar J, Herberger C, MacDonald E, Feldhausen T, Lee Y. Review of *in situ* process monitoring for metal hybrid directed energy deposition. *J Manuf Processes*. 2024;109:128-139.

   doi: 10.1016/j.jmapro.2023.12.004

8. Azarniya A, Colera XG, Mirzaali MJ, *et al*. Additive manufacturing of Ti-6Al-4V parts through laser metal deposition (LMD): Process, microstructure, and mechanical properties. *J Alloys Compounds*. 2019;804:163-191.

   doi: 10.1016/j.jallcom.2019.04.255

9. Choi YR, Sun SD, Liu Q, Brandt M, Qian M. Influence of deposition strategy on the microstructure and fatigue properties of laser metal deposited Ti-6Al-4V powder on Ti-6Al-4V substrate. *Int J Fatigue*. 2020;130:105236.

   doi: 10.1016/j.ijfatigue.2019.105236

10. Zhou X, Xu D, Geng S, *et al*. Mechanical properties, corrosion behavior and cytotoxicity of Ti-6Al-4V alloy fabricated by laser metal deposition. *Mater Characterization*. 2021;179:111302.

    doi: 10.1016/j.matchar.2021.111302

11. Dinda GP, Dasgupta AK, Mazumder J. Laser aided direct metal deposition of Inconel 625 superalloy: Microstructural evolution and thermal stability. *Mater Sci Eng A*. 2009;509(1):98-104.

    doi: 10.1016/j.msea.2009.01.009

12. Rao J, Leong Sing S, Liu P, Wang J, Sohn H. Non-destructive testing of metal-based additively manufactured parts and processes: A review. *Virtual Phys Prototyp*. 2023;18(1):e2266658.

    doi: 10.1080/17452759.2023.2266658

13. Chen C, Sun H, Zhang Z, Zhao Y, Liu Y, Chen H. Grain structure control of TC11 alloy in laser direct energy deposition by a static magnetic field. *Materialia*. 2024;38:102267.

    doi: 10.1016/j.mtla.2024.102267

14. Chen C, Zhang K, Zhao R, *et al*. Laser powder bed fusion of GH4099 Ni-based superalloy under a static magnetic field with tailored microstructure and enhanced mechanical performance. *Virtual Phys Prototyp*. 2024;19(1):e2411023.

    doi: 10.1080/17452759.2024.2411023

15. Qin Y, Liao Y, Li G, Cui J, Jiang H. Numerical simulation and parameter analysis of electromagnetic riveting process for Ti-6Al-4V titanium rivet. *Coatings*. 2021;11(8):878.

    doi: 10.3390/coatings11080878

16. Li Y, Xu W, Su Q, Wang Q. Microstructure and properties of Ti-Al coating on titanium alloy surface assisted by electromagnetic field. *ACS Omega*. 2024;9(46):46176-46191.

    doi: 10.1021/acsomega.4c06757

17. Song X, Qi H, Li S, Hu Y, Yang W, Li Z. Effect of cryogenic coupled magnetic field treatment on the microstructure and mechanical properties on Ti-6Al-4V titanium alloy. *Mater Today Commun*. 2024;40:109417.

    doi: 10.1016/j.mtcomm.2024.109417

18. Bachmann M, Avilov V, Gumenyuk A, Rethmeier M. Numerical assessment and experimental verification of the influence of the Hartmann effect in laser beam welding processes by steady magnetic fields. *Int J Therm Sci*. 2016;101:24-34.

    doi: 10.1016/j.ijthermalsci.2015.10.030

19. Velde O, Gritzki R, Grundmann R. Numerical investigations of Lorentz force influenced Marangoni convection relevant to aluminum surface alloying. *Int J Heat Mass Transfer*. 2001;44(14):2751-2762.

doi: 10.1016/S0017-9310(00)00299-4

20. Kelly SM, Kampe SL. Microstructural evolution in laser-deposited multilayer Ti-6Al-4V builds: Part II. Thermal modeling. *Metall Mater Transact A*. 2004;35(6):1869-1879.

doi: 10.1007/s11661-004-0094-8

21. Wirth F, Wegener K. A physical modeling and predictive simulation of the laser cladding process. *Addit Manuf*. 2018;22:307-319.

doi: 10.1016/j.addma.2018.05.017

22. Hirt CW, Nichols BD. Volume of fluid (VOF) method for the dynamics of free boundaries. *J Comput Phys*. 1981;39(1):201-225.

doi: 10.1016/0021-9991(81)90145-5

23. Pinkerton AJ. Advances in the modeling of laser direct metal deposition. *J Laser Appl*. 2014;27(S1):S15001.

doi: 10.2351/1.4815992

24. Sun Z, Guo W, Li L. Numerical modelling of heat transfer, mass transport and microstructure formation in a high deposition rate laser directed energy deposition process. *Addit Manuf*. 2020;33:101175.

doi: 10.1016/j.addma.2020.101175

25. Wei S, Wang G, Shin YC, Rong Y. Comprehensive modeling of transport phenomena in laser hot-wire deposition process. *Int J Heat Mass Transfer*. 2018;125:1356-1368.

doi: 10.1016/j.ijheatmasstransfer.2018.04.164

26. Morville S, Carin M, Peyre P, *et al*. 2D longitudinal modeling of heat transfer and fluid flow during multilayered direct laser metal deposition process. *J Laser Appl*. 2012;24:032008.

doi: 10.2351/1.4726445

27. Gan Z, Liu H, Li S, He X, Yu G. Modeling of thermal behavior and mass transport in multi-layer laser additive manufacturing of Ni-based alloy on cast iron. *Int J Heat Mass Transfer*. 2017;111:709-722.

doi: 10.1016/j.ijheatmasstransfer.2017.04.055

28. Gan Z, Yu G, He X, Li S. Surface-active element transport and its effect on liquid metal flow in laser-assisted additive manufacturing. *Int Commun Heat Mass Transfer*. 2017;86:206-214.

doi: 10.1016/j.icheatmasstransfer.2017.06.007

29. Arrizubieta JI, Lamikiz A, Klocke F, Martínez S, Arntz K, Ukar E. Evaluation of the relevance of melt pool dynamics in laser material deposition process modeling. *Int J Heat Mass Transfer*. 2017;115:80-91.

doi: 10.1016/j.ijheatmasstransfer.2017.07.011

30. Bai X, Colegrove P, Ding J, *et al*. Numerical analysis of heat transfer and fluid flow in multilayer deposition of PAW-based wire and arc additive manufacturing. *Int J Heat Mass Transfer*. 2018;124:504-516.

doi: 10.1016/j.ijheatmasstransfer.2018.03.085

31. Saldi ZS. *Marangoni Driven Free Surface Flows in Liquid Weld Pools*. The Netherlands: Delft University of Technology; 2012. Available from: https://resolver.tudelft.nl/uuid:8401374b-9e9c-4d25-86b7-fc445ec73d27

32. Spiegel EA, Veronis G. On the boussinesq approximation for a compressible fluid. *Astrophys J*. 1960;131:442.

doi: 10.1086/146849

33. Boivineau M, Cagran C, Doytier D, *et al*. Thermophysical properties of solid and liquid Ti-6Al-4V (TA6V) alloy. *Int J Thermophys*. 2006;27(2):507-529.

doi: 10.1007/PL00021868

34. Hagqvist P, Sikström F, Christiansson AK. Emissivity estimation for high temperature radiation pyrometry on Ti-6Al-4V. *Measurement*. 2013;46(2):871-880.

doi: 10.1016/j.measurement.2012.10.019

35. Soylemez E, Beuth J, Taminger K. Controlling Melt Pool Dimensions Over a Wide Range of Material Deposition Rates in Electron Beam Additive Manufacturing. In: *International Solid Freeform Fabrication Symposium*; 2010.

doi: 10.26153/tsw/15221

36. Tang Q, Pang S, Chen B, Suo H, Zhou J. A three dimensional transient model for heat transfer and fluid flow of weld pool during electron beam freeform fabrication of Ti-6-Al-4-V alloy. *Int J Heat Mass Transfer*. 2014;78:203-215.

doi: 10.1016/j.ijheatmasstransfer.2014.06.048

37. Liu C, Xie L, Qian D, *et al*. Microstructure evolution and mechanical property response of TC11 titanium alloy under electroshock treatment. *Mater Design*. 2021;198:109322.

doi: 10.1016/j.matdes.2020.109322

38. Wen Y, Sun X, Zhou J, *et al*. Influence of electroshocking treatment on microstructure and mechanical properties of Ti-6.5 Al-3.5 Mo-1.5 Zr-0.3 si thin-wall specimen manufactured by laser melting deposition. *Acta Metall Sin* (*Engl Lett*). 2024;37(1):145-158.

doi: 10.1007/s40195-023-01592-x

39. Liu C, Yin F, Xie L, *et al*. Evolution of grain boundary and texture in TC11 titanium alloy under electroshock treatment. *J Alloys Compounds*. 2022;904:163969.

doi: 10.1016/j.jallcom.2022.163969

40. Zhou J, Liu C, Wu Y, *et al*. Evolution mechanism of grain orientation and texture distribution of Ti-6.5 Al-3.5 Mo-1.5 Zr-0.3 Si alloy under electroshocking treatment. *J Mater Res Technol*. 2023;25:5693-5704.

doi: 10.1016/j.jmrt.2023.07.028

ACCSCIENCE PUBLISHING

Materials Science in Additive Manufacturing

ORIGINAL RESEARCH ARTICLE

Selective laser melting of ferritic/martensitic oxide dispersion-strengthened steel: Processing, microstructure, and mechanical properties

Maria Zaitceva*, Artem Borisov, Anatoliy Popovich, and Vadim Sufiiarov

Institute of Machinery, Materials and Transport, Peter the Great St. Petersburg Polytechnic University, Saint Petersburg, Russia

Abstract

Oxide dispersion-strengthened (ODS) ferritic/martensitic steels have emerged as a promising structural material for nuclear power applications due to their high heat resistance. However, the fabrication of complex ODS steel components remains a significant challenge. T his study presents the influence of the main selective laser melting process parameters and heat treatment on the densification, microstructure, and tensile properties at room and elevated temperatures of high chromium ferritic/martensitic ODS steel strengthened with 0.25 wt.% yttrium oxide (Y_2O_3). The optimization of process parameters and platform pre-heating enabled the production of parts with a density above 98%. The application of pre-heating allowed for higher scanning speeds to be used to achieve similar relative density and avoid cracking. Partial recrystallization after heat treatment was noted, affecting grain morphology by increasing equiaxedness and decreasing size. X-ray analysis was employed to determine the phase composition. However, the results were ambivalent and required confirmation by other methods. The addition of 0.25 wt.% Y_2O_3 resulted in an ultimate tensile strength value of 978 MPa for the as-built material at room temperature. At elevated temperatures, the properties are comparable to those of the base steel, indicating the necessity for further research.

Keywords: Selective laser melting; Oxide dispersion-strengthened steel; Tensile testing; Heat treatment; Additive manufacturing; ODS steel; Laser powder bed fusion

***Corresponding author:**
Maria Zaitceva
(zajtsevamya@yandex.ru)

Citation: Zaitceva M, Borisov A, Popovich A, Sufiiarov V. Selective laser melting of ferritic/martensitic oxide dispersion-strengthened steel: Processing, microstructure and mechanical properties. *Mater Sci Add Manuf.* 2025;4(1):025060004. doi: 10.36922/MSAM025060004

Received: February 6, 2025

1st revised: February 28, 2025

2nd revised: March 11, 2025

Accepted: March 12, 2025

Published online: March 24, 2025

1. Introduction

Ferritic/martensitic oxide dispersion-strengthened (ODS) steels are regarded as promising candidates for structural materials in next-generation nuclear reactors. This is attributed to their high radiation resistance and acceptable mechanical properties at elevated temperatures.[1] The desirable properties of ODS steels result from the presence of stable nanosized oxide particles, which inhibit grain boundary and dislocation migration, thereby maintaining the material's microstructural stability during service. In addition, the interfaces between matrix and dispersed oxides can serve as sinks for radiation-induced defects, which result in increasing irradiation resistance.[2] ODS steels based on high chromium ferritic/martensitic steels containing 9 – 12 wt.% Cr have garnered significant interest due to their proven performance in past fast reactors. Furthermore, ferritic/martensitic steels are highly resistant to void

swelling,[3] which is quite necessary for nuclear reactor application.

At present, the most extensively studied and widely utilized method of strengthening involves the incorporation of yttrium-based nano-oxides. Numerous studies have demonstrated the efficacy of yttrium oxide (Y_2O_3) additions in enhancing the mechanical strength of steels and various other alloys. This enhancement in strength is accompanied by an improvement in resistance to radiation-induced swelling under exposure to fission ions or neutrons. Furthermore, dispersion strengthening through nano-oxides significantly increases the hardness of the matrix material, thereby contributing to an improvement in wear resistance.[4] The most common addition of oxides is in the order of 0.25 – 1.0 wt.%. In addition to yttrium, other elements may be added to form complex oxides such as $Y_nX_mO_p$, where X = Ti, Al, Zr, Hf, V, Si, or Ta.[5,6] The formation enthalpy of this type of oxide is lower than that of Y_2O_3.

The fabrication of ODS steels remains a significant challenge. The most prevalent method of production involves powder metallurgy, specifically mechanical alloying.[7-10] Creating products with complex geometries using powder metallurgy methods is an expensive and time-consuming process. One of the most common processes used to produce ODS steels is hot isostatic pressing (HIP)[2,11,12] and spark plasma sintering.[13-15] However, the use of these techniques is advisable in cases of production of simple and symmetrical shapes.

Another critical limitation is the relatively poor weldability of ODS steels, which increases the cost and complexity of manufacturing components with intricate geometries. Consequently, there is growing interest in exploring the feasibility of producing ODS steels through additive manufacturing (AM) techniques. AM has already shown itself to be a state-of-the-art manufacturing process that allows the production of complex-shaped products with high mechanical properties. One of the most commonly used technologies for the production of metal products is selective laser melting (SLM). The process consists of layer-by-layer laser processing of powder material according to a CAD model. SLM technology is already widely used in areas such as aerospace, medicine, and turbine engineering. An important feature of the SLM process is the high cooling rates (10^3 – 10^8 K/s).[16]

A number of published studies demonstrate the feasibility of producing ODS steels by SLM.[1,5] A study suggests that optimization of the process parameters could lead to a density of more than 98%.[17] The results also showed the possibility of obtaining a material with a uniform distribution of nanosized oxides. However, the size of oxides in the materials obtained by SLM is larger (in the order of 30 – 60 nm), compared to particles obtained by powder metallurgy methods (typically 1 – 10 nm).[18-20] The size of the yttrium-based dispersoids influences coherency, and the size above 20 nm results in agglomeration and coarsening,[21] which reduces the positive effect of their implementation.

A notable challenge associated with the use of powders derived from mechanical alloying is their splintered morphology,[22] resulting from the high mechanical stresses applied during the process. This irregular particle shape leads to poor flowability, which may be a limitation for the applications of mechanically alloyed powders in AM.[23] Furthermore, studies have demonstrated that the morphology and particle size distribution of the powder material significantly influences the final properties of products fabricated through AM methods. To address these limitations, mechanically alloyed powders require spheroidization before use.[24] The plasma spheroidization process involves a melting stage during which oxide particles tend to coagulate and migrate to the surface of the molten material due to their relatively lower density compared to the metallic matrix. Consequently, the resulting spherical powder exhibits non-uniform oxide dispersion,[24] which can negatively impact the mechanical properties of the final product.

For the production of ODS steels by SLM, not only can mechanically alloyed powders be used, but also various *in situ* synthesis methods when oxides are forming during the printing process. In Jia *et al.*'s study,[25] pre-alloyed powders were used for the *in situ* synthesis of nanoparticles in ODS steel during SLM by controlling the partial pressure of oxygen to prevent the abnormal growth of particles. This approach resulted in the formation of a microstructure characterized by finer nanoparticles, a higher volume fraction, and a more uniform spatial distribution and size consistency compared to the majority of ODS steels manufactured using SLM with mechanically alloyed powders. The influence of the properties of *in situ* formed nitride and oxide particles in the ODS steel produced by laser powder bed fusion in a nitrogen-rich atmosphere (with Y_2O_3 = 0.45 wt.%) was studied by Cakmak *et al.*[26] The incorporation of nanosized Y_2O_3 reduces the length of typical for SLM as-built parts columnar grains (from 70 μm to 40 μm).[26] In addition to Y_2O_3, Al-O aluminum oxides, and Y-Al-O yttrium aluminum oxides were observed in the microstructure. A significant challenge in the production of ODS steel through *in situ* synthesis during the SLM process lies in the inherent complexity of the technological workflow. This complexity necessitates precise monitoring and control of all process parameters

to ensure the consistency and stability of the material's quality.

In addition to mechanical alloying, soft-mixing techniques are employed to produce ODS steels by SLM.[27] This approach facilitates uniform adhesion of oxide particles onto the surface of steel powders, in contrast to alloying processes involving dispersed particles of the matrix material. By maintaining the original spherical morphology of the powder particles, the soft-mixing method ensures good flowability. The advantage of this method of powder preparation is the relatively simple and fast mixing process compared with mechanical alloying. Zhai *et al.*[28] investigated the influence of interface wettability of 316L ODS steel strengthened by Y_2O_3 on tensile properties. Poor interface wettability of the nanoparticles and the basic steel was the reason for the Y_2O_3 agglomerations forming, which led to internal defects. Besides, the increases in yield strength (YS) and ultimate tensile strength (UTS) were neglectable, and the nanoparticle agglomeration significantly decreased the elongation. The results of the investigation and comparison of tensile properties and tribological behavior of the two alloys (basic and ODS) fabricated by SLM showed a significant reduction in wear rate (by 51%) when 0.3 wt.% Y_2O_3 nanoparticles were added compared to the matrix alloy.[1]

The acoustic mixing method has been successfully utilized to achieve a uniform distribution of oxides in a NiCoCr medium-entropy alloy.[23] The introduction of 1 wt.% Y_2O_3 led to a significant enhancement in mechanical properties, as confirmed by tensile testing. Notably, the addition of Y_2O_3 resulted in a marked improvement in strength, particularly at elevated temperatures, highlighting the efficacy of this approach in optimizing high-temperature performance.

Presently, the details of AM processes of high chromium ferritic/martensitic steels remain underexplored. These steels are susceptible to cracking, which complicates their production by methods such as SLM. There are virtually no studies devoted to the investigation of the production of ODS steels based on high-chromium ferritic/martensitic steels, despite their promising application in nuclear power engineering.

This research is aimed at studying the possibilities of fabrication of ferritic/martensitic ODS steel by SLM and analyzing the structure and tensile properties of the obtained material, including at elevated temperatures (720°C). The present study also employed platform pre-heating as a method to mitigate cracking and enhance material density. Given the significance of this steel in the context of next-generation reactor applications, the tensile properties were assessed within the anticipated operational temperature range. This study will serve as a basis for subsequent studies aimed at studying the specifics of the production of high chromium ferritic-martensitic ODS steels.

2. Materials and methods

2.1. Materials

In this study, ferritic-martensitic steel powder with the chemical composition presented in Table 1 was employed as the base material. The base gas atomized ferritic/martensitic steel powder had a particle size distribution of 22 – 63 μm.

For the production of ODS steel through SLM, the base steel powder was mixed with 0.25 wt.% Y_2O_3 using an acoustic mixing process. The acoustic mixing process was performed on a laboratory unit. The particle size distribution study was carried out on an Analysette 22 NanoTec plus analyzer (Fritsch GmbH, Idar-Oberstein, Germany) operating in the particle measurement range from 0.01 to 2000 μm. The flowability of the powder was determined using a Hall flowmeter.

2.2. SLM and heat treatment

The SLM process was performed on a 3DLAM Mid system (Biograd CJSC, St. Petersburg, Russia) equipped with a platform pre-heating module capable of achieving temperatures up to 300°C and a laser with a maximum output power of 500 W. To optimize the process parameters, two sets of samples were fabricated: One without the platform pre-heating and another with the platform pre-heating of 300°C. Each set comprised 20 cubic samples (10 mm × 10 mm × 10 mm) produced directly on the baseplate without supporting structures. Scanning speed and laser power were systematically varied, while the hatching distance was maintained at 120 μm, and the layer thickness was fixed at 30 μm. The applied SLM process parameters are detailed in Table 2. A stripe-hatching pattern with a 67° rotation between layers was employed to enhance mechanical properties and minimize residual stresses.[29]

Since the energy input to the material significantly affects melt pool formation and the properties of the resulting structure, the volumetric energy density (*VED*, J/mm^3) was calculated using the following equation:

$$VED = P/(v \times h \times t), \quad \text{(I)}$$

where P = laser power (W); v = scanning speed (mm/s); h = hatch distance (mm); and t = layer thickness (mm).

The typical heat treatment mode for this material involves quenching at 1050 – 1100°C for 30 min, followed

Table 1. Chemical composition of the base ferritic/ martensitic steel

Element	C	Si	Mn	Cr	Ni	Mo	Nb	V	P	Fe
wt. %	0.12	0.2	0.2	12.1	0.1	1.3	0.35	0.2	0.001	Bal.

Table 2. Process parameters of selective laser melting

Parameters	Range
Laser power	150 – 225 W
Scanning speed	420 – 820 mm/s
Hatch distance	120 μm
Layer thickness	30 μm

by high-temperature annealing at 720°C for 60 – 180 min.[30] In the present study, the heat treatment was performed in a vacuum at 1050°C for 30 min with subsequent quenching, followed by high-temperature annealing at 720°C for 60 min. The heat treatment process was carried out using a vacuum furnace Carbolite Gero LHTW 200 – 300/22-1G (Carbolite Gero Ltd., Derbyshire, UK).

2.3. Characterization

Subsequent to the printing process, the samples were separated from the platform by wire-cut electrical discharge machining. The estimation of the density of all samples was performed by the Archimedes method. Cubic samples with dimensions of 10 mm × 10 mm × 10 mm were prepared for microstructural investigations, phase composition analysis, and microhardness testing. The samples were pressed into epoxy resin and then subjected to grinding and mechanical polishing. Porosity and inner defects fraction were calculated of the pore fraction in relation to the whole image plane using ImageJ image analysis software on optical microscope images with ×50 magnification. The grain size estimation was performed using optical micrographs along the building direction.

Phase analysis was conducted using a Bruker D8 Advance X-ray diffractometer (XRD; Bruker Corporation, Billerica, MA, USA) with Cu-Kα radiation (a = 1.5418 Å) in the range 2θ = 30° – 100°. A scanning interval of 0.02° was used. Before microstructural analysis, the specimens were etched using a 3:1 solution of hydrochloric acid and nitric acid. The microstructural characterization was carried out utilizing a Leica DMI5000 optical microscope (Leica Microsystems GmbH, Wetzlar, Germany) and a Tescan Mira3 LMU scanning electron microscope (SEM) (TESCAN GROUP, Brno, Czech Republic).

The hardness of the samples was evaluated using a Buehler Micromet 5103 hardness tester (Buehler Ltd., USA) employing the Vickers hardness method. The tests were carried out at a load of 10 N with a dwell time of 5 s. Uniaxial tensile tests were performed on three specimens for each condition to determine the tensile strength, YS, and relative elongation of the specimens. The specimens' blank parts were initially printed, heat-treated, and then machined. These tests were performed under ambient conditions using a Zwick/Roell z100 tensile testing machine. Tensile testing at an elevated temperature of 720 ± 10°C was carried out using a Zwick/Roell z050 machine (ZwickRoell GmbH & Co., Ulm, Germany). For all the specimens, tests were carried out under a crosshead displacement velocity of 0.8 mm/min on the elastic section, and 2 mm/min on the plastic section. An examination of the fractured surfaces from the tensile tests was conducted using SEM.

3. Results and discussion

3.1. Material preparation

The application of acoustic mixing facilitated the production of steel powder with a spherical morphology and uniformly distributed oxide particles on the surface, as demonstrated by the SEM image (Figure 1). The presence of nanosized oxides on the particle surfaces resulted in a slight reduction in the powder's flowability, from 12 s/50 g to 16 s/50 g. Zhai *et al.*[28] reported the flowability of ODS 316L-Y_2O_3 steel powder was not decreased after low-energy ball milling. Nevertheless, the outcome can be ascribed to the diminished wettability and flowability of Y_2O_3, which, being located on the surface of the base material particles, predictably reduces the flowability of the obtained material. However, flowability remains for utilization in the SLM process.

3.2. The influence of SLM process parameters on relative density

The effects of laser power and scanning speed on relative density are presented in Figure 2. Laser power varied in the range from 150 to 225 W. As the laser power increases, the relative density increases until it reaches a threshold value of VED. In general, the density of samples fabricated using laser powers of 200 W and 225 W is higher compared to those produced with laser powers of 150 W and 175 W. Scanning speed varied in the range from 420 to 820 mm/s. Contrary to the influence of laser power, increasing scanning speed resulted in lower density. A similar tendency has been observed in another study.[31]

When samples were fabricated without platform pre-heating, all of them exhibited horizontal surface cracks, caused by thermal stresses arising from high temperature gradients during the SLM process. To address this issue, a set of samples was fabricated using a platform pre-heating

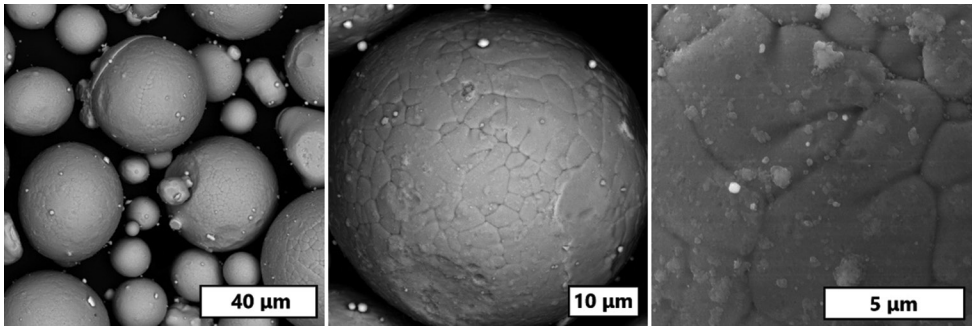

Figure 1. SEM-BSE images of the mixed ODS-steel powder. Magnification: 2000×, 5000×, 20000×
Abbreviations: BSE: Backscattered electrons; SEM: Scanning electron microscopy.

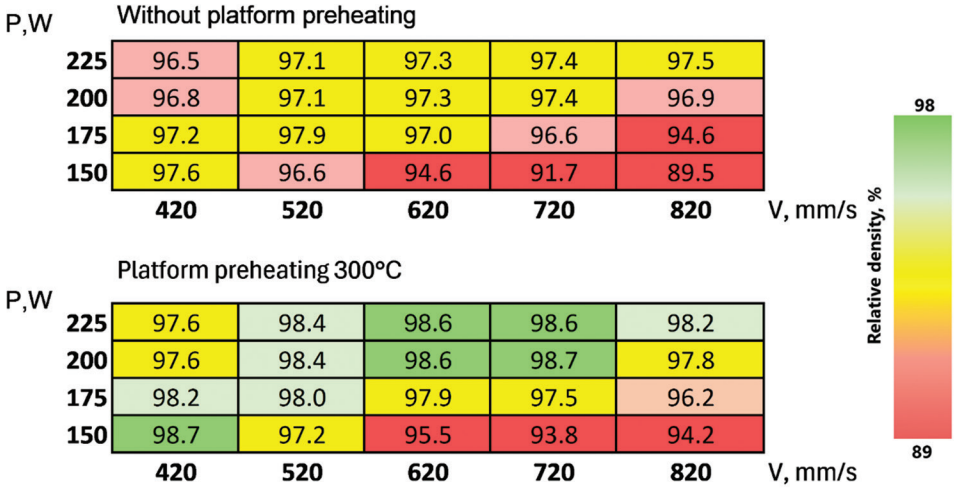

Figure 2. Effect of laser power (*P*) and scanning speed (*V*) on the density of as-built SLM material
Abbreviation: SLM: Selective laser melting

at 300°C to reduce the temperature gradient during printing.

In Figure 3, the effect of *VED* of the SLM process on relative density is shown. When pre-heating was applied, the trends of influence of laser power and scanning speed on the density of as-built SLM material were the same as it was observed without pre-heating. However, density depending on these parameters, did not exhibit very pronounced variations. The lowest density was obtained with the *VED* lower than 70 J/mm^3. It can be attributed to a lack-of-fusion defect formation. This type of defect can be seen in Figure 4, which resulted in a significant reduction in material density. Conversely, samples produced at high energy densities (higher than 110 J/mm^3) exhibited spherical pores as a result of changing melting from conduction to key-hole mode and attributed to material overheating.

Platform pre-heating not only resolved the surface cracking issue but also enhanced the material density,

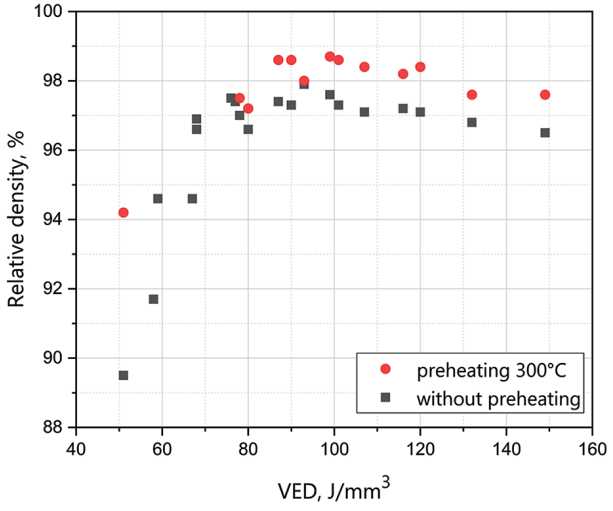

Figure 3. Effect of VED on the relative density of as-built SLM material with and without platform pre-heating
Abbreviations: SLM: Selective laser melting; VED: Volumetric energy density

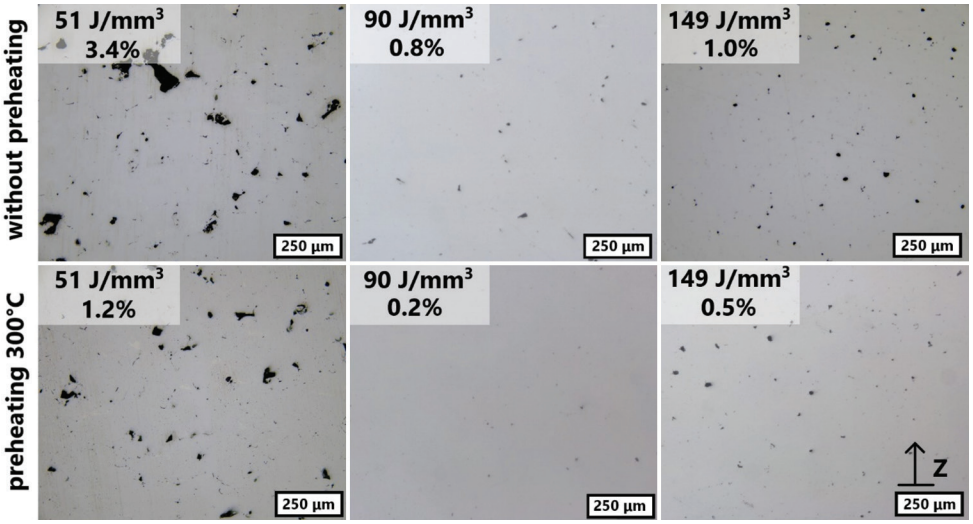

Figure 4. Macrostructure of the as-built SLM samples. VED and porosity values of the samples are presented. Magnification: ×100
Abbreviations: SLM: Selective laser melting; VED: Volumetric energy density

as evidenced by the density measurements presented in Figure 3 and the microstructural observations in Figure 4. It was demonstrated that when the same SLM process parameters with pre-heating are employed, the relative density is increased. This, in turn, facilitates the use of higher scanning speeds to achieve equal density. This finding is also consistent with the results obtained by Qin *et al.*[32] The range of *VED* from 80 to 110 J/mm³, and pre-heating allow for building samples with a density above 98%. Numerous studies have shown[33] that the application of HIP results in decreasing porosity of AM parts, thereby enhancing their mechanical properties.[34] This process is planned to be studied in future research.

The obtained specimens exhibit no visible defects, such as cracks or lack-of-fusion. While the highest material density was obtained at *VED* values in a range of 90 – 100 J/mm³, all samples printed within this energy range exhibited discontinuities between the contours and the bulk material. In addition, their surface quality was inferior compared to samples fabricated at higher *VED* values. To align both density and surface quality, a hybrid approach was implemented wherein the contours were built with the higher *VED*, and for the bulk material fabrication, *VED* of 90 J/mm³ was applied. This method resulted in improved material density by minimizing internal defects and enhanced surface quality. All subsequent analyses were conducted on samples fabricated using this optimized mode.

3.3. Microstructural characterization

The X-ray diffraction (XRD) analysis revealed that all samples exhibited the same phase composition,

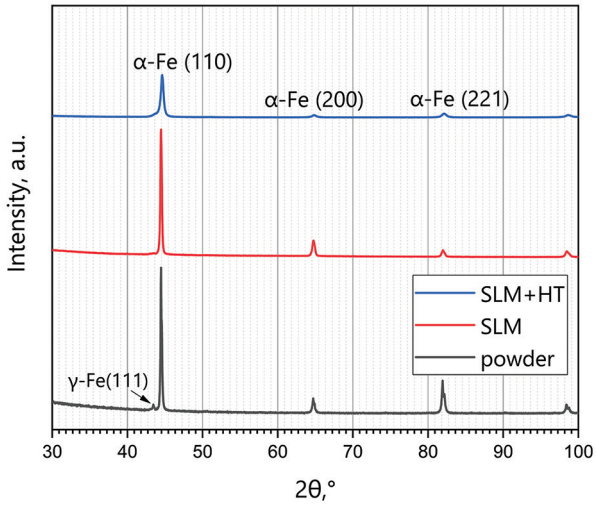

Figure 5. X-ray diffraction lines of mixed powder and fabricated specimens
Abbreviations: HT: Heat treatment; SLM: Selective laser melting

characterized by peaks corresponding to the body-centered cubic lattice of iron, as shown in Figure 5. No carbide phases were detected on the XRD, likely due to the low volume fraction and nanoscale size (up to 300 nm) of carbide particles. Apparently, the mass fraction and size of precipitates are lower than the XRD analysis method allows to determine.[35,36] Similarly, determining Y_2O_3 peaks is also challenging.

After heat treatment, a displacement of the peaks slightly toward higher 2θ angles was observed. This phenomenon may be explained by the removal of internal stresses. The peak corresponding to the position of the

face-centered cubic iron phase peak (2θ = 43.1°) in the powder probably indicates the presence of a small amount of residual austenite. However, after SLM, this peak intensity undergoes a notable reduction. This is probably due to the lower cooling rates of SLM compared to gas atomization. This observation signifies a modification in the material's structural configuration, probably related to the redistribution of chromium and carbon in the process. The evident broadening of the peaks of the material after heat treatment signifies a reduction in grain size, which was further supported by the microstructural observations presented in Figure 6.

The microstructure of the samples after SLM with pre-heating is characterized by columnar grains oriented along the building direction, as shown in Figure 6A and B, which are typical for this group of materials in SLM production.[17] The appearance of melt pools and heat-affected zones, typically observed after SLM, is not strongly evident in our samples.[37] However, the addition of Y_2O_3 decreased the grain length compared to the base material.[38] The base steel produced by SLM without pre-heating exhibited an average grain length of 156 μm and an average grain width of 30 μm.[38] After the incorporation of 0.25 wt.% Y_2O_3, the average grain length decreased to 112.0 ± 20 μm, and the average grain width increased to 57.0 ± 11 μm. In a previous study, Ghayoor *et al.*[39] reported a significant change in grain shape from columnar to equiaxed when 5 wt.% yttrium was added to 304 L steel. A decrease in grain length has also been observed in other research.[26] The application of platform pre-heating results in a decrease in the temperature gradient, consequently leading to the creation of more favorable conditions for epitaxial growth during the transition between layers and the formation of elongated grains along the building direction. The sample obtained by SLM with pre-heating is characterized by an average grain length of 133.2 ± 55 μm and an average width of 21.1 ± 8 μm. After heat treatment, the material became partially recrystallized and the shape of the grains was almost equiaxed. The grain size reduction in heat-treated samples, as compared to materials before heat treatment, is shown in Figure 7. The average grain length and width decreased to 39.9 ± 11 μm and 18.5 ± 7 μm, respectively. The structure obtained after heat treatment became more similar to the structure of materials fabricated by conventional manufacturing methods.[36] Besides, the formation of small equiaxed grains was also observed. Y_2O_3 probably act as crystallizing centers during heterogeneous nucleation, resulting in smaller equiaxed grains.

3.4. Mechanical properties

Finally, the tensile properties of the samples produced by SLM with and without subsequent heat treatment were assessed. The results of tensile testing at room and at

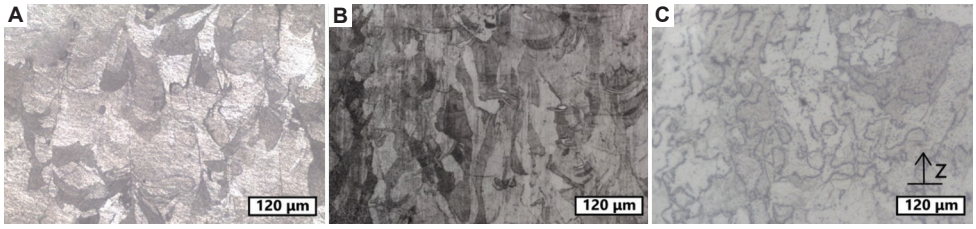

Figure 6. Microstructure of samples: (A) SLM sample without pre-heating, (B) SLM sample pre-heating at 300°C, and (C) SLM sample after heat treatment. ×200
Abbreviation: SLM: Selective laser melting

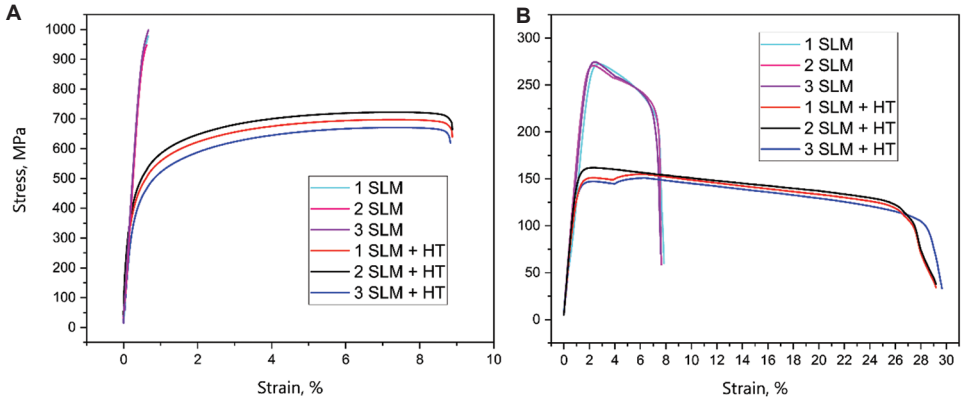

Figure 7. Stress strain curves for samples after SLM without and with heat treatment tested at: 20°C (A) and 720°C (B).
Abbreviations: HT: Heat treatment; SLM: Selective laser melting

operating (720°C) temperatures are presented in Figure 7 and Table 3. The results of the tests conducted on specimens produced without pre-heating are not presented. This decision is due to the presence of a significant number of cracks in the specimens, which made the tests invalid.

The as-built SLM ODS specimens exhibited a brittle behavior. At room temperature, fracture occurred at 978 MPa with no evidence of plastic deformation before fracture. This UTS value was comparable to the values for the similar ferritic/martensitic ODS steel plates and tubes manufactured through powder metallurgy (UTS = 991 MPa),[40] but the problem was YS and elongation was absent. Following heat treatment, the mechanical response of the SLM ODS specimens during tensile transition to a ductile mode. The YS and UTS achieved were lower than the base steel produced through powder metallurgy techniques (YS = 525 MPa, UTS = 711 MPa, ε = 16%).[41] The elongation of the heat-treated SLM ODS specimens remained significantly lower than that of the powder metallurgy-derived base material. The findings revealed the substantial impact of incorporating 0.25 wt.% Y_2O_3 on the tensile properties. In a prior investigation of base steel produced by SLM, the maximum tensile strength was also observed for the specimen after SLM without heat treatment. The UTS was 567 MPa, aligning with the absence of plastic characteristics.[38] Consequently, the incorporation of Y_2O_3 resulted in a 72% increase in UTS compared to the base steel.

The mechanical properties of heat-treated SLM samples, when tested at elevated temperatures, were not very significant. The tensile properties of the material tested at 720°C after SLM were comparable to those of base steel obtained by powder metallurgy methods (YS = 279 MPa, UTS = 284 MPa, ε = 25%).[41] However, the elongation was much lower. The relatively low ductility of all specimens after SLM can be explained by the quenched state and internal stresses.

Fractography was used to study the fracture surfaces of the specimens. From Figure 8, it can be observed that the SLM specimen tested at 20°C exhibited an undeveloped fracture surface. The fracture occurred without necking, and the fracture mode appears to be of an intergranular nature. The specimen, after heat treatment, featured a more developed fracture surface with a few cleavage platforms and a number of dimples. As the specimen after SLM underwent tensile testing at 720°C, its fracture surface exhibited a significant increment in the number of dimples of a lower size. The fracture character of the specimens is classified as higher ductility, accompanied by the presence of brittle fracture areas. The specimen after SLM and heat treatment tested at 720°C had dimples and micro-voids, an indication of the ductile nature of the fracture. In all the cases, no visible cracks, inclusions, or unmelted powder particles were detected.

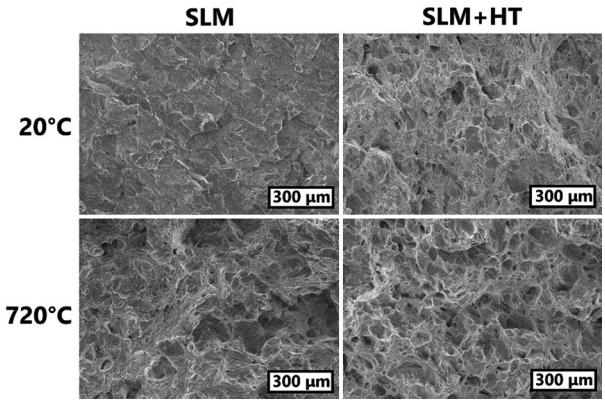

Figure 8. Fracture surfaces of samples after SLM without and with heat treatment after tensile testing at 20°C and 720°C. Magnification: ×100
Abbreviation: SLM: Selective laser melting

Table 3. Tensile properties of specimens fabricated in the present work

Condition	Temperature, °C	YS, MPa	UTS, MPa	ε, %
SLM ODS	20	-	978±24	-
	720	266±2	272±2	7.7±0.1
SLM ODS+HT	20	440±14	697±25	8.6±0.2
	720	144±8	156±5	29.3±0.3

Abbreviations: ε: Elongation; HT: Heat treatment; ODS: Oxide dispersion-strengthened; SLM: Selective laser melting; UTS: Ultimate tensile strength; YS: Yield strength.

The results of the microhardness measurements supported the conclusions regarding the quenched state of the material after SLM. The sample produced without pre-heating exhibited a value of microhardness of 441 ± 23 HV. The application of pre-heating was found to result in a reduction of material internal stresses by decreasing the thermal gradient, thereby leading to a decrease in microhardness to 390 ± 20 HV. After heat treatment, a microhardness of 288 ± 26 HV was measured.

These results underscore the need for a change in the heat treatment mode after SLM. The selected heat treatment mode was found to exert a negative impact on the tensile properties of the material. The results of the study indicated the formation of a quenched structure in as-built material and subsequent quenching within the heat treatment did not have a positive effect on the structure. Despite the lower values of average grain length and width, the specimens after heat treatment exhibited lower UTS values. During the heat treatment process, which involves quenching and high-temperature annealing, a recrystallization

phenomenon occurs, leading to the dissipation of internal stresses. This resulted in a reduction in tensile strength and an enhancement in ductility. In this instance, it is probable that the impact of grain size on strength properties is less significant than the impact of internal stresses. Therefore, we propose carrying out only high-temperature tempering for stress relief in future studies.

The presented results indicate the beneficial effects of the Y_2O_3 strengthening. Thus, the process of fabrication of ferritic/martensitic ODS steels through SLM should be further investigated. Further research is necessary to enhance the material's density and to conduct a thorough examination of its resulting microstructure. Further studies employing Transmission electron microscopy, Electron Backscatter Diffraction, and Small-angle X-ray scattering are necessary to investigate the size and distribution of the Y_2O_3. It is anticipated that in the future, this approach may facilitate the creation of material that exhibits both high strength and plastic properties.

4. Conclusion

In the present work, the ferritic/martensitic ODS steel with 0.25 wt.% Y_2O_3 was fabricated by SLM. The main conclusions of the study are summarized as follows:

(i) High material density, with a relative value of more than 98%, was achieved by adopting *VED* in the range of 80 – 110 J/mm^3 and platform pre-heating. *VED* is identified as the most significant factor affecting relative density in this work

(ii) After heat treatment, partial recrystallization of grains was noted, as indicated by a shift in grain morphology from elongated to more equiaxed forms. In addition, the grain size decreased as a result of partial recrystallization. The impact of pre-heating on the process of structure formation was also observed, resulting in the formation of elongated and narrow grains

(iii) At room temperature, reinforcement with 0.25 wt.% Y_2O_3 resulted in UTS values (978 MPa) of as-built material close to those for the similar ferritic/martensitic ODS steel plates and tubes fabricated by traditional methods. The selected heat treatment mode led to a substantial decrease in strength properties (UTS = 697 MPa), whereas ductility was increased. However, the obtained material exhibited brittleness, indicating the necessity of employing a different heat treatment mode to ensure both enhanced strength and plastic properties.

Acknowledgments

None.

Funding

This work is supported by the Russian Science Foundation (No. 23-79-30004, https://rscf.ru/project/23-79-30004/).

Conflicts of interest

The authors declare no conflicts of interest.

Author contributions

Conceptualization: Vadim Sufiiarov
Data curation: Maria Zaitceva
Funding acquisition: Anatoliy Popovich
Investigation: Maria Zaitceva, Artem Borisov
Project administration: Vadim Sufiiarov
Resources: Anatoliy Popovich
Supervision: Vadim Sufiiarov
Writing – original draft: Maria Zaitceva
Writing – review & editing: Vadim Sufiiarov

Ethics approval and consent to participate

Not applicable.

Consent for publication

Not applicable.

Availability of data

The data presented in this study are available on request from the corresponding author.

References

1. Li A, Chen Q, Wang P, *et al*. Microstructure and properties of oxide-reinforced FeCrAl matrix alloy manufactured by selective laser melting. *Mater Today Commun*. 2024;39:109226.

   doi: 10.1016/j.mtcomm.2024.109226

2. Wang M, Sun H, Zou L, Zhang G, Li S, Zhou Z. Structural evolution of oxide dispersion strengthened austenitic powders during mechanical alloying and subsequent consolidation. *Powder Technol*. 2015;272:309-315.

   doi: 10.1016/j.powtec.2014.12.008

3. Little EA, Stow DA. Void-swelling in irons and ferritic steels: II. An experimental survey of materials irradiated in a fast reactor. *J Nucl Mater*. 1979;87(1):25-39.

   doi: 10.1016/0022-3115(79)90123-5

4. Shashanka R. Non-lubricated dry sliding wear behavior of spark plasma sintered nano-structured stainless steel. *J Mater Environ Sci*. 2019;10(8):767-777.

5. Walker JC, Berggreen KM, Jones AR, Sutcliffe CJ. Fabrication of Fe-Cr-Al oxide dispersion strengthened PM2000 alloy using selective laser melting. *Adv Eng Mater*.

2009;11(7):541-546.

doi: 10.1002/adem.200800407

6. Wilms MB, Rittinghaus SK, Goßling M, Gökce B. Additive manufacturing of oxide-dispersion strengthened alloys: Materials, synthesis and manufacturing. *Prog Mater Sci*. 2023;133:101049.

doi: 10.1016/j.pmatsci.2022.101049

7. Suryanarayana C. Mechanical alloying and milling. *Prog Mater Sci*. 2001;46(1-2):1-184.

doi: 10.1016/S0079-6425(99)00010-9

8. Ou Lahcen EM, Ángel Alcázar MM, Almeida CP. New high strength ODS Eurofer steel processed by mechanical alloying. *Mater Sci Eng A*. 2021;817:141288.

doi: 10.1016/j.msea.2021.141288

9. Noh S, Choi BK, Kang SH, Kim TK. Influence of mechanical alloying atmospheres on the microstructures and mechanical properties of 15Cr ODS steels. *Nucl Eng Technol*. 2014;46(6):857-862.

doi: 10.5516/NET.07.2013.096

10. Verma L, Dabhade VV. Synthesis of Fe-15Cr-2W oxide dispersion strengthened (ODS) steel powders by mechanical alloying. *Powder Technol*. 2023;425:118554.

doi: 10.1016/j.powtec.2023.118554

11. Oksiuta Z, Ozieblo A, Perkowski K, Osuchowski M, Lewandowska M. Influence of HIP pressure on tensile properties of a 14Cr ODS ferritic steel. *Fusion Eng Design*. 2014;89(2):137-141.

doi: 10.1016/j.fusengdes.2014.01.052

12. Deng L, Luo J ru, Tu J, *et al*. Achieving excellent mechanical properties of ODS steel by Y2O3 addition. *Mater Sci Eng A*. 2023;872:145008.

doi: 10.1016/j.msea.2023.145008

13. Shi W, Yu L, Liu C, *et al*. Evolution of Y2O3 precipitates in ODS-316 L steel during reactive-inspired ball-milling and spark plasma sintering processes. *Powder Technol*. 2022;398:117072.

doi: 10.1016/j.powtec.2021.117072

14. Macía E, García-Junceda A, Serrano M, Hong SJ, Campos M. Effect of mechanical alloying on the microstructural evolution of a ferritic ODS steel with (Y-Ti-Al-Zr) addition processed by Spark Plasma Sintering (SPS). *Nucl Eng Technol*. 2021;53(8):2582-2590.

doi: 10.1016/j.net.2021.02.002

15. Zhao M, Zhang P, Xu J, *et al*. Optimization of microstructure and tensile properties for a 13Cr-1W ODS steel prepared by mechanical alloying and spark plasma sintering using pre-alloyed powder. *Mater Character*. 2024;207:113581.

doi: 10.1016/j.matchar.2023.113581

16. Li XP, Kang CW, Huang H, Sercombe TB. The role of a low-energy-density re-scan in fabricating crack-free $Al8_5Ni_5Y6Co_2Fe_2$ bulk metallic glass composites via selective laser melting. *Mater Des*. 2014;63:407-411.

doi: 10.1016/j.matdes.2014.06.022

17. Vasquez E, Giroux PF, Lomello F, *et al*. Elaboration of oxide dispersion strengthened Fe-14Cr stainless steel by selective laser melting. *J Mater Process Technol*. 2019;267:403-413.

doi: 10.1016/j.jmatprotec.2018.12.034

18. Sagaradze VV, Kozlov KA, Kataeva NV. Oxide-dispersion strengthened radiation-resistant steels. *Phys Met Metallogr*. 2018;119(13):1350-1353.

doi: 10.1134/S0031918X18130112

19. Tanno T, Ohtsuka S, Yano Y, Kaito T, Tanaka K. Effects of manufacturing process on impact properties and microstructures of ODS steels. *J Nucl Mater*. 2014;455(1):480-485.

doi: 10.1016/j.jnucmat.2014.07.075

20. Gil E, Ordás N, García-Rosales C, Iturriza I. Microstructural characterization of ODS ferritic steels at different processing stages. *Fus Eng Des*. 2015;98-99:1973-1977.

doi: 10.1016/j.fusengdes.2015.06.010

21. Hsiung LL, Fluss MJ, Kimura A. Structure of oxide nanoparticles in Fe-16Cr MA/ODS ferritic steel. *Mater Lett*. 2010;64(16):1782-1785.

doi: 10.1016/j.matlet.2010.05.039

22. Amini R, Alijani F, Ghaffari M, Alizadeh M, Okyay AK. Formation of B19′, B2, and amorphous phases during mechano-synthesis of nanocrystalline NiTi intermetallics. *Powder Technol*. 2014;253:797-802.

doi: 10.1016/j.powtec.2013.12.029

23. Smith TM, Thompson AC, Gabb TP, Bowman CL, Kantzos CA. Efficient production of a high-performance dispersion strengthened, multi-principal element alloy. *Sci Rep*. 2020;10(1):9663.

doi: 10.1038/s41598-020-66436-5

24. Ozerskoi N, Volokitina E, Razumov N, Popovich A. Mechanical properties of ODS steel fabrication by mechanical alloying and sparking plasma sintering. *AIP Conf Proc*. 2024;3154(1):020029.

doi: 10.1063/5.0201304

25. Jia H, Zhou Z, Li S. A new strategy for additive manufacturing ODS steel using Y-containing gas atomized powder. *Mater Character*. 2022;187:111876.

doi: 10.1016/j.matchar.2022.111876

26. Cakmak O, Yeom H, Cho JW. *In-situ* synthesis of Yttria-based precipitates and their effects on Fe12Cr6Al in laser powder bed fusion. *J Mater Res Technol*. 2024;33:6714-6721.

doi: 10.1016/j.jmrt.2024.11.059

27. Autones L, Aubry P, Ribis J, Leguy H, Legris A, De Carlan Y. Assessment of ferritic ODS steels obtained by laser additive manufacturing. *Materials* (*Basel*). 2023;16(6):2397.

doi: 10.3390/ma16062397

28. Zhai W, Zhou W, Nai SML. Effect of interface wettability on additively manufactured metal matrix composites: A case study of 316L-Y2O3 oxide dispersion-strengthened steel. *Metals*. 2024;14(2):170.

doi: 10.3390/met14020170

29. Jia H, Sun H, Wang H, Wu Y, Wang H. Scanning strategy in selective laser melting (SLM): A review. *Int J Adv Manuf Technol*. 2021;113(9):2413-2435.

doi: 10.1007/s00170-021-06810-3

30. Polekhina NA, Litovchenko IY, Tyumentsev AN, Astafurova EG, Chernov VM, Leontyeva-Smirnova MV. The effect of tempering temperature on the features of phase transformations in the ferritic-martensitic steel EK-181. *J Nucl Mater*. 2014;455(1-3):496-499.

doi: 10.1016/j.jnucmat.2014.08.012

31. Qin SS. *Influence of Preheating Temperature on Microstructure Evolution and Hardness of High-Speed Steel AISI M50 Processed by Laser Powder Bed Fusion - Qin - 2023 - Steel Research International*. Wiley Online Library. https://onlinelibrary.wiley.com/doi/10.1002/srin.202200784 [Last accessed on 2025 Jan 29].

32. Qin S, Saewe J, Kunz J, *et al*. Influence of preheating temperature on microstructure evolution and hardness of high-speed steel AISI M50 processed by laser powder bed fusion. *Steel Res Int*. 2023;94(6):2200784.

doi: 10.1002/srin.202200784

33. Masuo H, Tanaka Y, Morokoshi S, *et al*. Effects of defects, surface roughness, and HIP on fatigue strength of Ti-6Al-4V manufactured by additive manufacturing. *Proc Struct Integr*. 2017;7:19-26.

doi: 10.1016/j.prostr.2017.11.055

34. Shi Y, Lu Z, Xu H, Xie R, Ren Y, Yang G. Microstructure characterization and mechanical properties of laser additive manufactured oxide dispersion strengthened Fe-9Cr alloy. *J Alloys Compd*. 2019;791:121-133.

doi: 10.1016/j.jallcom.2019.03.284

35. Spiridonova KV, Litovchenko IYu, Polekhina NA, *et al*. Structural-phase transformations of 12% chromium ferritic-martensitic steel EP-823. *Izv Ferrous Metall*. 2023;66(6):725-732.

doi: 10.17073/0368-0797-2023-6-725-732

36. Wang Z, Liu Z, Ma J, *et al*. Investigation on microstructure and mechanical properties of electron-beam-welded joint of reduced activation ferritic/martensitic steel fabricated by selective laser melting. *Mater Sci Eng A*. 2023;881:145333.

doi: 10.1016/j.msea.2023.145333

37. Seede R, Zhang B, Whitt A, *et al*. Effect of heat treatments on the microstructure and mechanical properties of an ultra-high strength martensitic steel fabricated via laser powder bed fusion additive manufacturing. *Addit Manuf*. 2021;47:102255.

doi: 10.1016/j.addma.2021.102255

38. Zaitceva M, Erutin D, Popovich A, Sufiiarov V. Effect of pre-heating during selective laser melting of chromium steel on structure and properties. *Global Energy*. 2024;30(3):43-51.

doi: 10.18721/JEST.30303

39. Ghayoor M, Mirzababaei S, Lee K, *et al*. Strengthening of 304L Stainless Steel by Addition of Yttrium Oxide and Grain Refinement during Selective Laser Melting. In: *Solid Freeform Fabrication 2019: Proceedings of the 30th Annual International Solid Freeform Fabrication Symposium-An Additive Manufacturing Conference*; 2019. p. 967-976.

40. Sagaradze VV, Kochetkova TN, Kataeva NV, *et al*. Structure and creep of Russian reactor steels with a BCC structure. *Phys Metals Metallogr*. 2017;118(5):494-506.

doi: 10.1134/S0031918X17050131

41. Votinin SN, Balashov VD, Krylov EA, *et al*. Effect of Neutron Irradiation on High-Temperature Properties of Stainless Steels type Cr13 (Влияние Нейтронного Облучения на Высокотемпературные Свойства Нержавеющих Сталей Типа Х13). In: *Proceedings of the Scientific and Technical Conference "Nuclear Energy: Fuel Cycles, Radiation Materials Science", Ulyanovsk, October 5-10*; 1971. p. 351-379.

ACCSCIENCE PUBLISHING

Materials Science in Additive Manufacturing

ORIGINAL RESEARCH ARTICLE

Evaluation of microstructure, tensile, and fatigue testing on angled walls of NASA HR-1 using laser powder direct energy deposition

Javier Lares[1,2†*], Edel Arrieta[2,3], Lawrence E. Murr[1], Colton Katsarelis[4†], Paul Gradl[4†], and Francisco Medina[2,3]

[1]Department of Metallurgical, Materials and Biomedical Engineering, College of Engineering, The University of Texas at El Paso, El Paso, Texas, United States of America

[2]W.M. Keck Center for 3D Innovation, College of Engineering, The University of Texas at El Paso, El Paso, Texas, United States of America

[3]Department of Mechanical Engineering, College of Engineering, The University of Texas at El Paso, El Paso, Texas, United States of America

[4]National Aeronautics and Space Administration, Marshall Space Flight Center, Huntsville, Alabama, United States of America

Abstract

This study investigates the influence of varying deposition angles on the tensile strength and low cycle fatigue (LCF) performance of National Aeronautics and Space Administration (NASA) HR-1 alloy using laser powder-directed energy deposition. This study investigates the influence of varying deposition angles on the tensile strength and LCF performance of NASA HR-1 alloy using laser powder-directed energy deposition. Two sets of build parameters, 1,070 W and 2,620 W, were employed alongside three different build angles to assess their influence on mechanical properties following a uniform heat treatment regimen. This heat treatment encompassed stress relief, homogenization, solution annealing, and double aging. Samples deposited at 1,070 W showed a slightly lower porosity percentage compared to those produced at 2,620 W. All samples displayed similar grain sizes and a homogenized microstructure, indicating the effectiveness of the heat treatment in achieving a uniform microstructure across samples deposited at different build angles and laser power settings. The varying deposition angles did not significantly affect the microstructure or mechanical properties of the alloy. Fractography analysis revealed that all samples fractured through transgranular micro-void coalescence, with fracture initiation predominately occurring at the edges of both tensile and fatigue samples.

Keywords: NASA HR-1 alloy; Laser power direct energy deposition; Build angle; Laser power

†These authors contributed equally to this work

***Corresponding author:**
Javier Lares
(jelaresmona@miners.utep.edu)

Citation: Lares J, Arrieta E, Murr LE, Katsarelis C, Gradl P, Medina F. Evaluation of microstructure, tensile, and fatigue testing on angled walls of NASA HR-1 using laser powder direct energy deposition. *Mater Sci Add Manuf.* 2025;4(1):8069. doi: 10.36922/msam.8069

Received: December 19, 2024

1st revised: January 14, 2025

2nd revised: January 30, 2025

Accepted: February 3, 2025

Published Online: March 26, 2025

1. Introduction

National Aeronautics and Space Administration (NASA) HR-1, developed by the NASA, is an iron-nickel-chromium-based superalloy used in high-pressure hydrogen applications. It is an iron-nickel-based gamma prime-strengthened superalloy derived

from A-286 and JBK-75 alloys. NASA HR-1 was designed to improve strength and corrosion resistance while offering superior weldability compared to A-286 and JBK-75. The alloy's chemical modifications include an increased nickel and molybdenum content to mitigate solidification fractures. In addition, the tungsten content was increased to enhance the solution hardening treatment and reduce the formation of the acicular η-Ni_3Ti phase. Furthermore, titanium and aluminum levels were also elevated to promote the formation of spherical γ' precipitates, thereby improving the alloy's strength. The chromium and vanadium volume fractions were maintained to ensure that NASA HR-1 retains the high corrosion resistance characteristic of A-286 and JBK-75 alloys.[1,2]

The alloy NASA HR-1 is used in aerospace components, particularly in liquid rocket engines. These components, such as regeneratively cooled nozzles, are designed to withstand extreme conditions, including high temperatures, high cyclic pressures, and hydrogen-rich environments, which render materials susceptible to hydrogen embrittlement.[1,3-5] Conventionally, regeneratively cooled nozzles were produced using vacuum induction melting and vacuum arc remelting, followed by hot or cold rolling to fabricate individual parts that are subsequently assembled into the final engine components. This conventional process is expensive and time-consuming. In contrast, additive manufacturing (AM) processes, such as laser powder direct energy deposition (LP-DED), are being explored as viable alternatives due to their potential to reduce production costs and facilitate the fabrication of large-scale components with complex features.[4,6] In addition, AM is considered more sustainable than traditional manufacturing processes, such as casting and powder metallurgy, which have low efficiency in terms of material utilization and energy consumption.[7,8] At present, AM is employed across different industries, including aerospace, oil and gas, industrial, power, and energy, to create new components and repair damaged parts. DED is capable of producing parts from a range of high-performance materials, such as stainless steel, titanium, nickel, cobalt, and aluminum-based alloys.[9] For instance, Inconel 718 has been manufactured using the same technology and has shown an ultimate tensile strength (UTS) of 711 MPa and a yield strength (YS) of 464 MPa after heat treatment.[10] These mechanical properties can be achieved by designing a suitable heat treatment process that facilitates the creation of the desired microstructure. The LP-DED process involves creating a melt pool using a laser while simultaneously feeding metal powder into the melt pool; this powder melts and solidifies during cooling. In addition, the use of an inert gas is essential to prevent any contamination between layers during the deposition process.[11]

The LP-DED process has some limitations, such as geometric build angles, variations in thickness and surface texture, and the potential for process defects.[1,9] It has been shown that walls with angles >30° begin to fail during deposition, whereas failure occurs at angles above 45° in laser powder bed fusion.[9] In addition, varying the orientation of the build can lead to different degrees of anisotropic characteristics in the AM microstructure.[12] To optimize the LP-DED process, the build parameters must be adjusted during printing to strike a balance between build deposition rates and geometric resolutions. Key parameters include laser power and spot size, powder flow rate, gas flow rate, travel speed, layer height, and hatching.[1,13] High laser power is particularly important for alloys like NASA HR-1, as it has a high melting point and high thermal conductivity that enables rapid heat dissipation.[2] Consequently, laser power levels between 1,200 W and 3,000 W are essential for effectively additively manufacturing this alloy using LP-DED. Increased laser power may produce deeper melt pools, allowing higher deposition rates and thus, enhancing raw material utilization efficiency.[14] It is also crucial to maintain a balance between these parameters, as they can alter the thermodynamics during solidification, which, in turn, affects the microstructure and mechanical properties of the alloy.[1,10,11] The primary objective of this study is to assess the impact of different laser power settings and build angles on the microstructure and mechanical properties of walls following heat treatment. The variables used in this study were selected based on previous research that demonstrated variations in performance when using 1,070 W and 2,620 W before any heat treatment. This study evaluated the effectiveness of heat treatment in achieving a homogeneous microstructure across all angled walls. In addition, mechanical properties such as microhardness, tensile strength, and low cycle fatigue (LCF) were compared to evaluate different manufacturing parameters for angled walls in component fabrication.

2. Materials and methods

Angled walls with a thickness of 13 mm were built using rotary-atomized NASA HR-1 powder supplied by Homogenized Metals Inc. (HMI; USA) in a boxed-shaped structure, employing two different sets of parameters, 1,070 W and 2,620 W. This geometry was chosen to facilitate the formation of desired build angles. The layer height, travel speed, and powder feed rate are shown in Table 1. These parameters were modified to create the desired build angle and laser power settings. The walls were deposited at angles of 0°, 20°, and 30° relative to the build direction, as shown in Figure 1. The walls were heat treated in the following order: Stress relief, homogenization,

Table 1. Summary of laser powder direct energy deposition samples with their respective printing parameters

Wall type	Parameter set	Powder type	Layer height (cm)	Travel speed (cm/min)	Powder feed rate (gr/min)
0 Box-0.180″ wall	1,070 W	HMI-HR-1	0.101	101.6	16
20 Box-0.180″ wall	1,070 W	HMI-HR-1	0.101	101.6	16
30 Box-0.180″ wall	1,070 W	HMI-HR-1	0.101	101.6	16
0 Box-0.400″ wall	2,620 W	HMI-HR-1	0.038	76.2	27.1
20 Box-0.400″ wall	2,620 W	HMI-HR-1	0.038	76.2	27.1
30 Box-0.400″ wall	2,620 W	HMI-HR-1	0.038	76.2	27.1

Abbreviation: HMI: Homogenized Metals Inc.

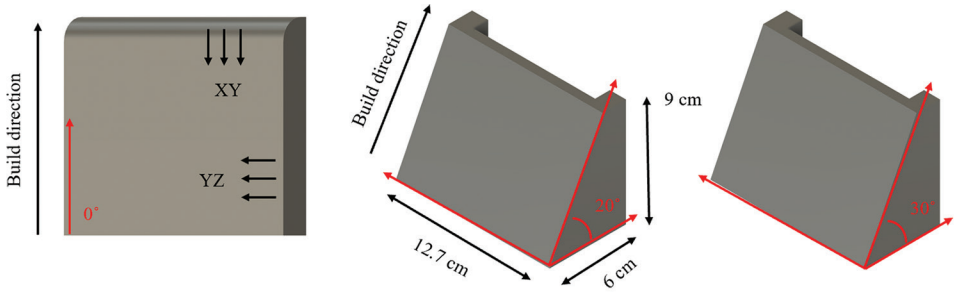

Figure 1. Computer-aided design representation of walls printed at different angles

solution annealing, and two-step aging. The complete heat treatment developed by NASA is outlined in Table 2. This heat treatment has been refined over the years to ensure consistency and to prevent detrimental phases, such as the η-phase, which can reduce the alloy's ductility.[1,12,15]

2.1. Sample identification and powder specifications

A total of six heat-treated samples were evaluated, as shown in Table 1, with their respective deposition angles (0°, 20°, and 30°) and parameters (1,070 W and 2,620 W). Figure 2 provides a photograph of the actual walls produced during this study. The powder feedstock had an average particle size distribution (PSD) of 45 – 105 μm, conforming to a +140 mesh at 0% and −325 mesh at 2.31% based on ASTM B214.[16] The chemical composition of the powder, provided by the vendor, is detailed in Table 3 (HMI powder lot HRA18). Notably, the oxygen and nitrogen content in the feedstock were measured at 77 ppm and 10 ppm, respectively.

2.2. Powder characterization

The PSD of the NASA HR-1 powder was measured using a Dynamic Image Analyzer CAMSIZER X2 (MICROTRAC, United States). A JSM-IT500 scanning electron microscope (SEM) (Jeol, Japan) was used to evaluate the morphology of the powder. In addition, the Hall flow rate of powder was measured following ASTM B213-20[17] using a non-metallic funnel with a nominal orifice diameter of 2.54 mm and a stopwatch. The formula used to calculate flowability is as follows:

$$FR_H = \frac{average\,time\ (sec)}{50\,grams} \quad \text{(I)}$$

2.3. Defect content or density

ImageJ software[18] (Version 15.4) was used to determine the porosity for each of the two-dimensional images of the angled walls captured with an optical microscope (Olympus, Japan.)

(One image from each sample was used to measure the percentage area occupied by porosity in the XY plane.)

2.4. Metallographic preparation and grain size measurement

All walls were sectioned using an ATM Brilliant 220 precision cutter (QATM, Germany) to obtain samples in the XY and YZ planes. A mixture of phenolic and epoxy powder, in a 2:1 ratio, was used with a ratio to create the metallographic sample in an ASTM Opal 460 hot mounting press (ATM, Germany).

Grinding was performed using silicon carbide grinding paper, starting with a grit size of 220 and progressing through finer grits until finishing with a 1,000-grit size. Initial polishing utilized diamond suspension pads with particle sizes ranging from 9 μm to 3 μm, followed by final

polishing with a 0.1 μm fumed silica pad. Force was lowered from 30 N to 20 N during final polishing until a mirror-like surface was achieved. Both grinding and polishing processes were performed using a Saphir 530 machine (QATM, Germany). Grain sizes were measured using the intercept method according to ASTM E-112[19] to determine the average grain size within each sample's microstructure.

2.5. Mechanical testing

Four tensile dog bone samples were extracted from each heat-treated wall and subjected to tensile testing using an Instron 1,125 machine (Instron, USA) with a 100 kN frame according to ASTM E8-2.[20] The tests were conducted until fracture to obtain the UTS, 0.2% offset YS, elongation, and reduction area. LCF was performed according to ASTM E606-21.[21] using three machined dog bone samples also obtained from the angled walls. The LCF tests were conducted under fully reversal tensile-compressive conditions (R = −1) at a frequency of 0.5 Hz and strain range of 1% on a GLC DXF machine (Instron, USA) with a 100 kN frame. Microhardness measurements were taken using Qness CHD master hardness tester (QATM, Germany), which involved five indentations along each sample in the XY plane, following ASTM E2546.[22]

Table 2. Heat treatment cycle for NASA HR-1 consisting of stress relief, homogenization, solution annealing, and aging

Heat treatment	Temperature (°F)/duration (hours)
Stress relief	1,065°C/1.5
Homogenization	1,162°C/6
Solution annealing treatment	1,065°C/1
Two-step aging	690°C/16 and 621°C/16

Table 3. Chemical composition of NASA HR-1 alloy powder

Chemical	Fe	Ni	Cr	Co	Mo	Ti	Al	V	W
Percentage by weight (Wt%)	Bal	34.04	14.68	3.77	1.87	2.4	0.25	0.30	1.62

Abbreviation: Bal: Balance; NASA: National Aeronautics and Space Administration.

2.6. Fractography

Fracture surfaces on each sample were observed under JSM-IT500 SEM (Jeol, Japan). The working distance was adjusted between 23 and 35 mm to evaluate and identify the fracture mechanism of all samples, allowing for comparisons to determine whether they exhibited similar or differing behaviors during fracture. Sample preparation included the application of conductive tape to ensure electrical contact between the metal piece and the mount.

2.7. Statistical analysis

A *t*-test was performed to assess whether the results from tensile and fatigue testing exhibited significant differences, with $P < 0.05$ considered significant. Statistical analysis was performed using Minitab software (version 22.1.0).[23]

3. Results and discussion

3.1. Powder characterization

The powder exhibited an average Hall flow rate (FR_H) of 23.1 s/g and an apparent density of 1.10 g/cm^3. The D10, D50, and D90 values were measured at 57 μm, 74 μm, and 95 μm, respectively. The PSD is shown in Figure 3. Furthermore, the spherical morphology and dendritic texture of the powder are shown in Figure 4.

In addition, Figure 5 displays the cross-section of the powder in both polished and etched conditions. In both states, gas porosity entrapment is evident in some particles, with an average diameter of 7.85 μm, as indicated by the arrows (Figure 5). This porosity can affect the defect content of the deposited beads. In the etched condition, a dendritic microstructure with very well-defined grain boundaries is observable in all particles, illustrating how these particles solidified during the rotary atomized process.

3.2. Defect content or density

The percentage of porosity was measured and compared in the XY plane for different power settings and deposition angles of the AM-angled walls. All samples exhibited small voids that can be classified as gas porosity based

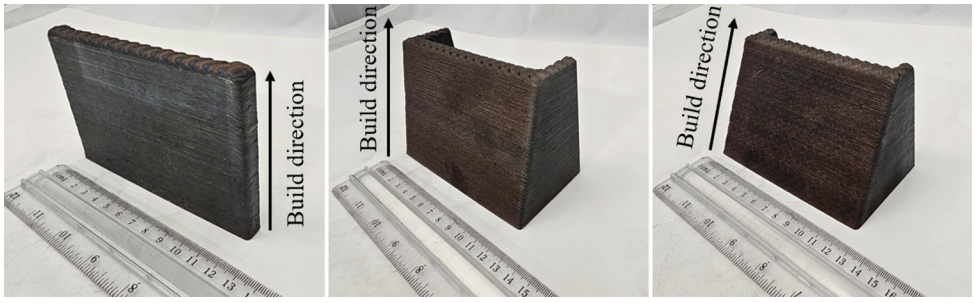

Figure 2. Photo of actual walls showing the 0°, 20°, and 30° angle deposition

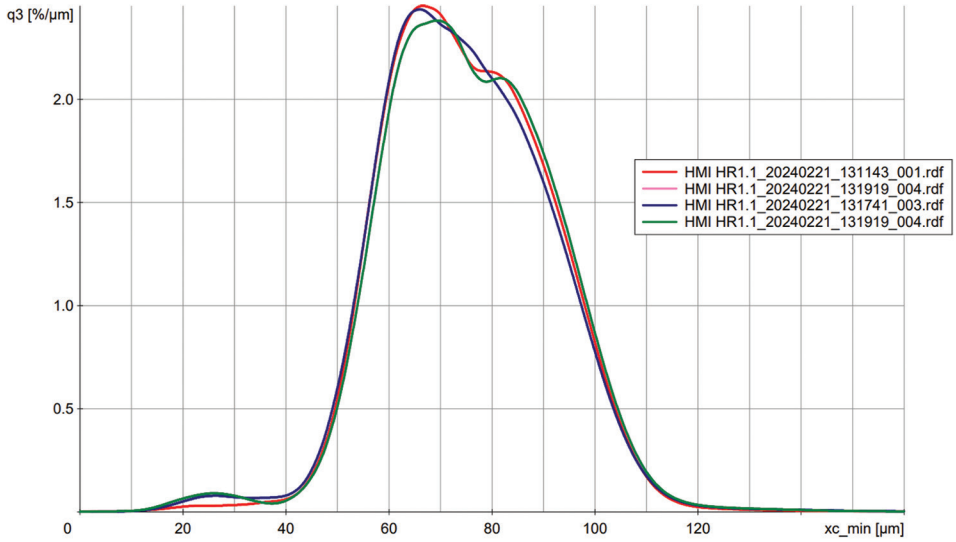

Figure 3. Graphical representation of powder particle size distribution

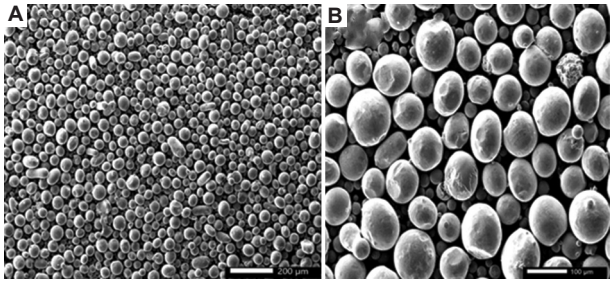

Figure 4. Image of HR1 powder under scanning electron microscope at magnifications of (A) ×55 and (B) ×140. Scale bar: (A) 200 µm; (B) 100 µm

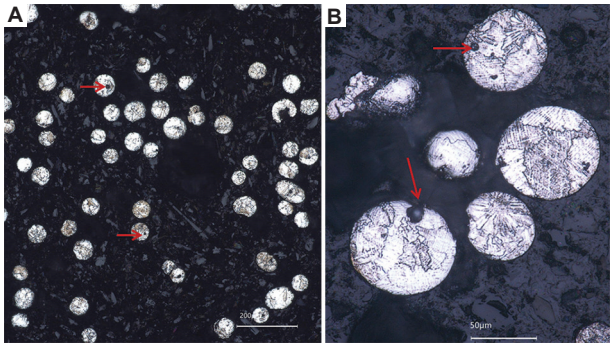

Figure 5. The cross-section area of HR1 powder in the etched condition at (A) ×150 and (B) ×400 magnification. The red arrows indicate gas porosity entrapment. Scale bar: (A) 200 µm; (B) 50 µm

on their spherical morphology.[24] Varying the deposition angle did not significantly impact porosity, as shown in Table 4. Moreover, this variation in angle did not reveal any additional defects. However, when comparing the effects of increasing the laser power to 2,620 W, it was observed

Table 4. Comparison of porosity percentage on laser powder direct energy deposition NASA HR-1 angled walls

Sample	Porosity %
0° 1,070 W	0.08
0° 2,620 W	0.21
20° 1,070 W	0.07
20° 2,620 W	0.20
30° 1,070 W	0.01
30° 2,620 W	0.12

that the porosity increased across all build angles. Figure 6 illustrates that the sample at 0° with 2,620 W has more pores compared to the sample at 0° with 1,070 W. This increase in porosity can be attributed to gas being more easily entrapped in the deeper melt pools created by higher laser power.[1,24]

3.3. Microstructure analysis

Two samples with the same angle deposition (30°) and different laser power, 1,070 W and 2,620 W, were examined in their as-built condition. Both samples showed a dendritic microstructure resulting from the rapid cooling rates associated with DED, which typically ranges from 103 to 105 °C/s.[25] This microstructure is depicted in Figure 7. In addition, a tendency toward a globular microstructure (indicated by arrows) was observed on the downskin side of the wall. Partial melting of some particles was noted on the downskin surface, while the outer edges showed slightly higher void content compared to the bulk material. A similar trend was observed in the sample processed

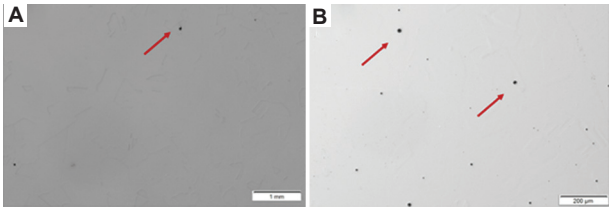

Figure 6. Microscopic images of (A) 1,070 W and (B) 2,620 W laser power heat-treated samples printed at 0°. The red arrows show the pores within the sample. Scale bar: 1 mm, magnification: ×200

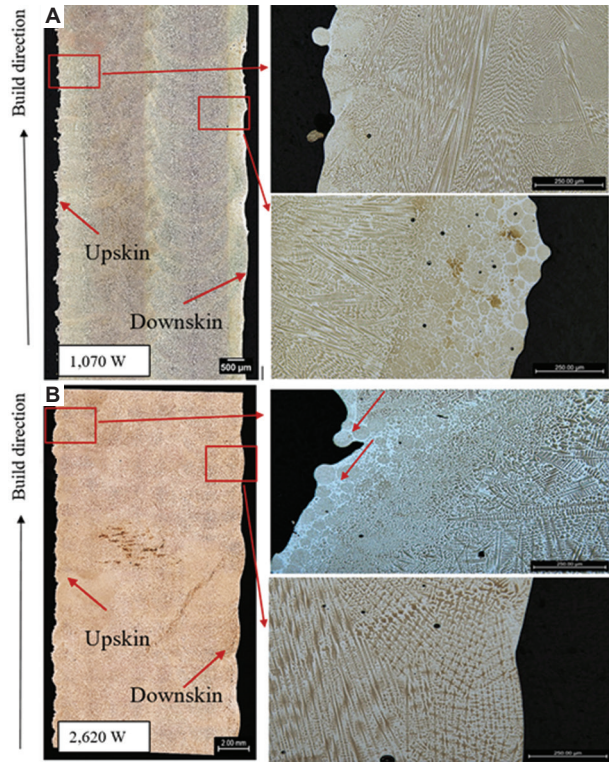

Figure 7. Microstructure in the non-heat-treated condition of the (A) 1,070 W and (B) 2,620 W samples in the YZ plane. Red arrows indicate a dendritic microstructure with globular features at the inner side of angled walls. Scale bar: (A) 500 µm, 250,000 µm; (B) 200 µm, 250,000 µm; magnification: Magnification for left images is ×20. Magnification for right image is ×100

at 2,620 W, where the globular microstructure formed between layers.

After heat treatment, the microstructure of two samples with the same deposition angle but different laser power settings was compared. Figure 8 illustrates the microstructure of two samples at 0° processed at different laser power, 1,070 W and 2,620 W. Both samples exhibited an austenitic microstructure characterized by equiaxed grains, along with duplex grain size and well-defined grain boundaries. The duplex grain size may result from differences in cooling rates between the periphery and the

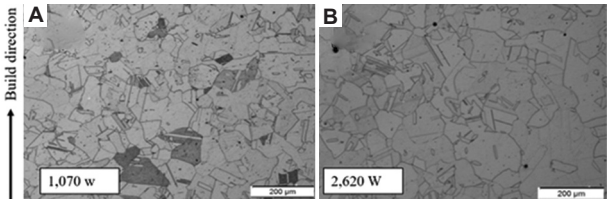

Figure 8. Microstructures of samples processed at (A) 1,070 W and (B) 2,620 W laser power. Scale bar: 200 µm; magnification: ×100

bulk of melt pools.[25] In addition, no η phase (Ni_3Ti) was observed at the grain boundaries under optical microscopy. This acicular phase may affect the ductility of the alloy by promoting intergranular fracture.[25,26] The absence of the η phase suggests that the heat treatment was effective at preventing titanium segregation.

The grain size was compared between the samples processed at 0° with 1,070 W and 2,620 W, revealing average grain diameters of 189 µm and 181 µm, respectively. Figure 9 shows the microstructure of samples at 0°, 20°, and 30° processed at 1,070 W, with measured grain sizes at 189 µm, 196 µm, and 186 µm, respectively. The results for grain size are summarized in Table 5. In addition, no microcracks were found in the polished or etched conditions of any of the samples examined.

Figure 10A shows the distribution of carbides within the γ matrix of the 0° 1,070W sample, highlighting the well-defined grain boundaries observed at higher magnification. Figure 10B shows the distribution of γ' precipitates in the γ matrix of NASA HR-1 samples used in the literature.[1] This observation suggests that the heat treatment was effective in promoting γ' formation through titanium diffusion from the grain boundaries to the grain bulk.[15] Given that physical and mechanical properties are directly related to the microstructure, it was anticipated that tensile strength, LCF, and microhardness would be very similar across all samples, due to their comparable grain size and shape, defect content, and absence of the η phase.[26,27]

3.4. Mechanical testing

3.4.1. Microhardness

Among the samples tested, the 20° 2,620 W sample exhibited the highest hardness, measuring an average of 356 HV1. However, no statistically significant differences were found when comparing the hardness values among the samples. Figure 11 presents the hardness values obtained from testing across the different samples.

3.4.2. Tensile strength

UTS, YS, and percentage elongation are compared in Figure 12. All samples exhibited elongation values approaching 40%, indicating that the increased number

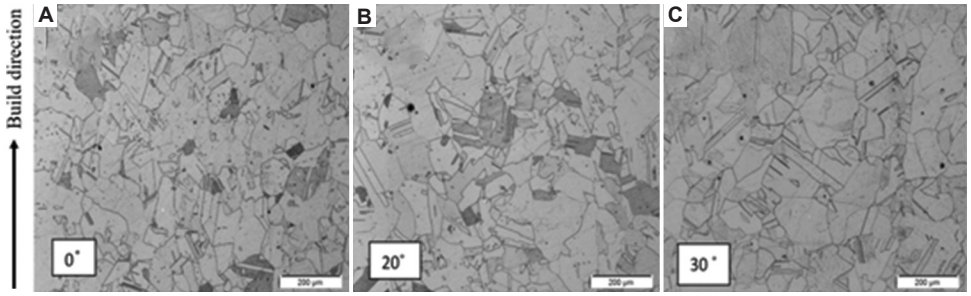

Figure 9. Samples were *printed at* (A) 0°, (B) 20°, and (C) 30° deposition *angles.* Scale bar: 200 µm; magnification: ×100

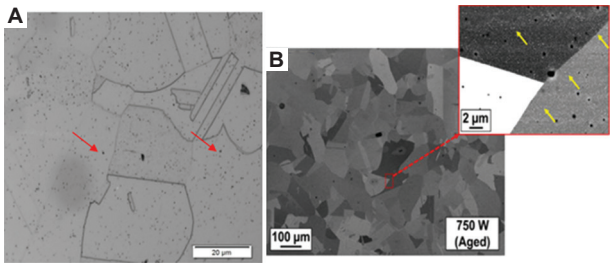

Figure 10. Distribution of carbides. (A) Sample 0° 1,070W shows the distribution of carbides within the γ matrix and (B) γ' precipitates found in literature.[1] Red arrows indicate γ' precipitates under optical microscope. Yellow arrows also indicate γ' under scanning electron microscope. Scale bar: (A) 20 µm, (B) 100 µm; magnification: ×500

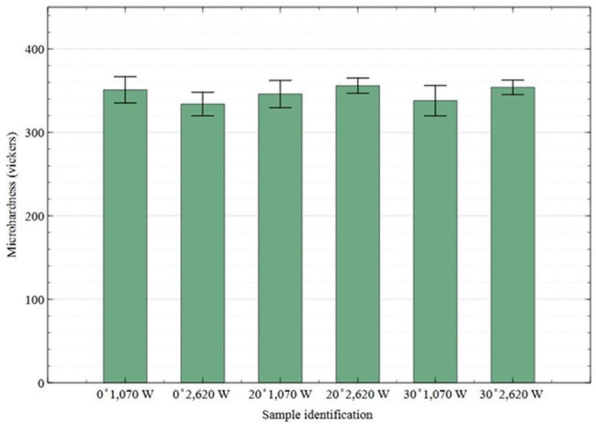

Figure 11. Graphical comparison of microhardness on laser powder direct energy deposition heat-treated samples deposited with different deposition angles or laser power.

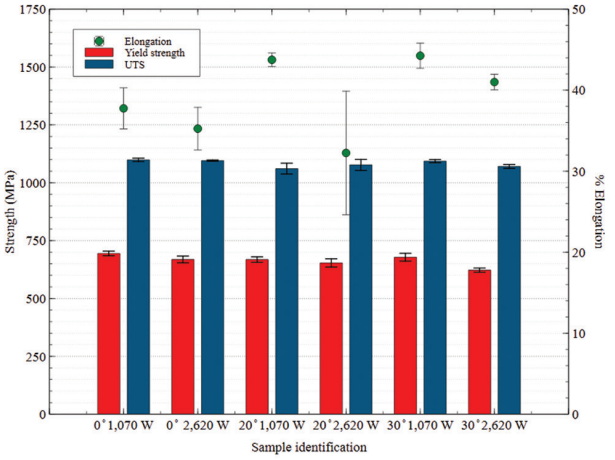

Figure 12. Tensile properties of laser powder direct energy deposition heat-treated samples printed with different deposition angles deposition or laser power

Table 5. Comparison of grain size measured on XY plane on laser powder direct energy deposition NASA HR-1 angled walls

Sample	Average grain size (µm)
0° 1,070 W	189
0° 2,620 W	182
20° 1,070 W	195
20° 2,620 W	194
30° 1,070 W	188
30° 2,620 W	193

of defects present in the 2,620 W samples did not affect the ductility of the material.[28] However, the 20° 2,620 W sample showed a slightly lower elongation of approximately 30%. This sample also showed a significantly higher standard deviation compared to the rest, which may be attributed to possible local process instabilities or material abnormalities, such as residual porosity, thermal stress, or internal defects.[29] Despite these variations, the UTS and YS of sample 2,620 were not statistically different from those of the other samples. This consistency can be linked to the similar grain size across all samples. In addition, the strength shown by the alloy is likely related to the γ' strengthening mechanism used for this material, which enhances strength without compromising ductility.[1,2]

Overall, no significant differences were found when varying laser power or deposition angles, as confirmed by the *t*-test. The only property that showed a statistically significant difference was the YS of the 20° 2,620 W sample

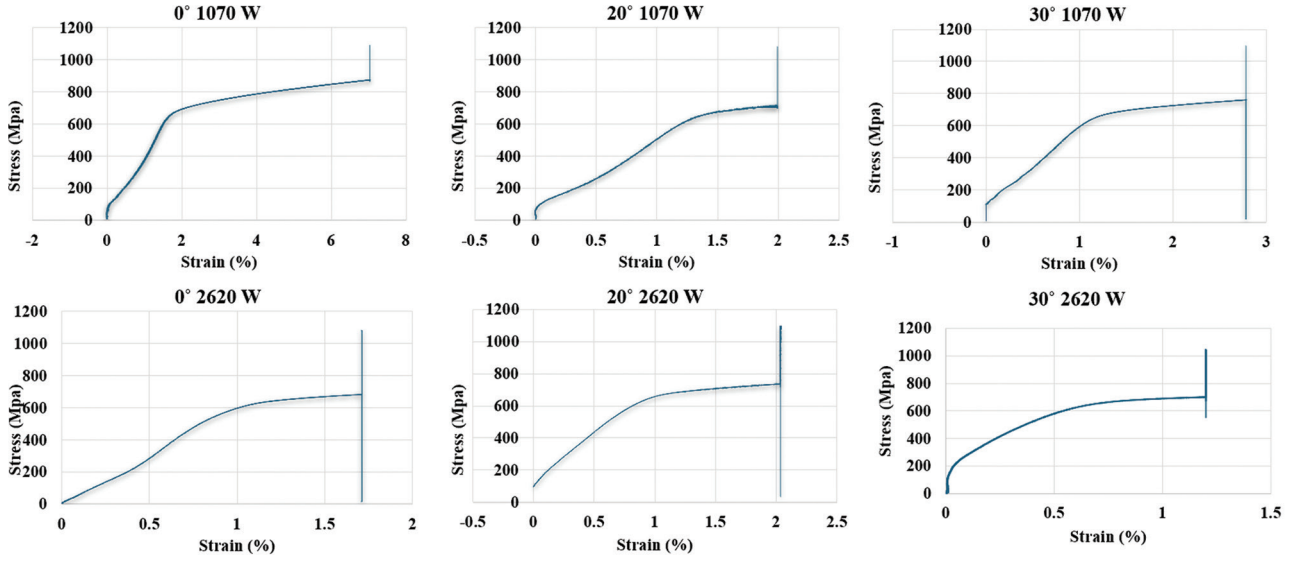

Figure 13. Tensile curves of laser powder direct energy deposition heat-treated samples printed with different deposition angles or laser power

when compared to the 0° sample. However, this difference was not found when compared to the 30° sample. This suggests that the statistical difference observed is insufficient to conclude that YS is being affected at this deposition angle, as other evidence does not support this statement. Figure 13 shows one tensile curve for each sample, illustrating their mechanical performance characteristics.

One sample from each build angle and laser power setting was selected to examine the fracture surface and compare their fracture behavior. Figure 14 shows the fracture surface of the 0° 1,070 W sample as observed under an SEM. Gas-entrapped pores, indicated by red arrows, were observed at the center of the sample and were found more frequently in the 2,620 W samples, corroborating the results found during porosity measurements. In addition, all fractured surfaces exhibited dimples and cup-and-cone features, with small cleavage areas showing a predominant ductile fracture mechanism.[30] The dimples measured approximately 2 µm in diameter and were consistent across different laser power settings and build angles. The fracture appearance suggests that it resulted from micro-void coalescence, with gas entrapment potentially contributing to fracture propagation. This behavior was observed in all samples, regardless of deposition angle or laser power.

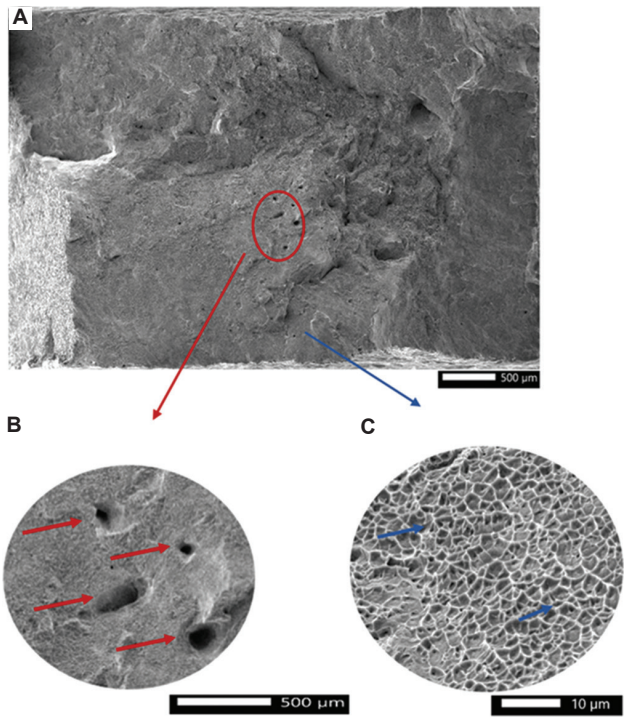

Figure 14. The fracture surface of (A) specimen 0° 1,070 W observed under a scanning electron microscope. (B) The defects were found to be more concentrated at the center of the sample surface. Red arrows indicate gas-entrapped pores. (C) The fractured surface at a higher magnification (×1,000) showing the formation of dimples (blue arrows). Scale bar: (A & B) 500 µm, (C) 10 µm; magnification: (A) ×23, (C) ×1,000

3.4.3. LCF

The fatigue life of all samples was compared in terms of the number of reversal cycles required to failure (Nf) at high stress (~694 MPa), as shown in Figure 15. The 0° 2,620 W sample was the only one capable of withstanding nearly 6,000 reversal cycles. This sample also showed a higher standard deviation compared to the rest of the samples, which may be attributed to the previously mentioned abnormalities. Statistical analysis demonstrated that the number of cycles to failure was not significantly different

among the samples. All samples printed at 1,070 W, regardless of their angles (0°, 20°, and 30°), showed no statistical differences, as *P*-values were greater than 0.05 during testing. Furthermore, *t*-tests indicated no significant difference between the 1,070 W and 2,620 W samples. This similarity in fatigue behavior can be attributed to the comparable grain size and γ' distribution across the samples, as these features can impede the propagation of fatigue cracks.[27,31]

One sample from each build angle and laser power setting was selected for observation under an SEM to evaluate the fractured surface. Figure 16A shows multiple initiation sites (indicated by red arrows) at the edges of the fractured sample. In Figure 16B, striations are visible in different planes at one corner of the sample, resulting from cyclic loading. This observation suggests that cracks initiated at the surface of the flat testing bars, particularly at the corners, and subsequently propagated toward the opposite edge of the sample until complete rupture occurred. This behavior can be attributed to sharp corners acting as stress concentrators, which promote fatigue crack initiation.[32,33]

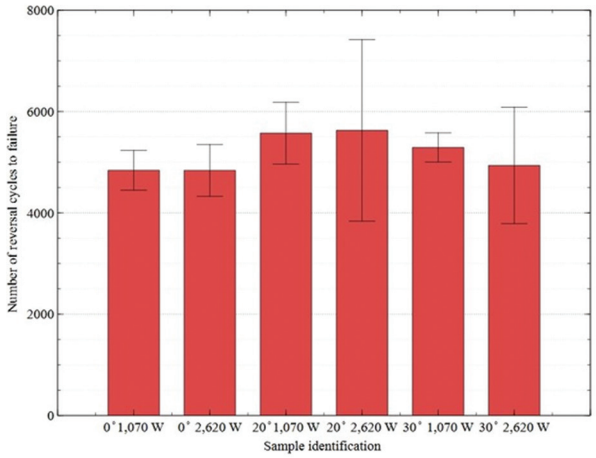

Figure 15. Comparison of reversal cycles required for the failure of laser powder direct energy deposition heat-treated samples printed with different deposition angles or laser power

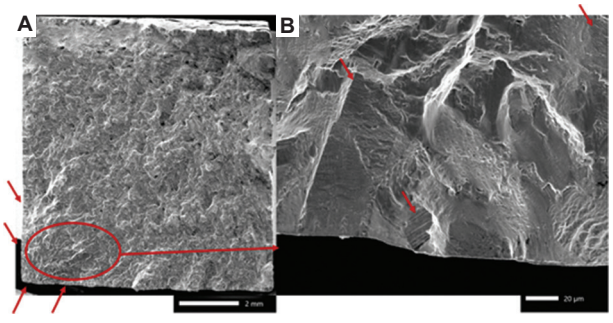

Figure 16. Scanning electron microscope image of the 0° 1,070 W sample. Images captured at (A) ×10 magnification and (B) ×200 magnification showing the formation of striations. Red arrows indicate multiple initiation sites. Scale bar: (A) 2 mm, (B) 20 µm; magnification: (A) ×10, (B) ×200

4. Conclusion

In this study, LP-DED NASA HR1 angled walls were manufactured using two different parameter sets, 1,070 W and 2,620 W, and three deposition angles: 0°, 20°, and 30°. The samples underwent a comprehensive heat treatment process comprising stress relief, homogenization, solution annealing, and aging. Evaluations were conducted following heat treatments, including tensile and low-cycle fatigue testing. The following conclusions were obtained based on the results:

(i) Increasing the laser power from 1,070 W to 2,620 resulted in a higher defect content due to increased porosity. This increase can be attributed to gas being more easily entrapped in the deeper melt pools created by higher laser power. Despite the rise in porosity, the mechanical properties of NASA HR-1 appeared unaffected.

(ii) After heat treatment, all samples formed an austenitic microstructure, effectively eliminating the dendritic microstructure typically formed by LP-DED due to rapid cooling rates. In addition, the heat treatment successfully produced a homogeneous microstructure across all samples, with no-η phase observed at grain boundaries under optical microscopy.

(iii) During tensile testing, the YS of the 20° samples was slightly lower compared with the 0° and 30° samples. However, this was the only statistical difference observed during the study. UTS and elongation values indicated all samples performed similarly. Microhardness was also unaffected by variations in processing parameters or build angles after heat treatment.

(iv) In terms of LCF life, the number of reversal cycles required for failure at high stress (~700 MPa) was not significantly different among the samples. This suggests that fatigue life remains consistent regardless of variations in parameters following heat treatment.

Acknowledgments

The authors would like to acknowledge the support from the NASA Marshall Space Flight Center. We are grateful to the Keck Center for providing the facilities and equipment needed to perform the experiments required for this study. Finally, we appreciate our colleagues and peers from the University of Texas at El Paso (UTEP) for their encouragement and insightful discussions that contributed to the successful completion of this project.

Funding

Primary funding was provided by grant number 80NSSC23PC201 from the NASA Marshall Space Flight.

Conflicts of interest

The authors declare that they have no financial or personal conflicts of interest that could have appeared to influence the work reported in this paper.

Author's contributions

Conceptualization: Paul Gradl, Colton Katsarelis
Formal analysis: Javier Lares, Paul Gradl, Colton Katsarelis, Francisco Medina, Edel Arrieta
Investigation: Javier Lares
Methodology: Javier Lares, Edel Arrieta, Francisco Medina
Supervision: Francisco Medina, Edel Arrieta, Paul Gradl
Writing – original draft: Javier Lares
Writing – review and *editing:* Paul Gradl, Kolton Katsarelis, Edel Arrieta, Francisco Medina, Murr Lawrence

Ethics approval and consent to participate

Not applicable.

Consent for publication

Not applicable.

Availability of data

The data that support the findings of this study are available from the corresponding author on request.

References

1. Soltani-Tehrani A, Chen P, Katsarelis C, Gradl P, Shao S, Shamsaei N. Laser powder directed energy deposition (LP-DED) NASA HR-1 alloy: Laser power and heat treatment effects on microstructure and mechanical properties. *Addit Manuf Lett*. 2022;3:100097.

   doi: 10.1016/j.addlet.2022.100097

2. Chen PS, Mitchell M. Alloy NASA HR-1. *Aerospace Structural Metals Handbook;* 2005. Available from: https://ntrs.nasa.gov/api/citations/20050182936/downloads/20050182936.pdf [Last accessed on 2023 Mar 20].

3. Lee JA, Woods S. *Hydrogen Embrittlement*; 2016. p. 1-62. Available from: https://ntrs.nasa.gov/api/citations/20160005654/downloads/20160005654.pdf [Last accessed on 2024 Dec 08].

4. Birken A, Noel D. Metallurgical and thermal processing investigation of additively manufactured superalloys JBK-75 and NASA-HR-1. In: *Materials Engineering*; 2021. Available from: https://digitalcommons.calpoly.edu/matesp/233 [Last accessed on 2023 Mar 20].

5. Lu X, Ma Y, Wang D. On the hydrogen embrittlement behavior of nickel-based alloys: Alloys 718 and 725. *Mater Sci Eng A*. 2020;792:139785.

   doi: 10.1016/j.msea.2020.139785

6. Singh A, Kapil S, Das M. A comprehensive review of the methods and mechanisms for powder feedstock handling in directed energy deposition. *Addit Manuf*. 2020;35:101388.

   doi: 10.1016/j.addma.2020.101388

7. Su J, Ng WL, An J, Yeong WY, Chua CK, Sing SL. Achieving sustainability by additive manufacturing: A state-of-the-art review and perspectives. *Virtual Phys Prototyp*. 2024;19(1):e2438899.

   doi: 10.1080/17452759.2024.2438899

8. Ehmsen S, Glatt M, Aurich JC. Influence of process parameters on the power consumption of high-speed laser directed energy deposition. *Procedia CIRP*. 2023;116:89-94.

   doi: 10.1016/j.procir.2023.02.016

9. Svetlizky D, Das M, Zheng B, *et al*. Directed energy deposition (DED) additive manufacturing: Physical characteristics, defects, challenges and applications. *Mater Today*. 2021;49:271-295.

   doi: 10.1016/j.mattod.2021.03.020

10. Meng G, Gong Y, Zhang J, Jiang Z, Ren Q, Zhao J. Microstructure and mechanical properties of Inconel 718 thin walls prepared by laser direct energy deposition and selective laser melting. *Thin-Walled Struct*. 2023;193:111284.

    doi: 10.1016/j.tws.2023.111284

11. Gamon A, Arrieta E, Gradl PR, *et al*. Microstructure and hardness comparison of as-built inconel 625 alloy following various additive manufacturing processes. *Results Mater*. 2021;12:100239.

    doi: 10.1016/j.rinma.2021.100239

12. Zhi'En ET, Pang JH, Kaminski J. Directed energy deposition build process control effects on microstructure and tensile failure behaviour. *J Mater Process Tech*. 2021;294:117139.

    doi: 10.1016/j.jmatprotec.2021.117139

13. Aversa A, Marchese G, Bassini E. Directed energy deposition of AISI 316L stainless steel powder: Effect of process parameters. *Metals*. 2021;11(6):932.

    doi: 10.3390/met11060932

14. Li Z, Sui S, Ma X, *et al*. High deposition rate powder- and wire-based laser directed energy deposition of metallic materials: A review. *Int J Mach Tools Manuf*. 2022;181:103942.

    doi: 10.1016/j.ijmachtools.2022.103942

15. Hassan B, Corney J. Grain boundary precipitation in Inconel 718 and ATI 718Plus. *Mater Sci Technol*. 2017;33(16):1879-1889.

    doi: 10.1080/02670836.2017.1333222

16. *Standard Test Method for Sieve Analysis of Metal Powders*. Available from: https://compass.astm.org/document/?contentcode=astm%7cb0214-16%7cen-us&proxycl=https%3a%2f%2fsecure.astm.org&fromlogin=true [Last accessed on 2024 Jan 11].

17. *Standard Test Methods for Flow Rate of Metal Powders Using the Hall Flowmeter Funnel*. Available from: https://compass.astm.org/document/?contentCode=ASTM%7CB0213-20%7Cen-US&proxycl=https%3A%2F%2Fsecure.astm.org&fromLogin=true [Last accessed on 2024 Feb 29].

18. Schneider CA, Rasband WS, Eliceiri KW. NIH Image to ImageJ: 25 years of image analysis. *Nat Methods*. 2012;9(7):671-675.

    doi: 10.1038/nmeth.2089

19. *Standard Test Methods for Determining Average Grain Size*. Available from: https://www.astm.org/e0112-13r21.html [Last accessed on 2024 Jan 10].

20. *Standard Test Methods for Tension Testing of Metallic Materials*. Available from: https://compass.astm.org/document/?contentCode=ASTM%7CE0008-04%7Cen-US&proxycl=https%3A%2F%2Fsecure.astm.org&fromLogin=true [Last accessed on 2024 Jan 11].

21. *Standard Test Method for Strain-Controlled Fatigue Testing*. Available from: https://compass.astm.org/document/?contentCode=ASTM%7CE0606_E0606M-21%7Cen-US&proxycl=https%3A%2F%2Fsecure.astm.org&fromLogin=true [Last accessed on 2024 Jan 11].

22. E28 Committee. *Practice for Instrumented Indentation Testing*. ASTM International; 2023. Available from: https://www.astm.org/e2546-15.html [Last accessed on 2024 Jan 11].

23. Grima Cintas P, Marco-Almagro L, Tort-Martorell Llabres J. *Industrial Statistics with Minitab*. United States: Wiley; 2012.

24. Brennan MC, Keist JS, Palmer TA. Defects in metal additive manufacturing processes. *J Mater Eng Perform*. 2021;30(7):4808-4818.

    doi: 10.1007/s11665-021-05919-6

25. Ahn DG. Directed energy deposition (DED) process: State of the art. *Int J Precis Eng Manuf-Green Technol*. 2021;8(2):703-742.

    doi: 10.1007/s40684-020-00302-7

26. Layer J, Adler T, Ahmed R, *et al*. Failure analysis and prevention. In: *ASM INTERNATIONAL® Publication Information and Contributors*. Vol 11. Ohio: ASM International® The MaterialsInformation Society; 2002.

27. Lasalmonie A, Strudel JL. Influence of grain size on the mechanical behaviour of some high strength materials. *J Mater Sci*. 1986;21(6):1837-1852.

    doi: 10.1007/BF00547918

28. Du Plessis A, Yadroitsava I, Yadroitsev I. Effects of defects on mechanical properties in metal additive manufacturing: A review focusing on X-ray tomography insights. *Mater Des*. 2020;187:108385.

    doi: 10.1016/j.matdes.2019.108385

29. Frölich F, Bechtloff L, Scheuring BM, *et al*. Evaluation of mechanical properties characterization of additively manufactured components. *Prog Addit Manuf*. 2024;10:1217-1229.

    doi: 10.1007/s40964-024-00700-2

30. Bagnoli DL, Banerji K, Boardman B, *et al*. Fractography. In: *ASM INTERNATIONAL ® The Materials Information Company*. Vol 12. Ohio: ASM International® The MaterialsInformation Society; 1987.

31. Komarasamy M, Shukla S, Williams S, Kandasamy K, Kelly S, Mishra RS. Microstructure, fatigue, and impact toughness properties of additively manufactured nickel alloy 718. *Addit Manuf*. 2019;28:661-675.

    doi: 10.1016/j.addma.2019.06.009

32. Zhao B, Song J, Xie L, Hu Z, Chen J. Surface roughness effect on fatigue strength of aluminum alloy using revised stress field intensity approach. *Sci Rep*. 2021;11(1):19279.

    doi: 10.1038/s41598-021-98858-0

33. Javidi A, Rieger U, Eichlseder W. The effect of machining on the surface integrity and fatigue life. *Int J Fatigue*. 2008;30(10-11):2050-2055.

    doi: 10.1016/j.ijfatigue.2008.01.005

ACCSCIENCE PUBLISHING

Materials Science in Additive Manufacturing

ORIGINAL RESEARCH ARTICLE

Topology optimization of an aluminum bicycle pedal crank using laser powder bed fusion

Jose Manuel Costa[1,2]*, Mariana Cerqueira Maia[1], Adriana Pinho Fernandes[1], Elsa Costa Oliveira[1], Manuel Fernando Vieira[1,2], and Elsa Wellenkamp Sequeiros[1,2]

[1]Department of Mechanical Engineering, Faculty of Engineering, University of Porto, Porto, Portugal

[2]LAETA, Institute of Science and Innovation in Mechanical and Industrial Engineering, Porto, Portugal

Abstract

This study investigates the application of topology optimization (TO) in combination with laser powder bed fusion (LPBF) to design a lightweight, high-performance bicycle pedal crank using AlSi10Mg alloy. The optimization process was carried out using Fusion 360 and nTopology, resulting in a 20% mass reduction while ensuring compliance with the ISO 14781 standards for pedal cranks. The component was characterized in terms of microstructure, surface roughness, dimensional accuracy, powder distribution, and Vickers hardness. The microstructure exhibited the characteristic melt pool patterns associated with LPBF, indicative of the manufacturing process. Surface roughness measurements showed a mean value of 23.4 µm, with dimensional analysis revealing a mean deviation of 7% from nominal dimensions. The powder distribution analysis indicated a narrow particle size distribution, contributing to consistent print quality. The component's hardness was measured at 134 HV0.3, highlighting its promising mechanical properties. This work demonstrates the potential of TO and LPBF to produce structurally optimized, lightweight components with enhanced performance, providing valuable insights into the application of Design for Additive Manufacturing for metallic materials.

Keywords: Bike crank; AlSi10Mg; Laser powder bed fusion; Design for Additive Manufacturing; Topology optimization; Metallographic characterization; Roughness dimensional analysis; Powder characterization

***Corresponding author:**
Jose Manuel Costa
(jose.costa@fe.up.pt)

Citation: Costa JM, Maia MC, Fernandes AP, Oliveira EC, Vieira MF, Sequeiros EW. Topology optimization of an aluminum bicycle pedal crank using laser powder bed fusion. *Mater Sci Add Manuf.* 2025;4(1):025040003. doi: 10.36922/MSAM025040003

Received: January 24, 2025

1st revised: February 15, 2025

2nd revised: February 18, 2025

3rd revised: February 20, 2025

Accepted: February 21, 2025

Published online: March 26, 2025

1. Introduction

Technological advancements continue to revolutionize the manufacturing sector, with additive manufacturing (AM) at the forefront of these innovations. AM is poised to significantly impact sustainability and society at large, offering transformative solutions across various industries.[1] ISO/ASTM 52900:2021 defines AM as joining materials to fabricate parts from three-dimensional (3D) model data, typically layer upon layer, diverging from traditional subtractive and formative manufacturing methodologies.[2,3] This method facilitates the construction of lightweight structures with complex geometries by emulating biological processes inspired by biomimetic principles.[4] The principal advantages of AM include diminished production expenses, enhanced

geometric versatility, customization potential, generative design, and waste minimization.[5,6] These attributes are pivotal across environmental, social, and economic dimensions.[3,7]

Even with this, AM has limitations. It has not fulfilled all prognosticated expectations despite being integrated into the big data revolution. Compared to traditional manufacturing techniques, challenges include mass production scalability, size constraints, surface finishing imperfections, and the costs associated with raw materials, equipment, and initial capital.[8,9]

Various AM technologies have been broadly adopted, including fused filament fabrication, powder bed fusion (PBF), stereolithography, selective laser sintering, and digital light processing.[10,11] The selection among these technologies is predicated on the desired functional, esthetic, and mechanical outcomes alongside financial considerations.[12] Critical factors include part volume, layer volume, material deposition rate, and the balance between material flexibility and mechanical requirements. AM materials span polymers, metals, ceramics, and composites in diverse forms such as liquid, wire, powder, or sheet.[9,12,13]

AM furnishes extensive modeling capabilities through various design instruments that enable engineers and designers to forecast mechanical responses and economic viability and automate part manufacturing processes.[14] Among these, PBF systems, capable of utilizing either electron beam or laser energy sources, offer exceptional versatility. This article focuses on laser PBF (LPBF), an AM technology classified by ISO/ASTM. LPBF employs concentrated thermal energy from a laser to fuse materials, depositing them layer by layer.[10]

The LPBF process is initiated with a 3D computer-aided design (CAD) model and machine programming, encompassing material loading, thermal heating, and environmental setup (either vacuum or protective gas). A recoater deposits a powder layer onto a construction plate, followed by selective laser melting of the powder according to predetermined parameters. The construction plate descends for each layer, replicating the process until the component is complete. Post-processing involves component removal, heat treatment, and finishing to achieve desired performance standards.[1]

Raw material characteristics are vital in the LPBF process, determining the final component's mechanical and physical properties. Spherical powders, produced through gas atomization, are preferred for their enhanced fluidity during deposition, contributing to reduced porosity and satisfactory surface quality.[15,16] The spherical geometry aids in stable molten pool formation and elevated packing density – Van der Waals forces, particle radius, and friction influence powder flowability. Smaller particles with increased surface areas encounter augmented Van der Waals forces and friction, impeding fluidity during layer formation. Non-spherical shapes further augment the surface area, adversely affecting flowability.[17-21]

AM technologies, such as LPBF, provide the flexibility to fabricate complex geometries and intricate internal features. By integrating Design for AM (DfAM), the design process can be optimized to leverage these capabilities fully, enabling the production of lightweight, highly functional parts.[22-24] Topology optimization (TO) is used in the DfAM approach, and it is a numerical approach that identifies the optimal material distribution within a given design space to achieve the desired functionality, enhancing performance while minimizing material usage.[25-27] The TO approach algorithmically determines the most structurally efficient design within a defined space and under given constraints, resulting in organic, optimized shapes that use material only where necessary for structural integrity.[23,28,29]

The integration of TO (and DfAM) in AM enhances components' structural performance and material efficiency and plays a significant role in improving the sustainability of manufacturing processes. TO reduces material waste, optimizes distribution within a given design space, and ensures that only the necessary material is used for structural integrity. This reduces both the material consumption and the overall weight of the part, contributing directly to sustainability. TO and AM technologies such as LPBF contribute to energy efficiency.[30,31] The ability to fabricate complex geometries that would be impossible or highly inefficient to produce using traditional subtractive manufacturing methods allows for more efficient use of resources. By reducing material usage and minimizing waste during the manufacturing process, TO and AM provide an effective strategy for lowering the environmental impact of industrial production.[3,23]

Previous studies, such as those by Mata *et al.*[32] and Oliveira *et al.*,[24] have explored the successful integration of DfAM and TO in designing various components, showcasing how these approaches enable the creation of highly efficient, lightweight structures. Mata *et al.* optimized a metal door-handle design using nTopology and AM, focusing on lattice structures and generative design to reduce weight and enhance mechanical properties. Similarly, Oliveira *et al.* applied DfAM and TO to an office stapler, leveraging MEX technology for mass reduction without compromising the part's mechanical integrity. These studies illustrate the effectiveness of DfAM and TO in producing lightweight, efficient structures, a

crucial aspect for applications in industries ranging from aerospace to consumer products.

In this context, LPBF is particularly advantageous for materials such as AlSi10Mg, an aluminum alloy known for its low density, high thermal conductivity, and good mechanical properties. This makes AlSi10Mg ideal for creating lightweight, cost-efficient products. The integration of DfAM and TO enhances LPBF by optimizing material distribution within a design space, enabling the creation of complex geometries, including internal lattices, which are often impractical or impossible to achieve with traditional manufacturing methods.[1,33,34]

This investigation endeavors to optimize a bicycle pedal crank component for fabrication through AM, explicitly employing LPBF with an aluminum alloy (AlSi10Mg). The objective is to substantiate its production viability and catalyze interest for future integration into the market.

2. Materials and methods

2.1. TO and manufacturing

The first step in designing the bike component was to model the conventional component. For this, the Shimano SLX M7000 Hollowtech II Crank[35] was used as a base model with a crank length of 170 mm. The conventional model was developed to fit an 82/61 mm pedal. Figure 1 shows the model canvas and the resulting component.

From this point onward, the optimization process for AM began to minimize the mass of the component while ensuring a safety factor of 2 as per the typical design standards. It was essential to define the design variables, which were chosen based on a typical usage scenario for a bicycle pedal crank and the requirements outlined in ISO 14764:2022.[36] According to this standard, the deflection of the crank arm should not exceed 20%. The standard specifies that a fatigue test must be performed to assess the component's performance, with a dynamic force of 1300 N

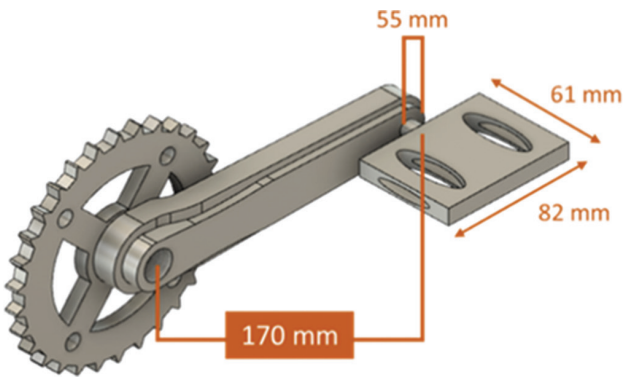

Figure 1. Model canvas and the resulting modeling component of a conventional bike crank

applied over 100,000 cycles.[36] In this study, however, the safety factor was not directly measured but retrieved from industry standards and bibliographical sources that align with the material properties and typical loading conditions for similar components. This was used as a design criterion to guide the optimization process.

The TO process used the GD module in Autodesk Fusion 360 (San Francisco, CA, USA). The following procedure was adopted to achieve an optimized design suitable for AM:

1. *Initial setup.* The optimization began by defining the geometries to preserve (parts of the component that need to remain intact) and obstacle geometries (areas where material could not be added). These parameters were essential to ensure the final design adhered to functional and manufacturing constraints
2. *Design constraints and load cases.* A set of boundary conditions and load cases was applied, as prescribed by ISO 14781.[10] These constraints included:
   (a) Pin and fixed geometries: To simulate the component's attachment to the bike and fix its orientation
   (b) A 1300 N load was applied to the crank arm, simulating the forces during cycling
   (c) A safety factor of 2 was defined to ensure the design met structural integrity requirements under typical operating conditions
3. *Material selection.* The material selected for the optimization process was AlSi10Mg alloy, chosen for its low density and high specific mechanical resistance (UTS/density, Young's modulus/density), making it ideal for LPBF applications
4. *Manufacturing constraints.* The AM process was defined with specific constraints:
   (a) An overhang angle of 45° was allowed to ensure manufacturability
   (b) A minimum material thickness of 3 mm was enforced to maintain the part's structural integrity during printing
5. *Optimization and design generation.* The optimization process was executed using Fusion 360's GD module, which utilized the specified load cases and constraints to generate the optimized crank model. The resulting design aimed to reduce mass while maintaining the required safety factor and ensuring functionality.

The study setup and the resulting best outcome are shown in Figure 2.

After generating the optimized model, it was subjected to a simulated static test in the software's simulation module. The same constraints and loads used for the optimization were considered. Based on the resulting

values and the designer's critical opinion, some adaptations were made to improve the component to improve the safety factor to 5. When a safety factor of 5.24 was attained, the component was transferred to new software, nTopology. The topologically optimized was used to add interior (Figure 3A) and external lattices (Figure 3B) to the component. The lattices were introduced to increase the complexity of the part in the study since this research has developed as a hands-on teaching technique. The first lattice was created in the solid part of the component, and the exterior lattice was used to substitute the central depression in the model, intending to decrease mass and improve esthetic appeal.

In the TO process, the first step involved the introduction of an internal lattice within the solid part of the component (Figure 3A). This lattice structure was specifically designed to optimize the internal support of the crank while simultaneously reducing the overall mass. Following this, an external lattice structure was applied to replace the central depression in the crank (Figure 3B). The external lattice not only aimed to reduce the weight further but also contributed to the esthetic appeal of the part, ensuring that both functional and visual considerations were addressed in the optimization process.

Once the optimized design with the added lattices was finalized, a final static test was conducted within nTopology, maintaining the same load and displacement constraints. The results of these tests will be discussed in section 3.2.

The LPBF process was used to manufacture the final component. The components were produced using a Renishaw AM400 machine (Wotton-under-Edge, United Kingdom) at Hypermetal–Metal AM (Porto, Portugal). The manufacturing process was prepared using Renishaw's software, which defined the part orientation, added necessary supports, and adjusted the laser parameters for optimal printing.

The part was printed using 30-micron layers with a stripe strategy and block path. To conserve resources, the bike crank was produced at a 1/5th scale. Once printed, the supports were mechanically removed, and the part was micro-sandblasted using a Guyson machine (North Yorkshire, United Kingdom).

Despite the scale reduction, all static simulations were performed with the accurate dimensions of the full-size crank. The size reduction impacts only manufacturability, as it could present challenges in ensuring adequate heat dissipation in intricate features, such as lattices, which could affect print success.

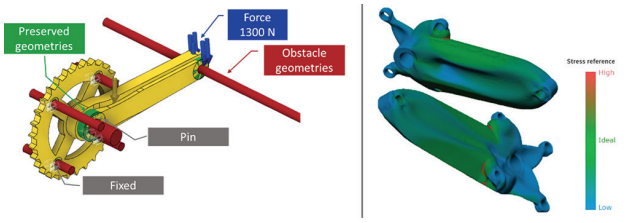

Figure 2. Study setup and the best resulting bike crank (the color scheme displays the stress distribution on the safety factor defined)

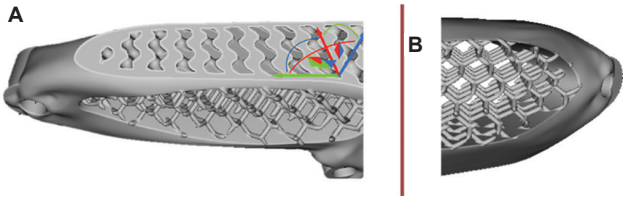

Figure 3. Topology optimization of a bike crank. (A) Interior lattice developed in the solid part of the component; (B) exterior lattice developed in the central depression

2.2. Powder characterization and chemical composition of AlSi10Mg alloy

This study used powders of an aluminum alloy, AlSi10Mg, from Osprey (Sandvik, Sandviken, Sweden). The chemical composition is shown in Table 1.

Figure 4 shows scanning electron microscopy (SEM) images of AlSi10Mg metal powders supplied by Hypermetal (Porto, Portugal), using Osprey powder as the feedstock material. The powders were analyzed using SEM/energy-

Table 1. Chemical composition of AlSi10Mg alloy from Osprey[37]

Al	Si	Mg	Fe	Ti	Mn	Cu	Ni
Balance	9 – 11	0.2 – 0.4	≤0.55	≤0.15	≤0.45	≤0.03	≤0.04

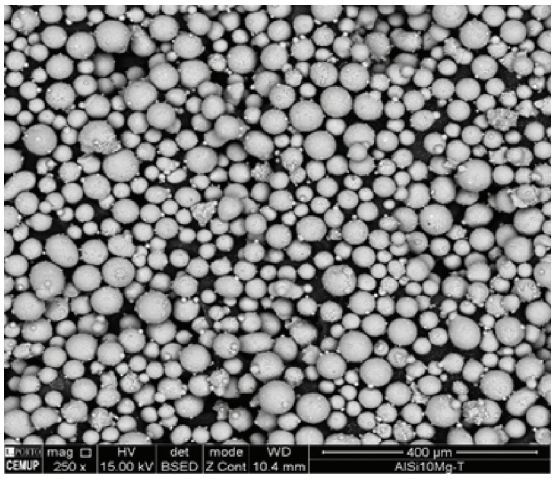

Figure 4. SEM images of AlSi10Mg metal powders supplied
Abbreviation: SEM: Scanning electron microscopy

dispersive X-ray spectroscopy electron microscopy at the Materials Centre of the University of Porto (CEMUP, Porto, Portugal).

The study focused on three zones (indicated in Figure 5), confirming the predominant presence of aluminum, silicon, and magnesium in the matrix, which aligns with the nominal chemical composition of the alloy.

2.3. Metallography and roughness measurement

To avoid the destruction of the topologically optimized component in its mechanical characterization, Hypermetal provided an additional cube with a prismatic shape, produced under the same processing conditions as the topologically optimized bicycle pedal crank using LPBF. The prismatic sample was chosen to facilitate microstructural characterization and surface roughness measurements, which were more easily performed on this simpler geometry than the pedal crank's complex geometry. Due to the pedal crank intricate shape, it was challenging to achieve flat surfaces for accurate roughness testing. A schematic representation of the experimental procedure, including the use of both the prismatic sample and the pedal crank, is shown in Figure 6.

The surface roughness analysis was achieved using the LAX software and was conducted on two components, aiming for a more precise construction of the topological profile, considering different axial references. In parallel, a non-destructive visual inspection test was performed to detect possible surface defects. The cutting was done with an abrasive disc in the equipment designated for this purpose – Presi Mecatome T210 (Eybens, France). The metallographic preparation comprised the steps of hot mounting in acrylic resin, using the equipment Buehler SIMPLIMET 1000 (Leinfelden-Echterdingen, Germany), grinding to 4000 µm abrasive sandpaper, smoothing in 1 µm cloth, and etching (0.5% hydrofluoric acid + 99.5% water) for 1 min. Micrography was obtained using the Leica® DVM6 (Wetzlar, Germany) equipment and its analysis software – LAX. Thus, the melt pool size was not directly measured in this study, it influences heat distribution and solidification is a known factor in LPBF. Understanding its potential impact on material properties is important. While the precise measurement of melt pool size requires further experimentation, this study focused on optimizing process parameters that influence the final part quality. The dimensions of the melt pools were measured using the image processing software ImageJ on the micrographs obtained. Finally, to complete the mechanical characterization, Vickers microhardness measurements were carried out with SHIMADZU M microdurometer (Kyoto, Japan) and Duramin software (Kyoto, Japan) along 14 sample points, applying a weight of 0.3 kgf following standard ISO 6507-1: 2011.

3. Results and discussion

3.1. Microstructure analysis

Figure 7 presents the microstructure of an AlSi10Mg component produced via LPBF, revealing a characteristic fish-scale pattern of molten pools that emphasizes the build direction. The microstructure displays elongated cells along the laser scan path, while cells appear more equiaxed in the direction perpendicular to the scan path. Three distinct regions within the melt pool microstructure are observable: the core of the pool, which contains finer cellular structures; an intermediate region characterized by coarser cells; and the heat-affected zone, which exhibits a partially disrupted cellular structure. The heat-affected zone is typically found at the boundary of the melt pools, where the cooling rates diverge significantly, leading to microstructural variation and changes in material properties such as strength and porosity.[38]

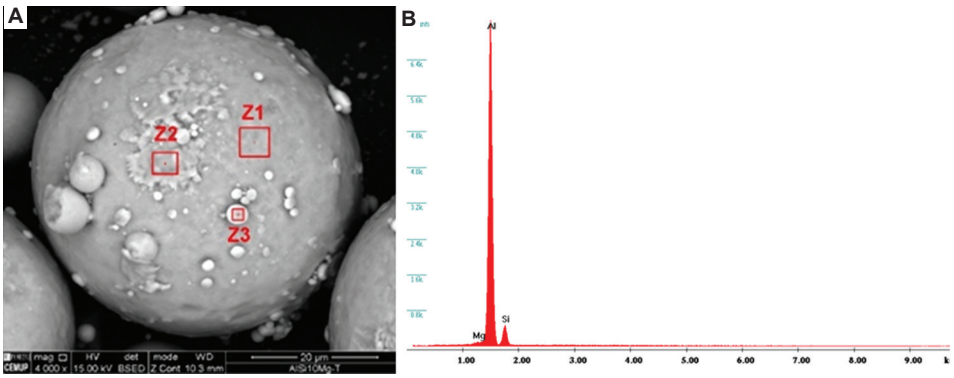

Figure 5. SEM/EDS analysis of AlSi10Mg powders. (A) SEM image shows the locations of the analysis areas marked as Z1, Z2, and Z3, selected for EDS analysis. Scale bar: 20 µm. (B) The corresponding EDS spectrum of the analyzed powder confirms the predominant presence of aluminum (Al), silicon (Si), and magnesium (Mg), consistent with the nominal chemical composition of the alloy
Abbreviation: EDS: Energy dispersive X-ray spectroscopy; SEM: Scanning electron microscopy

While melt pool size was not the primary focus of this study, it is essential for understanding heat distribution and solidification behavior during LPBF. As demonstrated in previous studies,[1,2] melt pool dimensions significantly influence material properties, including porosity, strength, and microstructural integrity. To accurately characterize these effects, it is recommended that future investigations employ single-track experiments, which provide more precise measurements of the melt pool, especially at the top surface (last layer), where no subsequent layers affect the measurements.

1 A novel paradigm for feedback control in LPBF: layer-wise correction for overhang structures
E. Vasileska, A. G. Demir, B. M. Colosimo and B. Previtali
Advances in Manufacturing 2022 Vol. 10 Issue 2 Pages 326-344
DOI: 10.1007/s40436-021-00379-6

2 A Review on Discrete Element Method Simulation in Laser Powder Bed Fusion Additive Manufacturing
H. Chen, Y. Sun, W. Yuan, S. Pang, W. Yan and Y. Shi
Chinese Journal of Mechanical Engineering: Additive Manufacturing Frontiers 2022 Vol. 1 Issue 1 Pages 100017
DOI: https://doi.org/10.1016/j.cjmeam.2022.100017

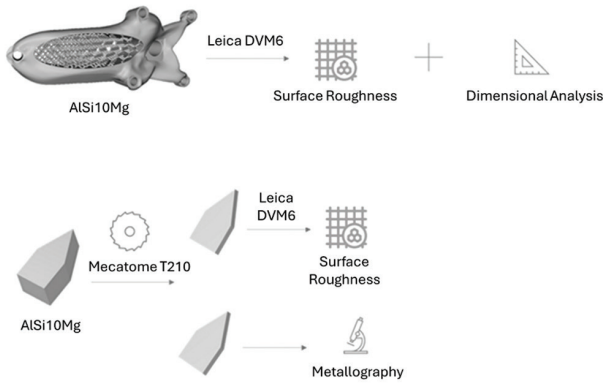

Figure 6. Experimental procedure for microstructural and mechanical characterization

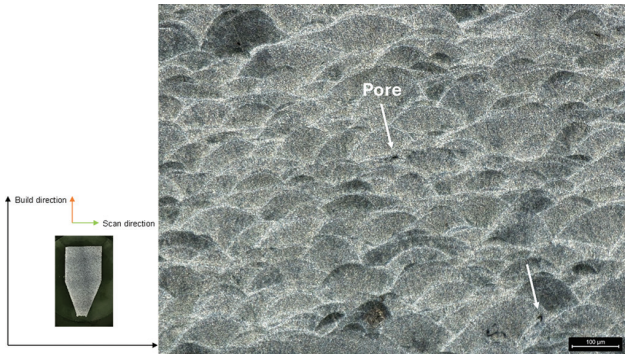

Figure 7. An optical micrograph of melt pools perpendicular to the build direction of AlSi10Mg shows the characteristic fish-scale pattern, with elongated cells along the laser scan path and equiaxed cells perpendicular to it. Scale bar: 100 μm

In this study, melt pool dimensions were analyzed using ImageJ software (Figure 8), revealing an average width (W) of 153.6 μm (in purple) and a depth (h) of 60.7 μm (in green). These values were obtained from the laser scan tracks on the last layer, as these tracks are unaffected by remelting during subsequent layers. For a more detailed characterization of the melt pool, including its chemical composition and morphological changes, we recommend utilizing advanced techniques such as transmission electron microscopy (TEM),[39] and SEM with electron backscatter diffraction.[38,40,41]

3.2. Simulation of static test

The topologically optimized component (Figure 2), with an initial mass of 886 g, underwent a static load test under a 1300 N load. The maximum local stress during static loading under 1300 N is 214 MPa, which is below the yield strength of AlSi10Mg (240 MPa). This results in a safety factor of 1.12. While no plastic deformation is expected under typical loading conditions, elastic deformation may still occur, particularly in the lattice structure. Lattice structures, designed to optimize material usage and reduce weight, behave differently under load than solid components due to internal voids. These internal voids lead to localized strain, resulting in elastic deformation without exceeding the yield strength. This deformation is reversible, and the material returns to its original shape once the load is removed. While the simulation suggests that the component will not undergo permanent deformation under the applied load, the safety factor derived from stress analysis may vary depending on the specific criteria and calculation method. Simulation plays a crucial role in predicting the mechanical behavior of components and guiding design adjustments before manufacturing. However, static simulations are not a substitute for empirical mechanical testing. Fatigue testing remains essential to ensure

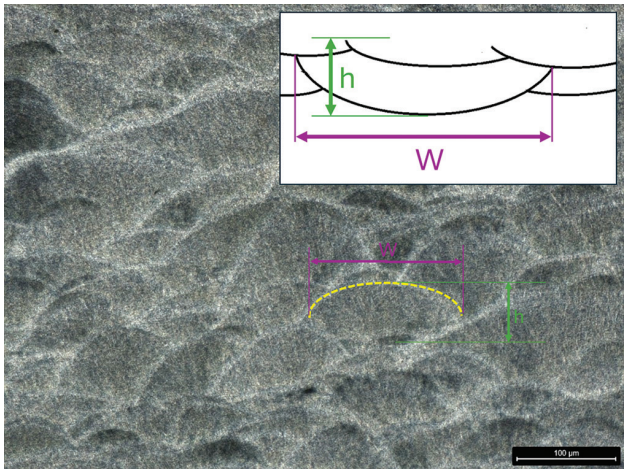

Figure 8. Melt pools' dimensions. Scale bar: 100 μm

compliance with industry standards and verify long-term durability under cyclic loading conditions.

Figure 9A and B present the final component obtained. Strain distribution in the component was relatively uniform, with a maximum value of 0.0016. The maximum stress, an important metric for evaluating permanent deformation, was recorded at 214 MPa, below the material's yield strength of 240 MPa. This suggests that no permanent deformation is expected under the 1300 N load.

Figure 10 shows the simulation results where some local deformation is indicated in the region of maximum stress, especially near the lattice structures. These regions with stress concentrations warrant further investigation to optimize performance and enhance the structural integrity in these localized areas.

Lattices are commonly used in AM for their ability to reduce weight while maintaining strength. However, lattice design can be complex as cell geometry must be carefully chosen to ensure structural performance and manufacturability. In this study, a hive structure lattice was selected, which achieved a nearly 50% weight reduction, resulting in a final component mass of 458 g. This design provides the required mechanical integrity while ensuring manufacturability within the LPBF process.

3.3. Roughness analysis

Despite advancements in process optimization, surface roughness in parts produced by LPBF remains highly variable. Li *et al.*[42] highlighted that laser energy density and part orientation significantly influence surface roughness. This characteristic is critical, as surface roughness directly affects the component's interaction with its environment, performance in service, and manufacturing costs.

Given the anisotropic properties of AM components, a comparative study assessed the roughness of two surfaces on the opposite sides of a complementary part. This analysis examined the W-profile in both transversal and longitudinal directions, and the same was true for the component. The study adhered to the ISO 4287[43] and ISO 25178[44] Standards. It is essential to note that only one profile was evaluated per direction, and therefore, the reported values may only partially represent the surface quality across the entire part.

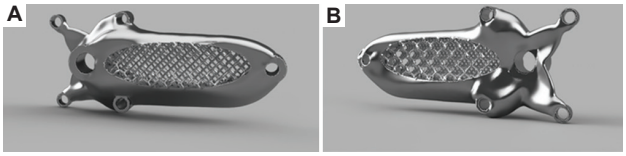

Figure 9. Illustration of the final component obtained: (A) front view, (B) back view

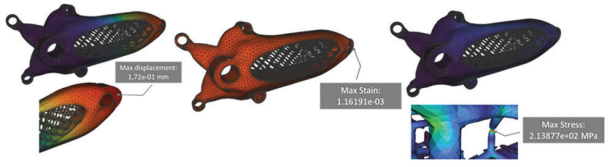

Figure 10. Results of the static test held in nTopology (1300 N)

The arithmetical mean roughness (Ra) and mean roughness depth (Rz) are widely used parameters to characterize surface roughness; however, more parameters are needed to provide more insight into surface features. Ra gives a mean value unaffected by surface variation and does not account for the shape of the surface; profiles with different geometries may share the same Ra. Similarly, Rz does not fully capture surface fluctuation details. In this study, the transversal direction exhibited a Ra of 6.71 µm, whereas the longitudinal direction had a Ra of 5.47 µm (Figure 11). The corresponding Rz values were 22.4 µm and 19.5 µm, respectively. The maximum peak height (Rp) in the transversal direction was 9.88 µm; in the longitudinal direction, it was 7.73 µm. The deepest valley (Rv) reached 12.6 µm and 11.8 µm in the transversal and longitudinal directions, respectively. The total roughness (Rt) was 33.3 µm in the transversal direction and 54.6 µm in the longitudinal direction, the latter exhibiting higher roughness due to its alignment with the build direction.

On the opposite side of the part (Figure 12), lower roughness values were observed, with a Ra of 3.56 µm in the transversal direction and 3.77 µm longitudinally. The Rz values were 12.8 µm and 14.7 µm, respectively. The maximum peak heights (Rp) were 6.07 µm in the transversal profile and 6.55 µm in the longitudinal one. The deepest valleys (Rv) were 6.75 µm and 8.10 µm, respectively. For the total roughness (Rt), the values were 31.1 µm in the transversal direction and 23.1 µm longitudinally, with the higher roughness remaining in the longitudinal direction.

It was found that overall roughness values were higher on the first face. However, these various are very common in this technology since the roughness will vary with a lot of factors, namely the position of the part relating to the argon flow, part orientation (down skins vs. up skins), and support location. Furthermore, the Roughness Directional Coefficients (Rdc) was higher on the first face, with values of 15.3 µm in the transversal and 10.9 µm in the longitudinal direction, compared to 6.93 µm and 6.54 µm on the second face. These differences in section height may have contributed to the disparity in roughness measurements.

Tribological parameters, such as skewness (Rsk) and kurtosis (Rku), provide additional insights into surface

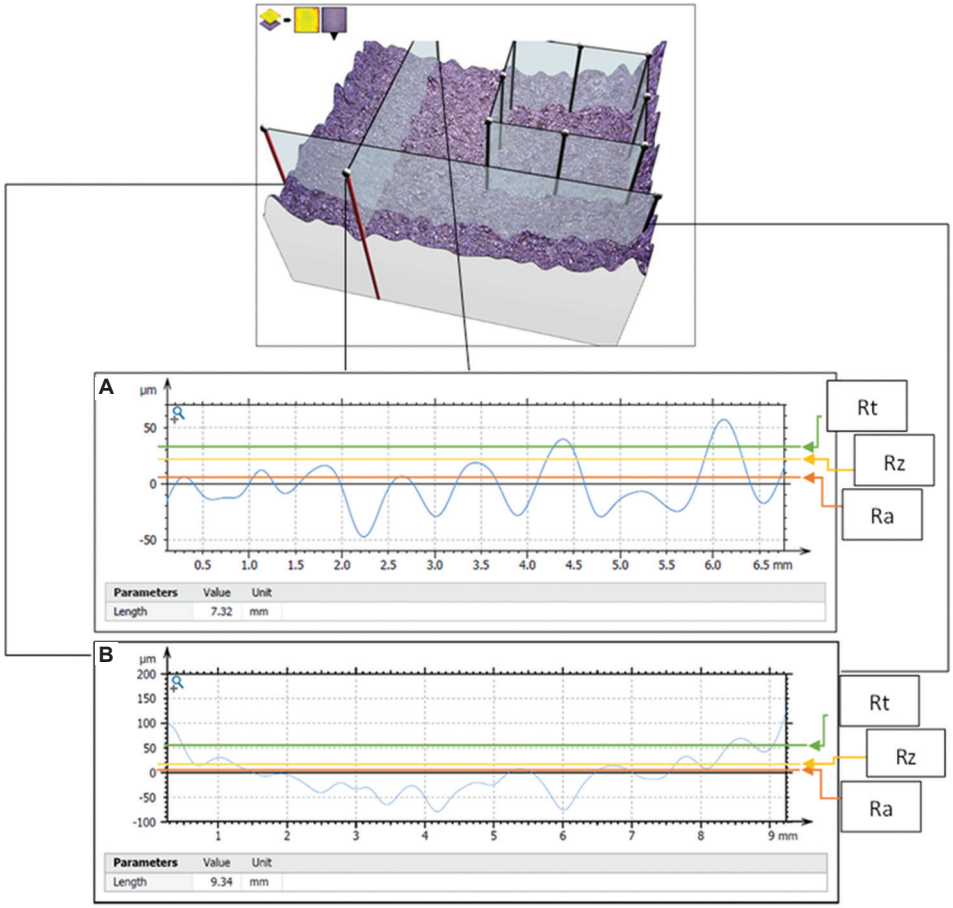

Figure 11. Cube with a prismatic shape face 1 W-profile: (A) transversal, (b) longitudinal

shape and height distribution. For the first face, the Rsk and Rku values were −0.29 and 1.96, respectively, in the transversal direction and −0.0702 and 1.91 in the longitudinal direction. For the second face, the values were −0.06 and 2.10 in the transversal direction and −0.0703 and 2.56 in the longitudinal direction. Negative Rsk values indicate surfaces with predominantly valleys, typical of sliding surfaces, whereas Rku values suggest compact surface textures without significant peaks. This is consistent with the post-treatment micro sandblasting process, which removes excess material and creates a visibly rough surface.

For the printed component (Figure 13), the mean roughness (Ra) values were 4.55 µm and 4.13 µm for the transversal and longitudinal directions, respectively. The maximum peak heights (Rp) were 5.36 µm and 5.05 µm, whereas the deepest valleys (Rv) were 8.02 µm and 8.57 µm. The total roughness (Rt) was 26.5 µm in the transversal direction and 39.5 µm in the longitudinal direction. The deeper valley in the longitudinal profile suggests inconsistent application of sandblasting post-treatment in that area.

Table 2. Comparison of the tribological values, Rsk and Rku, between the three parts

Sample	Rsk	Rku
Cube with a prismatic shape face 1		
Transversal	−0.29	1.96
Longitudinal	−0.0702	1.91
Cube with a prismatic shape face 2		
Transversal	−0.06	2.10
Longitudinal	−0.0703	2.56
Produced Component		
Transversal	0.208	2.17
Longitudinal	−0.0732	2.48

Abbreviations: Rku: kurtosis; Rsk: skewness.

Tribological values, Rsk and Rku, were used to compare the roughness of the three parts evaluated (Table 2). The roughness values for the cube with a prismatic shape face 2 were very similar to those of the printed component, which is expected since the parts were produced simultaneously

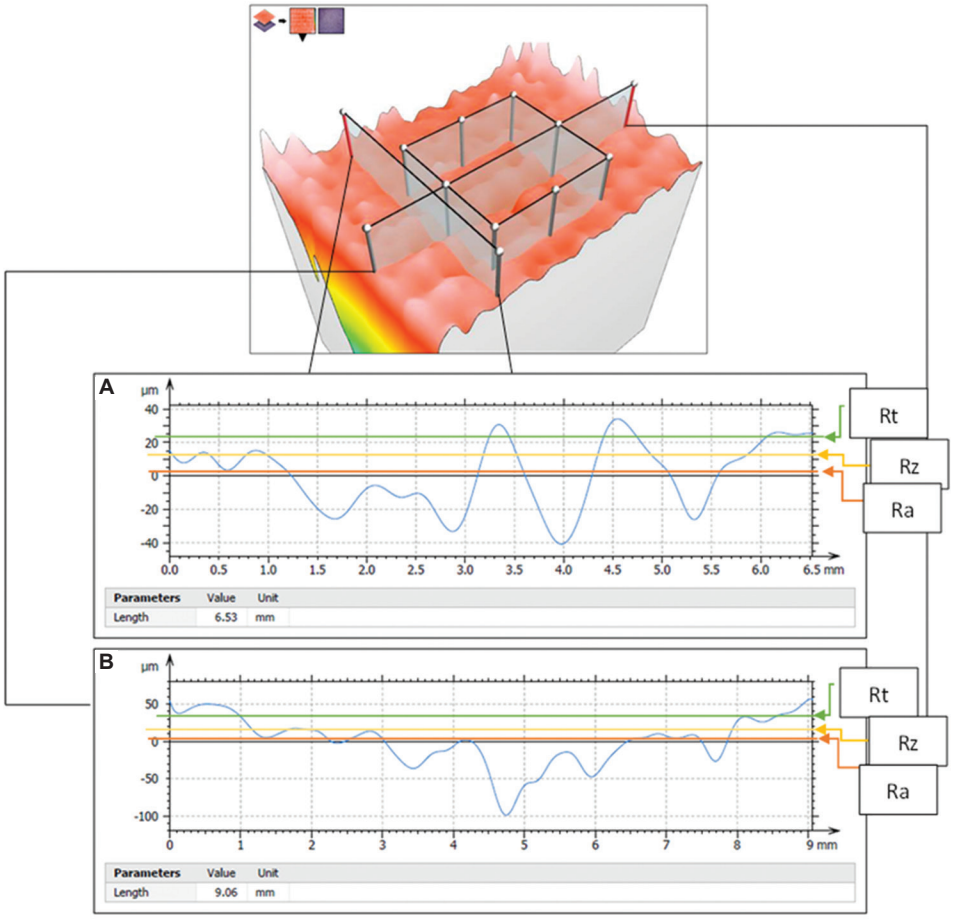

Figure 12. Cube with a prismatic shape face 2 W-profile: (A) transversal, (B) longitudinal

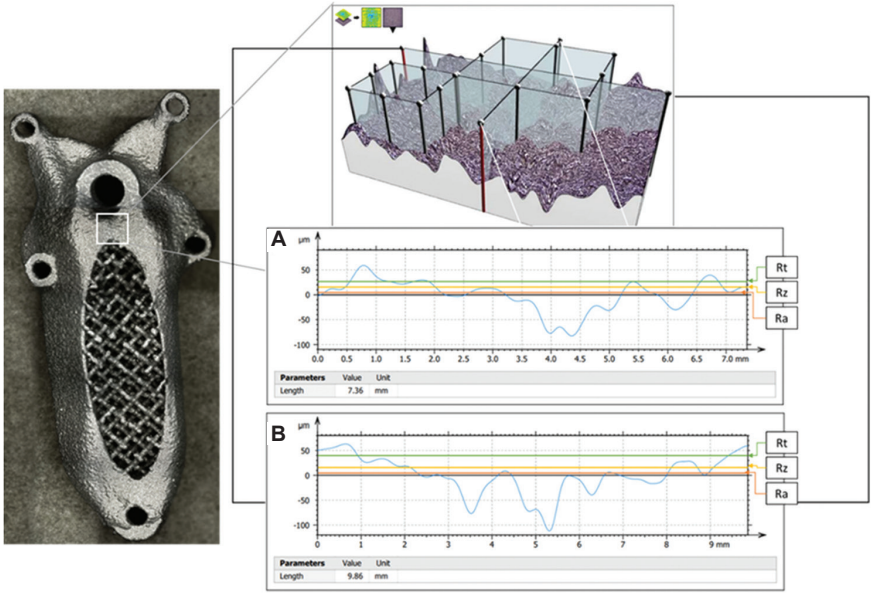

Figure 13. Printed component W-profile: (A) transversal, (B) longitudinal

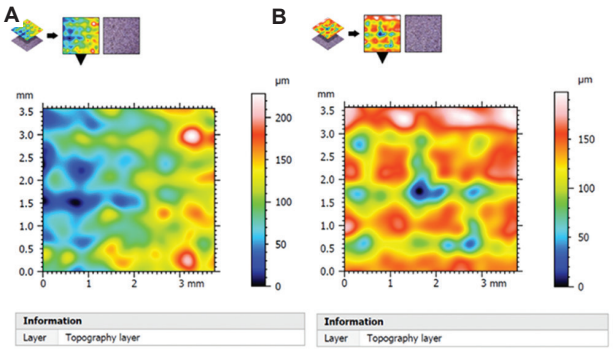

Figure 14. 3D surface texture after micro sandblasting of Alsi10Mg part: (A) transversal, (B) longitudinal

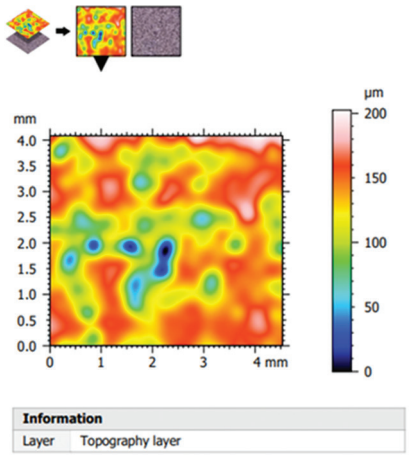

Figure 15. The 3D surface texture of the printed component after micro sandblasting Alsi10Mg part

and with the same laser parameters. The largest difference in Rsk occurs in the printed component's transversal direction. The positive Rsk in this section indicates a surface with predominantly peaks and asperities characteristic of a downskin surface, differing from the valley-dominated surfaces of the other parts (upskin surface). The down surface cloud's quality is only improved with more aggressive post-processing, such as a cycle on the vibratory tumbler.

Additional topological analysis using a 3D optical profilometer (Figure 14A and B for transversal and longitudinal, respectively) provided a more comprehensive representation of surface roughness than the 2D study. Here, roughness was expressed using areal parameters rather than directional profile measurements, with the arithmetical mean height (Sa) and maximum height (Sz) used instead of the profile-based parameters Ra and Rz. The Sa values were 30.1 µm and 25.2 µm for surfaces 1 and 2, respectively, and Sz values were 229 µm and 198 µm, respectively. The 15% reduction in roughness between the two surfaces is attributed to the micro sandblasting treatment and the natural fluctuations in the deposition process. Face 2 exhibited greater homogeneity than face 1, though neither showed symmetrical height distribution around the mean plane. Face 1 had a skewed height distribution (Ssk) below the mean plane with a value of 0.161, while face 2 had an Ssk of −0.604, indicating remaining surface peaks on face 2. This observation is consistent with the 2D data, where face 2 showed higher peak values (Sp) of 133 µm compared to 72.3 µm for face 1, while the deepest valleys (Sv) were 95.5 µm and 126 µm, respectively.

For the printed component (Figure 15), the arithmetical mean height (Sa) was 23.4 µm, while the maximum height (Sz) was 203 µm. The height distribution skewness (Ssk) was −0.812 – a higher value than that found in the cube – indicating that the printed component had greater valleys than its average height. As expected, the printed component displayed higher roughness than the cube, which is more complex geometry can explain.

Khan *et al.*[45] noted that roughness in LPBF parts is highly dependent on geometry, build position, and support volume. Horizontal surfaces typically have smoother finishes than inclined or vertical surfaces, which are more affected by the staircase effect. Larger volumes of support structures help reduce surface roughness by improving heat dissipation and reducing energy accumulation in processed layers. However, areas where the support structures are connected to the part often show localized roughness. Post-processing methods, such as sandblasting, significantly impact roughness on the surface. Mehta *et al.*[46] reported a reduced Sa of up to 43.2% after sandblasting. Parameters such as laser power and energy density can be adjusted to improve surface roughness. Maamoun *et al.*[47] achieved roughness as low as 4.5 µm by increasing energy density to 65 J/mm^3, though laser scanning speed must be carefully controlled due to its inverse relationship with roughness. Alternatively, surface treatments such as polishing shot blasting, and shot peening can further reduce roughness, with the latter reducing Sa by up to 79%.[48] However, these processes also increase production time and costs. Finally, Chu *et al.*[49] observed that satellite particles in the LPBF microstructure lead to defects such as lack of fusion, contributing to surface roughness. Visual analysis using ImageJ software and comparison to Chu *et al.*'s study suggests that the metallic powders supplied by Hypermetal had sufficient flowability and sphericity to produce a uniform topographic profile. The powder's narrow size distribution (d10, d50, and d90) did not appear to hinder the compaction process, though further analysis using laser diffraction could provide additional insights

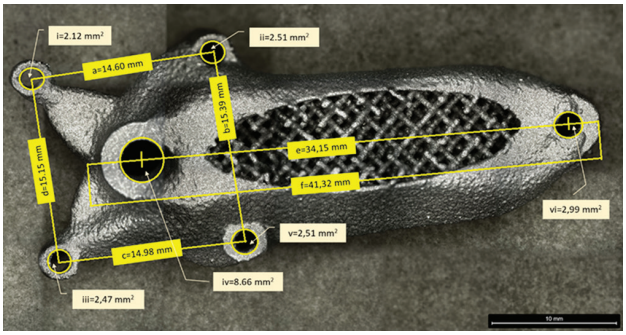

Figure 16. Features are measured directly in the component with the Leica® DVM6 and the analysis software LAX. Scale bar: 10 mm

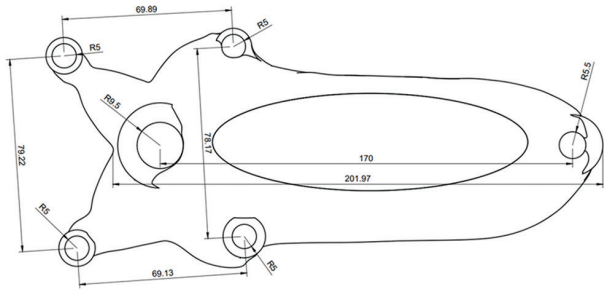

Figure 17. Technical drawing generated from the computer-aided design model and measurements of the interest features measured

into flowability and agglomeration. This would help address potential systematic errors in image processing and ensure accurate particle size measurements.

3.4. Dimensional analysis

Dimensional analysis compared measurements taken directly from the printed component using a Leica® DVM6 microscope with the dimensions specified in the original CAD model.

Figure 16 presents the raw measurement data from the Leica device, whereas Figure 17 shows the corresponding technical drawing. Since the component was produced at one-fifth of its original design size, all values in the technical drawing were divided by five to facilitate an accurate comparison. It is important to note that this scaling introduces an additional source of error that must be considered in the analysis.

For the linear dimensions (a to f), the mean difference between the printed component and the CAD model was 0.66 ± 0.39 mm, with a maximum deviation of 1.15 mm observed in dimension c. This represents a mean contraction/expansion of 3.34 ± 2.82%. The greatest contraction was recorded for measurement d (4.38%), while the largest expansion was observed in dimension c (8.35%).

The results indicate that the dimensional accuracy of the printed component does not meet the requirements for integration into a functional bicycle component, where high precision is essential. The most problematic deviations were observed in the holes intended for screw threads, where significant reductions in available space could compromise the component's functionality. Achieving greater dimensional accuracy is paramount, particularly for applications where precision is critical.

Dimensional accuracy in LPBF can be influenced by several factors, including powder quality, laser energy density, scanning speed, layer thickness, and the part's positioning relative to the assisted gas nozzle. In addition, material shrinkage during solidification plays a critical role, with the thermal expansion coefficient for this material being 2.1×10^{-5} mm/°C.[17] Although the laser path is typically programmed to account for this shrinkage, variations in powder quality, which were not accounted for in this study, may have contributed to the observed deviations. Other sources of error in this analysis stem from the manual nature of the measurements. Geometric figures were drawn manually on images captured with the optical microscope, as seen in Figure 17.

Furthermore, the conversion of dimensional values before comparison introduces additional uncertainty. These factors, combined with the laser spot diameter of 70 µm used for this build, suggest that the reduced size of the component led to lower dimensional accuracy, as finer details could not be captured with precision. Despite these challenges, the overall dimensional accuracy of the component can be considered acceptable, given the reduction in scale. However, the component should be fully scaled and analyzed using a Coordinate-Measuring Machine (CMM) to ensure the highest accuracy. A CMM would enable reverse engineering of the printed part, generating a new CAD model based on the actual measurements of the printed component. This model could then be compared directly with the original design, allowing for a more thorough evaluation of dimensional accuracy.

3.5. Hardness and material properties

In this study, the higher hardness of the AlSi10Mg component compared to similar studies in the literature can be attributed to differences in microstructure, particularly the grain size or the number of different phases (*e.g.*, precipitates) formed during the AM process. While the parts in this study and those in the literature exhibit similar relative densities, and both sets of parts are defect-free with no porosity, the microstructural features could contribute significantly to the observed variations in hardness.

Although the parts in this study and the literature used optimized process parameters to achieve highly dense, defect-free parts, it is possible that differences in the microstructure, such as finer or coarser grains or the presence of different phases, could lead to changes in hardness. These factors influence the mechanical properties of materials, including hardness, and may explain the higher hardness in our study compared to literature values.[50,51]

Thus, the higher hardness observed in this study is not solely due to differences in powder characteristics or densification but is more likely attributable to microstructural differences, including grain size and precipitates or other phases. Further studies focusing on the microstructure characterization in both this study and the literature would provide a more comprehensive understanding of how these factors contribute to variations in hardness and other mechanical properties.

4. Conclusions

This study explored a bicycle crank's TO and AM in AlSi10Mg using LPBF. The research successfully developed a lightweight and structurally optimized component by integrating advanced design strategies such as lattice structures. Rigorous testing and analysis validated the prototype's compliance with standards, manufacturability, and mechanical performance. The findings underscore the potential of TO and LPBF for creating high-performance, lightweight components while identifying areas for further improvement. Key conclusions drawn from this study are as follows:

- Component achievement:
  - Successfully designed and manufactured a topology-optimized bicycle crank in AlSi10Mg using LPBF
  - The single-part component complies with ISO 14781 and was validated through static testing
  - A lightweight design of 458 g was achieved by incorporating lattice structures into the topology-optimized component
  - Despite the production process's complexity, careful lattice cell selection ensured the successful fabrication of a functional prototype.
- Validation and testing:
  - Microstructure analysis:
    - Revealed elongated melt pools aligned with the scan direction, consistent with LPBF technology
    - Confirmed the absence of excessive porosity, ensuring manufacturing integrity.
- Surface roughness analysis:
  - Highlighted the impact of process variables, including part orientation, argon flow, supports, and post-processing
  - Identified limitations in surface quality inherent to LPBF technology, suggesting potential improvements through optimized process parameters or advanced post-processing methods such as vibratory tumbling or electrochemical polishing
  - Findings emphasize the importance of refining process parameters and post-processing techniques to achieve a smoother surface finish, which is critical for improving esthetic quality and tribological performance.
- Tribological investigations:
  - Surface roughness is critical in tribological performance, influencing friction and wear behavior
  - The tribological behavior of the component showed that surface roughness values directly correlate with friction and wear performance. Further optimization of the surface texture through post-processing may enhance the component's durability and functionality in real-world applications.
- Dimensional analysis:
  - Demonstrated variability in dimensional accuracy, with deviations of 0.66 ± 0.39 mm for lengths and 0.12 ± 0.05 mm for circle radii
  - Suggested improvements through additional supports, changes in part orientation, or adjustments to the geometry for enhanced manufacturability.
- Material and powder characteristics:
  - The narrow particle size distribution of AlSi10Mg powders facilitated consistent production results despite a 40% satellite particle presence.
- Considerations for future studies:
  - Conduct more detailed roughness studies, focusing on stair-stepping effects
  - Define dimensional tolerances for prototypes to enhance validation accuracy
  - Investigate the effects of particle size distribution and satellite particle percentages on the component's mechanical and surface properties
  - Explore scalability and economic feasibility for potential industrial applications
  - Examine the tribological performance of the component in greater detail, including wear resistance and friction in operational conditions
  - Further, optimize post-processing methods to enhance surface quality and tribological performance.

This research highlights the transformative potential of TO and LPBF in producing lightweight, high-performance components. It also identifies areas that need improvement to encourage broader industrial adoption. Future studies should concentrate on detailed microstructural analysis and the influence of process parameters on mechanical properties, particularly hardness. In addition, examining factors such as residual stresses, thermal gradients, and powder characteristics – such as particle size distribution and packing density – will offer valuable insights into optimizing component performance and consistency. These efforts will help bridge the gaps in understanding and enable more precise control over the manufacturing process for industrial applications.

Acknowledgments

This work results from Agenda "Hi-Rev – Recuperação do Setor de Componentes Automóveis", nr. C644864375-00000002, investment project nr. 64, financed by the Recovery and Resilience Plan (PRR) and by the European Union-NextGeneration EU.

Funding

This research received no external funding.

Conflicts of interest

The authors declare no conflicts of interest.

Author contributions

Conceptualization: Jose Manuel Costa, Manuel Fernando Vieira, Elsa Wellenkamp Sequeiros

Formal analysis: Jose Manuel Costa, Elsa Wellenkamp Sequeiros, Manuel Fernando Vieira

Investigation: Adriana Pinho Fernandes, Elsa Costa Oliveira, Mariana Cerqueira Maia, Jose Manuel Costa, Elsa Wellenkamp Sequeiros;

Methodology: Jose Manuel Costa, Elsa Wellenkamp Sequeiros;

Project administration: Jose Manuel Costa, Elsa Wellenkamp Sequeiros;

Supervision: Jose Manuel Costa, Manuel Fernando Vieira, Elsa Wellenkamp Sequeiros;

Validation: Jose Manuel Costa, Elsa Wellenkamp Sequeiros;

Visualization: Adriana Pinho Fernandes, Elsa Costa Oliveira, Mariana Cerqueira Maia, Jose Manuel Costa, Elsa Wellenkamp Sequeiros

Writing–original draft: Adriana Pinho Fernandes, Elsa Costa Oliveira, Mariana Cerqueira Maia, Jose Manuel Costa, Elsa Wellenkamp Sequeiros

Writing–review and editing: Jose Manuel Costa, Elsa Wellenkamp Sequeiros

All authors have read and agreed to the published version of the manuscript.

Ethics approval and consent to participate

Not applicable.

Consent for publication

Not applicable.

Availability of data

Not applicable.

References

1. Costa JM, Sequeiros EW, Santos RF, Vieira MF. Benchmarking L-PBF systems for die production: Powder, dimensional, surface, microstructural and mechanical characterisation. *Metals Basel.* 2024;14:520

   doi: 10.3390/met14050520

2. ISO/ASTM. *ISO/ASTM 52900: 2021-Additive Manufacturing-General Principles-Fundamentals and Vocabulary*. London: ISO; 2021. p. 28.

3. Pei E. *Springer Handbook of Additive Manufacturing*. Berlin: Springer; 2023.

4. Bar-Cohen Y. *Advances in Manufacturing and Processing of Materials and Structures*. United States: CRC Press; 2018.

5. Ford S, Despeisse M. Additive manufacturing and sustainability: An exploratory study of the advantages and challenges. *J Clean Prod.* 2016;137:1573-1587.

   doi: 10.1016/j.jclepro.2016.04.150

6. Costa JM, Sequeiros EW, Vieira MF. Fused filament fabrication for metallic materials: A brief review. *Materials.* 2023;16:7505.

   doi: 10.3390/ma16247505

7. Zutin GC, Pulquerio EC, Pasotti AV, Barbosa GF, Shiki SB. Application of robotic manipulator technology and its relation to additive manufacturing process-a review. *Int J Adv Manuf Technol.* 2024;133:257-271.

   doi: 10.1007/s00170-024-13710-9

8. Prakash KS, Nancharaih T, Rao VVS. Additive manufacturing techniques in manufacturing -an overview. *Mater Today Proc.* 2018;5:3873-3882.

   doi: 10.1016/j.matpr.2017.11.642

9. Zhou L, Miller J, Vezza J, *et al*. Additive manufacturing: A comprehensive review. *Sensors.* 2024;24:2668.

   doi: 10.3390/s24092668

10. Gibson I, Rosen DW, Stucker B. *Additive Manufacturing Technologies: Rapid Prototyping to Direct Digital Manufacturing*. New York: Springer US; 2010.

11. Costa J, Sequeiros E, Vieira MT, Vieira M. Additive manufacturing: Material extrusion of metallic parts. *U Porto J Eng.* 2021;7:53-69.

doi: 10.24840/2183-6493_007.003_0005

12. Gebhardt A, Kessler J, Thurn L. 5 Perspectives and Strategies of Additive Manufacturing. In: *3D Printing.* 2nd ed. Germany: Hanser; 2019. p. 137-165.

13. Gibson I, Rosen D, Stucker B, Khorasani M. *Binder Jetting.* Berlin: Springer International Publishing; 2021. p. 237-252.

14. Egan PF. Design for additive manufacturing: Recent innovations and future directions. *Designs.* 2023;7:83.

doi: 10.3390/designs7040083

15. Chen H, Wei Q, Wen S, Li Z, Shi Y. Flow behavior of powder particles in layering process of selective laser melting: Numerical modeling and experimental verification based on discrete element method. *Int J Mach Tool Manuf.* 2017;123:146-159.

16. Sun X, Chen M, Liu T, *et al*. Characterization, preparation, and reuse of metallic powders for laser powder bed fusion: A review. *Int J Extreme Manuf.* 2024;6:012003.

doi: 10.1088/2631-7990/acfbc3

17. Veetil JK, Khorasani M, Ghasemi A, *et al*. Build position-based dimensional deviations of laser powder-bed fusion of stainless steel 316L. *Precis Eng.* 2021;67:58-68.

doi: 10.1016/j.precisioneng.2020.09.024

18. Sehhat MH, Mahdianikhotbesara A. Powder spreading in laser-powder bed fusion process. *Granular Matter.* 2021;23:89.

doi: 10.1007/s10035-021-01162-x

19. Parteli EJR, Poschel T. Particle-based simulation of powder application in additive manufacturing. *Powder Technol.* 2016;288:96-102.

doi: 10.1016/j.powtec.2015.10.035

20. Haferkamp L, Haudenschild L, Spierings A, *et al*. The influence of particle shape, powder flowability, and powder layer density on part density in laser powder bed fusion. *Metals-Basel.* 2021;11:418.

doi: 10.3390/met11030418

21. Mostafaei A, Ghiaasiaan R, Ho IT, *et al*. Additive manufacturing of nickel-based superalloys: A state-of-the-art review on process-structure-defect-property relationship. *Prog Mater Sci.* 2023;136:101108.

doi: 10.1016/j.pmatsci.2023.101108

22. Costa JM, Vieira MF. Teaching design for AM to science materials engineering graduate students: Hand-on approach. *Modern Concepts Mater Sci.* 2024;6.

doi: 10.33552/MCMS.2024.06.000640

23. Costa JM, Sequeiros EW, Figueiredo D, Reis AR, Vieira MF. *Optimizing Metal AM Potential through DfAM: Design, Performance, and Industrial Impact*. London: IntechOpen; 2024.

24. Oliveira C, Maia M, Costa J. Production of an office stapler by material extrusion process, using DfAM as optimization strategy. *U Porto J Eng.* 2023;9:28-41.

doi: 10.24840/2183-6493_009-001_001635

25. Brackett D, Ashcroft I, Hague R. Topology optimization for additive manufacturing. In: *Proceedings of the 22nd Annual International Solid Freeform Fabrication Symposium-An Additive Manufacturing Conference*, SFF 2011, Austin, TX; 2011. p. 348-362.

26. Plocher J, Panesar A. Review on design and structural optimisation in additive manufacturing: Towards next-generation lightweight structures. *Mater Design.* 2019;183:108164.

doi: 10.1016/j.matdes.2019.108164

27. Ibhadode O, Zhang Z, Sixt J, *et al*. Topology optimization for metal additive manufacturing: Current trends, challenges, and future outlook. *Virtual Phys Prototy.* 2023;18:2181192.

doi: 10.1080/17452759.2023.2181192

28. Diegel O, Nordin A, Motte D. *A Practical Guide to Design for Additive Manufacturing*. Berlin: Springer; 2019.

29. ASM International. *Aluminum Science and Technology.* Vol. 2A. Netherlands: ASM International; 2018.

doi: 10.31399/asm.hb.v02a.9781627082075

30. Su J, Ng WL, An J, Yeong WY, Chua CK, Sing SL. Achieving sustainability by additive manufacturing: A state-of-the-art review and perspectives. *Virtual Phys Prototyp.* 2024;19:e2438899.

doi: 10.1080/17452759.2024.2438899

31. Sbrugnera Sotomayor NA, Caiazzo F, Alfieri V. Enhancing design for additive manufacturing workflow: Optimization, design and simulation tools. *Appl Sci.* 2021;11:6628.

doi: 10.3390/app11146628

32. Mata M, Pinto M, Costa J. Topological optimization of a metal extruded doorhandle using ntopology. *U Porto J Eng.* 2023;9:42-54.

doi: 10.24840/2183-6493_009-001_001620

33. Rometsch PA, Zhu Y, Wu X, Huang A. Review of high-strength aluminium alloys for additive manufacturing by laser powder bed fusion. *Mater Design.* 2022;219:110779.

doi: 10.1016/j.matdes.2022.110779

34. Tofail SAM, Koumoulos EP, Bandyopadhyay A, Bose S, O'Donoghue L, Charitidis C. Additive manufacturing: Scientific and technological challenges, market uptake and opportunities. *Mater Today.* 2018;21:22-37.

doi: 10.1016/j.mattod.2017.07.001

35. Shimano. *Shimano SLX M7000 Hollowtech II Crank*.

Available from: https://bike.shimano.com/technologies/details/hollowtech-2.html [Last accessed on 2024 Jul 10].

36. ISO. *ISO/IEC/IEEE 14764:2022-Software Engineering-Software Life Cycle Processes-Maintenance*. Switzerland: ISO; 2022. p. 36.
37. Sandvik. *Osprey® AlSi10Mg Powder for Additive Manufacturing - DATASHEET*. Available from: https://www.metalpowder.sandvik/en/syssiteassets/metal-powder/datasheets/osprey-alsi10mg-and-alsi7mg.pdf [Last accessed on 2024 Oct 19].
38. Li P, Kim Y, Bobel AC, *et al*. Microstructural origin of the anisotropic flow stress of laser powder bed fused AlSi10Mg. *Acta Mater.* 2021;220:117346.

    doi: 10.1016/j.actamat.2021.117346
39. Zhou L, Mehta A, Schulz E, McWilliams B, Cho K, Sohn Y. Microstructure, precipitates and hardness of selectively laser melted AlSi10Mg alloy before and after heat treatment. *Mater Charact.* 2018;143:5-17.

    doi: 10.1016/j.matchar.2018.04.022
40. Aboulkhair NT, Simonelli M, Parry L, Ashcroft I, Tuck C, Hague R. 3D printing of aluminium alloys: Additive manufacturing of aluminium alloys using selective laser melting. *Progress Mater Sci.* 2019;106:100578.

    doi: 10.1016/j.pmatsci.2019.100578
41. Mower TM, Long MJ. Mechanical behavior of additive manufactured, powder-bed laser-fused materials. *Mater Sci Eng A*. 2016;651:198-213.

    doi: 10.1016/j.msea.2015.10.068
42. Li BQ, Li Z, Bai P, Liu B, Kuai Z. Research on surface roughness of AlSi10Mg parts fabricated by laser powder bed fusion. *Metals Basel.* 2018;8:524.

    doi: 10.3390/met8070524
43. ISO_4287. *Geometrical Product Specifications (GPS)-Surface Texture: Profile Method-Terms, Definitions and Surface Texture Parameters*. Switzerland: ISO; 1997.
44. ISO/ASTM. *ISO 25178-600:2019-Geometrical Product Specifications (GPS)-Surface Texture: Areal-Part 600: Metrological Characteristics for Areal Topography Measuring Methods*. Switzerland: ISO; 2019. p. 21.
45. Khan HM, Karabulut Y, Kitay O, Kaynak Y, Jawahir IS. Influence of the post-processing operations on surface integrity of metal components produced by laser powder bed fusion additive manufacturing: A review. *Machining Sci Technol.* 2021;25:118-176.

    doi: 10.1080/10910344.2020.1855649
46. Mehta B, Hryha E, Nyborg L, Tholence F, Johansson E. Effect of surface sandblasting and turning on compressive strength of thin 316L stainless steel shells produced by laser powder bed fusion. *Metals Basel.* 2021;11:1070.

    doi: 10.3390/met11071070
47. Maamoun AH, Xue YF, Elbestawi MA, Veldhuis SC. Effect of selective laser melting process parameters on the quality of al alloy parts: Powder characterization, density, surface roughness, and dimensional accuracy. *Materials.* 2018;11:2343.

    doi: 10.3390/ma11122343
48. Sagbas B. Post-processing effects on surface properties of direct metal laser sintered AlSi10Mg parts. *Metals Mater Int.* 2020;26:143-153.

    doi: 10.1007/s12540-019-00375-3
49. Chu F, Zhang K, Shen H, *et al*. Influence of satellite and agglomeration of powder on the processability of AlSi10Mg powder in Laser Powder Bed Fusion. *J Mater Res Technol.* 2021;11:2059-2073.

    doi: 10.1016/j.jmrt.2021.02.015
50. Al Njjar A, Mazloum K, Sata A. Optimization of powder metallurgy parameters for improving the major properties of AA7075/SiC composites for aerospace applications. *J Mater Eng Perform.* 2024.

    doi: 10.1007/s11665-024-09998-z
51. Zhang P, Li X, Dong S, *et al*. Superhigh yield ratio and considerable plasticity in powder metallurgy Al-Zn-Mg-Cu alloy prepared with elemental powder. *JOM.* 2024;77:1241-1251.

    doi: 10.1007/s11837-024-07018-y

Our Journals

International Journal of Bioprinting is an international journal covering the technology, science and clinical application of the broadly defined field of Bioprinting. Bioprinting is defined as the use of 3D printing technology with materials that incorporate viable living cells or biological elements to produce tissue or biotechnological products. We are interested in the scientific topics spanning all stages of bioprinting process from concept creation to fabrication and beyond. Knowledge generated in these researches must be related to bioprinting. *IJB* covers subject areas, including but not limited to the following:

- Information technologies and basic research
- Materials and formulation
- Cell source and biotechnology for additive manufacturing
- 3D Bioprinting technologies
- New design and fabrication paradigm
- Applied research purpose & evaluation of 3D printed products
- Associated social implications

International Journal of AI for Materials and Design is an international, peer-reviewed open-access journal that aims to bridge the cutting-edge research between AI and materials, AI and design. In recent years, the tremendous progress in AI is leading a radical shift of AI research from a mainly academic endeavor to a much broader field with increasing industrial and governmental investments. The maturation of AI technology brings about a step change in the scientific research of various domains, especially in the world of materials and design. Machine learning (ML) algorithms enable researchers to analyze extensive datasets on material properties and accurately predict their behavior in different conditions. This subsequently impact the industry to leverage on big data and advanced analytics to build scientific strategies, scale operational performance of processes and drive innovation. In addition, AI and ML are uniquely positioned to enable advanced manufacturing technologies across the value chain of different industries. Integration of multiple and complementary AI techniques, such as ML, search, reasoning, planning, and knowledge representation, will further accelerate advances in scientific discoveries, engineering excellence and the future of cyber-physical systems manufacturing.

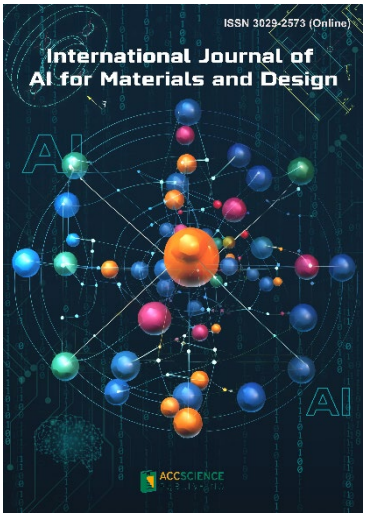

International Journal of AI for Materials and Design covers the following topics: AI or machine learning for material discovery, AI for process optimization, AI and data-driven approaches for product or systems design, application of AI in advanced manufacturing processes such as additive manufacturing, IoT, sensors, robotics, cloud-based manufacturing, intelligent manufacturing for various applications, autonomous experiments, material intelligence, energy intelligence, and AI-linked decarbonization technologies.

Start a new journal

Write to us via email if you are interested to start a new journal with AccScience Publishing. Please attach your CV, professional profile page and a brief pitch proposal in your email. We shall inform you of our decision whether we are interested to collaborate in starting a new journal.

Contact: info@accscience.com

https://accscience.com/journal/MSAM

Access Science Without Barriers

Contact

www.accscience.com
8 Burn Road, #15-03 Trivex, Singapore 369977
E-mail: editorial@accscience.com
Phone: +65 8182 1586